Fracture characteristics from two reactivated basement fault zones: examples from Norway and Shetland

Sleight, Janine Michelle

Fracture Characteristics from Two Reactivated Basement Fault Zones: Examples from Norway and Shetland

by

Janine Michelle Sleight

A thesis submitted in fulfilment of the requirements of the University of Durham for the degree of Doctor of Philosophy

Department of Geological Sciences
University of Durham

2001

Volume I of II

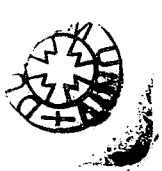

Declaration

No part of this thesis has been previously submitted for a degree at this, or any other university. The work described in this thesis is entirely that of the author, except where reference is made to previously published work.

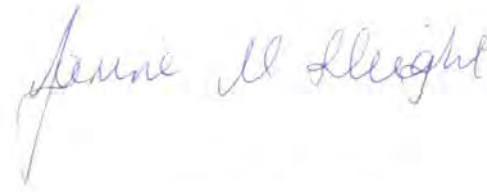

Janine M. Sleight

Department of Geological Sciences,
University of Durham
November 2001

Abstract

Detailed analyses of fracture attributes developed in basement rocks associated with two, crustal-scale faults, have enabled the characteristics and evolution of the fracture system geometry to be documented quantitatively. Data sets of fracture attributes have been collected adjacent to faults within the Møre-Trøndelag Fault Complex (MTFC) in Central Norway, and the Walls Boundary Fault System (WBFS) in Shetland. Both structures are of Palaeozoic origins and contain multiply reactivated fault strands that extend offshore to bound several hydrocarbon-rich sedimentary basins of Mesozoic-Cenozoic age along the North Atlantic margin.

Fracture characteristics from the MTFC were measured within one dominant lithology (acid gneiss) and therefore each data set of fracture characteristics is directly comparable. A number of different fracture parameters were measured using either 1-D or 2-D techniques and were collected over four data scales. These data indicate different signatures for the two main faults within the MTFC: the Verran Fault (VF), a highly reactivated structure and the Hitra-Snåsa Fault (HSF), which has experienced little reactivation, and also for a smaller, kinematically simple fault, the Elvdalen Fault (EF). The parameters measured are the exponent values from exponentially distributed spacing and length data sets, mean fracture spacing, fracture density, mean fracture length, fracture intensity and fracture connectivity (defined by the numbers of fractures and nodes per cluster, fracture cluster length and the number of nodes per unit area). Based on analyses of these parameters, the VF is characterised by a *tall* peak in values (or trough for measurements such as mean length and mean spacing), with a *wide* zone (~500m) of above-background values to the NW of the Verran Fault Plane. The HSF on the other hand is characterised by a *tall* and *narrow* zone of above-background values (or below for mean spacing and mean length parameters), which decrease to background levels within 100m either side of the Hitra- Snåsa Fault Plane. The EF is also characterised by a *narrow* but *shorter* peak in above background values, where the height of the peak is less than half that associated with the VF and HSF. These different signatures are most likely to be related to the differing reactivation histories between the three faults. In addition, the VF shows widespread evidence for multiple phases of fluid-related alteration and mineralisation, suggesting that the fracture network characteristics play an important role in controlling fluid flow in these otherwise relatively impermeable basement rocks.

The data sets of fracture characteristics collected adjacent to four faults within the WBFS display general trends consistent with the changes in fracture attributes observed adjacent to faults within the MTFC. However, the results are considered to be less reliable. Firstly, the data sets were collected within seven different lithologies, meaning that the fracture attributes must be considered separately, resulting in small data sets compared to those collected from gneisses within the MTFC. In addition, the four faults studied all have different kinematic histories.

The findings of this study show that detailed studies of fractures may potentially be used to fingerprint fault reactivation and enable its' recognition in the subsurface.

Acknowledgements

Firstly thanks to my supervisors, Ken McCaffrey and Bob Holdsworth in Durham, David Roberts from NGU in Trondheim and Tony Doré from Statoil, for their invaluable guidance and encouragement throughout this project.

Thanks also to the people who made fieldwork much more luxurious than most PhD students experience, namely John and Sandy in Shetland for the use of the hotel and those mad real ale nights, and Elin, Odd, Juliet and Jan in Trøngsundet for the use of the amazing Sjøhus, and for the introduction to the Norwegian ways of life (bars in the basement etc !).

I also appreciate the support that Statoil and Conoco have provided during this project, both financially and through the very useful and interesting work placements that I have undertaken in Stavanger and Houston.

To the unsung heros of the geology department in Durham, Karen, Dave and Gary, thanks for all your help over the years. Special thanks too to the postgrads in the department, especially Abi, Rich, Dave, Helen, Phill, Jules and Ade for the moral support and great memories.

Finally, thanks to the people without whom I probably wouldn't be writing this now. To Mum, Dad, Sis and Bro and the rest of my family for all their love and support throughout all my years of university life, and for always being there when I needed them. It is to you that I dedicate this thesis, for without you all, it would never have materialised. Lastly thanks to Lee for so many things. For persuading me that I really could carry on measuring millimetre-scale fracture spacings even after dropping my beloved dictaphone in the river, for not hitting the roof (or me) when I dropped a (large) rock on his compass clino (in the middle of nowhere), for being my field assistant and supervisor, but most of all for making the last four years the best years of my life.

List of Contents

VOLUME I

VOLUME II

LIST OF TABLES

CHAPTER 1 - FAULT ZONE DEFORMATION AND FRACTURE ANALYSIS

1.1 Introduction and aims of research

Brittle discontinuities are the major expression of strain within the Earth's uppercrust, occurring on all scales from millimetre- (microfractures) to metre- (fractures) to kilometre-scales (faults/fault zones). Large-scale fault zones control the location, architecture and evolution of a wide range of geological features, such as rift basins and orogenic belts, and are also associated with seismic activity (earthquakes), therefore constituting one of the most important geological hazards. The degree of fault/fracture network development also plays an important role in fluid transport in the uppercrust. Fracture networks can act as key conduits for the migration of fluids through otherwise impermeable (or low-permeability) rocks (e.g. basement rocks, chalk), thus enhancing fluid flow, but can also act as barriers to flow when sealed fractures occur within highly porous/permeable rocks (e.g. sandstone), and therefore restrict fluid flow.

The ability of fractures/faults to transmit fluids, and act as secondary permeability within rocks, has important consequences on, for example, a) the migration of hydrothermal fluids and the location of ore deposits, b) movement of contaminants within groundwater supplies (e.g. pesticides), c) emplacement of igneous intrusions, d) possible escape of radioactive and toxic waste from underground repositories, and e) the migration and accumulation of hydrocarbons.

Oil and gas accumulations within fractured reservoirs have long been challenging targets for the hydrocarbon industry. It was suggested in 1960 by Landes, that "*oil deposits within the basement rocks should be sought with the same professional skill and zeal as accumulations in the overlying sediments*". Yet today, forty years on, hydrocarbons produced from fractures are still a rarity, and are usually discovered by accident (e.g. White Tiger (Bach Ho) field, Cuu Long Basin, offshore Vietnam, which produces oil from fractured granite (Bergman & Woodroof, 2001)). This is partly due to the technical difficulties experienced when attempting to exploit oil/gas within fractures. A good understanding of the fracture network geometry is essential for

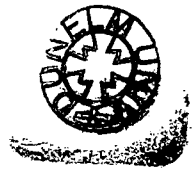

production at maximum efficiency (i.e. ensuring that wells drilled intersect the maximum number of fractures within the reservoir). For example, the Clair Oil Field, which lies ~75km to the west of the Shetland Isles, was discovered in 1977 by BP (Coney et al., 1993). Oil is accumulated within fractured Lewisian basement, and overlying Devonian Old Red Sandstones. Total oil in place (OIP) in the Clair field is estimated to be >3000 million barrels, making the field the largest undeveloped oil discovery on the UK continental shelf. The field is currently projected to come on-stream in 2004, meaning that it will have taken more than 25 years from discovery to production, due, amongst other things, to the occurrence of oil within fractures, and the associated difficulties of exploitation. Therefore, understanding the location, density, intensity and connectivity of fractures within rocks is essential for evaluating the hydraulic parameters of impermeable reservoirs.

Onshore studies of fracture parameters can be used as analogues to help understand, and possibly predict, the geometry of fracture networks in the sub-surface. Numerous studies have been carried out onshore to analyse the characteristics of fracture networks, usually from simple geological settings within sedimentary rocks (e.g. Narr and Suppe, 1991, Odling, 1995, Bloomfield, 1996, Castaing et al., 1996, Peacock, 1996, Odling, 1997, Pascal et al., 1997, Rochford, 1997, Odling et al., 1999, Gillespie et al., 2001). However, there have been relatively few detailed studies of fracture attributes either along large-scale strike-slip fault systems, or within geologically complicated areas, such as in the vicinity of multiply reactivated fault systems (one example is Beacom, 1999).

The aim of this thesis is to quantitatively assess the fracture parameters associated with two, large-scale, crustal fault zones. The structures chosen are the Møre-Trøndelag Fault Complex (MTFC) in Central Norway, and the Walls Boundary Fault System (WBFS) in Shetland. Both structures contain multiply reactivated fault strands, and extend offshore to bound several hydrocarbon-rich sedimentary basins along the North Atlantic margin. As well as characterising the fracture networks associated with each structure, parameters such as length, spacing and connectivity have been compared between highly reactivated structures and those that have experienced little reactivation, and also within different lithologies. This allows an assessment of both lithological and structural controls on fracture network attributes and their evolution.

1.2 Outline of thesis

- **Chapter 1** – Processes and products within fault zones are introduced, together with key fracture attributes and fracture population analysis.
- **Chapter 2** – Introduces the geological setting of the Møre-Trøndelag Fault Complex, Central Norway, highlights the key structural components and exposures of the fault complex, and presents a summary of previous work on the kinematic evolution of the fault system.
- **Chapter 3** – Describes fracture attribute data (orientations, infills, kinematics and spacings) collected in the field along 1-dimensional transects, adjacent to the two main structures within the MTFC (Verran Fault and Hitra-Snåsa Fault), along with two other linking faults within the system (Rautingdalen Fault and Elvdalen Fault).
- **Chapter 4** – Presents fracture attribute data (spacing, length and connectivity) collected from four different data scales within the MTFC (thin section, outcrop, air photograph and Landsat™), measured within 2-dimensions.
- **Chapter 5** – Introduces the geological setting of the Walls Boundary Fault System (WBFS), Shetland, highlights the key structural components and exposures of the fault system, and presents a summary of previous work on the kinematic evolution of the WBFS.
- **Chapter 6** - Describes fracture attribute data (orientations, infills, kinematics and spacings) collected in the field along 1-dimensional transects, within a variety of lithologies adjacent to faults within the WBFS.
- **Chapter 7** - Presents fracture attribute data (spacing, length and connectivity) collected at outcrop scale and measured in 2-dimensions, within a variety of lithologies adjacent to faults within the WBFS.
- **Chapter 8** – Synthesises and discusses the statistical analysis of fracture attributes from both the MTFC and WBFS. Data from the two fault systems are compared and contrasted, and possible signatures of fault reactivation using fracture parameters are discussed.

1.3 Fault zone structure / components

Fault zones occur in both inter-plate and intra-plate settings, at all scales in the earths crust. A *fault* is defined by Twiss & Moores (1992) as 'a surface or narrow zone along which one side has moved relative to the other in a direction parallel to the surface or zone'. The term *fracture* is used to describe small-scale faults that have observable offset. *Joints* are breaks in a rock with no observable displacement (section 1.4.1.1). Faults and fractures are classified by the sense of displacement into dip-slip, strike-slip and oblique-slip structures.

Conventionally faults are defined and drawn schematically as single planar structures, where all displacement and deformation occurs on a single surface. This is however a gross oversimplification, as illustrated by numerous field studies of faults at all scales. It is often more appropriate to characterise fault zone structure using the geometry and connectivity of fractures and subsidiary faults.

In simplified terms there are three principal components that define an upper crustal fault zone: a) the fault core, a central zone of highest fracture/strain intensity, b) the damage zone, a zone of increased deformation, c) the protolith, which is defined as the area where deformation intensity is decreased to regional or background levels (Evans et al., 1994, Caine et al., 1996, Gudmundsson et al., 2001) (**Figure 1.1**).

Caine et al., (1996) describe four possible end members for upper crustal fault zone architecture and fault-related fluid flow, depending on the relative permeabilities of the fault core and damage zone (**Figure 1.2**).

1.3.1 *Fault Core*

This portion of the fault zone is usually where most of the displacement has been accommodated. The narrow (c. >10m) fault core may contain slip surfaces and fault rocks such as fault gouge, breccia and cataclasite (see section 1.4), geochemically altered rock and mineral precipitation.

1.3.2 *Damage zone*

The damage zone is described by Knott et al., (1996) as the deformed rock volume around the master fault. More specifically the damage zone is described in this thesis

as the high strain zone around large faults, adjacent to the fault core, where a concentrated population of micro- and meso-scale fault related structures (e.g. small faults, fractures, veins) occurs. The deformation in damage zones occurs during fault-tip propagation and during slip along the master fault surface (Kelly et al., 1998, Knott et al., 1996). Damage zones are characterised by decreasing fracture length, increasing fracture frequency and increasing fracture connectivity towards the fault core (Arnesen 1995). The geometry and location of damage zones are important as they may contribute to compartmentalisation of a reservoir, or provide fracture-controlled pathways for fluid migration. The width of the damage zone is dependent on a number of geological variables including lithology, fault kinematics, and fault reactivation (Arnesen 1995). A wide fault damage zone may indicate multiple episodes of slip (reactivation), overprinting successive deformation events (Caine et al., 1996). The structures in the damage zone are mostly unrecognisable on seismic sections due to the resolution of the data being only down to ~20m.

1.3.3 *Protolith*

The protolith is defined as the relatively undeformed area of rock, where deformation is regional and classed as being at "background" level, and not related to the tectonic event(s) that produced the fault core and damage zone.

1.4 Fault zone deformation processes and products

Deformation processes within large, crustal-scale fault zones fall into two categories – frictional (brittle) and viscous (ductile), (**Figure 1.3**). The depth of the transition between dominantly brittle and dominantly ductile deformation is dependant on many geological factors such as fluid pressure, lithology, stress field orientation, geothermal gradient, pre-existing fabrics and bulk strain rate. The assemblage of fault rocks produced depends on the operating deformation processes.

1.4.1 *Frictional (brittle) deformation processes*

Frictional deformation processes include fracture, frictional grain boundary sliding, cataclasis and frictional melting.

1.4.1.1 Fracture

The term fracture, from the Latin *fractus* meaning broken, is used to describe a discrete break or physical discontinuity within a rock mass, across which cohesion was lost or reduced due to stresses exceeding the rupture strength of the rock. This definition includes faults, joints, veins and stylolites. Fractures may be classified by *origin*, *size* or *mechanism*, as detailed in the following sections.

1.4.1.1.1 *Classification by fracture origin*

This classification, proposed by Stearns & Friedman (1972) and modified by Nelson (1979), is based on the origin of the causative forces, as determined by laboratory data and fracture system geometry.

a) Tectonic fractures – "Those whose origin can, on the basis of orientation, distribution and morphology, be attributed to or be associated with, a local tectonic event. As such, they are developed by the application of surface or external forces" (Nelson 1985). Tectonic fractures are directly associated with a structural feature, and their characterisation, geometry and connectivity are essential with respect to fluid flow (for example hydrocarbons, water, and leakage of nuclear waste). It is this type of fracture that this thesis is concerned with.

b) Regional fractures appear to be unrelated to local structures and are developed over large areas of the earth's crust with little change in orientation, and with no evidence of offset (Stearns & Friedman 1972, Nelson 1982). It has been suggested that the most likely explanation for the existence of regional fractures is regional uplift (Aguilera 1995), although there are other possible causes. Due to little offset and their lateral extent, these fractures are very conductive to fluid flow. In some cases, excellent hydrocarbon production can be obtained from regional fractures superimposed over local tectonic fractures (Aguilera 1995).

c) Contractional fractures are associated with a general bulk-volume reduction throughout the rock, and can be either tensional or extensional. They are the result

of either desiccation, syneresis (dewatering), thermal contraction during cooling of hot rocks (e.g. columnar jointing) or mineral phase changes (Nelson 1979). These fractures are initiated by internal body forces rather than external surface forces.

d) Surface-related fractures have diverse origins, and are developed as a result of the application of body forces. This group includes fractures developed during unloading, and both mechanical and chemical weathering for example during freeze-thaw cycles (Nelson 1979). "Weathering fractures" should not be confused with the weathering or erosion of pre-existing fractures in outcrop.

1.4.1.1.2 *Classification by fracture size*

Fractures develop in the upper crust on all scales, and are generally classified into four groups based on size – micro-scale, meso-scale, macro-scale and mega-scale (Ameen 1995, Engelder 1987). Micro-scale fractures include structures that affect individual crystals or grains such as intergranular fractures, intragranular fractures, and grain boundary fractures. These structures occur on a microscopic scale, and may be observed using optical microscopy. Meso-scale fractures are observable in hand specimen and at outcrop scale in continuous exposures. Macro-scale fractures are generally too large or too poorly exposed to be observed in outcrop, but may be identified on air photographs as lineaments. Mega-scale fractures may occur on continental scales and are generally hundreds or thousands of kilometres in length; for example the Walls Boundary Fault Zone, Shetland, Scotland and the Møre-Trøndelag Fault Complex, Central Norway (comprising the Verran and Hitra-Snåsa Faults) which are the focus of this study. Mega-scale fractures may be observed on Landsat™ and other satellite images. The "damage zone" of deformation (section 1.3.2) associated with macro-scale and mega-scale structures is composed of micro- and meso-scale fractures.

1.4.1.1.3 *Fracture classification by mechanism*

In fracture mechanics, meso-scale tectonic fractures can be subdivided into three groups depending on the relative motion that has occurred across the fracture surface during formation (e.g. Atkinson 1987, Goldstein & Marshak 1988, Twiss & Moores 1992, Pollard & Aydin 1988, Schultz 2000):

a) Mode I fracture propagation occurs when the opening displacement is perpendicular to the plane of fracture (**Figure 1.4a**). This type of motion describes extension fractures, including joints and veins, for dilation normal to the fracture surface, and anticracks (pressure solution surfaces or stylolites) for contraction normal to the fracture surface.

b) Mode II fracture propagation occurs when the motion of displacement is parallel to the fracture walls. This displacement describes a type of shear fracture. For Mode II shear fractures, the motion is perpendicular to the propagation front of the fracture (**Figure 1.4b**).

c) Mode III fracture propagation also occurs when the motion of displacement is parallel to the fracture walls, as in Mode II, and describes the second type of shear fracture. For Mode III shear fractures motion is parallel to the propagation front of the fracture (**Figure 1.4c**).

d) Mixed-mode fractures are described as having components of displacement both perpendicular and parallel to the fracture surface, and are also known as oblique extension fractures, transitional tensile joints and hybrid extension/shear fractures. Mixed-mode fractures propagate by a combination of either mode I + mode II or mode I + mode III displacement.

Each mode of fracture propagation can be represented on a Mohr-Coulomb diagram. Mode I (extension) fractures occur when the failure envelope is in contact with the Mohr circle at only one point. Mode II and III (shear) fractures occur when the Mohr circle is in contact with the envelope of failure at two points. Mixed-mode fractures occur when the envelope of failure is in contact with the Mohr circle in two places, but such that one of the principle stresses is tensile (**Figure 1.5**) (Hancock 1985, Goldstein & Marshak 1988, Price & Cosgrove 1991, Twiss & Moores 1992, Schultz 2000).

Based on the classification of fractures by opening displacement, Schultz (2000) devised a simple kinematic classification of geological fractures displayed in **Figure 1.6**.

1.4.1.2 Cataclasis

Sibson (1977) defines cataclasis as "the brittle fragmentation of mineral grains with rotation of grain fragments accompanied by frictional grain boundary sliding and

dilatency". The fault rock products may be incoherent clastic materials (breccia, gouge), or cohesive rocks (cataclasite) (sections 1.4.2.1, 1.4.2.2, 1.4.2.3).

1.4.1.3 Frictional grain boundary sliding

Frictional grain boundary sliding is the process of individual grains sliding past each other, and occurs when the frictional and cohesive forces between the grains have been overcome. This process commonly occurs during the deformation of poorly lithified, fluid-rich sediments, and is associated with little intragranular deformation (Maltman 1994). The process of frictional grain boundary sliding contributes to the formation of deformation bands or granulation seams within porous sandstones (Gabrielson et al., 1998).

1.4.1.4 Frictional melting

During an earthquake under dry conditions, at depths less than 10-15km, frictional heating can cause melting of the rocks. The resulting material is known as pseudotachylite (section 1.4.2.4) (Twiss & Moores 1992).

1.4.2 *Frictional (brittle) deformation products*

The products of frictional deformation are determined 'cataclastic fault rocks' (**Figure 1.3, Table 1.1**) (Sibson 1977, Twiss & Moores 1992, Holdsworth et al., 2001) and include gouge, breccia, cataclasites and pseudotachylites.

Fault gouge is an incohesive rock composed mostly of very fine-grained clay minerals, with few wall rock fragments. A breccia comprises more than 30% angular fragments from the wall rock, surrounded by a fine-grained matrix. When less than 30% of the fault rock volume is composed of fragments in a fine matrix, the rock is defined as a cataclasite. Pseudotachylite is a cohesive rock that occurs as distinct dark veins of glassy material. It contains very fine-grained mineral or wall rock fragments cemented by glass or devitrified glass. Pseudotachylite is formed as a result of frictional melting (section 1.4.1.4)

			RANDOM FABRIC	FOLIATED
INCOHESIVE			Fault breccia (visible fragments >30% rock mass)	?
			Fault gouge (visible fragments <30% rock mass)	?
COHESIVE	Nature of matrix	Glass	Pseudotachylite	?
		Tectonic reduction in grainsize dominates grain growth by recrystallisation and neomineralisation	Crush breccia (fragments > 0.5cm) Fine crush breccia (fragments 0.1 – 0.5cm) Crush microbreccia (fragments < 0.1cm)	Proportion of matrix: 0 – 10%
			Protocataclasite / Cataclasite / Ultracataclasite — Cataclasite series	Proto mylonite / Mylonite / Ultra – Mylonite — Phyllonite varieties — Mylonite Series; Proportion of matrix: 10 – 50% / 50 – 90% / 90 – 100%
		Grain growth pronounced	?	Blastomylonite

Table 1.1 Textural classification of fault rocks (after Sibson 1977)

1.4.3 *Viscous deformation processes and products*

Viscous deformation involves mechanisms such as diffusive mass transfer (DMT) and crystal plasticity (Knipe 1989).

Fault rocks produced by viscous deformation are termed the mylonite series (**Figure 1.3, Table 1.1**) (Sibson 1977, Holdsworth et al., 2001) and include mylonite and phyllonite. A mylonite is a foliated and usually lineated rock that shows evidence for strong viscous deformation (White et al., 1980, Passchier & Trouw 1996). Many mylonites contain porphyroclasts, which are remnants of resistant mineral grains. A commonly used mylonite classification is based on the percentage of matrix compared to porphyroclasts (Sibson 1977, Passchier & Trouw 1996). Rocks with 10-50% matrix are classified as *protomylonites*, rocks with 50-90&% matrix are classified as *mylonites*, and rocks with >90% matrix are classified as *ultramylonites* (**Table 1.1**). A phyllonite is a fine-grained, phyllosilicate rich mylonite (Passchier & Trouw 1996).

1.5 Kinematic indicators

The following sections describe some of the most useful criteria for determining the sense of displacement (sinistral, dextral, normal, reverse or oblique) in both brittle and ductile regimes. Identification of kinematic indicators in the field with the human eye, should be complemented with observations in orientated thin-sections, cut parallel to the lineation (shear direction) and perpendicular to the foliation (flattening plane).

1.5.1 *Brittle indicators*

There are principally three ways of obtaining information on the displacement direction of faults and fractures, by the displacement of markers, by direct observation of the fault plane, or by the geometry and kinematics of subsidiary fault and fracture arrays.

1.5.1.1 Displacement markers

If two points either side of the fault plane can be identified that were originally coincident, for example a displaced dyke, the apparent sense of fault movement may be identified, and the amount of displacement measured.

1.5.1.2 Direct fault plane observations

A more accurate method of analysing fault/fracture movement is the direct observation of linear striations (slickensides) on the fault/fracture plane, which form parallel to the direction of displacement. Two main types of lineation are identified, slickenlines, and slickenfibres (Price & Cosgrove 1991). Slickenlines are grooves and linear features that occur on a polished (slick) fault/fracture plane. They are the result of gouging by resistant minerals and rock particles as movement occurred (**Figure 1.7**). Slickenfibres (also known as growth fibres) are commonly composed of minerals such as calcite or quartz. They occur on fault/fracture planes, having grown as movement occurred (**Figure 1.10**).

1.5.1.3 Subsidiary structures

The geometry and kinematics of subsidiary sets of fractures associated with larger fault/fracture planes can also be used to identify the sense of shear.

1.5.1.3.1 *Conjugate fractures and Riedel shears*

Fracture orientations can be used to determine shear sense in two main ways, either by using conjugate fracture geometries, or by the development of Riedel structures. When conjugate pairs of shear fracture planes are identified and their orientations established, the slip direction can be inferred by using the Navier-Coulomb theory of brittle failure (**Figure 1.8**). After a study based on simple shear experiments, subsidiary shear fractures called Riedel shears can also be used to determine shear sense (Riedel 1929, Tchalenko, 1970, Hancock 1985, Passchier & Trouw 1996). Riedel structures are identified by their kinematics and geometry with respect to the principal displacement direction, which is parallel to the fault boundary (**Figure 1.9**). Riedel structures are divided into R, R', P and Y shears, each with a characteristic orientation and shear sense relative to the fault boundary (Passchier & Trouw 1996).

1.5.1.3.2 *Fibrous vein infills*

Syntaxial and antitaxial fibrous vein infills of minerals such as quartz and calcite are in some cases displacement controlled, i.e. the fibres grow in the opening direction of the vein, and can therefore be used as an indicator of wall rock displacement (Passchier & Trouw 1996) (**Figure 1.10a**). The fibres in undeformed extensional veins are perpendicular to the vein margin, whereas the fibres in shear veins or hybrid fractures are oblique to the vein margin (Hancock 1985) (**Figures 1.10b).** Veins that lie at a high angle to the extension direction, and develop parallel to the maximum principal stress, are known as tension gashes (**Figure 1.10c**). Fibrous infills formed at a small angle to the opening direction, e.g. subparallel to the vein wall, are known as slickenfibres (Passchier & Trouw 1996), and are often observed directly on fault/fracture surfaces (section 1.5.1.2) (**Figure 1.10d**).

1.5.1.3.3 *En-echelon fracture arrays*

Tension gashes (section 1.5.1.3.2) develop in sets that are often arranged en-echelon, and this arrangement can be used as a kinematic indicator in brittle fault zones (Beach 1975, Price & Cosgrove 1991, Passchier & Trouw 1996). The acute angle between the tension gash and the fault plane points in the direction of movement and is a unique indicator of shear sense (Twiss & Moores 1992) (**Figure 1.11**). With progressive deformation, the tips of tension gashes may be rotated into 'S' or 'Z' shapes depending on the overall shear sense of the fault zone. However, the veins will continue to grow at 45° to the fault zone margins, because the principal stresses are fixed (**Figure 1.11**). The amount of rotation of the veins may reflect the amount of shear until a new set propagates through (Price & Cosgrove 1991, **Figure 1.11b**).

1.5.2 *Viscous Indicators*

- One of the simplest kinematic indicators is the deflection of layering or foliation into a shear zone. The foliation may have a characteristic curved shape that can be used to determine the sense of shear, only if the movement direction (defined by the lineation) is normal to the axis of curvature (Passchier & Trouw 1996) (**Figure 1.12a, 1.12b**).

- Compositional layering or mica-preferred orientation in ductile fault rocks such as mylonite (section 1.4.2) may be cross-cut at a small angle by sets of sub-parallel minor shear zones known as shear bands (Passchier & Trouw 1996) (**Figure 1.12a, 1.12c**). Shear bands are composed of two sets of planar anisotropies, C-surfaces referring to 'cisaillement' (from French for shear), and S-surfaces referring to 'schistosite' (schistosity /foliation) (Simpson & Schmid 1983). Two sets of shear band cleavage are described in the literature, C-type and C'-type (**Figure 1.12c**). Shear bands are also known as S-C or C-S fabrics, they often form in weakly foliated mylonites and can be used as reliable shear sense indicators.
- Mylonitic gneisses in shear zones often contain larger grains referred to as porphyroclasts or augen within a more fine-grained ductile matrix. The porphyroclasts often have tails/beards of finer grained recrystalised material, which extend along the foliation planes in the direction of movement. These can be used to determine the sense of shear and are commonly known as mantled porphyroclasts. (**Figure 1.12a, 1.12d**) (Simpson & Schmid 1983).
- When a high contrast in the ductility between the porphyroclast and the finer-grained matrix occurs, the sense of rotation of the porphyroclast and the resulting pressure shadows can be used to determine the sense of shear (**Figure 1.12a**) (Simpson & Schmid 1983). However in determining the sense of shear from porphyroclasts using either tails or pressure shadows due to rotation, it may be necessary to examine several examples in a specimen before the shear sense can be determined with confidence.
- Large porphyroclasts such as feldspars or pyroxenes can become displaced and broken in sheared rocks and can be used as shear sense indicators (**Figure 1.12a, 1.12e**). However, it is important to note that the sense of displacement along microfractures orientated oblique to the foliation plane is in many cases opposite (antithetic) to the overall sense of shear (Passchier & Trouw 1996).
- Single crystals of mica within viscous fault rocks commonly have an elongate shape and are known as 'mica fish', and can be used as shear sense indicators (**Figure 1.12a, 1.12f**) (Passchier & Trouw 1996).

The above list of kinematic indicators in the viscous regime is not exhaustive, as illustrated by the additional indicators illustrated in **Figure 1.12a**. For a more detailed account readers are referred to Passchier & Trouw, 1996.

1.6 Fault zone reactivation

Reactivation is defined as "the accommodation of geologically separable displacement events (intervals >1Ma) along pre-existing structures" (Holdsworth et al., 1997). These long-lived zones of weakness include major compositional/ rheological boundaries, faults and shear zones in the continental lithosphere and they tend to repeatedly reactivate in preference to the formation of new zones of deformation (Holdsworth et al., 1997). Pre-existing heterogeneities in the lithosphere therefore strongly influence the location and architecture of features such as fault bounded sedimentary basins and orogenic belts (Dewey et al., 1986, Daly et al., 1989).

Two types of reactivation have been identified depending on the senses of relative displacement for successive events **Figure 1.13** (Holdsworth et al., 1997):

a) Geometric reactivation where for successive events, reactivated structures display different senses of relative displacement,

b) Kinematic reactivation where for successive events, reactivated structures display similar senses of relative displacement.

Four groups of criteria have been identified (Holdsworth et. al., 1997) that are considered reliable in recognising reactivation: stratigraphic, structural, geochronological and neotectonic (**Figure 1.14**)

Wherever possible, several criteria should be recognised in order to be certain reactivation has occurred, ideally with absolute age constraints of fault movements and repeated displacement events.

1.7 Fracture parameter analysis

Fracture parameter analysis involves the characterisation of all fracture attributes to describe the fracture network geometry. The geometry of the fracture network may then be used to analyse fracture connectivity. The following sections describe the fracture parameters that contribute to the network geometry.

1.7.1 *Aperture*

The fracture aperture is defined as the perpendicular distance across the void between adjacent fracture walls. The ability of the fracture to transmit fluid (fracture permeability) is primarily dependent on the size of the opening – or aperture (Neuzil & Tracy, 1981). Apertures can be described by the terms described in **Table 1.2**.

Aperture width	Description	Summary
< 0.1 mm	Very tight	"Closed" features
0.1 – 0.25 mm	Tight	
0.25 – 0.5 mm	Partially open	
0.5 – 2.5 mm	Open	"Gapped" features
2.5 – 10 mm	Moderately wide	
> 10 mm	Wide	
1-10 cm	Very wide	"Open" features
10-100 cm	Extremely wide	
> 1m	Cavernous	

Table 1.2 Aperture width classification (after Barton, 1978)

In the field, fracture aperture is often enhanced by solution processes and weathering, leading to falsely wide openings. During this study it was impractical to measure the majority of fracture apertures in the field in both study areas. The openings are predominantly less than 1mm wide, and are therefore at or below the resolution limit of field measurements and difficult to define accurately. Fractures that have infilled apertures (e.g. by mineralisation) are described in section 1.7.3.

1.7.2 *Orientation*

The orientation of a fracture is defined as its attitude in space. Fracture orientation is commonly described by the strike direction and dip of the line of steepest inclination in the plane of the fracture (Barton, 1978), measured using a compass clinometer. These values can then be plotted as poles to fracture planes on lower hemisphere stereographic projections to identify fracture orientation clusters (**Figure 1.15a**). Alternatively, the strike of the fractures may be plotted as rose diagrams (**Figure**

1.15b) or Von Mises diagrams (**Figure 1.15c**), to identify dominant fracture orientations.

Fracture orientation patterns often consist of several preferred orientations, each cluster represents a fracture set. There are three main ways of graphically presenting orientation data: stereographic projection plots (stereonets), Von Mises diagrams or rose diagrams:

a) Stereographic projection plot, known as stereonets (**Figure 1.15a**). The only method of graphical presentation for orientation data that can represent both strike and dip simultaneously is a spherical projection plot of fracture planes. It is important to use an equal-area plot as opposed to an equal-angle plot, so that the fracture data may be contoured, and fracture sets/clusters identified. Planes (2-D surfaces) are represented on the stereographic projection as lines or great circles. The line perpendicular to any given great circle can be represented as a point, and is known as the 'pole' to the plane. All stereonets presented in this thesis were created using GEOrient© version 8.0.

b) Rose diagrams (**Figure 1.15b).** In this instance, fracture orientation measurements are represented on a simplified compass rose marked from 0° - 360° for fracture strike, 0° - 90° for fracture dip, with radial lines at intervals (usually 5° or 10°). This method can not present fracture strike and dip data simultaneously. The number of observations (frequency) is represented along the radial axes. Rose diagrams are widely used in orientation analysis, but bias occurs by preferentially exaggerating large concentrations, and suppressing smaller ones (Barton, 1977). The major advantage of rose diagrams is that the data is easily visualised, however, it is often difficult to visually distinguish between sets/clusters which are less than 15° apart, depending on the frequency intervals chosen.

c) Von Mises diagram (**Figure 1.15c**). This type of plot is similar to a rose diagram, in that frequency is plotted against either fracture strike or fracture dip. Both variables cannot be plotted together. However, instead of a radial plot the orientation values on a Von Mises diagram are plotted along a horizontal linear axis. The advantage to this type of plot is that mean orientations are easily recognised, and no bias occurs between large and small concentrations. As with rose diagrams, the resolution of orientation clusters depends on the frequency interval chosen.

Fracture orientation data are generally affected by a bias resulting from the preferential sampling of fractures orientated perpendicular to the measurement line during 1-D sampling (section 1.9.1), or perpendicular to the sampling surface during 2-D analysis (section 1.9.2). In the field, it is important to carry out fracture orientation measurements in different directions in order to reduce orientation bias. When dealing with vertical outcrop surfaces, it is important to measure fracture orientations along at least two perpendicular surfaces in the field, as fractures approximately parallel to an outcrop surface will not be measured adequately, but will be observed in a surface perpendicular to it. In the field, gently dipping (near horizontal) fractures are often undersampled, because outcrops are insufficient in their vertical extent. When analysing fracture orientations in 2-dimensions, fracture maps (section 1.9.2) should be created for both horizontal and vertical surfaces, where possible.

The orientations of fractures in a damage zone around a larger fault are often assumed to have a simple, systematic relationship to the orientation of the larger structure. For example Riedel shear structures are often used to explain the orientations of faults and fractures within a fault zone (**Figure 1.9,** section 1.5.3.1). However, the exact orientation of Riedel shears is likely to vary with parameters such as lithology, presence/absence of layering, continued fault displacement causing rotation of structures, and fault reactivation.

It has been shown in the literature that heterogeneities within rocks can affect fault and fracture orientations (Peacock & Sanderson 1992, and references therein). Examples of heterogeneities include layering (of rocks with different mechanical properties), cleavage, bedding planes, and pre-existing faults. Peacock and Sanderson (1992) illustrate the effects of layering on the geometry of conjugate fault sets, using field observations. The authors conclude that for rock types with weak/absent anisotropy, the assumption that faults form conjugate sets, usually 25° to σ_1 is reasonable. However, they illustrate that layering affects the orientation of conjugate sets, and can cause variations in the angle between σ_1 and shear fractures. An important factor is the angle between σ_1 and the anisotropy (e.g. layering).

1.7.3 *Infill*

Material separating adjacent fracture walls is described as the fracture infill. Common fracture infills are minerals such as quartz, calcite and chlorite, fault gouge, breccia and cataclasite. It is important to identify and record any infills recognised in the field, as the material may give an indication of the history of fluid movement, and an insight into the relative timing of fracture events. When two different fracture-fills are present, the fill in the centre of the fracture is likely to be the youngest. Materials within fractures are also important in determining the ability of the fracture network to transmit fluid. Clay-rich or well-cemented fractures commonly act as barriers to flow, whereas vuggy infills are often more conductive.

1.7.4 *Spacing*

Fracture spacing is defined as the distance between two adjacent fractures, either for individual sets defined by orientation clusters that are approximately parallel, or for all fractures intersecting a 1-dimensional sample line.

Two methods have been identified to analyse the spatial variability of a fracture system (Rouleau & Gale, 1985), a) methods based on distances (section 1.7.4.1), and b) methods based on density (section 1.7.4.2).

1.7.4.1 Spatial variability based on distance

Distance between fractures (spacing) is easily measured along 1-dimensional transects/scanlines (section 1.9.1), but is harder to define for 2-dimensional and 3-dimensional data. Fracture spacings in this study were measured along 1-dimensional line transects (section 1.9.1) both perpendicular and parallel to the main trend of the fault zone (N/S for Walls Boundary Fault Zone, ~ENE/WSW for Møre-Trøndelag Fault Complex), in both vertical and horizontal surfaces. Fracture spacings have also be measured from 2-dimensional fracture maps (section 1.9.2) by carrying out a series of 1-dimensional line transects in different orientations. In this study, the distances between fractures in the field have been measured to a resolution of 0.5mm. Fracture spacing data from individual transects, or from whole data sets may then be plotted against frequency or cumulative frequency to investigate the statistical frequency distribution of the sample population (see section 1.8).

1.7.4.2 Fracture density

A fracture spacing distribution from 1-D, 2-D or 3-D data sets may be described by a single number known as fracture density. Fracture density is described in the literature as having a number of different meanings, and is often confused with fracture intensity (**Table 1.3**, section 1.7.5.2). Fracture density, as expressed in this thesis, is the *fracture/spacing frequency per unit length* for 1-dimensional data and the *number of fractures (or spacings) per unit area* for 2-dimensional data sets. Fracture density is directly related to the value of average fracture frequency/spacing (**Figure 1.16a**).

1.7.4.2.1 *Fracture Spacing Index as a measure of density*

Fracture density has been described using the Fracture Spacing Index (FSI) (Narr 1991) which relates fracture spacing to layer thickness and is described in detail in section 1.7.4.3.1.

1.7.4.2.2 *Spacing ellipses as a measure of density*

Fracture density is often quoted for 1-dimensional line transects, but this value can depend significantly on the orientation of the sample line relative to the observed fracture orientations (Hudson & Priest 1983). The amount of variation is a function of the fracture network geometry (section 1.7.7). Due to the variation in fracture frequency with scan line orientation, the use of a single value of fracture density for a rock mass/outcrop is generally insufficient. Hudson & Priest (1983) propose the construction of loci for fracture data sets, where the number of fractures intersecting line samples every 20 degrees across a rock surface are plotted on a polar plot (or rose diagram) (**Figure 1.16b, c**). The method proposed by Hudson & Priest (1983) assumes that each line transect is the same length. Often in the field, outcrop is limited, and line sample lengths are variable. Therefore I propose a method for presenting the variation of fracture density across an 2-dimensional outcrop surface using the *average fracture spacing* measured along 1-dimensional line transects every 30 degrees (**Figure 1.16d**). The result is an ellipse created by plotting average fracture spacing, which is inversely proportional to fracture density, on a rose diagram, and the magnitude and direction of minimum and maximum values of density can be established. It is important to note that the orientation of the line transect that represents the maximum average spacing, corresponds to minimum fracture density,

Fracture Parameter	Key Fracture Attribute	Description	References
Density	**Spacing**	**Fracture frequency per length (1-D), area (2-D) or volume (3-D)** **(where frequency refers to presence/absence of fractures, or fracture centres)**	Einstein & Baecher 1983 Robinson 1983 Smith & Schwartz 1984 Long & Witherspoon 1985 Rouleau & Gale, 1985 Long & Billaux 1987 Pollard & Aydin, 1988 Gillespie et al., 1993 Jackson 1994, Skamvetsaki 1994 Gervais et al., 1995 Needham et al., 1996 Rochford 1997 Berkowitz & Alder 1998 Younes et al., 1998 Berkowitz et al., 2000 Schulz & Evans, 2000 Bonnet et al., 2001 Mauldon et al., 2001
Density	Length	Fracture length per area (2-D)	Rouleau & Gale 1985 Gillespie et al., 1993 Gervais et al., 1995 Odling 1995, Castaing et al., 1996 Odling 1997 Younes et al., 1998 Zhang & Sanderson 1998
Density	Spacing	Fracture Spacing Index (FSI) & Fracture Index (FI) (where fracture density is related to bed thickness)	Narr & Lerche 1984 Narr, 1991 Narr & Suppe 1991 Price & Cosgrove 1991
Intensity	**Length**	**Fracture length per unit area (2-D)** **Fracture surface area per unit volume (3-D)**	Fookes & Denness 1969 Goldstein & Marshak 1987 Dershowitz & Herda, 1992 Renshaw 1999 Zhang & Einstein 2000 Mauldon et al., 2001
Intensity	Spacing	Fracture frequency per length (1-D)	Skempton et al., 1969 Piteau 1970 Renshaw 1999 Mauldon et al., 2001
Intensity	Spacing	1/(average spacing)	Hennings et al., 2000

Table 1.3 Definitions of fracture density and fracture intensity from literature. (Those in bold are the definitions used in this thesis)

and is most likely related to fractures orientated perpendicular to the sample line (**Figure 1.16e**). The area of the ellipse gives a relative measure of fracture density across the 2-dimensional sample area.

1.7.4.3 Factors affecting fracture density

Fracture spacing (and therefore fracture density) can be influenced by a number of factors such as lithology, layer/bed thickness, and number of fracture sets present. The spacing between fractures in thick beds is commonly larger than the fracture spacing in thinner beds. This relationship between spacing and unit thickness can vary with lithology (Narr 1991).

1.7.4.3.1 *Bed thickness*

Within a single lithology, both theoretical and model experiments have indicated a linear relationship between fracture spacing and bed thickness of an individual fracture set, with the trend line passing near the origin (Price & Cosgrove 1991, Narr 1991, Narr & Suppe 1991, Ji & Saruwatari 1998) (**Figure 1.17a**). The slope of this linear regression line has been used to express the density of fractures as the ratio of *layer thickness*: *median joint spacing,* and is known as the Fracture Spacing Index (FSI), as described in **Table 1.3** (Narr 1991), and described as the co-efficient of spacing (K-value) by Ji & Saruwatari (1998). The Fracture Spacing Index (FSI or I) = T/S, where T = layer thickness, S = spacing. Relatively high values of FSI correspond to close fracture spacings and high fracture densities. The FSI can be used to compare density in beds of unequal thickness, or to characterise the thickness-spacing relationship of a group of beds (Narr, 1991).

1.7.4.3.2 *Lithology*

Different lithologies exhibit different FSI ratios, reflecting the influence of lithology on fracture density (**Figure 1.17b**). However, the linear relationship between spacing and unit thickness does not hold for all strata such as thick, cross-bedded sandstone or thick, massive shales (Narr 1991).

1.7.4.3.3 *Lithological contacts*

As well as bedding/layering within a single lithology, lithological contacts and pre-existing fractures can affect fracture spacing. Lithological contacts and pre-existing

fractures can act as mechanical layer boundaries that confine fractures to individual units (Gross et al., 1995, Ruf et al., 1998). The termination of fractures at lithological boundaries and pre-existing fractures/joints occurs because the mechanical boundary suppresses the crack-tip stress field necessary for continued growth (Ruf et al., 1998).

1.7.5 *Length*

This parameter is defined as the measurable length of a linear trace produced by the intersection of a planar fracture with an outcrop surface (Priest & Hudson 1981). The fracture will either terminate at another discontinuity, or within the rock material. The length of fractures is one of the most important rock mass parameters for assessing connectivity and the ability of the fracture network to transmit fluids, however, fracture length is probably the most difficult to accurately quantify. Fracture length observed on vertical or horizontal exposures depends on the size and shape of the fracture, the orientation of the fracture relative to the outcrop surface, and the dimensions of the exposed outcrop.

1.7.5.1 Fracture length sampling errors

Trace lengths of fractures observed on finite exposures are frequently biased due to sampling errors. Whether fracture trace lengths are measured along 1-dimensional transects, or within 2-dimensional areas (section 1.9), three main biases occur, *truncation bias*, *censoring bias* and *size/geometric bias*. (Priest & Hudson 1981, Laslett 1982, Baecher 1983, Einstein & Baecher 1983, Kulatilake & Wu 1984, Pickering et al., 1995, Zhang & Einstein 2000) (**Figure 1.18**).

a) Large, persistent fractures may extend beyond the limits of the exposed outcrop, or be obscured due to vegetation cover, resulting in only a minimum recordable fracture length. This bias is called *censoring bias*, and is dependent on the extent of exposure, and the orientation of the fracture relative to the outcrop.
b) Fracture trace lengths that are very small are difficult or impossible to observe and measure accurately; therefore the lengths of fractures below a cut-off value are not recorded. The value of cut-off can be set manually, agreed before sampling, but also naturally depends on the resolution of the human eye, and the quality and resolution of the data set (if using field photographs, or Landsat™ images for

example). This type of bias, occurring when the scale range of a sample of data is less than the scale range of the whole data population, is called *truncation bias*. In this study, all observed fractures were measured without a manual cut-off length, but natural cut-off will inevitably affect measurements.

c) *Size bias or geometric bias* results because relatively longer fractures are more likely to intersect a 1-dimensional sample line, or 2-dimensional sampling area than shorter, less persistent fractures.

1.7.5.2 Fracture intensity

Fracture length measurements exposed in a field outcrop can provide a direct, unbiased estimate of fracture intensity (Mauldon et al., 2001). In 2-dimensional settings, fracture intensity can be represented by the *total fracture trace length per unit area*, which for 3-dimensional data sets equates to *total fracture surface area per unit volume*. This definition for fracture intensity will be used in this study. Other definitions of fracture intensity are used in the literature, as illustrated in **Table 1.3**. Fracture intensity is a function of the orientation of the plane in which fracture length is measured relative to the orientations of fracture present. The intensity of *connected* fractures (section 1.7.8) can be assessed by dividing fracture cluster length by the sample area.

1.7.6 *Displacement*

The surface of fault and fracture displacement ranges from a maximum at the centre to zero at the edge or tip-line (Barnett et al., 1987, Walsh & Watterson 1987). The tip-line is ideally elliptical. For dip-slip faults, the displacement direction is approximately parallel to the shorter axis of the ellipse, whereas for strike-slip faults, the displacement direction is approximately parallel to the longer axis of the ellipse (**Figure 1.19**). In ideal cases, contours of equal displacement form concentric ellipses centred on the point of maximum displacement. Fault/fracture size, kinematic history and the mechanical properties of the host rock cause variations in the displacement gradient; the fault radius to maximum displacement ratio ranges from 5 to 500 (Barnett et al., 1987). Kinematic indicators observed on fault and fracture planes, such as slickenslides caused by mineral growth, can be used to identify the movement direction of the structure (section 1.5.1).

At outcrop scale, quantification of fracture displacement is very difficult, either due to exposure, or the small scale of the structures. In this study, fault and fracture displacements are documented where possible, but there is an insufficient data set for the statistical analysis of fracture displacement from either study area.

1.7.7 *Geometry*

The geometry of the fracture network is a summation of all fracture attributes (sections 1.7.1 – 1.7.6) to give an overall pattern and shape resulting from the processes of fracture initiation, propagation and termination. Geometry is defined in the literature as " *a) density of fractures (number of fractures per unit area or volume, related to fracture spacing), b) orientation distribution of the fractures, c) fracture size (i.e. length), d) fracture shape and e) fracture aperture* (Long & Billaux 1987)".

Lithological layering is already mentioned in section 1.7.4 as influencing fracture spacing, but in reality, the nature of layering/bedding is a primary influence on the overall fracture network geometry (Odling et al., 1999). Two end members of layering have been identified: stratabound and non-stratabound (**Figure 1.20**). Stratabound systems are developed where there is little mechanical coupling between layers, and hence fractures and joints are confined to layers. In this instance, fracture length is restricted and fracture spacing tends to be regular (Odling et al., 1999). More massive rock types that host laterally and vertically continuous fractures and joints are described as non-stratabound systems. In this instance, a broad distribution of fracture lengths generally occurs, with fracture spacing random or clustered. As well as lithological layering, the geometry of any fracture network is likely to be controlled by both the kinematic history and degree of reactivation.

An understanding of the geometry of the fracture network can be achieved by accurately characterising the fracture attributes. This then allows an assessment of the network connectivity – the ability of the network to transmit fluid (section 1.7.8).

1.7.8 *Connectivity*

1.7.8.1 Importance and controls

Fractures are important as fluid pathways in the earth's crust. They can act as key conduits for the migration of fluids such as oil and gas in petroleum reservoirs, and

principal pathways for the escape of radioactive and toxic waste, and groundwater contamination. Conversely, however, sealed fractures within a porous rock can act as barriers to flow, and therefore limit fluid flow. Therefore, the extent to which individual fractures are linked to form continuous pathways through the rock (i.e. the connectivity of fractures) is of the upmost importance when assessing the capabilities for fluid flow.

Different authors place emphasis on specific fracture attributes which they consider to be most important for fluid flow though rocks. For example, a set of parallel fractures is unlikely to intersect emphasising the importance of fracture orientation for fracture connectivity (Manzocchi et al., 1998, Odling et al., 1999). Fracture infill and fracture apertures are also important parameters when determining the ability of fractures to transmit fluid (e.g. Bloomfield 1996, Odling et al., 1999). Narrow or mineral filled fractures will probably transmit less fluid than wider and open fractures. Overall fracture connectivity is dependent on the geometry of the fracture network, which is a summation of all fracture parameters (section 1.7.7) and determines the ability of impermeable rocks to transmit fluid.

1.7.8.2 Percolation theory

Fracture connectivity has been investigated in the literature using a branch of statistical physics, *percolation theory* (e.g. Robinson 1983, Berkowitz & Balberg, 1993, Stauffer & Aharmony 1994, Odling 1997, Rochford 1997, Zhang & Sanderson, 1998, Odling et al., 1999). Fracture networks are compared to an abstract regular lattice composed of points/sites. Lattice points/sites can either be connected to form a cluster, or be unconnected (**Figure 1.21**). The probability of a site being connected (occupied) or unconnected (empty) is random, and this is where the application of percolation may not be perfectly suited to describing natural situations. The position of a natural fracture in a 2-D area or 3-D volume of rock may not be random, but instead be dependent on criteria such as stress intensity, distance to other fractures, and rock properties (Rochford 1997). However, percolation theory provides useful terminology for the description of fracture network connectivity at different scales.

1.7.8.3 Fracture clusters

Inter-linked fractures form clusters, defined as a group of interconnected fractures, where the interconnections are commonly referred to as nodes. The term node

includes both fracture intersections, and fracture branch points. The terminology adopted in this study identifies three types of cluster (based on Rochford, 1997):

- single clusters (isolated fractures with no nodes)
- small clusters (<15 nodes)
- large cluster (≥ 15 nodes)

1.7.8.3.1 *The percolating cluster*

When one large cluster intersects all sample boundaries (i.e. all four sides of a 2-D fracture map), the cluster is known as the percolating or infinite cluster, and percolation threshold (p_c) is reached (Reynolds et al., 1980). Below the p_c, the fracture network is not fully connected in the sample area; above p_c the system is connected by an infinite cluster that spans the whole area (Bour & Davy 1997). Not all parts of the percolating cluster are necessary for percolation threshold to be reached.

1.7.8.3.2 *Cluster backbone and dead-ends*

Portions of the cluster that do not lie on direct pathways through the system are known as "dead ends". Removing the dead ends from the percolating cluster leaves the "backbone", the part of the fracture network essential for fluid-flow at percolation threshold (**Figure 1.22**). If the largest cluster of fractures in a sample area does not connect all sample boundaries, the network does not possess a backbone (Odling 1997).

1.7.8.3.3 *Maximum and minimum cluster connectivity*

The connectivity of a fracture cluster, defined using the number of fractures and the number of nodes, can be constrained by two equations that define the maximum and minimum end-members of connectivity (**Figure 1.23**). It is important to note that the equations only hold for planar fractures, and not curved fractures. Minimum cluster connectivity occurs when another fracture is added to the system, and only one more node is created. Maximum cluster connectivity occurs when each fracture in the cluster intersects with every other fracture. The percolation threshold can occur at either maximum or minimum connectivity of the percolating cluster, but is more likely to occur at an intermediate value.

1.7.8.4 Measures of connectivity

Apparently "dense" 2-dimensional fracture networks may not be fully connected, i.e. above p_c. The ability to measure the relative connectivity of fracture networks that are both above and below p_c is important to be able to compare different fracture densities and intensities, and fracture networks from different scales. There are essentially two units of measurement for connectivity – per unit area and per cluster. Measuring connectivity per unit area does not mean that all fractures are connected in the sample area (i.e. there may be more than one cluster). Parameters such as the total number of fracture intersections (nodes) can then be assessed either per cluster or per area (**Figure 1.24**).

1.7.8.4.1 *Percolation threshold (p_c)*

The p_c value of a fracture network is an absolute measure of connectivity. However, a more relative measure of connectivity using p_c is detailed below. Taking a sample area that has 4 sides, when p_c is reached, all 4 sides must be intersected by the percolating cluster. A fracture cluster below p_c may intersect 3, 2, 1 or 0 of the sample area sides. We can therefore use percolation threshold as a relative measure of percolation (**Figure 1.25**), i.e.

When all 4 sides of the sample area are intersected, $p_c = 1$

When 3 out of 4 sides of the sample area are intersected, $p_c = 0.75$

When 2 out of 4 sides of the sample area are intersected, $p_c = 0.5$

When 1 out of 4 sides of the sample area are intersected, $p_c = 0.25$

When no sides of the sample area are intersected, $p_c = 0$

If the orientation of the sample area is known relative to the overall fault orientation, connectivity can then be assessed relative to the structure in 2-dimensions. When p_c = 0.5, and two opposite sides of the sample area are intersected, then the fracture network is either connected parallel or perpendicular to the fault trend (**Figure 1.25**).

1.7.8.4.2 *Nodes per cluster*

The total number of intersections (nodes) per fracture cluster can be measured and used as a relative indicator of connectivity (i.e. higher values of nodes per cluster represent better connected systems). The value of nodes per cluster can be plotted against distance to assess the change in connectivity away from the fault zone, and investigate how connectivity changes with data scale.

1.7.8.4.3 *Nodes per unit area*

The number of fracture intersections can also be calculated across a sample area by measuring the number of nodes per unit area (e.g. per cm^2). This assessment of connectivity does not account for all fractures being connected, and does not analyse the connectivity of individual fracture clusters, but is a useful way of comparing connectivity between areas and between data scales.

1.7.8.4.4 *Nodes per fracture*

The average number of intersections (nodes) per fracture (either per cluster or per unit area) in a sample area, is often used as a measure of connectivity (Robinson 1983, Berkowitz & Balberg 1993, Berkowitz 1995, Bour & Davy 1997). This is a reliable way of comparing connectivity between data scales, or with distance away from a fault zone. Robinson (1983) investigated the average number of intersections per fracture at the percolation threshold. It was found that for various fracture systems considered, the number of nodes per fracture does not vary significantly. However, to ensure connectivity as the size of the sample area increases, the density of fractures (number of fractures per unit area) must increase.

The following statements are applicable to data sets with any number of fractures.: 1) The maximum value of fractures per node that can be calculated in a unit area is infinite, as for example if 10 unconnected fractures occur, the number of fractures per node is equal to 10 divided by zero, which equals infinity. 2) Similarly, the minimum value of nodes per fracture calculated in a unit area is equal to zero, which occurs when no fractures intersect. 3) The maximum number of nodes per fracture in a unit area is equal to the maximum number of nodes per fracture in a cluster. 4) The maximum number of fractures per node in a cluster is equal to the minimum number of fractures per node in a unit area.

The actual values of a) maximum number of fractures per node and nodes per fracture in a cluster, b) minimum values of fractures per node and nodes per fracture in a cluster, c) maximum number of nodes per fracture in a unit area, and d) minimum value of fractures per node in a unit area, *are all dependant on the number of fractures in the data set.*

When a data set possesses more than four fractures, the following statements can be made regarding the connectivity of the data set: 1) When the number of nodes is equal

to the number of fractures (calculated either per cluster or per unit area) then the values of fractures per node and nodes per fracture will be equal to unity. 2) When the number of fractures is greater than the number of nodes, then the value of fractures per node will be >1 and the value of nodes per fracture will be <1, and the data set may be considered relatively poorly connected. 3) When the number of fractures is less than the number of nodes, then the value of fractures per node will be <1, and the value of nodes per fracture will be >1, and the data set can be considered relatively well connected.

1.7.8.4.5 *Fracture cluster length*

A long cluster length (i.e. the summation of the lengths of all connected fractures) does not necessarily equate to a well-connected network (**Figure 1.26**). However, cluster length can be used as a measure of connectivity by calculating the proportion of the total fracture trace length that belongs to the largest cluster (Odling 1995, Odling 1997, Odling et al., 1999). Studies of a natural fracture system in Norway (Odling 1997, Odling et al., 1999) have shown that the boundary between connected and unconnected systems (p_c) occurs when the largest cluster contains around half the total fracture trace length in the sample area. Odling et al., (1999) then suggest that for a fracture network to be considered well connected, more than 75% of the total fracture trace length in the sample area must contribute to the percolating cluster.

1.7.8.4.6 *Interconnectivity Index*

The interconnectivity index proposed by Rouleau & Gale (1985) can be used to measure the degree of connectivity between two fracture sets (**Figure 1.27**). The index includes three important fracture parameters: orientation, spacing and length, and is independent of fracture aperture. The interconnectivity index (I) for two fracture sets 'a' and 'b' is expressed by the following equation:

$$I\,ab = \left\{ \frac{(\text{mean length set } a)}{(\text{mean spacing set } b)} \right\} \times \sin(\text{average angle between orientation of set } a \,\&\, b)$$

In general, I*ab* is different to I*ba*. A larger value of I*ab* indicates a greater importance for fracture set 'a'. For an idealised system of two fracture sets (*a* and *b*), the interconnectivity index of *a* increases as the trace length of that set increases, and/or

when the spacing of set b is small, and/or when the angle between a & b increases. The interconnectivity index approaches zero as the two fracture sets approach parallelism (as the angle between them decreases) (Bloomfield 1996).

1.7.8.5 Relationship between connectivity and fracture length (intensity/density)

When fracture density (number of fractures per unit area) is high, and more than one orientation of fractures is present, the majority of fractures are likely to be connected and contribute to the network connectivity. In this instance, the fracture density controls the connectivity of the network, largely irrespective of fracture lengths. At lower fracture densities, the connectivity of the network depends on both the fracture density and the distribution of fracture lengths in the sample area (Renshaw 1999). Fracture/fault length data sets are often described in the literature as being best-fitted to a power-law distribution, exponents (slopes) ranging from –1.5 to –3 (see section 1.8.2.4 for a detailed description of power law distributions). The exponent of power-law length distributions for random 2-D fracture networks has been shown to have an important influence on network connectivity (Bour & Davy 1997, 1998). The exponent has been used to characterise the abundance of large and small fractures with respect to the 2-D dimensions of the sample area (system size). Large fractures are classed as being larger than the system size, i.e. longer than the extent of the sample area; small fractures are shorter than the sample dimensions.

The value of exponent/slope from a power-law distribution is termed *a*. In general, small values of exponent (*a*) represent a high probability of long fractures in the network. Larger values of *a* represent a low probability of having long fractures, and therefore percolation threshold (p_c) is reached with all fractures being shorter than the sample dimensions (Bour & Davy 1997).

In more detail, Bour & Davy (1997) identified three basic relationships between connectivity and fracture length distribution, where *a* = exponent of power-law cumulative frequency fracture length distribution:

- When $a < 1$ (relatively shallow slopes) - very few fractures belong to the infinite (percolating) cluster, almost all clusters are composed of a single fracture, and total number of nodes is very small. Connectivity is ensured by the largest possible fracture.

- When $a > 3$ (relatively steep slopes) - the infinite cluster represents 50-60% of the total number of fractures, and small fractures rule the connectivity
- When $1 < a < 3$ - the percentage of fractures belonging to the infinite cluster varies from 1 – 50%, and both large and small fractures rule the connectivity in a ratio that depends on a. When $a = 2$, the relative contribution of large and small fractures is identical.

1.7.8.6 Fracture connectivity in permeable rocks.

The above analysis and discussion of fracture connectivity largely assumes that the host rock matrix is impermeable, and fluid flow is controlled by the fracture network only. However, it has been shown by numerical simulation that fractures can also have a significant effect on fluid transportation where the rock matrix is porous and permeable (Odling & Roden 1997). When the rock mass is permeable, dead-ends (section 1.7.8.2) that occur as part of the percolating cluster can also contribute to fluid flow. The influence of fractures on fluid flow in permeable rocks is dependent on the permeability contrast between the matrix and the fractures. Even if fractures present in permeable rocks are unconnected, they can still play an important role in the transportation of fluids (Odling & Roden 1997).

1.8 Fracture attribute population analysis

Statistical analysis of fracture parameters, such as spacing and length, allows the quantitative characterisation of the fracture system, and enables absolute comparisons to be made between fracture data sets collected from different lithologies and tectonic settings, and at different distances to major structural features.

All data sets of fracture parameters collected at various scales (e.g. outcrop, or seismic) represent samples from an underlying population. The *target population* is defined as the collection of elements about which information is desired, for example the population of fracture trace lengths in a rock mass. The *sampled population (or available population)* is defined as the collection of elements that are available for sampling, for example the population of fracture trace lengths exposed and intersecting outcrops (Swan and Sandilands, 1995). The *sample* is defined as the

collection of elements whose properties are actually measured, i.e. the fracture trace lengths that intersect the 1-dimensional sample line, or 2-dimensional sample area. Analysis of the measured sample using statistical methods allows quantitative inferences to be made about the properties of the sampled population (Einstein & Baecher 1983, Swan & Sandilands 1995). Inferences can also be made about the properties of the target population, but this is more difficult, involving the extrapolation of the sample properties between data scales, and between dimensions (i.e. using a 1-dimensional or 2-dimensional data set to infer a 3-dimensional population).

An important property of both the sample population and the target population is the statistical distribution that best describes the data set. However, the statistical distribution that best describes the sample data set may not be the best distribution to describe the sample population or target population, if the collected sample is biased (Einstein & Baecher 1983, Pickering et al., 1995). The amount of bias in a data sample is generally inversely proportional to the size of the data set, i.e. the longer the 1-dimensional line transect, or the larger the 2-dimensional sample area, the less bias is likely to occur (Sen & Kazi 1984). However, both the number of data points collected in the field and the maximum size of parameters (for example fracture length) are often limited by the extent of outcrop. Ideally, sample data sets (e.g. fracture length) that range over one order of magnitude are needed before the different statistical distributions can be easily distinguished (Bonnet et al., 2001).

1.8.1 *Methods used to analyse the best-fit statistical distribution*

There are two main ways that a data set can be plotted in order to assess the best-fit statistical distribution: a *frequency distribution*, or a *cumulative frequency distribution* (Pickering et al., 1995, Swan & Sandilands 1995). Measurements of a fracture parameter (such as length) are plotted on the x-axis, against either frequency or cumulative frequency on the y-axis.

When plotting a *frequency distribution*, the measurements of the fracture parameter (such as fracture length values) are 'binned' into equal intervals known as classes along the x-axis. The number of measurements (or counts) in each class is the frequency, and the series of counts describe the frequency distribution. A visual representation of a *frequency distribution* is given by a *histogram*, where the area of

each rectangle representing each class, corresponds to the proportion of total values that lie in the class interval (Swan & Sandilands 1995) (**Figure 1.28b**). When a large data set of values is available, the outline of the histogram with narrow class intervals may be approximated to a smooth curve known as the *probability density function* (p.d.f) (**Figure 1.28c**). A disadvantage of frequency distributions is that they can result in zero values for some class sizes, which cannot be plotted on logarithmic axes (Gillespie et al., 1993).

To plot a *cumulative frequency distribution*, the data values (such as fracture lengths) are sorted in descending order on the x-axis, and plotted against cumulative number on the y-axis (**Figure 1.28d**). *Cumulative frequency distributions* are the established way of describing fracture population distributions (Gillespie et al., 1993, Marrett 1994, Bonnet et al., 2001). The cumulative frequency plots are easily computed, and the data does not have to be divided into bin sizes as it does for the frequency distribution, the choice of which can be arbitrary.

1.8.2 *Types of statistical distribution*

Four main statistical distributions are commonly used to describe numerous phenomena, such as fracture attributes: normal, log-normal, exponential and power-law, but others such as gamma are also used (**Table 1.4**). The probability density functions (section 1.8.1) and characteristic parameters for each of these statistical distributions are illustrated in **Figure 1.29**, and their cumulative frequency plots are shown in **Figure 1.30**. The characteristics of the four main distributions are described in the following sections.

1.8.2.1 Normal distribution (or Gaussian distribution)

The normal distribution is the most widely used probability distribution in statistical analysis (Swan & Sandilands 1995). A sample is normally distributed if the values are fairly uniform, and clustered around the mean value which is the most commonly occurring value (coinciding with the mode). The probability density function is bell-shaped and symmetrical about the mean value (**Figure 1.29**). The spread of the distribution around the mean is described by the variance and standard deviation. The cumulative frequency distribution for the normal distribution plots as a slightly curved line on linear x and y axes (**Figure 1.30**).

Parameter	Scale	Method	Lithology	Feature	Distribution	Exponent*	Author	Year
SPACING					**Exponential**		Baecher et al., [4]	1977
SPACING	outcrop	cfd	quartz-mica schist	fractures	**Exponential**		Beacom et al.,	2001
SPACING	outcrop	histogram & probability plot	chalk	unrefined joints	**Exponential**		Bloomfield	1996
SPACING	10s-100s m	interval count. method & cfd	crystalline rock	faults	**Exponential**		Brooks et al.,	1996
SPACING					**Exponential**		Call et al., [4, 5, 6]	1976
SPACING	outcrop	histogram	various	discontinuity	**Exponential**		Hudson & Priest	1979
SPACING	outcrop	histogram	chalk	discontinuity	**Exponential**		Priest & Hudson	1976
SPACING	outcrop	histogram	sandstone	discontinuity	**Exponential**		Priest & Hudson	1976
SPACING	outcrop	histogram	mudstone	discontinuity	**Exponential**		Priest & Hudson	1976
SPACING	outcrop	histogram	chalk	discontinuity	**Exponential**		Priest & Hudson	1976
SPACING	outcrop	histogram	sedimentary	joints	**Exponential**		Rives et al.,	1992
SPACING					**Exponential**		Rouleau & Gale	1985
SPACING					**Exponential**		Sen & Eissa [4]	1992
SPACING			crystalline rock		**Exponential**		Snow [6]	1970
SPACING	core & outcrop	histogram	granite	discontinuity	**Exponential**		Wallis & King	1980
SPACING	various	cfd	sandstone	joints/ fractures	**Exponential & Log-Normal**		Aarseth et al.,	1997
SPACING	outcrop	cfd	various	veins	**Exponential & Log-normal**		McCaffrey et al.,	1994
SPACING					**Exponential & Log-normal**		Sen & Eissa [4]	1992
SPACING	various individual	histogram	sandstone	various	**Gamma**		Castaing et al.,	1996
SPACING					**Log-normal**		Barton [4, 5, 6]	1978
SPACING	outcrop	cfd	amphibolite	fractures	**Log-normal**		Beacom et al.,	2001
SPACING					**Log-normal**		Bridges [4, 5, 6]	1976
SPACING	outcrop (Belah)	cfd & histogram	sandstones & shales	faults	**Log-normal**		Gillespie et al.,	1993
SPACING	borehole	histogram	psammites & schists	veins	**Log-normal**		McCaffrey & Johnston	1996
SPACING	outcrop	histogram	various	joints	**Log-normal**		Narr & Suppe	1991
SPACING	outcrop (NashP)	histogram	sedimentary	joints faults	**Log-normal**		Rives et al.,	1992
SPACING	outcrop	histogram	turbidites	joints	**Log-normal**		Ruf et al.,	1998
SPACING					**Log-normal**		Sen & Kazi [4]	1984
SPACING	outcrop	histogram cfd	limestone	joints	**Log-normal & Normal**		Gillespie et al., Aarseth et al.,	2001 1997

Table 1.4 (continued overleaf)

Parameter	Scale	Method	Lithology	Feature	Distribution	Exponent*	Author	Year
SPACING	outcrop	cfd		fractures	**Normal**		Malthe-Sorenssen et al.,	1998
SPACING					**Normal**		Priest & Hudson	1981
SPACING					**Normal**		Rouleau & Gale	1985
SPACING	outcrop	cfd	acid & mafic gneiss	fractures	**Power-law**		Beacom et al.,	2001
SPACING	outcrop	cfd	various	faults & fractures	**Power-law**		Cello et al.,	2000
SPACING	outcrop (Round O)	cfd & histogram	sandstones & shales	faults	**Power-law**	-0.4	Gillespie et al.,	1993
SPACING	outcrop (Star cross)	cfd & histogram	glacial sands	faults	**Power-law**	-1.0	Gillespie et al.,	1993
SPACING	outcrop	cfd & histogram	limestone	veins	**Power-law**		Gillespie et al., Aarseth et al.,	2001 1997
SPACING	outcrop	cfd	various	fracture	**Power-law**		Jackson	1994
SPACING	core & seismic	cfd	carbonate & siliclastic	faults	**Power-law**		Knott et al.,	1994
SPACING	outcrop	cfd	sandstone	faults	**Power-law**	-0.63	Knott et al.,	1996
SPACING	seismic & core (N Sea)	cfd	various	faults	**Power-law**	-1.31	Knott et al.,	1996
SPACING	core	interval counting method	sandstone?	fractures	**Power-law**	0.17 to 0.72	Needham et al.,	1996
LENGTH	outcrop	histogram & probability plot	chalk	unrefined joints	**Exponential**		Bloomfield	1996
LENGTH			copper porphyry		**Exponential**		Call et al., [4, 5, 6]	1976
LENGTH			various		**Exponential**		Cruden [4, 5, 6]	1977
LENGTH	large		oceanic crust	faults	**Exponential**		McAllister	1994
LENGTH	outcrop	histogram	mudstone	discontinuity	**Exponential**		Priest & Hudson	1981
LENGTH	outcrop	histogram	sandstone	discontinuity	**Exponential**		Priest & Hudson	1981
LENGTH					**Exponential**		Robertson [4, 5, 6]	1970
LENGTH			various		**Exponential**		Steffan et al., [6]	1975
LENGTH					**Exponential & gamma**		Kulatilake [5]	1984
LENGTH	core & outcrop	histogram	granite	fractures	**Exponential & Log-normal**		Rouleau & Gale	1985
LENGTH					**Gamma**		Dershowitz [4]	1984

Table 1.4 (continued overleaf)

Parameter	Scale	Method	Lithology	Feature	Distribution	Exponent*	Author	Year
LENGTH					Log-normal		Baecher et al., [4, 5]	1977
LENGTH			metamorphic		Log-normal		Barton [4, 5, 6]	1978
LENGTH			metamorphic		Log-normal		Bridges [4, 5, 6]	1976
LENGTH	various individual	histogram & cfd	sandstone	various	Log-normal		Castaing et al., Odling et al.,	1996 1999
LENGTH	large (m-km)	pdf & cdf	various	faults	Log-normal		Davy	1993
LENGTH					Log-normal		Einstein et al., [5]	1979
LENGTH	outcrop	histogram	limestone	fractures	Log-normal		Gervais et al.,	1995
LENGTH	outcrop	histogram cfd	limestone	joints	Log-normal		Gillespie et al., Aarseth et al.,	2001 1997
LENGTH			various		Log-normal		McMahon [4, 6]	1971
LENGTH	various individual	cfd cfd	sandstone	joints/ fractures	Log-normal		Odling Aarseth et al.,	1997 1997
LENGTH	outcrop	cfd	limestone	joints	Log-normal		Odling et al.,	1999
LENGTH	outcrop	cfd	chalk	joints & faults	Log-normal		Odling et al.,	1999
LENGTH	outcrop			joints	Power-law	a = 1.74	Bahat [2]	1987
LENGTH	outcrop			joints	Power-law	a = 2.11	Bahat [2]	1987
LENGTH					Power-law	c = 1.32-1.7	Barton [3]	1995
LENGTH	large			faults	Power-law	c = 1.11	Blackstone [1, 2]	1988
LENGTH	large			faults	Power-law	a = 1.88	Bour & Davy [2]	1999
LENGTH	various amalgamated	cfd	sandstone	various	Power-law	d = 2.34	Castaing et al., Odling et al.,	1996 1999
LENGTH	outcrop	cfd	various	faults & fractures	Power-law		Cello et al.,	2000
LENGTH	seismic	cfd		faults	Power-law	c = 1.10, 1.42 & 1.69	Gauthier & Lake	1993
LENGTH	large			veins	Power-law	a = 0.9	Gudmundsson [2]	1987
LENGTH	large			veins	Power-law	a = 1	Gudmundsson [2]	1987
LENGTH	large			faults	Power-law	a = 1.76	Hatton et al., [2]	1993
LENGTH	various, outcrop, seismic	cfd		fractures/ faults	Power-law	c = 3	Heffer & Bevan	1990
LENGTH				faults	Power-law	c = 2	Heffer & Bevan [3]	1990
LENGTH	large			faults	Power-law	c = 0.97	Kakimi [1, 2]	1980
LENGTH	outcrop	cfd	sandstone+limestone	fault	Power-law	c = 1.02	Knott et al.,	1996

Table 1.4 (continued overleaf)

Parameter	Scale	Method	Lithology	Feature	Distribution	Exponent*	Author	Year
LENGTH	amalgamated data seismic, core	cfd	various	faults	**Power-law**	d = 1.29	Knott et al.,	1996
LENGTH	large			faults	**Power-law**	c = 0.67	Krantz [1, 2]	1988
LENGTH	outcrop	cfd		fractures	**Power-law**		Malthe-Sorenssen et al.,	1998
LENGTH	seismic	cfd	sandstone	faults	**Power-law**	c = 2.04	Needham et al.,	1996
LENGTH	various amalgamated	cfd cfd	sandstone	joints/ fractures	**Power-law**	d = 2.1	Odling Aarseth et al.,	1997 1997
LENGTH	outcrop	cfd	limestone	veins	**Power-law**	c = 0.8	Odling et al.,	1999
LENGTH				faults	**Power-law**	c = 1.3	Okubo & Aki [3]	1987
LENGTH	outcrop			joints	**Power-law**	a = 1.9	Ouillon et al., [2]	1996
LENGTH	large			joints	**Power-law**	a = 2.1	Ouillon et al., [2]	1996
LENGTH	large			faults	**Power-law**	a = 2.1	Ouillon et al., [2]	1996
LENGTH	large			faults	**Power-law**	a = 3.2	Ouillon et al., [2]	1996
LENGTH	seismic	cfd		faults	**Power-law**	c = 1.18	Pickering et al.,	1997
LENGTH	outcrop			faults	**Power-law**	a = 2.2	Reches [2]	1986
LENGTH	landsat	cfd		lineament	**Power-law**	c = 4.01 to 5.07	Rogers	1994
LENGTH	large			faults	**Power-law**	a = 2.1	Scholz & Cowie [2]	1990
LENGTH	large			faults	**Power-law**	a = 2.02	Scholz [2]	1997
LENGTH	amalgamated datasets			faults	**Power-law**	d = 1.3	Scholz et al., [3]	1993
LENGTH	large			faults	**Power-law**	c = 1.21	Scott & Castellanos [1, 2]	1984
LENGTH	outcrop	histogram	granite	joints	**Power-law**	a = 1.3	Segall & Pollard	1983
LENGTH	outcrop	histogram	granite	joints	**Power-law**	a = 1.8	Segall & Pollard	1983
LENGTH	large			faults	**Power-law**	c = 1.84	Stewart [1, 2]	1980
LENGTH	seismic	cfd	various	faults	**Power-law**	c = 1.37, 1.42, 1.5, 1.43, 1.49, 1.35, 1.18, 1.75, 2.04, 1.87	Yielding et al.,	1996
LENGTH				faults	**Power-law**	c = 1.4	Villemin et al., [3]	1995
LENGTH	outcrop	cfd	coal seam	faults	**Power-law**	c = 1.36	Watterson et al.,	1996
LENGTH	outcrop	cfd	coal seam	faults	**Power-law**	c = 1.87	Watterson et al.,	1996
LENGTH	MODEL	cfd	-	-	**Power-law**	x = 1.58	Yielding et al.,	1996

Table 1.4 (continued overleaf)

Parameter	Scale	Method	Lithology	Feature	Distribution	Exponent*	Author	Year
LENGTH	MODEL			fractures	**Power-law**	x = 1.6	Zhang & Sanderson	1996
LENGTH	outcrop	histogram cfd	limestone	veins	**Power-law & Log-normal**		Gillespie et al., Aarseth et al.,	2001 1997
LENGTH	outcrop	cfd		faults	**Power-law**	c = 1.64	Ackermann & Schlische [2]	1997
LENGTH	large	cfd		faults	**Power-law**	c = 1.61	Belfield [2]	1992
LENGTH	large	cfd		faults	**Power-law**	c = 1.51	Clark et al., [2]	1999
LENGTH	outcrop	cfd		shear bands	**Power-law**	c = 0.6	Fossen & Hesthammer [2]	1997
LENGTH	large	cfd		faults	**Power-law**	c = 2.04	Needham et al., [2]	1996
LENGTH	outcrop	cfd		faults	**Power-law**	c = 1.4	Schlische et al., [2]	1996
LENGTH	large	cfd		faults	**Power-law**	c = 1.4	Villemin and Sunwoo [2]	1987
LENGTH	large	cfd			**Power-law**	d = 1.66	Line et al., [2]	1997
LENGTH	large	cfd			**Power-law**	d = 2	Yielding et al., [2]	1992

References with numbers adjacent to them, indicate quotes in the following references:
1 - Cladouhos & Marret, 1996
2 - Bonnet et al., 2001
3 – Yielding et al., 1996
4 – Mathab et al., 1995
5 – Zhang & Einstein 2000
6 – Baecher 1983
cfd = cumulative frequency distribution (cumulative plot)
histogram = frequency distribution (non cumulative plot)

* - measure of **exponent** varies between methods
a = density/frequency exponent,
c = cumulative exponent (c = a+1),
d = exponent from combined length distributions
x = unknown measure

Table 1.4 Literature review of the statistical analyses of fracture spacing and length parameters

1.8.2.2 Log-normal distribution

Most geological variables do not follow a normal distribution (section 1.8.2.1) but instead possess a highly skewed probability density function. An example of such a data set is plotted as a histogram in **Figure 1.31a** and corresponds to the volumes of oil fields in a region (Davis 1986). Most volumes are small, but there are decreasing numbers of larger fields, with a few rare giants that exceed all other field volumes. If the x-values plotted in **Figure 1.31a** are converted to logarithmic form (so then y = log x), the visual appearance of the histogram is almost bell-shaped, i.e. normal (**Figure 1.31b**). Such data sets are described as best fitting to log-normal distributions (**Figure 1.29**). The cumulative frequency distribution for a log-normal distribution plots as a straight line when the x-axis is plotted as a logarithmic scale, and the y-axis is plotted as a linear scale (**Figure 1.30**).

1.8.2.3 Exponential distribution

Many geological events may be represented as points in space or time, such as the occurrence of fractures along a 1-dimensional transect (the fracture spacing parameter). When fractures are randomly positioned, the intersection points between the fractures and the scanlines can be defined as random if the presence of one intersection point does not affect the chance of another occurring around it, i.e. there is no interaction between the fractures (Priest & Hudson 1976, Hudson & Priest 1979, Baecher 1983). From statistical theory, if each small segment of a 1-dimensional transect has a small but equal probability of being intersected by a fracture, the intersection points follow a Poisson process, and the associated fracture spacing values follow an exponential distribution with a negative slope (Priest & Hudson 1976, Hudson & Priest 1979, Baecher 1983, Sen & Kazi 1984).

The probability distribution function for an exponential distribution (a random distribution) is illustrated in **Figure 1.29**. The curve is characterised by a steep slope representing relatively more small values of x, and relatively fewer large values of x. The cumulative distribution function is illustrated in **Figure 1.30,** and is represented by a straight line relationship when the x-axis is a plotted as a linear scale, and the y-axis is plotted as a logarithmic scale.

The slope of the cumulative distribution function is known as the exponent and can be used to compare data sets. A steep slope corresponds to a high value of exponent, and

represents relatively more smaller values in the data set. When comparing data sets that may be best-described by an exponential distribution (e.g. fracture spacing data sets), the units of measurement must be equal, as this affects the exponent of the best-fit line.

The exponential exponent value of a data set is inversely proportional to the mean of the data set (Swan & Sandilands, 1995). The mean and standard deviation of a data set that is best described by an exponential distribution are equal, or for a large sample from the population, have the same expected value (Priest & Hudson 1981). An example is illustrated in **Figure 1.32**.

1.8.2.4 Power-law distribution

Many studies of fracture parameters such as spacing and length have been reported in the literature, and in recent years there has been a dramatic increase in the use of the power-law distribution for characterising fracture systems (Bonnet et al., 2001).

The probability density function for a power-law distribution is illustrated in **Figure 1.29**, and the cumulative frequency distribution is illustrated in **Figure 1.30,** represented by a straight line relationship when both the x and y axes are plotted on a logarithmic scale. The power-law density distribution $n(l)$ is equal to the number of fractures $N(l)$ belonging to an interval, divided by the bin size (Bonnet et al., 2001). The cumulative power-law distribution represents the number of fractures whose length (for example) is greater than any given length.

The key parameter in describing a power law distribution is the exponent, or slope of the line. The power-law exponent provides a measure of the relative importance of large and small objects. The larger the exponent for a given population, the more small objects there are for every large object. Using fracture length as an example, a larger exponent implies a greater number of shorter fractures for every long fracture (Yielding et al., 1996).

The value of the power-law exponent depends on the type of distribution on which the analysis is based, i.e. either the density function or cumulative density function. The important difference is that the exponent (or slope) calculated from a power-law density distribution is equal to one plus the exponent from the cumulative distribution if the interval bins are linear. It is therefore important to compare like with like for exponents quoted in the literature (Bonnet et al., 2001) (**Table 1.4**).

Power-law relationships between parameters are potentially very useful and powerful geological tools. If a data set is best described by a power law distribution it implies scale invariance, and provides predictive capabilities beyond the typical sampling limits (e.g. Brooks et al., 1996), for example to extrapolate below the scale of seismic resolution (e.g. Gauthier & Lake 1993). A scale invariant (self-similar) fracture system is one in which any portion of the system is a scaled down version of the whole (Mandelbrot 1967, 1982). The concept of fractals (section 1.8.2.4.1) provides a method for describing the self-similarity of fracture and fault geometries.

1.8.2.4.1 *Fractal theory*

Fractal geometry is a branch of mathematics that can identify and quantify how the geometry of patterns repeats from one scale to another (Barton et al., 1995). The theory of fractal geometry (Mandelbrot 1967, 1982, Turcotte 1992) has been used to study the self-similarity and scale-invariance of many geological phenomena such as fault and fracture patterns, earthquake occurrences, volcanic eruptions, mineral deposits and oil fields (Turcotte 1992). "*A fractal is a shape made of parts similar to the whole in some way*" (Mandelbrot, 1987, as quoted in Feder 1988 and Ghosh & Daemen 1993). For an object or set of objects to posses a fractal geometry and show scale-invariance (self-similarity), the relative numbers of large and small elements remain the same at all scales between the upper and lower fractal limits (section 1.8.2.4.2). Fractal theory is a means of describing the order and scale invariance in systems that at first appear complex.

1.8.2.4.2 *The fractal dimension*

The scaling relationship of a fractal geometry is described by the fractal dimension (D). The fractal dimension describes how an object 'fills' space, for example how a fracture pattern fills a 2-dimensional sample area. The Euclidian or topological dimension of a line segment is 1, of a square is 2, and of a solid cube is 3 (Turcotte 1992, La Pointe 1988). The fractal dimension can be an integer in which case it is equivalent to a Euclidean dimension (Turcotte 1992). Generally the fractal dimension of an object is not an integer, i.e. a fracture pattern does not totally fill a 2-dimensional sample area or 3-dimensional volume; but instead will be fractional, or fractal (Mandelbrot, 1967). For example the fractal dimension of a fracture pattern measured in a 2-dimensional sample area will be between 1 and 2; the fractional

dimension of a fracture pattern measured in a 3-dimensional volume will be between 2 and 3 (La Pointe 1988).

1.8.2.4.3 *The box-counting technique*

The most common method of calculating the fractal dimension of a fracture pattern is the *box-counting technique* (Turcotte 1992, Walsh & Watterson 1993) which is designed to measure the fractal dimension of a fractal on a plane (in 2-dimensions), but has also been adapted to analyse 1-dimensional data sets (known as the interval counting technique (Gillespie et al., 1993)). Grids containing boxes of a given side length (d) are superimposed onto the fracture pattern and the number of boxes containing fractures is counted (N_d). The procedure is repeated for boxes of different sizes, and a graph of d against N_d is plotted, both with logarithmic axes. For the fracture geometry to be fractal, the box-counting curve needs to be a straight line. The slope of the line is the fractal dimension (D), which has a value of $1<D<2$ for a 2-dimensional sample area.

There are limitations associated with the box-counting technique. It is sensitive to the shape of the 2-dimensional area being studied, and the resolution of the data set (Gillespie et al., 1993). It has also been argued in the literature (Gillespie et al., 1993, Walsh & Watterson 1993) that fractal relationships have been mis-identified in cases where the relationship between d and N_d are not in fact straight lines, but curves.

A fracture pattern is an amalgamation of a number of fracture parameters (section 1.7.7) and it is suggested that only the simplest fracture patterns are likely to be characterised by a single fractal dimension over a significant scale range (Walsh & Watterson 1993). It is concluded by Gillespie et al., (1993) that 2-dimensional box-counting techniques are too insensitive to characterise the many attributes of most fracture arrays. Instead fracture parameters that compose the fracture geometry should be characterised individually as opposed to simply characterising the fracture pattern, except for specific cases where a simple characterisation is known to be sufficient (e.g. for a single set of sub-parallel fractures) (Gillespie et al., 1993).

1.8.2.4.4 *The relationship between power-law distributions and fractals*

Many authors have used the term fractal to describe any power-law relationship (such as the relationship between fracture length and frequency), and the term "power-law exponent" has been used interchangeably with "fractal dimension" (Marret &

Allmendinger 1991, Walsh et al., 1994, Acuna & Yortsos 1995, Brooks et al., 1996, Schultz & Fori 1996, Yielding et al., 1996, Belfield 1998, Beacom, 1999, Cello et al., 2000, Gillespie et al., 2001). However, the term fractal should only be used to describe the spatial distribution of fractures (Mandelbrot 1982, Wantanabe & Takahashi 1995, Cowie et al., 1996, Odling et al., 1999, Bonnet et al., 2001). A fractal fracture network implies organisation and spatial correlation between fractures. This spatial correlation is independent of the distributions of fracture attributes such as spacing, aperture and length. It therefore follows that the geometry of a fracture network can be non-fractal (randomly distributed in space) whilst parameters such as spacing and length can follow power-law distributions; and that the fractal dimension of a fracture data set is independent of the distributions of individual fracture parameters (Bonnet et al., 2001). In essence, individual fracture attributes (such as spacing, length, aperture) cannot be fractal; only the overall fracture geometry can be fractal as it is this that defines the spatial distribution of the fracture network.

However, Bour & Davy (1999) have shown that the fractal dimension of a 2-D fracture network and power-law fracture length exponent may be related through the equation

$$x = (a-1)/D$$

where D = fractal dimension, a = power-law length exponent, x = exponent from a scaling law involving the average distance from a fault/fracture to its nearest neighbour of larger length. The relationship has been tested by Bour & Davy (1999) for the San Andreas fault system, and provides a useful method to test the compatibility of the fractal dimension of a fracture pattern created by a set of fractures with a power-law length exponent.

Odling et al. (1999) suggest that when the exponent from a power-law cumulative fracture length distribution (a) is equal to 2, the visualisation of the fracture pattern at different scales is indistinguishable, and have called this a 'strictly self-similar' system. When the exponent (a) is different from 2, the authors suggest the system is not 'strictly self-similar'; the length population either lacks long ($a>2$) or short ($a<2$) fractures.

1.8.2.4.5 *Upper and lower cut-offs for power-law distributions*

The scale over which a system shows self-similar properties usually has upper and lower limits, for two main reasons: a) a natural object is rarely exactly self-similar

over an infinite range of magnitudes. It may instead be limited for example by lithology, the thickness of the studied unit or by the anisotropies of the rock mass (Ghosh & Daemen 1993, Gauthier & Lake 1993). b) It is seldom possible to collect accurate data sets over two orders of magnitude scales, and the data sets collected in the field (especially length data sets) are often subject to errors such as censoring and truncation (defined in section 1.7.5.1 and illustrated in **Figure 1.18**). These errors can cause the frequency distribution of a power-law population to degrade and deviate from a perfect straight line that would be observed for an infinitely large system, and therefore limit the scale range over which the power-law relationship can be meaningfully measured (**Figure 1.33**) (Heffer & Bevan 1990, Marrett 1994, Pickering et al., 1995, Needham et al., 1996, Watterson et al., 1996, Pickering et al., 1997, Belfield 1998, Bonnet et al., 2001).

The effect of truncation on a power-law distribution plotted as a cumulative frequency curve, is to shallow the slope of the curve at the lower end of the scale range (**Figure 1.33**). The slope of a power-law curve will decrease with increasing truncation (Watterson et al., 1996). The effect of censoring on a power-law distribution plotted as a cumulative frequency curve is to cause an artificial steepening of the curve at the upper end of the scale range (**Figure 1.33**).

Most examples of censoring and truncation of power-law distributions found in the literature refer to fault/fracture *length-frequency* data sets (e.g. **Figure 1.33a**). However, fault *displacement-frequency* data sets are also described in the literature as being best described by a power-law distribution, and suffering from sampling effects (Needham et al., 1996). Fracture/fault *spacing-frequency* data sets can also in some cases be best described by a power-law distribution (**Figure 1.33b**) (Knott et al., 1996), and can suffer from censoring and truncation effects. Wide spacings are often under-represented in the data due to the size of the sample area, and narrow spacings are also undersampled due to the resolution of measuring equipment, and the human eye.

1.8.2.4.6 *The extrapolation of power-law exponents and fractal dimensions between sampling domains*

Fractures and faults are 3-dimensional features, but due to limitations such as outcrop extent and exposure, attributes of fractures and faults are commonly measured in either 1- or 2-dimensions and therefore the topologic dimension of sampling differs

from that of the desired parameter (Marrett & Allmendinger 1991, Marrett 1996). For populations observed in different sampling dimensions the value of the power-law exponent (for fracture attributes) and fractal dimension (for fracture geometry) will differ. Fractures are underrepresented in lower dimensions, and the exponents differ according to:

$$\xi_{3D} > \xi_{2D} > \xi_{1D}$$

where ξ_{3D} = 3-dimensional scaling exponent, ξ_{2D} = 2-dimensional scaling exponent, ξ_{1D} = 1-dimensional scaling exponent (Borgos et al., 2000).

These dimensional sampling effects have been corrected in the literature using the relationships:

$$\xi_{3D} = \xi_{2D} + 1 \quad \text{and} \quad \xi_{2D} = \xi_{1D} + 1$$

or

$$\xi_{1D} = \xi_{3D} - 2 = \xi_{2D} - 1$$

So that by changing the sampling domain by 1, for example from 1-dimension to 2-dimensions, or 2-dimensions to 3-dimensions, the power-law exponent also changes by 1 (Mandelbrot 1982, Marrett & Allmendinger 1991, Yielding et al., 1996, Berkowitz & Alder 1998, Borgos et al., 2000, Bonnet et al., 2001).

However, these relationships only hold for populations of well-sampled fractures with random orientations and a uniform spatial distribution where fault size is independent of position. Therefore the relationships are unlikely to hold for fracture sets with strong spatial correlation and clustering, or strong directional anisotropy (Borgos et al., 2000, Bonnet et al., 2001). The effects of en echelon clustering and spatial variations in fault density lead to a difference between ξ_{2D} and ξ_{1D} that is <1. This causes an overestimation of the relative numbers of small-scale fractures and an underestimation of the relative numbers of large-scale fractures when extrapolating from 1-dimension to 2-dimensions (Borgos et al., 2000).

An empirical relationship between 2- and 3- dimensional scaling exponents was proposed by Hatton et al (1993) which modified the original relationship given above:

$$\xi_{3D} = a_1 \xi_{2D} + a_2 \qquad \text{where } a_1 \text{ and } a_2 \text{ are constants}$$

However, no consensus of the values of a_1 and a_2 has been proposed in the literature to date (Hatton et al., 1994, Borgos et al., 2000).

Even when the spatial distribution of fractures are independently and uniformly distributed with a power-law size frequency distribution, Borgos et al., (2000) find that the exponent of simulated fault patterns (with 50-100 faults) estimated by

extrapolating between dimensions can deviate by up to 15% from the theoretically predicted difference. The error is reduced to <5% when the data set is increases to approximately 1000 faults.

A true estimate of the power-law exponent for any sampling dimension only occurs when the dimension of the sample is equal to the dimension of the underlying fracture attribute (Borgos et al., 2000).

1.8.2.4.7 *The extrapolation of power-law exponents and fractal dimensions between scales*

A data set of values such as fracture length or displacement commonly has three distinct segments. A steep right hand segment, straight central segment, and shallow left-hand segment. The left and right segments are probably the result of censoring and truncation (section 1.8.2.4.5). The central segment is therefore taken to be the significant portion of the curve, which determines either the power-law exponent or fractal dimension (depending on the parameters plotted). A power-law data set is said to be scale-invariant, and therefore the central portion of the curve can be extrapolated to predict the frequency of datapoints above and below the sampling limits. The central portion of the curve should ideally extend over at least one order of magnitude within the sampling limits, before extrapolation is deemed reliable (Childs et al., 1990).

If the same fault/fracture system can be investigated and mapped at different scales and resolutions, and at each scale the parameter measured is best described by a power-law distribution, then the relationship may be extrapolated between and beyond the scales investigated. This relationship is especially useful in the petroleum industry where the most common forms of data are seismic (10's metres- to kilometre-scale) and core (millimetre- to centimetre scale), and it is important to know what occurs between these scales. The extrapolation of data has been carried out by a number of authors (Heffer & Bevan 1990, Castaing et al., 1996, Knott et al., 1996, Needham et al., 1996, Odling 1997) and this has enabled the determination of length, spacing and displacement distribution exponents over many orders of magnitude (**Figure 1.34**). Cumulative frequencies are normalised per unit area, in order to compare data sets collected at different scales on the same graph (Yielding et al., 1996 Bonnet et al., 2001).

However, care must be taken when compiling data sets from different scales and extrapolating the power-law relationship. Each individual sample set may accurately reflect the population exponent, but when combined onto a single plot by normalising the cumulative frequency, the samples may be offset from each other because the normalised fault density is higher in the smaller sample areas (Yielding et al., 1996) (**Figure 1.35**). The overall slope of the combined dataset reported by Yielding et al., (1996) gives an exponent of 2, which they suggest reflects the dimension of the sampling domain, and not the power-law exponent of the total fault population. Similar cumulative frequency plots of fracture length measurements from a variety of data scales are presented by Castaing et al., (1996) and Odling (1997). The combined data sets indicate a power-law parent distribution with exponent of 2.34 and 2.1 respectively (**Figure 1.36**). Odling (1997) suggest that strict self-similarity would be indicated by a slope of 2 on the combined plot, and therefore suggest that the data sets presented by Odling (1997) and Castaing et al., (1996) do not represent strictly self-similar systems.

Furthermore, scaling laws may have naturally occurring upper and lower limits due to geological variables such as lithology, unit thickness, fracture type or rock mass anisotropy (section 1.8.2.4.8).

1.8.2.4.8 *Other tests of self-similarity for power-law data sets*

As well as extrapolating power-law exponents and fractal dimensions between data scales (section 1.8.2.4.7) self-similarity can be tested in other ways.

- Firstly a plot of the modal value of the power-law distribution from each data set (i.e. the modal length or spacing value from each fracture map) against scale (or box size, defined as the square root of the mapped area) can be plotted on logarithmic axes (**Figure 1.37 a-e**)
- Secondly fracture intensity (fracture length per unit area, referred to as fracture density by Castaing et al., 1996, and Odling 1997, in **Figure 1.37 f, g,** see **Table 1.3**, sections 1.7.4.2, 1.7.5.2) can be plotted against data scale (defined also by observation height), on logarithmic axes

For a strictly self-similar distribution of fracture trace lengths over the scale range sampled, the expected slope on each plot should be 1 and –1 respectively (Castaing et al., 1996, Odling 1997). This is because for a self-similar system the normalised

modal value for each sample trace length, and the normalised apparent intensity should be constant. If the slope on the graph of apparent intensity versus scale is between –1 and 0, this indicates that fracture densities in the small-scale data sets are larger than expected (Odling 1997). This could be a real feature of the system, or may be caused by sampling technique.

1.8.2.4.9 *Factors affecting the power-law exponent and fractal dimension*

Power-law relationships have been recorded for fracture length, spacing, aperture and displacement data sets. The power-law exponents for each parameter reported in the literature cover the range of possible values ($0<x<1$ for 1-dimensional data sets, $1<x<2$ for 2-dimensional data sets) (**Table 1.4**). There are two possible reasons for this wide range of reported exponents. Either a) the differences in slope are artefacts of sampling, and the underlying power-law population for each fracture parameter can be described by a single exponent value, or b) the differences in slope represent genuine differences in fracture populations (Childs et al., 1990).

Childs et al., 1990, suggest that insufficient data have been analysed to demonstrate conclusively that the differences in slope for the same fracture parameter are not artefacts. However a number of studies have been carried out since 1990, and there are a number of factors that are considered to have an effect on the exponent of the power-law distribution, which also affect the validity of extrapolating the power-law relationship between scales (section 1.8.2.4.7) and between dimensions (section 1.8.2.4.6). The factors that have been reported as affecting the exponent are:

- *Data quantity* – The data set collected to analyse a fracture parameter must be large enough to give an acceptable statistical representation of the population, and large enough to give a good statistical fit to the theoretical distribution. It is suggested that the dataset must be sampled over 2-3 orders of magnitude to give a statistical representation. However the exponent is usually calculated over a shorter range of magnitudes due to truncation and censoring effects. Bonnet et al., (2001) suggests that a minimum of 200 fractures should be sampled to provide an accurate exponent for a power-law fracture length distribution. At outcrop scale, the size of the data set is often limited by the extent of exposure.
- *Combining data sets* – In situations when data is sparse, data sets from parallel 1-dimensional transects are occasionally merged to form a larger data set, known as

'multi-line sampling' (Childs et al., 1990, Marrett 1994, Nicol et al., 1996). The result of combining data sets is an artificially steep slope for the largest fractures/faults on a population plot, as they are multiply sampled (Marrett 1994).

- *Geological variables* – Variations within a sample area or between sample areas such as a change in lithology, grain size, rock competency or layer thickness may affect the population characteristics of the fracture system (Gauthier & Lake 1993, Knott et al., 1996, Nicol et al., 1996).
- *Heterogeneity* – Local small-scale variations in stress or strain can develop as part of the faulting process, resulting in areas of clustering for example, and thus developing a complex geometry (Peacock 1996). This increase in variability of fault/fracture patterns with decreasing scale reflects the heterogeneous nature of the fault zone. Fracture density may change within the same sample scale range, and therefore the value of the power-law exponent may vary.
- *Maturity of the system* – It has been suggested based on numerical modelling and outcrop data, that the value of the power-law exponent decreases as a fault system grows, evolves and matures, due to the progressive concentration of strain onto the larger structures (Nicol et al., 1996, Bonnet et al., 2001). Natural fracture/fault systems probably represent a range of maturity levels, and therefore a range of exponent values are recorded.
- *Reactivation* – Reactivation of a fault/fracture system may cause complexity, especially if the pattern and scale of the superimposed deformation events are different, and change the statistical properties of the system (Gauthier & Lake 1993, Peacock 1996, Yielding et al., 1996). Vignes-Adler et al., (1991) suggest that the greater the number of tectonic events in an area, the more random the fracture geometry will be, therefore lowering the possibility of a fractal fracture pattern.

1.8.3 *Statistical analysis of fracture parameters*

Many data sets of fracture parameters have been collected and analysed at different scales in order to define the best fitting statistical distribution. Different statistical distributions have been fitted to the same fracture parameter, and a variety of exponents have been reported (**Table 1.4**). The sections below will briefly describe

and discuss the different distributions reported in the literature for fracture spacing, length and geometry, and suggest possible reasons for the different distributions recorded.

1.8.3.1 Spacing

The fracture spacing distribution has been modelled (analogue and numerical) by Rives et al., (1992) to simulate the development of spacings between a set of parallel joints, with increasing magnitude of strain, in a single bed or sedimentary layer. The spacing distribution is found to be *exponential* at the early stage with a low fracture density and little interaction, then *log-normal* at intermediate fracture density and interaction, and finally tends to a *normal* distribution at high fracture densities (**Figure 1.38**). This suggests that the fracture spacing distribution evolves with increasing fracture set development (i.e. increasing density, deformation and strain) from exponential (with a negative slope) through log-normal to normal. The initial spacing distribution is therefore suggested to be controlled by a random process, and with increasing strain the joints interact and become more organised leading to a change in spacing characteristics (Belfield 1998). The final stage in the development of the modelled joint set (the normal distribution) corresponds to the saturation level described by Narr & Suppe (1991). Therefore the type of spacing distribution reported from natural data sets could indicate the degree of maturity and evolution of the fracture set (Rives et al., 1992).

Belfield (1998) also modelled the joint spacing distribution by changing the spatial distribution of strain rather than its magnitude (as Rives et al., (1992) did). It was found that the spacing distribution function ranges from approximately exponential through to power-law depending on the spatial distribution of strain. Where the distribution of strain is homogeneous, an exponential fracture spacing distribution results; whereas when the distribution of strain is heterogeneous this leads to the development of a power-law fracture spacing distribution, and spatial clustering (Belfield 1998). It is suggested that when the spacing distribution is power-law, the degree of clustering in the system can be quantified by using the slope (exponent) of the spacing versus cumulative frequency graph (Belfield 1998). A high degree of clustering, where the strain spatial distribution is more intermittent, is indicated by small values of exponent. With decreasing clustering, the value of the power-law exponent will decrease. (In this case, the power-law exponent is not the same as the

fractal dimension as suggested by Belfield 1998). If the slope is steep (approaching an exponential fit) then the underlying strain distribution is said to be relatively homogeneous and lacking clustering.

The modelling undertaken by Rives et al. (1992) and Belfield (1998) corresponds to joint sets developed within mechanical boundaries (sedimentary layers). It has been suggested that in rocks without systematic mechanical boundaries, the spacing distribution is best described by a log-normal distribution (Ruf et al., 1998).

In a rock mass that has suffered several stages of fracturing (reactivation) it has been suggested that the distribution of fracture spacings measured along a 1-dimensional line transect is best described by an exponential distribution (with negative slope) (Priest & Hudson 1976, Hudson & Priest 1979). This is due to the superposition of several fracture sets causing random break-up of large fracture spacings (**Figure 1.39**).

When measuring fracture spacings along 1-dimensional transects in the field, the length of the transect is often restricted by the extent of the outcrop. This restriction could introduce some bias into the estimation of the spacing distribution (Sen & Kazi 1984). The relationship between the mean spacing value for a) the population and b) the finite length transect is illustrated in **Figure 1.40a** for an exponential distribution with negative slope, and in **Figure 1.40b** for a log-normal distribution. For longer transects the mean values for the population and the sample are more likely to be almost equal, and for a transect line of infinite length, the mean spacing of the sample and the population are equivalent. For shorter transects the sample mean spacing is greater than the population mean spacing, suggesting that the mean sample spacing is underestimated (Sen & Kazi 1984). The amount of bias decreases as the length of the transect increases, and the length of the transect required for unbiased estimates is dependant on the mean spacing value. When the mean spacing is small, shorter transects are required for accurate estimation from the sample.

A summary of fracture spacing distributions from natural fracture systems reported in the literature is presented in **Table 1.4**. The majority of data sets are best described by an exponential distribution with a negative slope (**Figure 1.41**).

1.8.3.2 Length

In extreme cases, the effects of sampling on a power-law fracture length population can result in a distribution that appears to be log-normal or exponential (Castaing et

al., 1996, Bonnet et al., 2001). These distributions can result through degradation of an underlying power-law distribution due to censoring and truncation (sections 1.7.5.1 and 1.8.2.4.5) (Heffer & Bevan 1990, Odling 1997, Renshaw 1999). For example, when 1-dimensional sample lines are used across 2-dimensional sample areas to measure fracture length, longer fractures are more likely to intersect the sampling line. This is known as size bias (section 1.7.5.1). The probability of a fracture appearing in the sample is the product of the probability of it appearing on the outcrop, and the probability of it intersecting the sample line. Therefore the sample of fracture lengths is said to be linearly biased (Baecher 1983, Einstein & Baecher 1983). The effect of linear bias is to transform many common statistical distributions into a log-normal form (**Figure 1.42**). This may suggest that the observation of a log-normal fracture length distribution is an artefact of sampling (Einstein & Baecher 1983).

Problems occur when trying to distinguish between censored and truncated power-law length data sets, and data sets that actually fit to a different distribution. The presence of a characteristic length scale in the system, (e.g. due to lithological layering) can result in a fracture length distribution that is best described by a log-normal or exponential distribution and is not as a result of sampling errors. In more massive rocks a power-law distribution may be more appropriate (Odling et al., 1999).

Numerical simulations of fracture systems have suggested that the best-fitting fracture length distribution may evolve over time, with increasing strain. Cowie et al., (1993) found that the length distribution evolves from following an exponential law to a power-law as the interaction of fractures increases. Linkage of fractures during evolution of the system allows fractures/faults to grow and cause a power-law population to develop. Modelling by Cladouhos & Marrett (1996) predicts a systematic temporal decrease of the power-law exponent with increasing strain and maturity of the system, as long as linkage occurs and is not balanced by the birth of small fractures/faults or the death of large faults (**Figure 1.43**). Laboratory experiments by Sornette et al., (1990) also suggest a decrease in power-law exponent with time, reflecting the growth of large faults and linkage of smaller structures dominating over nucleation.

A summary of fracture length distributions from natural fracture systems reported in the literature is presented in **Table 1.4**. The majority of data sets are best described by a power-law distribution (**Figure 1.44**), with a wide range of exponents (**Figure 1.45**). The range of exponents probably represents a variety of maturity levels, geological

variables such as lithology and layering, and various sampling effects on the fracture length data sets.

1.8.3.3 Geometry / network

Fractal analysis of natural and simulated fracture networks has been carried out by many authors, mostly using the box-counting method, and is summarised by Bonnet et al. (2001). The fractal dimensions of fracture geometries measured in 2-dimensions cover the range of theoretical values possible for that sampling dimension, (i.e. from 1 to 2) (**Figure 1.46**). The wide spread of values is probably due a combination of both sampling errors and differences due to real physical processes as described in section 1.8.2.4.9.

1.8.4 *Reliability tests for data analysis*

The majority of natural data sets (such as various fracture attributes) do not fit exactly to a specific statistical distribution. Instead, the data is described by a "best-fit" distribution – the closest to a perfect fit. Fitting "best-fit" distributions to natural data sets is often done by eye, and is therefore arbitrary. In order to test the reliability of best-fit statistical distributions, two statistical tests will be used in this thesis: the correlation co-efficient (r) and the Kolmogorov-Smirnov test. These tests are described in the following sections.

1.8.4.1 Correlation co-efficient (r) and regression (R^2)

The *correlation co-efficient* is used estimate the degree of linear correlation between two variables, and is commonly known as r. (See Davis 1986 or Swan & Sandilands 1995 for a detailed description and equations). The value of the correlation co-efficient ranges from $-1 < r < +1$. When r is equal to +1 or –1, a strong linear relationship exists between the two variables with positive and negative slopes respectively. When r is at or near to zero the two variables lack a rectilinear (straight line) trend. It is important to note that the correlation coefficient is not a general measure of the relationship between two variables, but specifically measures the degree of a rectilinear tendency (Swan & Sandilands 1995). Although the correlation coefficient (r) is a useful and convenient measure of the degree of correlation, a second type of 'best-fit' analysis called *regression analysis* is often preferred. There

are two main advantages to regression over the correlation coefficient, a) regression allows both rectilinear and curvilinear relationships to be tested, and b) the nature of the relationship between the variables can be defined by an equation. Linear regression is the fitting of a line through a given set of data points to summarise the relationship between the variables being studied. A 'best-fit' line is fitted to the data points in such a way as to minimise the deviation in the y-direction between the data points and the line. The deviations in the y-direction are known as the y-residuals, and can be either positive or negative. The sum of these squared differences is called the residual sum of squares. The sum of squared differences between actual y-values and the average of the y-values is called the total sum of squares. The goodness-of-fit statistic (also known as the coefficient of determination, and R^2) is often used to convey the quality of the regression. R^2 measures the amount of deviation of the data points from the best-fit line. The value of R^2 can vary between 0 and +1 where +1 indicates a perfect fit of the data points to the regression line and as R^2 approaches zero the 'fit' of the data to the line is reduced. The smaller the residual sum of squares is, compared with the total sum of squares, the larger the value of the coefficient of determination (R^2), which is an indicator of how well the equation resulting from the regression analysis explains the relationship (see Microsoft Excel help manual).

1.8.4.2 Kolmogorov-Smirnov test

The Kolmogorov-Smirnov test is used to compare the cumulative frequency distributions (cfd) between either a) a sample distribution and a theoretical distribution, or b) two sample distributions; and to investigate the significance of the difference between them (e.g. Miller & Kahn 1962, Miller & Miller 1989, Swan & Sandilands 1995). For the purposes of this thesis, the test is used to compare a theoretical distribution with a sample distribution.

Two hypotheses are drawn:

For **Ho** (the null hypothesis), the sample data set is from the same distribution as the theoretical distribution.

For $\mathbf{H_A}$ (the alternative hypothesis) the sample data set is not from the same distribution as the theoretical distribution.

Ho $F_S(x) = F_T(x)$ for all values of x

$\mathbf{H_A}$ $F_S(x) \neq F_T(x)$ for some values of x

(where $F_S(x)$ = cfd for theoretical distribution, $F_T(x)$ = cfd for sample distribution)

The statistic (D) used to measure the difference between the two distributions is the largest absolute vertical deviation, and can be positive or negative:

$$D = \max \{ F_S(x) - F_T(x) \} \quad \text{or} \quad D = \max \{ F_T(x) - F_S(x) \}$$

An example of a Kolmogorov-Smirnov test is illustrated in **Figure 1.47**, carried out on a data set of fracture spacing values, along with a summary of the main stages for the analysis.

The distribution of D depends on the size of the sample (n). Critical values of D for different sample sizes (D_{CRIT}) are available in tables in textbooks of statistics (e.g. Davis 1986) at different levels of confidence/significance (a 0.05 significance level corresponds to a 95% confidence level).

If the maximum vertical deviation between the two cumulative frequency distributions is greater than the critical value of D then the hypothesis that the sample comes from the same distribution as the theoretical distribution is rejected. i.e. reject Ho if $D > D_{CRIT}$. This is because if the sample was drawn from the theoretical distribution, then 95% of the time such a large discrepancy (D) would not be expected (at that confidence level).

The Kolmogorov-Smirnov test is a non-parametric statistical test, i.e. no assumptions about the form of the theoretical cfd are needed. One of the biggest advantages of the Kolmogorov-Smirnov test over other non-parametrical tests (such as the Chi-squared test) is that the sample values do not need to be grouped into arbitrary classes, and therefore the Kolmogorov-Smirnov test is deemed more sensitive (Davis 1986).

The Kolmogorov-Smirnov test has been used by many authors to compare sample data sets of fracture parameters such as length or spacing to theoretical data distributions (e.g. Baecher 1983, Einstein & Baecher 1983, Rouleau & Gale 1985, Mathab et al., 1995, Mabee & Hardcastle 1997, Odling 1997, Ehlen 1999, Zhang & Einstein 2000), and is used in this study with a confidence level of 95%.

1.8.5 *Other statistical methods for fracture analysis*

As well as calculating the statistical distribution which best describes a fracture parameter data set (such as length or spacing values), other statistical methods are available, two of which are used in the present study, and are outlined below.

1.8.5.1 Coefficient of variation (Cv)

The coefficient of variation, Cv, is method for characterising fracture spacing that can be used as an index of clustering. Cv is defined as the standard deviation of fracture spacings measured along a 1-dimensional line transect, divided by the mean spacing of the data set; and expresses the degree of clustering (Aarseth et al., 1997, Gillespie et al., 2001).

For fracture spacings that are randomly distributed along the line transect, and best described by an exponential distribution, the standard deviation and mean are equal, and therefore Cv = 1. If the fracture spacings are clustered, then Cv > 1, and conversely if the fracture spacings are anti-clustered (uniformly / normally distributed) then Cv < 1.

1.8.5.2 Step plots

The distribution of fractures along 1-dimensional line transects can also be investigated by plotting the cumulative spacing values against cumulative fracture frequency. If the fractures are regularly spaced then a straight-line relationship will occur. When the fractures are clustered into areas of small and wide spacings then the plot gives a stepped appearance; hence I have named this type of plot a 'step plot'. This type of analysis is particularly useful in analysing the density of fractures around a fault. A schematic representation of a 'step plot' is shown in **Figure 1.48**.

1.9 Data Collection

1.9.1 One-Dimensional (1-D) methods

Fracture parameters such as orientation, length and spacing can be collected along 1-dimensional line transects, (also known as sample lines, traverses and scanlines), across vertical and horizontal outcrop surfaces.

The advantages to this method are (McCaffrey et al., 2001, McCaffrey et al., in prep):

a) Data is easy to collect, analyse and visualise.

b) Method can be applied to core data collected from boreholes, and field outcrops.

The disadvantages are (McCaffrey et al., 2001, McCaffrey et al., in prep):

a) Dimensional problems occur when relating 1-D data to 2- and 3-D data.

b) Often exposure is limited to small outcrops and therefore only short transects are possible, whereas long transects are needed for areas where fracture density is low to give a representative sample. To overcome this problem, a series of parallel sample lines may be carried out across the same surface, known as *multi-line sampling* (Walsh et al., 1991, 1994). This method can result in over-sampling of large values (e.g. large fracture spacings), and an artificially steep slope on a power-law distribution plot, or an artificially shallow slope on an exponential distribution plot.

c) Variables such as average spacing and fracture density can vary depending on the orientation of the scanline relative to the fracture orientations. Shallowly dipping fractures are often under-represented by 1-dimensional sampling as they are only visible in vertical exposures which are often limited in height, or sampling is limited by the height of the sampler.

d) The data is often subject to censoring and truncation errors (section 1.7.5.1).

e) The method is very time consuming.

1.9.2 Two-Dimensional (2-D) methods

Fracture parameters such as length and connectivity can be assessed within 2-dimensional sample areas at a variety of scales. Scaled maps consisting of fracture traces constitute 2-dimensional fracture network samples or fracture maps.

The advantages to this method are (McCaffrey et al., 2001, McCaffrey et al., in prep):

a) The data can be compared to other data scales such as air-photographs, Landsat™ images and maps made from seismic data.

b) The overall fracture geometry can be assessed not just individual attributes.

c) Fracture network connectivity can be assessed, essential for fluid-flow modelling.

d) The method is likely to provide a more representative visualisation of the network than 1-dimensional data collection.

The disadvantages method are (McCaffrey et al., 2001, McCaffrey et al., in prep):

a) Dimensional problems occur when relating 2-D to 3-D data

b) Data is subject to censoring and truncation (section 1.7.5.1).

c) The method is very time consuming.

1.10 Method of Study

A total of eight months were spent in the field, four months in each study area, during the summers of 1998 & 1999. Initial reconnaissance studies were carried out on all exposures along the Møre-Trøndelag Fault Complex (MTFC) in the Fosen area of Central Norway, and the Walls Boundary Fault System (WBFS) in Shetland, in order to identify well-exposed locations for detailed work. These areas were then mapped at 1:10,000 scale to identify the large-scale structure and distribution of lithologies.

Fracture attribute data sets (orientation, infill, kinematics, spacing, length and connectivity) were collected within these key localities using two methods: a) Systematically orientated, one-dimensional (1-D) line transects were carried out, both perpendicular and parallel to the trend of the fault(s), on vertical and horizontal outcrop surfaces (section 1.9.1) and b) A series of photographs of outcrop surfaces were taken in the field to produce two-dimensional (2-D) fracture network maps (section 1.9.2). 1-D and 2-D data sets of fracture parameters were collected at different distances to all major faults within the MTFC and the WBFS (i.e. within different strain regions), and where possible within a variety of lithologies.

In general, exposures in the vicinity of major structures within the MTFC are more extensive than those adjacent to structures within the WBFS. The WBFS crops out at several coastal sections, along which the rocks are weathered and eroded, and exposure is often discontinuous. The MTFC is well-exposed inland, as well as along the coastlines of fjords in the area.

This study has been carried out contemporaneously with another PhD project by Lee Watts (University of Durham, 2001), whose aims were to evaluate the kinematic and structural evolution of the MTFC and the WBFS, and to assess the factors that control the multiple reactivations of these structures. Hand specimens collected in the field along the MTFC by Watts (2001), and cut into thin sections for microstructural analysis, have been used to investigate fracture attributes at thin-section scale. A Landsat™ image (provided by Statoil) and a series of air photographs (provided by the Geological Survey of Norway) have also been used to investigate fault/fracture characteristics at larger scales.

CHAPTER 2 - THE MØRE-TRØNDELAG FAULT COMPLEX

The ENE-WSW-trending Møre-Trøndelag Fault Complex (MTFC) in Central Norway, formerly designated the Møre-Trøndelag Fault Zone, is a 10-20 km wide, steeply dipping zone of fault-related deformation (Grønlie & Roberts 1989, Grønlie et al., 1991, Watts 2001). The fault complex extends onshore from the Grong-Olden Culmination (GOC) near Grong in the NE, through the Fosen Peninsula to the SW and offshore (Gabrielsen and Ramberg 1979) (**Figure 2.1, Figure 2.2**). The MTFC defines the coastline of Central Norway from the island of Hitra to Romsdal (62 to 64° N), and extends offshore to apparently define the southern margin of the Møre Basin, and the northern margin of the Viking Graben (Doré et al., 1997), suggesting that the MTFC played an important role in controlling the architecture of these Mesozoic basins (**Figure 2.1**). It has been proposed by several authors that the MTFC may extend to join the Walls Boundary Fault, Shetland, and the Great Glen Fault, Scotland (Norton et al., 1987, Ziegler 1985, Grønlie and Roberts 1989, Seranné 1992, Blystad 1995).

The following sections describe the regional setting of the MTFC, the main structural components of the fault complex, key fault zone exposures and the kinematic history of the MTFC.

2.1 Regional setting and protolith lithologies of the MTFC

On the Fosen Peninsula (the field area for this study), the MTFC cuts through a series of E-SE transported nappes emplaced during the Siluro-Devonian (Scandian) orogeny, and Devonian sedimentary rocks (**Figure 2.2**). Fosen forms part of the Western Gneiss Region (WGR) exposing some of the deepest levels of the Scandinavian Caledonides (Roberts 1998). The tectonostratigraphy of the Caledonides is divided into five main units, (from base to top) the Autochthon / Parautochthon, and four overlying allochthons – Lower, Middle, Upper and Uppermost. The correlation of the main tectonic and stratigraphic units in the Scandinavian Caledonides is summarised in **Table 2.1**. For more detailed accounts of the tectonostratigraphy the reader is referred to Gee et al., 1985, Roberts and Gee 1985, and references therein.

Fosen area

	Southwestern areas			Central areas		North of Grong–Olden Culmination (Stephens *et al.* this volume)	Eastern Areas
Tectonic units	Dombås (Guezou 1978)	Oppdal (Krill 1980)	Trollheimen (Gee 1980)	Western Trøndelag Eastern (Wolff and Roberts 1980; Roberts and Wolff 1981)			Central and Southern Jämtland (Gee 1975a)
Late-orogenic sediments				Late Silurian(?) to Mid-Devonian	Early Devonian		
Uppermost Allochthon						Helgeland Nappe Complex	
Upper Allochthon	Trondheim Nappe Complex: Fokstua Group, Musadal group, Skåkåhøi Group	Tronget unit		Støren Nappe Meråker; Gula Nappe Complex; Levanger Nappe Øyfjell		Gjersvik Nappe, Leipik Nappe, Gelvanakko Nappe, Stikke Nappe, Björkvattnet Nappe	Köli Nappes (Tännfors district) — Seve–Köli Nappe Complex
	Bottheim Group	Blåhø Unit		Skjøtingen Nappe Essandjø		Seve Nappes	
Middle Allochthon	Andbergshøi Complex: Veslefjell Group	Sætra Nappe		Leksdal Nappe: Dolerite-intruded Sandstone; Sandstone without dolerite; Hærvola Nappe	Remskiepp Nappe: For subdivision of this unit, see Sjöström (1983)	Särv Nappes (with Ottfjället Dolerites)	
		Risberget Unit	Indre Kam Formation (Hansen 1971) Augen gneiss			Augen gneiss	Offerdal Nappe; Tännäs Augen Gneiss Nappe
Lower Allochthon	Osen–Røa Nappe Complex (Nystuen 1981)	Not distinguished	Svarthammer unit (Hansen 1971) in part	Foliated granite and rhyolite; Bjørndalen Formation (Gee 1977)		Jämtland Supergroup in Jämtlandian Nappes	
Parautochthon and Autochthon	'sparagmite'	Åmotsdal Unit	Gjevilvatnet Group	Bjørndalen Formation	Quartzites and black phyllites	Tåsjön and Sjoutälven Groups	
	Precambrian gneiss and granite	Lønset Unit (gneiss)	Trollheimen Granite	Precambrian granite and rhyolite	Precambrian granite and rhyolite	Precambrian granite, gneiss, etc.	

Table 2.1 Correlation of main tectonic and stratigraphic units in the central southern part of the Scandinavian Caledonides (adapted from Gee et al. 1985).

In the study area for this thesis (north of the Verran Fault (section 2.2.2)), the amount of Precambrian gneiss within the Lower Allochthon makes it virtually impossible to distinguish this unit from the underlying parautochthonous gneisses (Gee et al., 1985); and the gneisses have been informally called the Banded Gneiss Complex (BGC) of Fosen by Möller (1988). (Gilotti and Hull (1993) refer to them as the Vestranden Gneiss Complex). The gneisses in the study area are derived from Proterozoic granitic-tonalitic orthogneisses, which were intruded by a series of Ordovician to Early Silurian diorites and granites. The orthogneisses and intrusions have both been highly reworked during Scandian deformation and metamorphism into strongly banded L-S tectonites (Roberts 1998). Due to intense deformation and metamorphism it is generally impossible to differentiate between the protolith orthogneisses, granites and diorites (Roberts 1998).

In hand specimen, the gneisses from the study area are pink/grey in colour, fine- to coarse-grained and equigranular, with crystals ranging from 0.5 to 1cm in size. In thin-section, the main minerals present are potassium feldspar, plagioclase feldspar and quartz, which collectively account for around 70 to 80% of the rock. Epidote, chlorite, biotite muscovite, hornblende and sphene comprise approximately 20 to 30% of the rock, together with accessory minerals such as magnetite and pyrite. The relative abundance of minerals varies spatially, reflecting variations in protolith composition and metamorphic grade.

The gneisses contain millimetre-scale banding of quartz-rich and feldspar-rich layers, within which the grains have been stretched and flattened to produce a strong ENE-WSW trending foliation, and a subhorizontal lineation defined by elongated grains (Watts 2001). The combination of banding and foliation have led to the gneisses displaying a strong anisotropy. The foliation was produced under amphibolite facies conditions, based on the highly recrystallised nature of the textures, and the presence of garnet porphyroclasts (Watts 2001). Retrograde chlorite and epidote is widespread within the gneisses, suggesting a greenschist facies overprint (Watts 2001).

2.2 Structural components and key exposures within the MTFC

The MTFC comprises two major fault strands, the Hitra-Snåsa Fault (HSF) to the north and the Verran Fault (VF) to the south (Grønlie & Roberts 1989, Grønlie et al.,

1991, Watts 2001) (**Figure 2.2**). These two major bounding lineaments are both sub-vertical structures striking ENE-WSW and are both well exposed on the Fosen Peninsula, lying approximately 11km apart in the SW and 5km apart in the NE. The VF and the HSF have localised along the opposite limbs of a pre-existing regional-scale antiform (**Figure 2.3**).

A detailed study of the fault rocks and structures within the MTFC has been carried out by Watts (2001). Previous field studies of the VF have also been carried out by Grønlie & Roberts (1989), Grønlie et al., (1991) and Bering (1992).

Fracture data for use in this study was collected adjacent to both of the main bounding structures within the MTFC (the VF and the HSF). Data has also been collected adjacent to two other structures, a) the Rautingdalen Fault (RF) - a kilometre-scale NNE-SSW trending fault, which splays off the VF (**Figure 2.4**) and b) the Elvdalen Fault (EF) - an ENE-WSW trending fault, parallel to the overall fault zone trend, which lies between the two main bounding structures (**Figure 2.4**).

In the following sections the HSF, VF, RF and EF will be described briefly, together with their key exposures and associated fault rocks.

2.2.1 *The Hitra-Snåsa Fault (HSF)*

The Hitra-Snåsa Fault Zone (HSFZ) refers to a narrow, ENE-WSW-trending, elongate region, in which the country rocks are deformed as a result of movement along the HSF, and extends either side of the Hitra-Snåsa Fault Plane (HSFP). The HSFP represents the most recent and most significant movement plane (Watts 2001), and is used in this thesis as a central reference line for this fault zone.

Fracture data has been collected from localities both within and outside the HSFZ, at 3 areas along the trace of the HSF – a) Mefjellet section, b) Hammardalen quarry and 719 road cut, c) Follavatnet and Brattreitelva sections (**Figure 2.5**).

2.2.1.1 Mefjellet section

The Mefjellet section provides the best exposures of the HSFZ on Fosen (**Figure 2.5**). Mefjellet is a hilly area (up to 650m) that lies to the north of the Ormsetvatnet reservoir, and is characterised by rocky exposures and scrubby moorland. The HSF

trace is defined by an ENE-WSW orientated valley containing an alignment of lakes (**Figure 2.6 a, b**).

In the Mefjellet area, the HSFZ comprises a 1 km-wide ductile shear zone containing mylonites, and a narrow central fault core containing epidote-rich cataclasite and pseudotachylite (Watts 2001). The mylonites, which overprint gneisses belonging to the Banded Gneiss Complex (section 2.1), formed during a period of sinistral shear (Watts 2001). Syn-tectonic white mica grains that crystallised during mylonitisation as overgrowths around feldspar clasts have been dated at 409 ± 12 Ma using an $^{40}Ar/^{39}Ar$ laserprobe technique by Sarah Sherlock at the Open University, in conjunction with Watts (2001). Pseudotachylites and coeval epidote-rich cataclasites formed later during a period of sinistral transtension (Watts 2001). Pseudotachylite veins have also been dated by Sherlock (in conjunction with Watts, 2001) using the same technique, and yield a mean age of 291 ± 14 Ma. Locally, within the HSFZ, zeolite- and calcite-filled fractures transect the cataclasites, and display dextral strike-slip offsets of several centimetres (Watts 2001). The highly polished HSFP is well exposed at grid reference locality 7900 8775, orientated 060/71NW, and contains sub-horizontal slickenside lineations (**Figure 2.6 c**). Outside the HSFZ, both to the NW and SE, gneisses belonging to the Banded Gneiss Complex of Fosen (section 2.1) are exposed.

Fracture data for this study has been collected at 8 localities (marked on Figure 2.5 b), at varying distances both north and south of the HSFP, within mylonitised gneisses.

2.2.1.2 Hammardalen quarry and 719 road cut

A disused quarry at Hammardalen and an ENE-WSW trending road cut along the 719 road, provide exposures to the S and N of the HSFP respectively (**Figure 2.5 b**). The HSFP itself is exposed in the heavily wooded Hammardalen, orientated 052/65NW and contains shallowly plunging slickenside lineations. Within the HSFZ, protomylonites overprinting gneisses belonging to the Banded Gneiss Complex of Fosen (section 2.1) are exposed. The protomylonites were formed during a period of sinistral shear (Watts 2001). Later brittle deformation led to the development of epidote cataclasites consistent with sinistral strike-slip movements along the HSFP (Watts 2001). Later zeolite and calcite mineralisation fills pre-existing calcite-filled faults and fractures (Watts 2001). The true extent of fault-related deformation at this

locality is unclear due to the lack of exposure. Outside the HSFZ, both to the NW and SE, gneisses belonging to the Banded Gneiss Complex of Fosen (section 2.1) are poorly exposed.

Fracture data for this study has been collected at one locality within the quarry, which lies to the south of the HSFP, and from two localities at different distances along the road cut, to the north of the HSFP.

2.2.1.3 Follavatnet and Brattreitelva sections

The HSFZ is partially exposed along the shore of Follavatnet and along a forestry track at Brattreitelva (**Figure 2.5 c**). The HSFP is not exposed in this area, but can be extrapolated from Mefjellet (section 2.2.1.1) using the Landsat™ image (presented in chapter 4, **Figure 4.1**). The HSFZ is at least 600m wide at this locality, and contains mylonitic rocks, formed during sinistral shear, derived from granodiorite and a series of meta-sedimentary rocks of uncertain origin (Watts 2001). Later brittle deformation is also present, and is consistent with sinistral strike-slip movements along the HSFP.

Fracture data for this study has been collected at 2 localities, both to the south of the HSFP, one within the HSFZ from mylonitised psammites and one outside the HSFZ from psammite.

2.2.2 *The Verran Fault (VF)*

The Verran Fault Zone (VFZ) refers to a narrow, ENE-WSW-trending, elongate region of rocks that are intensely deformed as a result of movement along the Verran Fault Plane. The VFP represents the most recent and most significant movement plane (Watts 2001), and is used here as a central reference line for this fault zone. The Verran Fault System (VFS) refers to all faults that link into and are associated with the VFP, and so includes the Rautingdalen Fault (section 2.2.3) and the Elvdalen Fault (section 2.2.4).

Fracture data has been collected from localities both within and outside the VFZ, at 4 areas along the trace of the VF – a) Ormsetvatnet reservoir road section (**Figure 2.7** locality a), b) 720 road cut (**Figure 2.7** locality b), c) Verrasundet fjordside (**Figure 2.7** locality b), d) Finesbekken stream section (**Figure 2.7** locality c).

2.2.2.1 Ormsetvatnet reservoir road section

The road to Ormsetvatnet provides a near-perpendicular profile through the outer parts of the VFZ (section starts ~ 450m from VFP) (**Figure 2.7**). Here the VFZ extends approximately 500m from the VFP into granodioritic gneiss belonging to the Banded Gneiss Complex (section 2.1). In the outer parts of the VFZ, thin (mm-thick) epidote-rich cataclasites consistent with sinistral strike-slip movements are overprinted by cm- to m-thick zeolite and calcite mineralised breccias, intense fracturing and veining. The mineralised breccias are bound by surfaces that show evidence for dip-slip (normal) movements, followed by a phase of dextral strike-slip movement (Watts 2001). Fracture data for this study has been collected within gneiss from a number of localities along the road section, from 500m to 2.25km north of the VFP.

2.2.2.2 720 road cut

The 720 road cut is orientated 040°, oblique to the VFP. The section extends for approximately 750m to the east of the Rautingdalen Fault (**Figure 2.7**). Intense cataclastic deformation overprints granodiorite gneiss from the Banded Gneiss Complex (section 2.1) (Watts 2001). Cataclastic deformation is most intense at the SW end of the road cut (closest to the VFP). A series of anastomosing epidote-rich cataclasites formed during sinistral shear are overprinted by intense zeolite and calcite veining, associated with the development of mineralised breccias. The breccias formed during a period of dip-slip (normal) movement, followed by dextral strike-slip faulting along the VFP. Later grey fault gouges formed during dextral strike-slip movements overprint the breccias (Watts 2001). Fracture data for this study has been collected from a number of localities along the road section, from 40 to 150m north of the VFP. All data sets of fracture parameters were collected from gneissose rocks, except one data set that was collected from amphibolite.

2.2.2.3 Verrasundet fjordside

The northern shore of Verrasundet provides good exposures close to the centre of the VFZ. The fjordside lies directly to the SW of the 720 road cut (section 2.2.2.2) (**Figure 2.7**). The VFP is interpreted to lie approximately 30m to the SW of the exposures, beneath the fjord. Here, banded gneisses from the Banded Gneiss Complex (section 2.2) are overprinted by fault-related deformation. The earliest recognised fault rocks are epidote-rich cataclasites, formed during sinistral strike-slip movements along the VFP (Watts 2001). The cataclasites are overprinted by intense calcite and zeolite mineralisation (Watts 2001). Two localities were chosen to collect fracture data sets along the fjordside, both lie within ~50m of the VFP, and at one locality, a data set of fracture characteristics was collected within cataclasite.

2.2.2.4 Finesbekken stream section

In the study area, the only exposures of the core of the Verran fault (VFC), located at the centre of the VFZ and containing the VFP, were located in a stream section to the SW of Verrasundet (**Figure 2.7**). The VFC is the region of most intense fault-related deformation, and is defined by a continuous sequence of fault rocks that extends from the wall rocks on either side and across the VFP (Watts 2001). Elsewhere in the study area, the VFC is eroded out, submerged beneath fjords or concealed under thick quaternary glacial deposits. Here, on either side of the VFP, granodioritic gneisses belonging to the BGC (section 2.2) are overprinted by fault-related deformation (**Figure 2.8**). The VFC at this locality is approximately 4m wide, and contains the VFP orientated 059/ 80 SE (**Figure 2.8**). The earliest fault rocks are epidote-rich cataclasites, indurated fault gouges and minor pseudotachylites which formed during sinistral transtensional movements along the VF (Watts 2001). The cataclasites are overprinted by zeolite- and calcite- mineralised breccias that formed during dip-slip (normal) movements, followed by a phase of dextral strike-slip movements. The mineralised breccias are overprinted by 2 gouges, a grey gouge formed during dextral strike slip, and a blue gouge formed during dip-slip movement (Watts 2001).

Fracture data for this study has been collected from gneiss at one locality along the stream section, and one locality from an adjacent road section, both localities lie within 20m of the VFP.

2.2.3 *The Rautingdalen Fault (RF)*

The Rautingdalen Fault (RF) is one of a number of NNE-SSW- trending faults that splay to the N off the VFP (**Figure 2.4**, **Figure 2.7**). The RF is well-exposed along a stream section at the base of a steep-sided gorge, especially after periods of dry weather. On either side of the gorge, tree-covered crags and high cliffs occur. Northern parts of the gorge are susceptible to rock-falls. (**Figure 2.9**).

The core of the RF (RFC) is exposed at locality grid reference 7946 7872, located in the centre of the RFZ, and contains the RFP orientated 008/ 81 W. The RFC is approximately 8m wide and represents the region of most intense fault-related deformation. On either side of the RFP, granodioritic gneiss from the BGC (section 2.2) is overprinted by fault-related deformation. The RF is interpreted by Watts (2001) to have formed as an extensional fault with the production of epidote-rich cataclasites, during sinistral transtension along the VFP. Intense zeolite and calcite mineralisation overprints the cataclasites, and formed during sinistral strike-slip reactivation along the RFP. During this event the RF is interpreted to be an R'-type Riedel shear which re-activated a pre-existing structure during dextral strike-slip movements along the VFP (Watts 2001).

Fracture data for this study has been collected at 7 localities, which lie at different distances along the strike of the RFP. Due to the nature of exposure, data could only be collected within 5m of the RFP.

2.2.4 *The Elvdalen Fault (EF)*

The Elvdalen Fault (EF) is an ENE-WSW trending fault that lies between the two bounding structures of the MTFC, approximately 1.5 km to the northwest of the VFP (**Figure 2.4, Figure 2.7**), and is possibly linked to the RF (section 2.2.3). The EF zone (EFZ) is exposed in a dried-up stream-bed adjacent to a Hydro-station along the road to the Ormsetvatnet reservoir (**Figure 2.10**). The EF plane (EFP) itself is not exposed, but the core of the EF is postulated to be no more than 1m wide. Within the EFZ granodioritic gneisses from the BGC (section 2.2) are overprinted by fault-related deformation. Earliest observed fault rocks are zeolite and calcite matrixed breccia,

coeval with intense zeolite and calcite veining, which formed during a period of dip-slip movement followed by dextral strike-slip movements along the EFP.
Fracture data for this study has been collected at a locality ~1m of the EFP, and also ~10m from the EFP.

2.3 The kinematic history of the MTFC

The MTFC is recognised by many authors as having prolonged history of polyphase deformation, ranging from strike-slip through oblique-slip to dip-slip at different structural levels; however, many conflicting accounts of the kinematic history of the MTFC have appeared in the literature (**Figure 2.11**).
The most detailed onshore study of the MTFC has been undertaken by Watts (2001), who also presents new dates from cross-cutting fault rocks collected along the MTFC. Watts (2001) recognises 3 main periods tectonic activity along the MTFC (Early Devonian, Permo-Carboniferous and Mesozoic) with a fourth phase suggested during Early Tertiary times (**Figure 2.11**).
Based on field evidence, Watts (2001) suggests that the two main faults within the MTFC (VF and HSF) have experienced different post-Permo-Carboniferous kinematic histories (**Figure 2.12**). The VF and the HSF are thought to have broadly initiated as part of a single system of sinistral shear zones in Early Devonian times: mylonites from HSFZ dated at 409±12 Ma, correlated with minor mylonites observed within the VFZ (Watts 2001). Permo-Carboniferous reactivation led to the development of cataclasites, pseudotachylites and indurated fault gouges formed during sinistral transtension; pseudotachylites from HSFZ dated at 291±14 Ma, coeval with cataclasites and correlated with texturally similar fault rocks from VFZ and RFZ (Watts 2001). During the Mesozoic, it is suggested that the HSF remained mainly inactive, whilst the focus of reactivation shifted towards the VF. Dip-slip and dextral strike-slip movements resulted in intense brecciation and extensive zeolite and calcite veining within the VFZ, EFZ and RFZ (Watts 2001). The most recent phase of movement recognised by Watts (2001) is represented by a thin blue gouge within the VFC. The gouge contains a strong dip-slip lineation, and is postulated to have formed during Tertiary times. The regional tectonic setting of the recognised movements along the MTFC are summarised in the right-hand column of **Figure 2.12**.

CHAPTER 3 - FRACTURE CHARACTERISTICS FROM 1-D OUTCROP DATA, MTFC, CENTRAL NORWAY

A series of 1-dimensional (1-D) line transects (section 1.9.1) were carried out in the field to collect fracture data at outcrop scale. Where possible, vertical and horizontal line transects were measured on surfaces both parallel and perpendicular to the overall trend of the MTFC (~060°) to measure all possible fracture orientations. Data has been collected at distances adjacent to four faults in the MTFC - the two main structures (the Verran Fault and the Hitra-Snåsa Fault), the Elvdalen Fault, and the Rautingdalen Fault - from the localities described in section 2.2.

3.1 The Verran Fault

The following sections describe in detail the fracture orientations, infills, kinematics and spacing values measured from a number of localities adjacent to the Verran Fault Plane (VFP) (section 2.2.2).

3.1.1 *Fracture orientation data*

A total of 8 stereographic projections (section 1.7.2) have been plotted to illustrate the change in fracture orientation with increasing distance from the VFP (**Figure 3.1**). Where possible, depending on exposure in the field, the stereonets are created using data from a variety of 1-D transect orientations to ensure that all fracture orientations are represented. The data are plotted as poles to fracture planes, and for each cluster of orientation values the mean girdle is shown, which represents the mean fracture plane for that cluster. The stereographic projections are accompanied by the Von Mises diagrams shown in **Figure 3.2** which represent the same data sets and illustrate frequencies of fracture strike (section 1.7.2).

At distances up to approximately 500m from the VFP four clusters of fracture orientations are recognised striking ENE-WSW (red girdles), E-W (green girdles),

NNW-SSE (blue girdles) and ~N-S (orange girdles) (**Figure 3.1 a, b, c, d, e** and **Figure 3.2 a, b, c, d, e**). The data collected at distances greater than 500m away from the VFP (**Figure 3.1 f, g, h** and **Figure 3.2 f, g, h**) show less clustering of the fracture orientations and more data scatter. The plots shown in **Figure 3.1 g & h** show only 1 mean girdle which corresponds to a weak cluster of foliation parallel fractures. The foliation close to the VFP (up to ~1300m away from VFP) is orientated ENE-WSW and dips steeply to the SE, but at distances of ~1930m (**Figure 3.1 g**) and ~2250m (**Figure 3.1 h**) the foliation orientated NNE-SSW and dips moderately to the ESE. This is due to the folding of the foliation into an antiformal structure. The two bounding structures of the MTFC lie on the NW and SE limb of this structure (VF and HSF) (section 2.2. **Figure 2.3**).

The table presented as part of **Figure 3.1** summarises the main fracture cluster orientations from each stereonet.

3.1.2 *Fracture infills and their relative ages*

Out of a total of 2387 fractures measured in the field adjacent to the VF, 824 (35%) have been recorded as having an infilling material. The most common fracture infills are green-coloured epidote-rich cataclasites, white/colourless calcite mineralisation, pink/orange zeolite mineralisation (stilbite and laumontite) and incohesive fault gouge. Other less common infills are pseudotachylite, chlorite and iron mineralisation. The photographs presented in **Figure 3.3** illustrate the variety of fracture infills observed in the field.

The orientations of all fractures with identified infills are plotted on a stereographic projection in **Figure 3.4 A (1)**. Although there is scatter in the data, four clusters can be identified – ENE-WSW (foliation parallel), E-W, N-S, and NNW-SSW, which correspond to the four clusters recognised in section 3.1.1. Individual stereonets are plotted for each type of fracture infill in **Figure 3.4 A (2-6)**. It is evident from the stereonets that different fracture infills are recorded in the same fracture orientations. ENE-WSW trending fractures contain the largest variety of fracture infills (epidote rich cataclasites, calcite and zeolite mineralisation, fault gouge and other infills). Fractures orientated N-S and NNW-SSE contain epidote-rich cataclasites, calcite and zeolite mineralisation, and other infills.

In the field, the different infills do not appear to occupy separate fracture sets, but instead fractures often contain multiple generations of infills (**Figure 3.5**). Out of 824 filled fractures identified and measured, 249 have multiple infills (30%) (**Figure 3.4 A (8)**). These fractures display three main clusters ENE-WSW (foliation parallel), N-S, and NNW-SSE.

The percentages of filled-fractures observed at different distances from the VFP are plotted in **Figure 3.4 B**. Overall, the total percentage of filled-fractures decreases away from the centre of the VF. The data set collected closest to the VFP shows an anomalously low percentage of total filled-fractures, but also shows a small proportion of gouge-filled fractures which do not occur farther from the centre of the fault. The most common infills observed adjacent to the VFP are coeval zeolite and calcite mineralisation, which extend to >500m from the VFP. Epidote-filled fractures are also common, and extend > 500m from the VFP.

A relative time sequence of fracture infills has been established based upon field and thin-section observations. Firstly, epidote-rich cataclasite consistently occurs as clasts within calcite and zeolite matrixed breccias (**Figure 3.5 a**), and also on the outside edge of syntaxial, filled fractures (**Figure 3.5 b**) suggesting that the epidote-rich cataclasite is earlier than the zeolite and calcite matrix breccias. The calcite and zeolite mineralisation within fractures is often intergrown (**Figure 3.3 c**) suggesting that these infills are contemporaneous; but multiple generations of calcite and zeolite mineralisation are also suggested by overprinting relationships (**Figure 3.5 c**). Calcite- and zeolite-filled fractures consistently cross-cut and offset fractures filled with epidote-rich cataclasites, suggesting that the calcite and zeolite mineralisation is younger than the epidote-rich cataclasites (**Figure 3.6**). Finally, in rare occurrences, fractures infilled with soft grey-coloured fault gouge are observed (**Figure 3.3 d**) and consistently cross-cut fractures filled with zeolite and calcite mineralisation (**Figure 3.5 d**), suggesting that the fault gouge is younger than the zeolite and calcite.

3.1.3 *Fracture kinematics*

It is often difficult to measure lineations on fracture planes due to the small nature of the structures, the effects of weathering and insufficient exposure. Out of the 824

infilled fractures measured and recorded in the field, a total of 89 (11%) of the fractures had slickenfibre lineations (section 1.5.1.2) (**Figure 3.7**). The epidote-filled fractures orientated N-S to NNW-SSE are associated with steeply plunging lineations and therefore dip-slip movements (**Figure 3.7 a**), whereas the fractures orientated ENE-WSW are associated with shallowly plunging lineations and therefore strike-slip movements (**Figure 3.7 b**). The lineation data recorded from slickenfibres of calcite and/or zeolite are more scattered (**Figure 3.7 c, d**). Both dip-slip and strike-slip lineations are observed for the fractures orientated N-S to NNW-SSE and fractures orientated ENE-WSW (**Figure 3.8 a, b, c**).

Field evidence suggests that the ENE-WSW foliation-parallel epidote-rich cataclasites are associated with *sinistral* strike-slip movements based upon the stepping of slickenfibres, and the geometries of extensional and R-type Riedel shears (**Figure 3.6**). The N-S and NNW-SSE epidote-rich cataclasites often link into the ENE-WSW trending fractures (**Figure 3.3 a**) and are associated with dip-slip normal movement. They are interpreted as T-type Riedel shears formed during regional sinistral transtensional movements along the ENE-WSW fractures.

Evidence from the field also suggests that the ENE-WSW-trending zeolite and calcite filled fractures are associated with both *dextral* strike-slip and dip-slip normal movements, whereas N-S and NNW-SSE-trending fractures filled with zeolite/calcite as associated with sinistral strike-slip and oblique movements. This is based upon the stepping of slickenfibres (**Figure 3.8 a, b, c**), offset markers such as quartz veins or pre-existing fractures (**Figure 3.6, Figure 3.8 d, e**) and fibrous infills of zeolite and calcite (**Figure 3.8 f**).

3.1.4 *Summary of fracture orientation, infill and kinematics from 1-D line transects, adjacent to the VFP.*

A summary of fracture orientation, infill and kinematics data collected and analysed adjacent to the VFP along 1-dimensional line transects is presented in **Table 3.1**.

Data sets used	>2200 fractures measured, 48 1-dimensional line transects (3 transect orientations vertical, parallel and perpendicular to the VF trend). All data sets gneissose lithology except 1 data set of amphibolite and 1 data set of cataclasite.
Orientation	0-500m from VFP = 4 clusters identified, ENE-WSW, E-W, NNW-SSE, N-S. >500m from VFP = more scatter and less clustering of fracture orientations.
Infill	35% of fractures measured have a recorded infill. Most common infills = epidote-rich cataclasite, coeval zeolite & calcite mineralisation and incohesive fault gouge. Different infills are recorded in the same fracture orientations. 30% of infilled fractures have multiple infills The overall number of filled-fractures increases towards the VFP, but is anomalously low at the centre of the VF where the only gouge-filled fractures are observed. Most common infills observed adjacent to the VFP are zeolite/calcite mineralisation Epidote-rich cataclasite infill is cross-cut by zeolite & calcite mineralisation, which is in turn cross-cut by incohesive gouge.
Kinematics	11% of infilled fractures have slickenfibre lineations. N-S to NNW-SSE fractures with epidote infills display dip-slip normal kinematics. ENE-WSW fractures with epidote infills display sinistral strike-slip kinematics. Fractures orientated N-S to NNW-SSE and ENE-WSW with zeolite and calcite infills display both dip-slip normal and dextral strike-slip kinematics

Table 3.1 Summary of orientation, infills and kinematics data collected adjacent to the VF

3.1.5 *Fracture spacing data*

The distance between fractures has been measured along a series of 1-dimensional line transects to investigate the changes in fracture spacing adjacent to the VF. Transects have been carried out on either horizontal or vertical outcrop surfaces in directions both parallel and perpendicular to the overall fault zone trend (ENE-WSW) and also on vertical surfaces, to encompass the spacings between various fracture orientations. A total of 19 localities have been used to collect spacing data at various distances away from the VFP (**Table 3.2**). The majority of fractures are measured within a gneissose lithology; one data set has been collected within an amphibolitic lithology, and one within cataclasite.

The following sections describe in detail fracture spacing parameters analysed from localities adjacent to the VF.

Place	locality	~ distance to VFP (m)	lithology	1-dimensional line transect details		
				transect name & orientation (degrees)	mean spacing (mm)	exponent from exponential spacing graph
720 fjordside	47	30	gneiss	T1 - 057	16.407	0.0803
				T2 & T4 - 145	16.665	0.072
				T3 - vertical	17.917	0.0712
	137	28	gneiss	T1 - 135	16.456	0.061
				T2 - 055	22.059	0.0545
			cataclasite	T3 - 128	25.136	0.0429
720 road section	46	40	gneiss	T1 - 055	37.853	0.0264
				T2 - vertical	20.5	0.0504
	48b	100	gneiss	T1 - 045	22.218	0.0475
				T2 - vertical	20.323	0.0412
	48g	140	amphibolite	T1 - 080	30.316	0.0349
				T2 - 160	38.973	0.0289
	48h	145	gneiss	T1 - 010	21.915	0.0484
				T2 - vertical	23.4	0.04
	48i	150	gneiss	T1a - 018	27.622	0.0343
			amphibolite	T1b - 018	46.093	0.0244
			gneiss	T2 - vertical	26.85	0.0321
			amphibolite	T3 - vertical	43.588	0.0142
Reservoir road section	28a	475	gneiss	T1 & T4 –043, 230	27.648	0.039
				T2 - 170	18.067	0.0849
				T3 - 315	40.514	0.0248
	28b	500	gneiss	T1 - 280	36.731	0.0351
	28c	600	gneiss	T1 - 230	57.75	0.0213
				T2 - 330	72.184	0.013
	132a	1926	gneiss	T1 - 305	133.559	0.0066
				T2 - 215	172.688	0.0049
				T3 - vertical	84	0.01

Table 3.2 Mean spacing and exponent data from 1-dimensional line transects adjacent to the VF. Negative distances represent localities south of VF, positive distances represent distances north of VF (continued on next page).

Place	locality	~ distance to VFP (m)	lithology	transect name & orientation (degrees)	mean spacing (mm)	exponent from exponential spacing graph
Reservoir road section	133	1300	gneiss	T1 - 045	139.537	0.0083, 0.0043
				T2 - 145	133.154	0.0073
	138	2250	gneiss	T1 - 230	135.85	0.0061
				T2 & T3 - vertical	83.075	0.0117
	157	500	gneiss	T1 - 315	43.966	0.0241
	164	475	gneiss	T1 - 325	57.04	0.0355, 0.0125
Verran Fault Core & road section	130	-3	gneiss	T1 - 227	32.971	0.0323
				T2 & T4 – 313, 300	18.522	0.0586
				T3 - vertical	38.607	0.0218
	139	20	gneiss	T1 - 050	26.778	0.0467
				T2 - 136	24.667	0.0412
				T3 - vertical	26.182	0.0358
	161	-3	gneiss	T1 - 140	23.258	0.0529
Verrabotn road section	140	-800	gneiss	T1 - vertical	90.125	0.0097
				T2 & T3 - 225	321.0536	0.0043, 0.0025
				T4 - 310	343.917	0.0024

Table 3.2 Mean spacing and exponent data from 1-dimensional line transects adjacent to the VF. Negative distances represent localities south of VF, positive distances represent distances north of VF (continued from previous page).

3.1.5.1 Cumulative frequency 'v' spacing

Plots of spacing values measured from 1-dimensional line transects 'v' cumulative frequency are presented in **Figure 3.9, Figure 3.10 & Figure 3.11**. Each graph represents a locality, and within each graph different data sets represent different transect orientations (see legends on graphs). The spacing values collected for all data sets plot as a straight line when the x-axis is plotted as a linear scale and the y-axis is plotted as a logarithmic scale, and therefore they are best described by an exponential distribution with a negative slope. This is confirmed when a Kolmogorov-Smirnov test (section 1.8.4.2) is carried out on each of the data sets. Some data sets show data points that do not fall onto the best-fit lines. On the right hand side of the graph, this is likely to be the result of under-representation of wide spacing values due to the limited size of the outcrops (e.g. locality 157, **Figure 3.9**). Some data sets are recorded as having 2 slopes, a steeper slope to the left hand side and a shallower slope to the right-hand side (e.g. locality 164, **Figure 3.9**). This may be interpreted as the data set having more smaller spacings than would be expected for an exponential distribution, and possible clustering of fractures at small spacing values.

3.1.5.2 Mean spacing 'v' standard deviation

For a data set to be best fitted by an exponential distribution, the mean and standard deviation values are expected to be similar. A plot of mean spacing versus standard deviation for each of the localities (and distinguished for different transect orientations) is presented in **Figure 3.12**. As expected for exponential data, there is a good relationship between average spacing and standard deviation.

3.1.5.3 Co-efficient of variation

The co-efficient of variation (Cv) is a measure of the degree of cluster within a data set (section 1.8.5.1) and is plotted in **Figure 3.13** for the VF outcrop localities (with transect orientations distinguished) against distance. The lowest values of Cv for all transect orientations occurs close to the centre of the VF suggesting that in this area the fracture spacings are relatively more anti-clustered.

3.1.5.4 Cumulative frequency exponent 'v' distance to VFP

The exponent (slope) values of the graphs plotted in **Figure 3.9, Figure 10 & Figure 11** can be used to assess the change in fracturing adjacent to the VF (**Table 3.2**). Steep slopes correspond to high exponent values and represent a relatively large number of narrow spacings, suggesting a higher fracture density.

The exponent values from the three transect orientations (fault parallel, fault perpendicular and vertical) are plotted against distance to VF in **Figure 3.14**. The highest values of exponent from all transect orientations occur close to the centre of the fault which suggests that this is where the closest spaced fracturing and highest fracture density occurs. The exponent values return to a background level of approximately 0.01, about 500m away from the centre of the fault. The exponents from the amphibolitic fracture spacing data set and the data set collected from cataclasite are significantly less than the exponents for the gneissose data set at the same distances for the fault, suggesting that lithology also has an effect on fracture spacing.

3.1.5.5 Mean spacing 'v' distance to VFP

The change in fracture spacing with distance can also be assessed by plotting the average fracture spacing from each transect orientation (**Figure 3.15, Table 3.2**). The smallest average spacing values occur at the centre of VF for all three data sets.

3.1.5.6 Mean spacing 'v' cumulative frequency exponent

In defining a data set that is best described by an exponential distribution, the mean value is used, and therefore a good relationship between the mean values and exponents from exponentially distributed data sets is expected (section 1.8.2.3). The spacing data collected adjacent to the VFP along 1-dimensional line transects show a good power-law relationship between mean and exponent values, with a power-law exponent value of -1.079 (**Figure 3.16, Table 3.2**).

3.1.5.7 "Step" plots of fracture spacing 'v' distance along 1-dimensional transects

The change in fracture spacing along 1-dimensional transects adjacent to the VF can be assessed by plotting the cumulative fracture frequency against the distance along the transect (cumulative fracture spacing) (section 1.8.5.2). The 1-dimensional line

transects must be of sufficient length (defined as greater than approximately 2m in this study except for very dense fracturing where shorter transects are sufficient) to illustrate the change in fracturing with distance from the fault plane. A total of 15 line transects (8 parallel and 7 perpendicular to the VF trend) measured at varying distances to the VFP have been selected and plotted (**Figure 3.17**).

For the transects measured parallel to the VF (which measure the spacings of fractures perpendicular to the VBF trend), the data sets collected between 0m and 600m from the VFP plot as steep straight lines, suggesting that fracture density is relatively high. Data sets collected at distances greater than 600m away from the VFP again plot as almost straight lines but with shallower slopes suggesting that fracturing is less dense **(Figure 3.17 a, b)**.

For transects measured perpendicular to the VF trend (which measure the spacings of fractures parallel to the VBF trend), the data sets collected less than 50m away from the VFP plot as steep straight lines suggesting dense fracturing (**Figure 3.17 c, d**). The data sets collected approximately 500m away from the VFP along fault perpendicular transects (localities 164 & 157) illustrate a pronounced stepping pattern of steep and shallow sections (**Figure 3.17 c, d & Figure 3.18 b, c, d, e**). This stepping pattern indicates partitioning of fracturing into areas of narrow spacings (steep slope, dense fracturing) and wider spacings (shallow slope, less dense fracturing). This meter-scale clustering of fractures can be seen in the field and is illustrated in **Figure 3.19**. The data sets collected along transects perpendicular to the fault trend, at distances greater than 600m, plot as shallow lines with no stepping suggesting low fracture density, and little partitioning of strain (**Figure 3.17 c, d & Figure 3.18 f, g**).

3.1.6 *Summary of fracture spacing data from 1-D line transects (VF).*

A summary of fracture spacing data collected and analysed adjacent to the VFP along 1-dimensional line transects is presented in **Table 3.3**.

Fracture spacing attribute/plot		Results from 1-D transects adjacent to the VFP
Cumulative frequency 'v' spacing		All data sets are best described by an exponential distribution.
mean spacing 'v' standard deviation		Good linear relationship close to x=y.
Coefficient of variation (Cv)		Cv values lowest near centre of fault for all three transect orientations. Suggests that fracturing less clustered in centre of fault.
exponent 'v' distance to VF		Exponential exponent values highest in centre of fault for all three transect orientations suggesting narrow fracture spacings and higher fracture densities. Values decrease away from centre over ~500m to background level. Exponents from amphibolite and cataclasite are lower than gneissose values at same distances form fault.
mean spacing 'v' distance to VF		Smallest mean spacings occur in the centre of the fault for all three transect orientations.
exponent 'v' mean spacing		Good power-law relationship, exponent value = -1.079.
Cumulative frequency 'v' distance along transect	Transects parallel to VF trend	Data plot as straight lines for all transects suggesting little/no clustering of fractures. Steeper slopes occur closest to centre of fault suggesting higher fracture densities.
	Transects perpendicular to VF trend	0-50m from VF data plot as straight lines with steep slopes = high fracture densities, little/no clustering. ~50-500m from VF data shows "stepped" appearance = clustering into zones of high and low density. >500m from VF data plot as straight lines with shallow slopes = low fracture densities, little/no clustering.

Table 3.3 Summary of fracture spacing data collected along 1-D line transects adjacent to the VFP

3.2 The Elvdalen Fault

The following sections describe in detail the fracture orientations, infills, kinematics and spacing values measured ~1m from the ENE-WSW striking Elvdalen Fault Plane (EFP) (section 2.2.4).

3.2.1 *Fracture orientation data*

Fracture orientations measured adjacent to the EFP are plotted as poles to fracture planes in **Figure 3.20 a**. The stereonet has been created using data from 3 1-dimensional line transects at different orientations to the overall MTFC trend to ensure that all fracture orientations are represented. For each cluster of orientation

values the mean girdle is shown which represents the mean fracture plane for that cluster.

The stereonet shows 3 clusters striking 1) ENE-WSW (*red* girdle in **Figure 3.20 a**, parallel to the MTFC trend and EFP orientation), 2) NNE-SSW (*orange* girdle in **Figure 3.20 a** reflecting re-orientated foliation at this locality due to folding), and 3) E-W (*green* girdle in **Figure 3.20 a**). These clusters are the similar to those observed adjacent to the VFP (section 3.1.1), RFP (section 3.3.1) and HSFP (section 3.4.1).

3.2.2 *Fracture infills and their relative ages*

A total of 212 fractures have been measured adjacent to the EFP from locality 132b, and 119 (56%) of these fractures have been recorded as having an infilling material. The most common infill observed is zeolite mineralisation (**Figure 3.21a**), occasionally associated with coeval calcite. Few fractures with green coloured epidote-cataclasite have also been observed, and no gouge-filled fractures.

The orientations of all filled fractures are plotted on a stereographic projection in **Figure 3.20 b**. 3 clusters of filled fractures can be recognised striking ENE-WSW, NNE-SSW and E-W which correspond to the clusters recognised in section 3.2.1. Stereonets are plotted for both types of fracture infill in **Figure 3.20 c, d**. Fractures striking ENE-WSW contain both types of infill; fractures striking NNE-SSW and E-W appear to contain only zeolite/calcite mineralisation.

The relative percentages of filled-fractures observed adjacent to the EFP are plotted in **Figure 3.20 g**, along with filled-fractures observed from other localities adjacent to the VFP. It is very apparent that the most dominant fracture-fill observed in the vicinity of the EFP is zeolite/calcite mineralisation. Very few epidote-filled fractures are observed. The overall percentage of filled fractures observed at the EFP is higher than that observed close to the VFP.

Although few fractures filled with epidote were observed in the field, zeolite mineralisation is observed overprinting the cataclasite in the same fracture, suggesting that the epidote cataclasite is older than the zeolite and calcite mineralisation. Zeolite and calcite veins are also observed cross-cutting fractures filled with epidote-rich cataclasite adjacent to the EFP. Zeolite veins offset by zeolite filled fractures are observed, suggesting multiple phases of zeolite mineralisation (e.g. **Figure 3.21 b**).

3.2.3 *Fracture kinematics*

Of the 119 filled fractures measured in the field, a total of 36 (30%) had slickenfibre lineations (section 1.5.1.2). Epidote cataclasite-filled fractures orientated ENE-WSW are associated with shallowly plunging strike-slip lineations (**Figure 3.20 e**). ENE-WSW and E – W striking fractures filled with zeolite/calcite are associated with both dip-slip movements (steeply plunging lineations, **Figure 3.21 c, d**) and strike-slip movements (shallowly plunging lineations) (**Figure 3.20 f**). Field evidence suggests that zeolite and calcite infills are associated with dextral strike-slip movements (**Figure 3.21 b**).

3.2.4 *Summary of fracture orientation, infill and kinematics from 1-D line transects, adjacent to the EFP.*

A summary of fracture orientation, infill and kinematics data collected and analysed adjacent to the EFP along 1-dimensional line transects is presented in **Table 3.4**.

Data sets used	>212 fractures measured, 3 1-dimensional line transects (orientations vertical, parallel and perpendicular to the MTFC trend). All transects carried out within gneiss. Data collected ~1m to SE of the EFP.
Orientation	3 fracture orientation clusters observed ENE-WSW, NNE-SSW and E-W. NNW-SSE set reflect folding of foliation.
Infill	56% of fractures measured are filled. Most common infill is zeolite, with coeval calcite associated with it. Few epidote-rich cataclasite filled fractures observed. Fractures striking ENE-WSW contain both types of infill. NNW-SSE and E-W striking fractures contain mainly zeolite & calcite. Zeolite and calcite mineralisation overprint and cross-cut epidote mineralisation. Evidence for multi-phases of zeolite mineralisation also observed. Epidote-cataclasite & infill is older than zeolite & calcite mineralisation.
Kinematics	30% of filled fractures have slickenfibre lineations. ENE-WSW fractures containing epidote-cataclasite are associated with strike-slip movements. NNW-SSE and E-W striking fractures with zeolite/calcite infill are associated with dip-slip and dextral strike-slip movements.

Table 3.4 Summary of orientation, infill and kinematics data collected adjacent to the EFP

3.2.5 *Fracture spacing data*

Three 1-dimensional line transects have been carried out to measure spacing values adjacent to the EFP at locality 132b (1m to SE of EFP). Data has been collected along a vertical transect and transects orientated both parallel and perpendicular to the overall trend of the EF and the MTFC (ENE-WSW). All data has been collected within a gneissose lithology (**Table 3.5**).

				1-dimensional line transect details				
locality	**~ perp. distance to EFP (m)**	**~ perp. distance to VFP (m)**	**lithology**	**transect name & orientation (degrees)**	**no. fractures measured**	**transect length (mm)**	**mean spacing (mm)**	**exponential spacing exponent**
132b	1	1936	gneiss	T1 – 125	112	7073	63.15	0.0277, 0.0117
				T2 – 225	50	1988	39.76	0.0280
				T3 – vertical	32	1258	39.31	0.0287

Table 3.5 Details of 1-dimensional line transects adjacent to the EF used to analyse fracture spacing.

3.2.5.1 Cumulative frequency 'v' spacing

Values of fracture spacing measured along each 1-dimensional line transect from locality 132b are plotted against cumulative frequency in **Figure 3.22**. The data sets each plot as a straight line when the x-axes is plotted as a linear scale and the y-axis is plotted as a logarithmic scale. This suggests that the data are best described by an exponential distribution, and this is confirmed when a Kolmogorov-Smirnov test (section 1.8.4.2) is carried out on the data.

3.2.5.2 Cumulative frequency exponent 'v' distance to EFP

The exponent values from the transects measured adjacent to the EFP are plotted against the perpendicular distance to the VFP in **Figure 3.23**, together with earlier data from the VF, in order to illustrate how the values from the EFP compare to the values from the VFP (**Table 3.5**). For each transect orientation, the value of exponent measured adjacent to the EFP is significantly higher than the background levels observed. However, the values recorded at the centre of the VFP are significantly

higher than the values recorded at the centre of the EFP suggesting that overall, fracture density is higher adjacent to the VFP than the EFP.

3.2.5.3 Mean spacing 'v' distance to EFP

The mean spacing value measured along a 1-dimensional line transect may also be used as a relative measure of fracture density. As in the previous section, the mean spacing values measured from transects adjacent to the EFP are plotted against the perpendicular distance to the VFP in order to illustrate how the values from the EFP compare to the values from the VFP (**Figure 3.24, Table 3.5**). For each transect orientation, the mean spacing values measured adjacent to the EFP are significantly lower than the background levels observed, but not as low as the values observed at the centre of the VFP.

3.2.5.4 Mean spacing 'v' cumulative frequency exponent

If data sets are best described by an exponential distribution, then a relationship may be expected to exist between the mean spacing and the exponent values, since the mean is a defining aspect of an exponential distribution (section 1.8.2.3). The values of mean spacing and exponential exponent recorded adjacent to the EFP are plotted along with data from the VF in **Figure 3.25**. A good power-law relationship is observed between these parameters on both linear and logarithmic axes, with an exponent value of -1.0701.

3.2.5.5 "Step" plots of fracture spacing 'v' distance along 1-dimensional transects

To analyse the change in fracture density immediately adjacent to the EFP, the cumulative fracture frequency from the line transects both perpendicular and parallel to the MTFC trend has been plotted against the distance along the line transect (which is equivalent to the cumulative fracture spacing) (section 1.8.5.2) (**Figure 3.26**).

The transect measured perpendicular to the EFP at locality 132b (which measures the spacings of fractures parallel to the MTFC and EF trend) is a continuous extension of the perpendicular transect measured at locality 132a. Therefore these transects can be plotted together to analyse the fracturing over a distance of almost 12m in a perpendicular direction from the EFP. The first fracture measured on the transect at locality 132b is the EFP. When the fracture frequency is plotted against the distance along the perpendicular transects (**Figure 3.26 b**) a pronounced stepping pattern is

observed at distances from 0m (i.e. at the EFP) to ~5m from the EFP. This stepping pattern indicates the partitioning of fractures into areas of high density (steep slopes e.g. 0.0788) and low density (shallow slopes e.g. 0.0134), and this can be visualised by plotting the fracture frequency as a histogram (**Figure 3.26 c**). The portion of the transect where the stepping occurs (0-5m from EFP) is enlarged in **Figure 3.26 d** & **Figure 3.26 e** and illustrated in **Figure 3.27**. At distances >5m away from the EFP, the stepping is much less pronounced suggesting that the fracture density is more homogeneous over large distances and relatively low.

The transect measured parallel to the EFP (~1m to the SW of the EFP position) is plotted in **Figure 3.26 f** and visualised as a histogram in **Figure 3.26 g**. No pronounced stepping occurs, but instead the graph shows a relatively steep continuous slope. This suggests that immediately adjacent to the EFP, fractures orientated perpendicular to the EFP have an intermediate fracture density (slope = 0.0256), and are not partitioned into areas of high and low density.

3.2.6 *Summary of fracture spacing data from 1-D line transects (EF).*

A summary of fracture spacing data collected and analysed adjacent to the EFP along 1-dimensional line transects is presented in **Table 3.6**.

Fracture spacing attribute/plot		Results from 1-D transects adjacent to the EFP
Cumulative frequency 'v' spacing		All data sets are best described by an exponential distribution.
exponent 'v' distance to VF/EF		Exponent values measured immediately adjacent to the EFP are significantly higher than the background levels observed. Values from different transect orientation are very similar (~0.028).
mean spacing 'v' distance to VF/EF		Mean spacing values measured immediately adjacent to the EFP are significantly lower than the background levels observed.
exponent 'v' mean spacing		EFP data amalgamated with data adjacent to VFP. Power-law relationship observed, exponent value = -1.0701
Cumulative frequency 'v' distance along transect	Parallel transects	No stepping observed, therefore no partitioning into areas of high and low fracture density. Slope of data = 0.0256.
	Perp. transects	Stepping pattern observed 0-5m away from the EFP. Steep portions = high density (e.g. slope = 0.0788). Shallow portions = low density (e.g. slope = 0.0134). Distances > 5m little/no stepping suggesting no partitioning of fracture densities.

Table 3.6 Summary of fracture spacing data collected along 1-D line transects adjacent to the EFP

3.3 The Rautingdalen Fault

In the following sections, the fracture orientations, infills, kinematic and spacing values measured from a number of localities adjacent to the Rautingdalen Fault Plane (RFP) will be described in detail. The RF is a NNE-SSW trending fault that links into the Verran Fault and is described as being part of the Verran Fault System (section 2.2.3). Due to the nature of the exposures (a narrow steep sided gorge) fracture parameters can only be measured up to 5m from the RFP, at varying distances along the strike of the fault. 1-D transects along the strike of the RFP have been carried out orientated both parallel and perpendicular to the trend of the VFP, in order to keep data collection consistent, and allow parameters to be compared between data sets collected from different faults.

3.3.1 *Fracture orientation data*

Fracture orientations adjacent to the RFP have been assessed by plotting 4 stereographic projections (section 1.7.2) which represent localities at varying distances along the strike of the RFP (i.e. at different distances to the VFP) (**Figure 3.28**). The stereonets have been plotted using data from a variety of 1-D transect orientations to ensure that all fracture orientations are represented. The fracture orientations are plotted as poles to fracture planes, and for each cluster of poles to fracture planes the mean girdle is shown, which represents the mean fracture plane for that cluster. The stereographic projections are accompanied by the Von Mises diagrams shown in **Figures 3.29** which represent the same data sets and illustrate frequencies of fracture strike (section 1.7.2).

The fracture orientations from all data sets show clusters striking ENE-WSW (parallel to the MTFC trend) and NNW-SSE, with clusters striking N-S and E-W to ESE-WNW also observed. These clusters are similar to those observed adjacent to the VFP (section 3.1.1), EFP (section 3.2.1) and HSFP (section 3.4.1). The data presented on stereonets c & d in **Figure 3.28** show 2 sets of fractures parallel to the trend of the MTFC, striking ENE-WSW, and dipping N and S. These N and S dipping foliation parallel fractures are likely to reflect the re-orientation of the foliation due to block rotation by meso-scale faults.

3.3.2 *Fracture infills and their relative ages*

A total of 732 fractures have been measured in the field from a number of localities adjacent to the RFP. Out of the fractures measured, 278 (38%) have been recorded as having an infilling material. The two most common fracture infills are 1) green-coloured epidote-rich cataclasites (**Figure 3.30 a**) and 2) coeval calcite and zeolite mineralisation (**Figure 3.30 b, c**).

The orientations of all filled fractures are plotted on a stereographic projection in **Figure 3.31 a**. Although there is scatter in the data, 4 clusters can be identified striking ENE-WSW, NNW-SSW, N-S, and E-W which correspond to the clusters recognised in section 3.3.1. Stereonets are plotted for both types of fracture infill in **Figure 3.31 b, c**. Different fracture infills are observed in the same fracture orientations. Fractures striking ENE-WSW, NNW-SSE and NS contain both types of fracture infill. Fractures striking E-W appear to contain predominantly zeolite and calcite mineralisation.

The percentages of filled-fractures observed at different distances from both the VFP and the RFP are plotted in **Figure 3.31 d, and e**. No consistent change in the amounts of filled fractures are observed on either plot.

In the field the different infills do not appear to occupy separate fracture sets, but instead fractures often contain multiple generations of infill. Overprinting relationships observed in the field enable the relative ages of the 2 fracture infills to be established. Epidote-rich cataclasite often occurs as clasts within zeolite and/or calcite matrixed breccias, on both a mm-scale within fractures, and on a cm- to m-scale adjacent to fault planes (**Figure 3.32 a, b**). Zeolite and calcite veins are also observed cross-cutting epidote-rich cataclasite adjacent to the RFP (**Figure 3.32**). This evidence suggests that the zeolite and calcite mineralisation fracture infill is younger than the epidote-rich cataclasite.

3.3.3 *Fracture kinematics*

A total of 53 (19%) of the 278 filled fractures measured in the field had slickenfibre lineations (section 1.5.1.2). Fractures orientated N-S and filled with epidote are associated with mainly steeply plunging, but also shallowly plunging, lineations and

therefore record both dip-slip and strike-slip movements. Epidote-filled fractures orientated ENE-WSW are associated with mainly shallowly plunging lineations (**Figure 3.33 a**), which are correlated with sinistral strike-slip indicators in the field. Fractures orientated ENE-WSW, N-S and ESE-WNW and filled with zeolite/calcite are all associated with both dip-slip movements (steeply plunging lineations) and strike-slip movements (shallowly plunging lineations) (**Figure 3.33 b**). Field evidence suggests that ENE-WSW-trending zeolite and calcite infills are associated with dextral strike-slip movements, whereas N-S-trending fractures filled with zeolite/calcite are associated with sinistral strike-slip movements.

3.3.4 *Summary of fracture orientation, infill and kinematics from 1-D line transects, adjacent to the RFP.*

A summary of fracture orientation, infill and kinematics data collected and analysed adjacent to the RFP along 1-dimensional line transects is presented in **Table 3.7**.

Data sets used	>700 fractures measured, 21 1-dimensional line transects (3 transect orientations vertical, parallel and perpendicular to the MTFC trend). 18 transects carried out within gneiss, 3 within cataclasite. Data collected at varying distances along the strike of the RFP.
Orientation	4 fracture orientation clusters observed ENE-WSW, NNW-SSE, N-S and E-W to ESE-WNW. 2 sets of ENE-WSW striking fractures observed at some localities dipping either NW or SE due to re-orientation during fault movements.
Infill	38% of fractures measured are filled. Most common infills are – epidote-rich cataclasite and coeval zeolite & calcite mineralisation. No systematic change in number of filled-fractures adjacent to, or along the strike of, the RFP Different infills are recorded in the same fracture orientations. Fractures striking ENE-WSW, N-S & NNW-SSE contain both types of infill, E-W striking fractures contain predominantly zeolite & calcite. Epidote cataclasite occurs as clasts within zeolite & calcite matrixed breccias. Zeolite & calcite veins consistently cross-cut cataclasite. Epidote-cataclasite & infill is older than zeolite & calcite mineralisation.
Kinematics	19% of filled fractures have slickenfibre lineations. N-S fractures containing epidote-cataclasite are associated with dip-slip & strike-slip movements. ENE-WSW fractures containing epidote-cataclasite are associated with sinistral strike-slip movements. ENE-WSW, N-S and ESE-WNW striking fractures with zeolite/calcite infill are associated with dip-slip and dextral strike-slip movements.

Table 3.7 Summary of orientation, infill and kinematics data collected adjacent to the RFP

3.3.5 *Fracture spacing data*

A series of 1-dimensional line transects have been carried out to measure fracture spacing values adjacent to the RFP. Transects have been carried out along the strike of the RFP, orientated both parallel and perpendicular to the trend of the VFP (i.e. perpendicular and parallel to the overall MTFC trend), in order to keep data collection consistent, and allow parameters to be compared between data sets collected from different faults. Transects have been carried out on both horizontal and vertical outcrop surfaces, to encompass the spacings between various fracture orientations. Spacing data has been collected at 7 localities adjacent to the RFP (**Table 3.8**). The fractures at 6 localities were measured within a gneissose lithology, and at 1 locality the fracture data was collected within cataclasite.

3.3.5.1 Cumulative frequency 'v' spacing

Spacing values measured from 1-dimensional line transects are plotted against cumulative frequency in **Figure 3.34**. Each graph represents a locality, and within each graph different transect orientations are plotted separately (see legends on graphs). For all data sets, the spacing values are best described by an exponential distribution, and this is confirmed when a Kolmogorov-Smirnov test (section 1.8.4.2) is carried out on the data. In some cases, there are data points that do not lie onto the best-fitting lines and these are likely to be the result of the under-representation of wide spacing values due to limited exposure.

3.3.5.2 Mean spacing 'v' standard deviation

The mean and standard deviation values from a data set that is best described by an exponential distribution are expected to be similar. The values of mean spacing and standard deviation from each 1-dimensional transect are plotted against each other in **Figure 3.35**, with different transect orientations distinguished. As expected for exponentially distributed data, there is a good relationship between average spacing and standard deviation, and the majority of values lie close to the x = y line.

	locality	~ perpendicular distance to RFP (m)	~ perpendicular distance to VFP (m)	lithology	1-dimensional line transect details				
					transect name & orientation (degrees)	no. fractures measured	transect length (mm)	mean spacing (mm)	exponent from exponential spacing graph
Rautingdalen	32a	2	235	gneiss	T1 – 165	85	2812	33.08	0.0302
					T5 – 165				
					T3 – 070	49	1606	32.78	0.0368
					T4 – 260				
					T2 – vertical	21	885	42.14	0.025
	32b	2	265	gneiss	T1 – 165	41	1332	32.49	0.033
					T2 – 255	38	1236	32.53	0.0322
	33	5	315	gneiss	T1 – vertical	19	546	28.74	0.0289
					T2 – 240	40	1193	29.83	0.0392
					T3 – 328	35	2568	73.37	0.0159
					T4 – 320				
	37	0.5	580	gneiss	T1 – 060	51	867	17.00	0.0703
					T2 – vertical	23	759	33.00	0.0281
	131a	1	1000	gneiss	T1 – 333	53	536	10.11	0.0653
					T2 – 065	46	752	16.35	0.0547
	131b	2	1000	gneiss	T1 – 063	58	1189	20.5	0.0569
					T3 – 255				
					T2 – vertical	25	760	30.40	0.0322
	131c	0.5	1000	cataclasite	T1 – 060	42	1018	24.24	0.0444
					T2 – vertical	40	513	12.83	0.0887
					T3 - 330	18	251	13.94	0.085

Table 3.8 Details of 1-dimensional line transects adjacent to the RF used to analyse fracture spacing. All localities lie to the west of the RFP.

3.3.5.3 Co-efficient of variation

The degree of clustering within a data set can be assessed by calculating the co-efficient of variation (Cv) (section 1.8.5.1). There appears to be no systematic change in value Cv with distance to the RFP (**Figure 3.36 a**). The change in Cv values along the strike of the RFP can be assessed by plotting the values against the perpendicular distance to the VFP (**Figure 3.36 b**), again there appears to be no systematic change in Cv value along strike. In both plots in **Figure 3.36** the values of Cv are distinguished for the different transect orientations.

3.3.5.4 Cumulative frequency exponent 'v' distance to RFP

The exponent values calculated from the exponential graphs in **Figure 3.34** can be used as a relative measure of fracture density. The values are separated into transect orientations and plotted against the perpendicular distance to the RFP in **Figure 3.37 a** to illustrate how the fracturing changes close to the RFP, and the perpendicular distance to the VFP in **Figure 3.37 b** to illustrate how fracture density changes along the strike of the RFP.

The maximum values of exponent in **Figure 3.7 a** are recorded from the fracture data sets measured within cataclasite 0.5m from the RFP along perpendicular and vertical transects. This suggests that fracture density is highest closest to the RFP (0.09), and that within these transect orientations the fracturing within cataclasite is higher than the fracture density within gneiss.

When the exponent values are plotted against the perpendicular distance to the VFP (**Figure 3.37 b**) the values (representing fracture density) appear to increase away from the VFP and therefore change along the strike of the RFP (see chapter 8 for discussion).

3.3.5.5 Mean spacing 'v' distance to RFP

The mean fracture spacing measured along a 1-dimensional line transect may also be used as a measure of fracture density, where low mean spacing values indicate high fracture densities. Values of mean spacing from each transect orientation are plotted against both the perpendicular distance to the RFP (**Figure 3.38 a**) and the perpendicular distance to the VFP (**Figure 3.38 b**). Mean spacing appears to increase away from the centre of the RF, suggesting that fracture density is highest close to the

RFP. Values of mean fracture spacing appear to broadly decrease away from the VFP, along the strike of the RFP, suggesting that fracture density changes along the strike of the RFP.

3.3.5.6 Mean spacing 'v' cumulative frequency exponent

A good relationship between the mean values and exponents from exponentially distributed data sets may be expected to exist since the mean value is a defining aspect of an exponential distribution (section 1.8.2.3). The values of mean spacing and exponential distribution exponents from all data sets collected adjacent to the RFP are plotted against each other in **Figure 3.39** on both logarithmic and linear axes. A good power-law relationship is observed between the two parameters, with an exponent value of -0.902.

3.3.5.7 "Step" plots of fracture spacing 'v' distance along 1-dimensional transects

Cumulative fracture frequency measured along a 1-dimensional line transect can be plotted against the distance along the transect (i.e. cumulative fracture spacing) (section 1.8.5.2) to illustrate the change in fracturing adjacent to the RFP. Unfortunately, the outcrops adjacent to the RFP are generally small in size (less than 2m in dimension) and long line transects, which are needed to illustrate the change in fracturing using this method, were not always available. Hence in **Figure 3.40**, only 6 transects are plotted to illustrate fracturing, 3 are from transects measured parallel to the MTFC trend and 3 are from transects measured perpendicular to the trend of the MTFC.

Transects measured parallel to the MTFC trend measure the spacing of fractures which are perpendicular to the fault trend. All 3 data sets plotted in **Figure 3.40 a** from parallel transects illustrate no stepping and therefore represent relatively regular fracture spacings (and fracture density) with no partitioning into areas of high and low density. The data set which is located closest to the RFP (from locality 131a, distance 1m from the RFP) and shows the steepest slope and therefore the highest fracture density.

Transects measured perpendicular to the MTFC trend measure the spacing of fractures which are parallel to the trend and parallel to the gneissose foliation (**Figure 3.40 b**). The data set which is located furthest from the RFP (locality 33, distance 5m) and furthest from the VFP (distance = 315m) shows the shallowest slope and therefore the

lowest fracture density with no stepping in the data curve. The data sets which are measured closest to the RFP (2m) and closest to the VFP (~235m & 265m) both illustrate a stepping pattern, suggesting that the fractures parallel to the MTFC trend adjacent to the RFP and close to the VFP are partitioned into areas of high and low fracture density.

3.3.6 *Summary of fracture data from 1-D line transects (RF).*

A summary of fracture data collected and analysed adjacent to the RFP along 1-dimensional line transects is presented in **Table 3.9**.

Fracture spacing attribute/plot		**Results from 1-D transects adjacent to the RFP**
Cumulative frequency 'v' spacing		All data sets are best described by an exponential distribution.
mean spacing 'v' standard deviation		Good linear relationship close to x=y.
Coefficient of variation (Cv)		Cv ranges from 0.7 to 1.7. No systematic change in Cv with increasing distance to RFP. Also no systematic change along strike of RFP.
exponent 'v' distance to RF		Maximum exponent values (~0.09) are recorded closest to RFP. Cataclasite values > gneissose values. Exponent values vary along strike of the RFP, and appear to increase away from VFP.
mean spacing 'v' distance to RF		Mean spacing values increase away from the centre of RF. Mean spacing values vary along strike of the RFP, and appear to increase away from VFP.
exponent 'v' mean spacing		Power-law relationship observed, exponent value = -0.902
Cumulative frequency 'v' distance along transect	Parallel transects	No stepping observed, therefore no partitioning into areas of high and low fracture density. Data set closest to RFP shows steepest slope and therefore highest fracture density.
	Perp. transects	Data furthest from RFP and VFP shows shallowest slope and no stepping suggesting low fracture density. Data sets closer to RFP and VFP show stepping pattern suggesting partitioning of fractures parallel to MTFC trend into areas of high and low fracture density.

Table 3.9 Summary of fracture spacing data collected along 1-D transects adjacent to the RFP.

3.4 The Hitra-Snåsa Fault

The following sections describe in detail the fracture orientations, infills, kinematics and spacing values measured from a number of localities adjacent to the Hitra-Snåsa Fault Plane (HSFP). Data has been collected both NW and SE of the HSFP at different distances normal to the fault plane and at a variety of localities along the strike of the HSF. The localities at Hammardalen quarry (locality 135) and the adjacent 719 road cut (localities 135, 136 & 148) are farthest to the SW, the Mefjellet localities (localities 141-145, & 158-160) are approximately 23 km to the NE of Hammardalen, and the data collected near Follavatnet (localities 146 & 147) are approximately 30 km to the NE of Mefjellet (section 2.2.1). Therefore, fracture parameters can be compared both along the strike of the HSFP, and with increasing perpendicular distance to the HSFP.

3.4.1 *Fracture orientation data*

The change in fracture orientation has been assessed by plotting 13 stereographic projections (section 1.7.2) which represent localities at varying distances both NW and SE of the HSFP (**Figure 3.41, Figure 3.42**). The stereonets have been plotted using data from a variety of 1-D transect orientations to ensure that all fracture orientations are represented. The fracture orientations are plotted as poles to fracture planes, and for each cluster of poles to fracture planes the mean girdle is shown, which represents the mean fracture plane for that cluster. The stereographic projections are accompanied by the Von Mises diagrams shown in **Figures 3.43** and **3.44** which represent the same data sets and illustrate frequencies of fracture strike (section 1.7.2).

Data collected from either side of the HSFP generally show the same common fracture clusters. At distances up to 250m NW and 150m SE of the HSFP, the fracture orientations show at least 3 clusters which strike ENE-WSW, NNW-SSE and N-S. At some localities within these distances an additional cluster of fracture orientations striking ESE-WSW is present. This cluster appears less common in the data sets collected at the Mefjellet section, suggesting some along strike variation in the orientation of fractures adjacent to the HSFP. These clusters of fracture orientations

are similar to those observed adjacent to the VFP (section 3.1.1), EFP (section 3.2.1) and RFP (section 3.3.1). It is important to note that near Follavatnet (localities 146 & 147) the gneissose foliation strikes ENE-WSW and dips moderately-steeply to the SE, whereas at the rest of the localities the foliation also trends ENE-WSW, but dips moderately to steeply to the NW. The fractures parallel to the foliation therefore also dip towards the SE near Follavatnet, but dip to the NW at the other localities.
The mean fracture cluster orientations from each locality are summarised in the tables as part of **Figure 3.41** and **Figure 3.42**.

3.4.2 *Fracture infills and their relative ages*

A total of 1835 fractures have been measured in the field from a number of localities adjacent to the HSFP. Out of the fractures measured, 276 (15%) have been recorded as having an infilling material. The most common fracture infills are green-coloured epidote-rich cataclasites, white/colourless calcite mineralisation, pink/orange zeolite mineralisation (stilbite and laumontite) and brown/black pseudotachylite. The photographs presented in **Figure 3.45** and **Figure 3.46** illustrate the variety of fracture infills observed in the field. No filled-fractures were observed at the Follavatnet section.
The orientations of all fractures with identified infills are plotted on a stereographic projection in **Figure 3.47 a**. Although there is scatter in the data, a number of clusters can be identified striking ENE-WSW, NNW-SSW, N-S, and ESE-WNW which correspond to the clusters recognised in section 3.4.1. Individual stereonets are plotted for each type of fracture infill in **Figure 3.47 b, c, d**. Different fracture infills are observed in the same fracture orientations. Fractures striking ENE-WSW and fractures striking N-S to NNW-SSE contain all 3 types of fracture infill, whereas fractures striking ESE-WNW contain only zeolite/calcite mineralisation, and this fracture set is rarely observed at localities within the Mefjellet section.
The percentages of filled-fractures from the Mefjellet section and the Hammardalen quarry/ road cut localities are plotted against distance to the HSFP in **Figure 3.47 e, f** respectively. The data from Mefjellet show an increase in the percentage of filled-fractures towards the centre of the fault, on both the NW and SE of the HSFP. The dominant infills are pseudotachylite and epidote; very few zeolite/calcite-filled

fractures are present. Although there are fewer data points than from the Mefjellet section, the fracture-fill data from the Hammardalen quarry and 719 road-cut also show an increase in the total amount of filled fractures towards the centre of the HSF. However, at these localities, the dominant fracture-fills observed are zeolite/calcite mineralisation, very few epidote-filled fractures are present, and no pseudotachylite-filled fractures were observed.

In the field the different infills do not appear to occupy separate fracture sets, but instead fractures contain multiple generations of infill. These overprinting relationships observed in the field together with thin-section observations, allow a relative time sequence of fracture infills to be established. Firstly, fractures filled with epidote-rich cataclasite often grade into or are linked to fractures filled with pseudotachylite. In thin-section and in the field the pseudotachylites both cross-cut and are present as clasts within the cataclasite matrix, suggesting that cataclasite and pseudotachylite development is broadly coeval. Fractures filled with epidote-rich cataclasite and pseudotachylite are consistently cross-cut and offset by fractures filled with zeolite and calcite (**Figure 3.48 a, b**). The zeolite and calcite mineralisation within fractures is often intergrown suggesting that the zeolite and calcite mineralisation is contemporaneous. Epidote-rich cataclasite occurs as clasts within calcite and zeolite matrixed breccias (**Figure 3.48 c, d**) and also on the outside edge of fractures (**Figure 3.48 e**) suggesting that the epidote-rich cataclasites are older than the zeolite and calcite matrix breccias.

3.4.3 *Fracture kinematics*

The effects of weathering, poor exposure and the overall small nature of the fractures measured in the field means that it is difficult to measure slickenside and slickenfibre lineations on fracture planes. Out of the 276 filled fractures measured in the field a total of 42 (15%) of the fractures had slickenfibre lineations (section 1.5.1.2) (**Figure 3.49**). The epidote-filled fractures orientated N-S are associated with mainly steeply plunging, but also a few shallowly plunging lineations and therefore indicate both dip-slip and strike-slip movements, whereas the epidote-filled fractures orientated ENE-WSW are associated with shallowly plunging lineations and therefore strike-slip movements (**Figure 3.50**). Zeolite and calcite slickenfibres are more complex. Strike-

slip lineations are observed along fracture planes orientated N-S (**Figure 3.50**) and NNW-SSE. Strike-slip and dip-slip lineations are observed along fracture planes orientated ENE-WSW.

Field evidence suggests that the ENE-WSW- trending epidote-rich cataclasites and coeval pseudotachylites are associated with *sinistral* strike-slip movements based upon the stepping of slickenfibres, the geometries of T- and R-type Riedel shears and offsets of quartz vein markers (**Figure 3.51, Figure 3.52, Figure 3.45a**).

Evidence from the field suggests that the ENE-WSW- trending zeolite- and calcite-filled fractures are associated with *dextral* strike-slip movements based upon the stepping of slickenfibres and offsets of quartz vein markers (**Figure 3.53**).

3.4.4 *Summary of fracture orientation, infill and kinematics from 1-D line transects, adjacent to the HSFP.*

A summary of fracture orientation, infill and kinematics data collected and analysed adjacent to the HSFP along 1-dimensional line transects is presented in **Table 3.10**.

Data sets used	>1800 fractures measured, 36 1-dimensional line transects (3 transect orientations vertical, parallel and perpendicular to the MTFC trend). Majority of fractures measured in gneiss or mylonitised gneiss. Localities from Follavatnet are within psammite & mylonitised psammite.
Orientation	Up to ~200m NW and SE of HSFP at least 3 clusters of fracture orientations = ENE-WSW, NNW-SSE, N-S. Also at some localities a cluster striking ESE-WNW is observed (less common from Mefjellet section). >200m from HSFP only 2/3 clusters occur.
Infill	15% of fractures measured are filled. Most common infills epidote-rich cataclasite, coeval zeolite/calcite & pseudotachylite. Different infills recorded in same fracture orientations. Fractures striking ENE-WSW and N-S to NNW-SSE contain all 3 types of infill. Fractures striking ESE-WNW contain zeolite & calcite only. Dominant fracture-fill changes along strike. Epidote-cataclasite links and grades into pseudotachylite. These infills are broadly coeval. Fractures containing epidote cataclasite and pseudotachylite are cross-cut by fractures filled with zeolite & calcite. Epidote cataclasite occurs as clasts in zeolite/calcite matrix breccias. Epidote-cataclasite & pseudotachylite infills are older than zeolite & calcite mineralisation.
Kinematics	15% of filled fractures have slickenfibre lineations. N-S fractures containing epidote-cataclasite are associated with dip-slip & strike-slip movements. ENE-WSW fractures containing epidote-cataclasite are associated with sinistral strike-slip movements. N-S, ESE-WNW, NNW-SSE striking fractures with zeolite/calcite infill are associated with dip-slip lineations. ENE-WSW striking fractures containing zeolite/calcite also associated with dextral strike-slip movements.

Table 3.10 Summary of orientation, infills and kinematics data collected adjacent to the HSFP

3.4.5 *Fracture spacing data*

Fracture spacing has been measured along a series of 1-dimensional line transects to investigate changes adjacent to the HSFP. Transects have been carried out on either horizontal or vertical outcrop surfaces in directions both parallel and perpendicular to the overall fault zone trend (ENE-WSW) and also on vertical surfaces, to encompass the spacings between various fracture orientations. In total, 14 localities have been used to collect spacing data at various distances from the HSFP (**Table 3.11**). Fractures from the Mefjellet and Hammardalen quarry/719 road sections are measured with a gneissose protolith, which is increasingly mylonitised near to the HSFP. Fractures from the Follavatnet section are measured within psammite at locality 146 and mylonitised psammite at locality 147.

The sections below describe in detail fracture spacing parameters analysed from localities adjacent to the HSFP.

3.4.5.1 Cumulative frequency 'v' spacing

Spacing values measured from 1-dimensional line transects are plotted against cumulative frequency in **Figure 3.54, Figure 3.55 & Figure 3.56**. Each graph represents a locality, and within each graph different data sets represent different transect orientations (see legends on graphs). The spacing values collected for all data sets are best described by an exponential distribution with a negative slope. This is confirmed when a Kolmogorov-Smirnov test (section 1.8.4.2) is carried out on each of the data sets. On the right hand side of some graphs, some data sets have spacing values that do not fall onto the best-fit lines. This is likely to be the result of under-representation of wide spacing values due to the limited size of the outcrops. Some other data sets are recorded as having two slopes, a steeper slope to the left hand side of the graph and a shallower slope to the left hand side (e.g. locality 143 T1, **Figure 3.54**). This may be interpreted as the data set having more smaller spacings than would be expected for an exponential distribution, and possible clustering of fractures at small spacing values.

Place	locality	~ perpendicular distance to VFP (m)	total number of fractures	lithology	1-dimensional line transect details				
					transect name & orientation (degrees)	no. fractures measured	transect length (mm)	mean spacing (mm)	exponent from exponential spacing graph
Mefjellet section	141	360	70	gneiss	T1 – 330	41	13935	339.88	0.0027
					T2 – 060	29	14853	512.17	0.0023
	142	375	93	gneiss	T1 & T4 – 068	38	9229	242.87	0.0035
					T2 – 335	55	7142	242.20	0.0079
	143	81	165	gneiss	T1 – 066	105	12156	115.77	0.019, 0.0055
					T2 – 153	60	7036	117.27	0.0088
	144	15	139	gneiss	T1 – 250	97	4433	45.70	0.0266, 0.0092
					T2 – 330	42	4584	109.14	0.0178, 0.0071
	145	-8	102	gneiss	T1 – 065	64	996	15.56	0.0805
					T2 – 340	38	1211	31.87	0.0371
	149	215	70	gneiss	T1 – 080	58	9095	156.81	0.0085
					T2 – vertical	12	799	66.58	0.0184
	158	-100	102	gneiss	T1 & T3 – 335	41	11367	277.24	0.0053
					T2 & T4 – 065	61	17895	293.36	0.0034, 0.0065
	159	-250	82	gneiss	T1 – 245	60	8242	137.37	0.0082
					T2 – 335	22	5438	247.18	0.0039
	160	-215	93	gneiss	T1 – 065	61	10972	179.87	0.0054
					T2 – 330	32	6123	191.34	0.0071
Follavatnet section	146	700	117	psammite	T1 – 070	82	32203	392.72	0.002
					T2 – 155	35	3892	111.20	0.0137
	147	150	76	psammite	T1 – 240	52	10445	200.87	0.005
					T2 – 325	24	795	33.13	0.0573
Hammardalen Quarry & 719 road sections	135	20	1545	gneiss	T1 – vertical	21	1583	75.38	0.0106
					T2 – 140	52	2662	51.19	0.0168
					T3 – 240	81	15100	93.21	0.01
	136	-35	166	gneiss	T1 & T2 – vertical	55	1907	34.67	0.0278
					T3 & T4 – 060	111	7007	63.13	0.0179
	148	-50	143	gneiss	T1 & T4 – 060	122	10828	88.75	0.0137
					T2 & T3 – vertical	21	2895	137.86	0.0064

Table 3.11 Details of 1-dimensional line transects adjacent to the HSF used to analyse fracture spacing. Negative distances represent localities NW of HSFP, positive distances represent localities SE of HSFP.

3.4.5.2 Mean spacing 'v' standard deviation

A good linear relationship is observed between the mean spacing and standard deviation values from the 1-dimensional line transects close to the x = y line (**Figure 3.57**). This supports the observations made in section 3.4.4.2 that the data sets are best described by an exponential distribution.

3.4.5.3 Co-efficient of variation

The co-efficient of variation (Cv) for each 1-dimensional line transect is plotted against the perpendicular distance to HSFP in **Figure 3.58** with transect orientations distinguished. The values of Cv for all data sets range from 0.44 to 1.5. The transects measured parallel to the MTFC trend appear to show, in general, higher values of Cv than the transects measured perpendicular to the MTFC trend. This suggests that fractures perpendicular to the MTFC trend (measured along transects parallel to the trend) may be more clustered that the fractures orientated parallel to the main fault trend.

3.4.5.4 Cumulative frequency exponent 'v' distance to HSFP

The exponent values (slopes) from the best-fit exponential distributions plotted in **Figure 3.54, Figure 3.55 & Figure 3.56** can be plotted against the perpendicular distance to the HSFP. This allows the change in fracture density adjacent to the HSFP to be assessed (i.e. steep slopes correspond to a relatively large number of narrow spacings and suggest a higher fracture density) (**Figure 3.59, Table 3.11**).

The highest value of exponent from transects orientated parallel to the MTFC is 0.0805 which occurs in the centre of the fault, 8m NW of the HSFP. The exponent values decrease rapidly within 100m of the HSFP, to a background level of less than 0.01.

Overall, the maximum exponent value measured from transects orientated perpendicular to the HSFP is 0.0573. This value is measured from data collected 150m to the south of the HSFP at the Follavatnet section. The highest exponent value measured from the Mefjellet section and the Hammardalen quarry/719 road sections is 0.0371, which occurs 8m north of the HSFP. The exponent values from Mefjellet and the quarry/road sections decrease rapidly within 100m of the HSFP, to a background level of less than 0.01. Although data was collected from only 2 localities at the

Follavatnet section the exponent values suggest that fracture density measured along transects perpendicular to the MTFC trend (i.e. the density of fractures parallel to the MTFC trend) is higher than the density measured from the Mefjellet and quarry/719 road sections. This may be a result of lithological differences between Follavatnet (psammite protolith) and the Mefjellet/Hammardalen quarry/719 road sections (gneiss protolith).

3.4.5.5 Mean spacing 'v' distance to HSFP

The mean fracture spacing from each transect orientation can be plotted against the perpendicular distance from the HSFP to also assess the change in fracture density (**Figure 3.60, Table 3.11**). The lowest mean spacing value from transects orientated parallel to the MTFC trend occurs at the centre of the fault (15.6mm, 8m north of HSFP). The lowest mean spacing value from transects orientated perpendicular to the MTFC trend is 31.9mm which occurs 8m north of the HSFP.

As was observed from the exponent data, the values of mean spacing measured from perpendicular transects at the Follavatnet section localities appear to be lower than the mean spacings measured at equivalent distances from the HSFP at the Mefjellet and quarry/719 road sections.

3.4.5.6 Mean spacing 'v' cumulative frequency exponent

If data sets are best described by an exponential distribution, then a relationship may be expected to exist between the mean spacing and the exponent values, since the mean is a defining aspect of an exponential distribution (section 1.8.2.3). A power-law relationship is observed when the mean spacing value from each transect measured adjacent to the HSFP is plotted against the exponent from the exponential spacing graphs, with an exponent value of -0.98 (**Figure 3.61, Table 3.11**).

3.4.5.7 "Step" plots of fracture spacing 'v' distance along 1-dimensional transects

By plotting cumulative fracture frequency along each 1-dimensional line transect against the distance along the transect (i.e. cumulative fracture spacing) (section 1.8.5.2) the change in fracture spacing can be assessed adjacent to the HSFP for both perpendicular and parallel transect orientations. The 1-dimensional line transects must be of sufficient length to illustrate the change in fracturing, which in this thesis is defined as greater than 2m except for very dense fracturing where shorter transects are

sufficient. In total, 22 line transects (11 parallel and 11 perpendicular to the MTFC trend) measured at varying distances to the HSFP have been selected and plotted (**Figure 3.62**).

Transects orientated parallel to the MTFC trend measure the spacings of fractures perpendicular to the MTFC trend. The data sets collected from the Mefjellet and quarry/719 road sections are plotted in green and blue and the data from the Follavatnet section are plotted in red (**Figure 3.62 a**). Parallel transects measured closest to the HSFP show steep slopes representing high fracture densities. The slope of the data sets decreases as the distance away from the HSFP increases suggesting that the fracture density decreases away from the centre of the fault (both NW and SE). Little/no stepping is observed within the data sets suggesting that the fracturing is not partitioned into areas of high and low fracture density.

Data from transects orientated perpendicular to the MTFC trend (measuring spacings of fractures parallel to the trend) are plotted in **Figure 3.62 b**, where the red data sets are localities from the Follavatnet section, blue and green data sets are localities from the Mefjellet and quarry/719 road sections. As for the parallel transects, the data sets closest to the centre of the fault are steep and suggest dense fracturing and the slopes of the data decrease with increasing distance both NW and SE of the HSFP. As observed in previous sections for perpendicular transects, the data from the Follavatnet localities appears to show higher fracture density than is observed at the Mefjellet and quarry/719 road sections at the equivalent distance from the HSFP. For example, the data set measured 150m from the HSFP at Follavatnet is steeper (i.e. shows higher fracture density) than the data set measured 20m from the HSFP at the Hammardalen quarry section and steeper than the data sets measured 15m from the HSFP at the Mefjellet section.

3.4.6 *Summary of fracture spacing data from 1-D line transects (HSF).*

A summary of fracture spacing data collected and analysed adjacent to the HSFP along 1-dimensional line transects is presented in **Table 3.12**.

Fracture spacing attribute/plot		**Results from 1-D transects adjacent to the HSFP**
Cumulative frequency 'v' spacing		All data sets are best described by an exponential distribution.
mean spacing 'v' standard deviation		Good linear relationship close to x=y.
Coefficient of variation (Cv)		Cv ranges from 0.44 to 1.5. Cv values measured from transects orientated parallel to MTFC trend are generally higher than Cv values measured from transects orientated perpendicular to the MTFC trend. This suggests fractures perpendicular to the MTFC trend may be more clustered than fractures parallel to it.
exponent 'v' distance to HSF		Highest exponent value from transects parallel to MTFC trend occurs 8m to NW of HSFP (= 0.0805). Values decrease to background level of < 0.01 within 100m from HSFP. For transects orientated perpendicular to MTFC trend values of exponent from Follavatnet localities are higher than equivalent exponent values from Mefjellet & quarry/719road sections. For Mefjellet & quarry/719 sections highest value occurs 8m NW of HSFP (= 0.0371) and values decrease to background level of <0.01 within 100m of HSFP.
mean spacing 'v' distance to HSF		Smallest mean spacings occur in the centre of the fault for all both transect orientations. Mean spacings measured along perpendicular transects at Follavatnet are less than equivalent mean spacings from Mefjellet and quarry/719 sections
exponent 'v' mean spacing		Power-law relationship observed, exponent value = -0.98
Cumulative frequency 'v' distance along transect	Parallel transects	Steeper slopes occur closest to centre of fault suggesting higher fracture densities. Slope decreases as the distance to the HSFP increases suggesting decreasing fracture density away from the HSFP.
	Perp. transects	Steeper slopes occur closest to centre of fault suggesting higher fracture densities. Slope decreases as the distance to the HSFP increases suggesting decreasing fracture density away from the HSFP. Data collected from Follavatnet show higher fracture densities compared to localities from Mefjellet/quarry/719 road at equivalent distances.

Table 3.12 Summary of fracture spacing data collected along 1-D transects adjacent to the HSFP

3.5 Summary of fracture parameters collected along 1-dimensional line transects adjacent to faults within the MTFC

Two main clusters of fracture orientations are observed adjacent to the VF, HSF, EF and RF, which are both steeply dipping, and trending ENE-WSW (parallel to the trend of the MTFC) and ~N-S (ranging from NNW-SSE to NNE-SSW). Additional clusters of fracture orientations trending E-W are observed adjacent to the VF, EF and RF. Away from the main faults, stereonets of fracture orientations show less clustering and more scatter.

The two most common fracture-fills observed within the MTFC are a) epidote-rich cataclasite, and b) coeval calcite and zeolite mineralisation. In addition, incohesive gouge-filled fractures are observed adjacent to the VFP only, and fractures filled with pseudotachylite (coeval with the cataclasites) are only widely observed adjacent to the HSFP. It is very common to observe more than one type of infill within a single fracture. The dominant types of fracture-fill observed adjacent to the HSFP changes along strike of the fault from being dominantly epidote-rich cataclasite and pseudotachylite fills towards the NE (Mefjellet locality), to being dominantly zeolite/calcite fills towards the SW (Hammardalen quarry / 719 road cut). The proportion of filled fractures is measured adjacent to the VF, EF and HSF is summarised in **Figure 3.63 b** (data for the HSF is from the Mefjellet locality). From field and thin-section observations, epidote cataclasites and coeval pseudotachylites are the oldest fracture fill, these are cross-cut by coeval zeolite/calcite mineralisation, and the youngest fracture-fill observed is incohesive gouge. No systematic change in the amount, or type, of filled-fractures is observed either adjacent to, or along strike of the RFP.

Very few slickenfibre lineations were observed on fracture planes, therefore only limited kinematic data was available. However, based on field evidence, a) fractures trending ENE-WSW and filled with epidote-rich cataclasite, are associated with sinistral strike-slip movements, b) epidote-filled fractures trending ~N-S are associated with predominantly dip-slip normal movements, c) zeolite/calcite-filled fractures trending ENE-WSW are associated with dip-slip normal and dextral strike-

slip movements and d) ~N-S trending fractures filled with zeolite/calcite, are mainly associated with sinistral strike-slip movements.

All data sets of fracture spacing values collected adjacent to the VF, HSF, RF, and EF is best described by an exponential distribution. The change in exponent value adjacent to the VF, HSF and EF is illustrated in **Figure 3.63 c**, for transects orientated both parallel and perpendicular to the MTFC trend. A background, regional, level of exponent values is observed (~0.01), above which the VF, HSF and EF can be recognised as marked perturbations in the data. The absolute maximum values of exponent and the width of the perturbation are different for all three faults. The VF is characterised by a tall peak, with exponent values lying above background level for a distance of ~500m from the VFP. The HSF is identified by a tall but narrow peak, and the EF is recognised by a shorter peak than the VF and the HSF.

The mean values of fracture spacings calculated from a number of localities within the MTFC, are inversely proportional to the values of exponential exponent described above, and are presented in **Figure 3.63 d**.

Finally, cumulative fracture frequency can be plotted against cumulative fracture spacing ("step plots"), and illustrate that fractures orientated ENE-WSW, parallel to the MTFC trend, are clustered into zones of high and low density up to 500m from the VFP. No clustering of fractures is observed adjacent to the HSF, EF or RF.

CHAPTER 4 - FRACTURE CHARACTERISTICS FROM FOUR 2-D DATA SCALES, MTFC, CENTRAL NORWAY

Data sets for the analysis of fracture characteristics in 2-dimensions (2-D) were selected for both the main faults in the MTFC, the Hitra-Snåsa and Verran Faults (sections 2.2.1, 2.2.2), as well as for the Elvdalen Fault (section 2.2.4). Fracture spacing, length and connectivity data are described and interpreted for each of the four scales.

4.1 Data sets available for 2-dimensional analysis

4.1.1 *Landsat Thematic Mapper (Landsat ™) data set*

A Landsat™ image of the Fosen peninsular was provided by Statoil (**Figure 4.1**) for this study. A lineament analysis was carried out on a portion of the image to identify the kilometre-scale geometry of the Møre-Trøndelag Fault Complex (**Figure 4.2**) (see chapter 2). A lineament has been defined by O'Leary et al., (1976) as "*a mappable simple or composite linear feature of a surface, whose parts are aligned in a rectilinear or slightly curvilinear relationship, and which differs distinctly from the patterns of adjacent features and presumably reflects a sub-surface phenomena*". The lineaments recorded in this study are based on a combined analysis of the Landsat™ image, geological maps and geological field data to help eliminate non-tectonic features such as lithological boundaries.

The Landsat™ interpretation carried out in this study appears to be the most detailed interpretation to date. A total of 241 lineaments were observed and recorded in an area of 757km², at a scale of 1:95500. The shortest recorded structure is 430m, and the longest is 56.92km.

Lineament analyses of satellite data from onshore Norway have been published by Ramberg et al., (1997) and Gabrielsen & Ramberg (1979). In both studies the interpretation has been divided into sub-areas to study the changes in lineament orientation and intensity. Both studies recognise the MTFC as a prominent NE-SW zone of high lineament density (**Figure 4.3**). Interpretations of satellite images specifically from area of the MTFC in Central Norway have also been carried out by Rindstad & Grønlie (1986) and Grønlie & Roberts (1989) (**Figure 4.4** & **Figure 4.5**).

4.1.2 *Air photograph data set*

Air photographs were provided by the Geological Survey of Norway (Norges Geologiske Undersøkelse, NGU) and were used to interpret the large-scale geometry (10's to 100's metres scale) over part of the MTFC (**Figure 4.6**). The area of the air photograph includes the Verran Fault, Elvdalen Fault and the Rautingdalen Fault, but does not cover the Hitra-Snåsa Fault. A total of 499 lineaments were observed and recorded in an area of 20.5km^2, at a scale of 1: 17300. The shortest recorded structure is 69m, and the longest is 4948m (**Figure 4.7**).

4.1.3 *Outcrop data sets*

Selected field photographs from outcrop localities were chosen to investigate the fracture characteristics of the MTFC at outcrop scale (metre scale). The localities were chosen based on the quality and resolution of the photographs, and also on the distance from the main structures (VF and HSF) to provide a range of fracture intensities. A total of 26 photographs were chosen from different localities and different faults (**Table 4.1, Figure 4.8, Figure 4.9, Figure 4.10**).

Fault	Place		Locality	Approx. perpendicular distance to fault (m)	Lithology	Photo area (cm²)	Total number fractures
VF	North of VFP	Reservoir Road	28a/164 (1)	475	gneiss	24251.88	175
			28a/164 (2)	475	gneiss	19884.22	215
			28c (1)	600	gneiss	31619.79	154
			28c (2)	600	gneiss	8695.33	175
			49	1650	gneiss	97138.57	64
			133	1300	gneiss	88773.40	105
			138	2250	gneiss	37630.02	112
		720Road & Fjordside	46	40	gneiss	28784.51	323
			48i a	150	amphibolite	9751.28	259
			48i g	150	gneiss	9177.06	72
			137	28	gneiss	2643.42	318
		Verran Fault core	139 (1)	20	gneiss	4829.05	180
			139 (2)	20	gneiss	4240.21	85
	S of VFP		140	800	gneiss	119453.49	47
HSF	South of HSF	Mefjellet	86	25	gneiss	16724.52	-
			144	15	gneiss	10324.79	84
			117	100	gneiss	2845.75	-
			142	375	gneiss	26793.34	31
			143	81	gneiss	19060.66	29
	North of HSF	Mefjellet	108	125	gneiss	50451.33	93
			145	8	gneiss	1175.37	199
			158	100	gneiss	16208.31	38
			159	250	gneiss	19289.23	50
			160	215	gneiss	21858.45	48
EF	Reservoir Road		132a	1926 (VF)	gneiss	15645.20	77
			132b	1936 (VF)	gneiss	16669.44	163

Table 4.1 Outcrop data sets from field photographs for 2-dimensional fracture analysis

Fault	Place		Thin-section number	Approximate perpendicular distance to fault (m)	Area of section (cm²)	Total number fractures
VF	Reservoir Road		V99/17	2800	5.83	91
			VM 2	510	3.28	62
	720 Road		VPS 2	50	6.17	296
	Fjordside		VMC 7	30	10.41	294
			V99/24	25	29.15	748
HSF	Mefjellet	North of HSFP	HS 21	430	6.57	119
			HS 19	180	4.74	139
			HS 3b	45	6.13	190
			HS 16	6	7.79	343
		South of HSFP	HS 13	4	6.18	964
			HS 42	8	7.56	346
			HS 43	25	6.16	86

Table 4.2 Thin section data sets for 2-dimensional fracture analysis

4.1.4 *Thin-section data sets*

Thin-sections were cut from selected hand specimens collected in the field to investigate the fracture characteristics of the MTFC on a millimetre-centimetre scale. The sections were chosen based on their quality and resolution, and also on the distance from the main structures (VF and HSF) to provide a range of fracture intensities. A total of 12 sections were chosen from different localities and different faults (**Table 4.2, Figure 4.8, Figure 4.11, Figure 4.12**).

4.2 Fracture Spacing

Fracture spacing data was collected from the 2-dimensional data sets by four methods outlined below (section 1.9.1):

a) a set of 1-dimensional line transects parallel to the main fault trend (060°) to analyse the spacing population of fractures perpendicular to the main trend,
b) a set of 1-dimensional line transects perpendicular to the main fault trend (~ 150°) to analyse the spacing population of fractures parallel to the main trend,
c) for data sets where the photographs are taken of vertical surfaces, a set of 1-dimensional line transects vertically across the photograph to analyse the spacing population of horizontal / sub-horizontal fractures,
d) a transect every 30° across the data set to enable the creation of ellipses from the average fracture spacing in each orientation, and a comparison of fracture density between localities.

Methods a), b) and c) all involve six 1-dimensional line transects (i.e. multi-line sampling, section 1.9.1) in the same orientation to provide a data set large enough to analyse the spacing population.

Fracture spacing can be used to calculate fracture density, which is defined in this thesis as the total number of fractures (or spacings) per unit length for sampling along 1-dimensional line transects, or the total number of fractures per unit area for a 2-

dimensional data set (section 1.7.4.2). Fracture density is directly related to average spacing along 1-dimensional line transects. Fracture density in 2-dimensions is also directly related to fracture spacing, as the wider the spacing of the fractures the less fractures per unit area and visa versa.

4.2.1 *Landsat ™Image*

The 1-dimensional line transects used to measure spacing values across the Landsat™ image are shown in **Figure 4.13**.

4.2.1.1 Fault-parallel line transects (060°)

The combined plot of spacing values from the six 1-dimensional line transects orientated at 060° across the Landsat™ image is presented in **Figure 4.14**. The data set plots as a straight line when the x-axis is plotted as a linear scale and the y-axis is plotted as a logarithmic scale, and therefore is best described by an exponential distribution with a negative slope. This is confirmed when a Kolmogorov-Smirnov test (section 1.8.4.2) is carried out on the data set. The equation for the best-fit line is shown on the graph (**Figure 4.14**) and has an exponent of 0.0007. There are 9 out of a total of 202 data points that do not fall onto the best-fit line. This is likely to be the result of multi-line sampling causing over-estimation of wide spacing values (section 1.9.1).

The six 1-dimensional line transects carried out at 060° across the image can also be analysed separately to investigate the change in spacing (of fractures and faults perpendicular to the main trend) relative to the two main structures (VF and HSF). The change in exponent (slope) and average fracture spacing for each of the transects are shown in **Figure 4.15**. The distance between VF and HSF changes along strike of the faults. The distances used for **Figure 4.15** are calculated from the third transect orientated at 150°, where the distance between VF and HSF is ~8740m. The exponent and average spacing values are inversely related. The average spacing is lowest (and fracture density is therefore highest) closest to the Verran Fault along 060° transect 1. This also

corresponds to a steep exponent and therefore a high proportion of smaller spaced faults. Transects 3, 4 and 5 have approximately constant values for average spacing and exponent, and show a lower fracture density than transects 1 and 2. The highest value of average spacing and the shallowest exponent (lowest density) occurs north of the HSFP along transect 6, which is outside the MTFC.

In summary the spacing data from 1-dimensional transects orientated at 060° across the Landsat™ image suggest that closest to the Verran Fault the average spacing of fault-perpendicular fractures is lowest, the spacing exponent is steepest and fracture density is highest.

4.2.1.2 Fault-perpendicular line transects (150°)

The combined plot of spacing values from the six 1-dimensional line transects orientated at 150° across the Landsat™ image is presented in **Figure 4.16**. The data set plots as a straight line when the x-axis is plotted as a linear scale and the y-axis is plotted as a logarithmic scale, and therefore is best described by an exponential distribution with a negative slope. This is confirmed when a Kolmogorov-Smirnov test (section 1.8.4.2) is carried out on the data set. The equation for the best-fit line is shown on the graph (**Figure 4.16**) and has an exponent of 0.0014. Out of a total of 89 data points, 2 do not fall onto the best-fit line. This is likely to be the result of the under-representation of wide spacing values due to the limited size of the sample area.

The change in spacing of fault-parallel fractures can be analysed by plotting the average spacing and exponent values for each of the six 1-dimensional line transects orientated at 150° separately (**Figure 4.17**). The distances on the x-axis of the graph correspond to the cumulative distance along the strike of VF, where transect 1 is at 0m, and lies furthest to the SW. The exponent and average spacing values are inversely related. The average spacing is similar for transects 1, 4, 5 and 6. There is insufficient data to calculate a statistically valid exponent for transect 5. Transects 2 and 3 have anomalously low average spacing values, and corresponding high exponent values. For transect 3 this can be explained by the presence of the Rautingdalen Fault (a N-S structure, and part of the MTFC) (section 2.2.3) causing an increase in smaller fracture spacings and higher

fracture density. Transect 2 crosscuts the hinge of the large antiform visible on the Landsat™ (**Figure 4.1**) image, which is associated with an increase in fracture density and therefore relatively smaller fracture spacing values.

In summary, spacing data from 1-dimensional transects orientated at 150° across the Landsat™ image suggest that the spacing of fault-parallel fractures changes along the strike due to the presence of the Rautingdalen Fault and the large antiform.

4.2.1.3 Fracture density

Fracture density from the Landsat™ data set can be quantified in two ways, a) by calculating the area of an ellipse from the mean fracture spacings, and b) by calculating the total number of fractures per unit area (**Table 4.3**).

Data set	Total number of fractures in sample	Density	
		Area of average spacing ellipse (km²)	Total number of fractures per km²
Landsat™	241	2.748	0.3184

Table 4.3 Fracture density values for the Landsat™ data set.

a) The variation of fracture spacing across the Landsat™ image can be quantified by calculating the average fracture spacing measured along 1-dimensional line transects every 30 degrees (section 1.7.4.2.2). The mean spacing values can then be plotted on a rose diagram to produce an ellipse which represents the change in fracture density (section 1.7.4.2) with transect orientation. The area of the ellipse provides a measure of fracture density across the 2-dimensional sample area. The ellipse can also be used to assess fracture density for different fracture orientations, as for example the transect orientated perpendicular to the fault trend will measure the density of fault-parallel fractures.

The ellipse created for the Landsat™ image is presented in **Figure 4.18**. The maximum value of average fracture spacing occurs along the transect orientated at 060°. This corresponds to a low fracture density along the transect, and is likely to be dominated by spacings of fracture perpendicular to the main fault trend. The minimum value of average

fracture spacing occurs along the transect orientated at 120°. This corresponds to the highest fracture density and is likely to be dominated by spacings of fractures parallel to the main fault trend.

The conclusion drawn from the spacing ellipse – that fractures parallel to the fault trend have a higher density – is supported by the exponent data described in section 4.2.1.1 and section 4.2.1.2. The exponent for the combined data set of 150° transects is steeper than the exponent for the combined data set of 060° transects, suggesting relatively more smaller fracture spacings and a higher fracture density for the 150° data set, which represents fractures parallel to the overall fault trend.

b) As well as using average fracture spacing as a measure of fracture density for 1-dimensional sampling, fracture density can also be assessed in 2-dimensions by calculating the total number of fractures per unit area, which is directly related to fracture spacing (section 1.7.4.2). The 2-dimensional fracture density value for the Landsat™ image is 0.318 fractures/faults per square kilometre. This value is inversely proportional to the area of the mean spacing ellipse (section 4.2.5) (**Table 4.3**).

4.2.2 *Air photograph data set*

The 1-dimensional transects used to measure fracture spacing across the air photograph data set are shown in **Figure 4.19**.

4.2.2.1 Fault-parallel line transects (050°)

The combined plot of spacing values from the six 1-dimensional line transects orientated at 050° across the air photograph data set is presented in **Figure 4.20**. The data set plots as a straight line when the x-axis is plotted as a linear scale and the y-axis is plotted as a logarithmic scale, and therefore is best described by an exponential distribution with a negative slope. This is confirmed when a Kolmogorov-Smirnov test (section 1.8.4.2) is carried out on the data set. The equation for the best-fit line is shown on the graph (**Figure 4.20**) and has an exponent of 0.0062. There is 1 data point out of a total of 176

that does not fall onto the best-fit line. This is likely to be the result of the over-representation of wide spacing values due to multi-line sampling (section 1.9.1).

The six 1-dimensional line transects carried out at 050° across the air photograph data set can also be analysed separately to investigate the change in spacing (perpendicular to the main trend) relative to the Verran Fault. The change in exponent (slope) and average fracture spacing for each of the transects are shown in **Figure 4.21** (an extra data point is shown for average spacing, labelled as transect 7 in **Figure 4.21**). The average spacing value is anomalously high and the exponent value is anomalously low from transects 3 and 6. These could be explained by a reduction in data quality/resolution in the area of those transects, although this does not appear true on the data set, or alternatively there could be a genuine decrease in fracture density in that area. The average spacings from transects 1, 2, 4, 5 and the extra data point show very similar values, suggesting that fracture density in these areas is also similar, although the exponent values are more varied.

In summary, spacing data from 1-dimensional transects orientated at 050° across the air photograph suggest that the average spacing of fault-perpendicular fractures is constant in most areas except for the areas of transects 3 and 6 which show a lower fracture density.

4.2.2.2 Fault-perpendicular line transects (140°)

The combined plot of spacing values from the six 1-dimensional line transects orientated at 140° across the air photograph data set is presented in **Figure 4.22**. The data set plots as a straight line when the x-axis is plotted as a linear scale and the y-axis is plotted as a logarithmic scale, and therefore is best described by an exponential distribution with a negative slope. This is confirmed when a Kolmogorov-Smirnov test (section 1.8.4.2) is carried out on the data set. The equation for the best-fit line is shown on the graph (**Figure 4.22**) and has an exponent of 0.0099. All of the 222 data points are incorporated into the best-fit line, but some data points lie slightly above the line and this is evidence for multi-line sampling (section 1.9.1)

The change in spacing of fault-parallel fractures can be analysed by plotting the average spacing and exponent values for each of the six 1-dimensional line transects orientated at

140° separately (**Figure 4.23**). The distances on the x-axis of the graph correspond to the cumulative distance along the strike of VF, where transect 1 is at 0m. The values of average spacing and exponent from transect 1 appear to be anomalous. The average spacing is low suggesting a high fracture density, and the exponent is high (steep) corresponding to a high proportion of small fracture spacings in the data set. The anomalous results of transect 1 are explained by the transect crosscutting the dense fracturing associated with Rautingdalen Fault (section 2.2.3). The other anomalous data points are from transect 4, where the average spacing value is high and the exponent value is low. This appears to be a real facet of the data and not due to poor data quality. The values of exponent and average spacing values from transects 2, 3, 5 and 6 are all similar, suggesting similar values of fracture density in those areas.

In summary, spacing data from the 1-dimensional transects orientated 140° across the air photograph suggest that the fracture density changes along the strike of the Verran Fault due to the presence of the Rautingdalen Fault. There is little evidence of a change in fracture spacing parallel to the strike of the fault.

4.2.2.3 Fracture density

Fracture density from the air photograph data set can be quantified in two ways, a) by calculating the area of an ellipse from the mean fracture spacings, and b) by calculating the total number of fractures per unit area (**Table 4.4**).

Data set	Total number of fractures in sample	Density	
		Area of average spacing ellipse (km²)	Total number of fractures per km²
Air photograph	499	0.059	24.34

Table 4.4 Fracture density values for the Air Photograph data set.

a) A series of 1-dimensional transects were carried out across the air photograph every 30°. An ellipse was created using the mean spacing values from each transect orientation to quantify the change in density across the 2-dimensional sample area and is presented in **Figure 4.24**. The maximum value of mean fracture spacing occurs along the transect

orientated at 060°. This corresponds to a low fracture density along the transect, which is likely to measure the spacings of fractures perpendicular to the main fault trend. The minimum value of average fracture spacing occurs along the transect orientated at N-S (0°). This corresponds to the highest fracture density and is likely to measure the spacings of fractures parallel and sub-parallel to the main fault trend.

The overall appearance of the ellipse calculated from the air photograph data set is not very similar to the shape of the ellipse calculated from the Landsat™ data set. The combination of fault-parallel and N-S fault trends give the air photograph ellipse a more complex shape and suggest a more varied fracture density than the Landsat™ ellipse. This is most likely due to the increased abundance of north-south fractures and faults which are more apparent at the scale of the air photograph data set than the Landsat™ scale (e.g. structures associated with the NNW-SSE trending Rautingdalen Fault).

b) As well as using average fracture spacing as a measure of fracture density for 1-dimensional sampling, fracture density can also be assessed in 2-dimensions by calculating the total number of fractures per unit area, which is directly related to fracture spacing (section 1.7.4.2). The 2-dimensional fracture density value for the air photograph data set is 24.3 fractures/faults per square kilometre. This value is inversely proportional to the area of the mean spacing ellipse (section 4.2.5) (**Table 4.4**).

4.2.3 *Outcrop data*

Fracture spacing data measured from 1-dimensional line transects across field photographs is presented and discussed below to analyse fracture spacing and density at the outcrop scale. Data is presented for the two main faults in the MTFC, the VF and HSF, and also for the Elvdalen fault (EF) which is parallel to the main structures, but has a shorter lateral extent and simpler kinematic history.

4.2.3.1 HSF

A total of 10 field photographs were selected from outcrop localities to analyse fracture spacing relative to HSF (**Table 4.1, Figure 4.9, Figure 4.10**). The localities chosen are at various distances both north and south of the Hitra-Snåsa fault plane (HSFP). All of the photographs used are horizontal or sub-horizontal outcrop surfaces with a gneissose lithology. Fracture spacing data was collected from the 2-dimensional data sets by some or all of the three methods outlined in section 4.2.

Plots of spacing values from the 1-dimensional line transects orientated at 060° and 150° across each outcrop photograph are presented in **Figure 4.25**. Each graph represents a locality, and within each graph the two data sets are for the two transect orientations. On each graph, the spacing data collected for 060° and 150° transects plot as a straight line when the x-axis is plotted as a linear scale and the y-axis as a logarithmic scale. Therefore they are best described by an exponential distribution with a negative slope (**Table 4.5**). This is confirmed when a Kolmogorov-Smirnov test (section 1.8.4.2) is carried out on each of the data sets. In some data sets there are data points that do not fall onto the best fit lines (on the right hand side of the graph). This is likely to be the result of either the under-representation of wide spacing values due to the limited size of the sample area, or over-representation of wide spacing values due to multi-line sampling (section 1.9.1).

For a data set to be best fitted by an exponential distribution, the mean and standard deviation values are expected to be similar. A plot of mean spacing versus standard deviation for each of the localities (and distinguished for different transect orientations) is presented in **Figure 4.26**. As expected for exponential data, there is a good relationship between average spacing and standard deviation.

If a data set is best described by an exponential distribution, the values are randomly distributed, that is neither clustered nor anti-clustered (regular). The co-efficient of variation (Cv) is a measure of the degree of cluster within a data set (section 1.8.5.1) and is plotted in **Figure 4.27** for the HSF outcrop localities (with transect orientations distinguished) against distance. The values of Cv for the HSF outcrop data set plot close to Cv = 1, and are all below the Cv = 1 line suggesting that the data is not strictly random, but slightly anti-clustered. There appears to be no consistent relationship between Cv and distance from the HSFP.

Fault	Locality	Transect orientation (degrees)	Best-fit statistical distribution	Exponent	R^2
HSF	142	060	exponential	0.0035	0.98
	142	150	exponential	0.0072	0.99
	143	060	exponential	0.0039	0.98
	143	150	exponential	0.0061	0.96
	144	060	exponential	0.0111	0.99
	144	150	exponential	0.0126	0.98
	145	060	exponential	0.0772	0.99
	145	150	exponential	0.0771	0.99
	158	060	exponential	0.0071	0.99
	158	150	exponential	0.0066	0.97
	159	060	exponential	0.0076	0.97
	159	150	exponential	0.0084	0.94
	160	060	exponential	0.0046	0.97
	160	150	exponential	0.006	0.96
VF	28a/164 1	112.5	exponential	0.0139	0.98
	28a/164 2	130	exponential	0.0229	0.98
			(2 slopes)	0.0075	0.98
	28c 1	240	exponential	0.0097	0.99
	28c 1	vertical	exponential	0.0067	0.99
	28c 2	150	exponential	0.0216	0.99
	46	vertical	exponential	0.0228	0.99
	46	45	exponential	0.0125	0.99
	133	195	exponential	0.002	0.96
	133	vertical	exponential	0.0017	0.99
	137	135	exponential	0.0774	0.98
	137	55	exponential	0.0603	0.98
	138	vertical	exponential	0.0046	0.98
	138	40	exponential	0.0067	0.99
	48i a	vertical	exponential	0.0136	0.99
	48i a	200	exponential	0.0147	0.98
	48i g	vertical	exponential	0.0256	0.99
	48i g	210	exponential	0.029	0.97
	139 2	325	exponential	0.0424	0.91
	139 1	vertical	exponential	0.0293	0.99
	139 1	50	exponential	0.0346	0.97
	140	vertical	exponential	0.0044	0.98
	140	40	exponential	0.0027	0.98
EF	132a	060	exponential	0.0021	0.99
	132a	150	exponential	0.0041	0.99
	132b	060	exponential	0.0136	0.99
	132b	150	exponential	0.0212	0.995

Table 4.5 Best-fitting spacing distribution and exponent values from outcrop data sets collected adjacent to the HSFP, VFP and the EFP

The exponents (slopes) from the spacing distribution graphs illustrated in **Figure 4.25** and **Table 4.5** can be used to assess the change in fracture spacing with distance to the HSFP. The exponent is a measure of the relative abundance of small and large spacings. A low exponent value corresponds to a shallow slope and a relatively high number of wide fracture spacings, suggesting a low fracture density. A high exponent value corresponds to a steeper slope and a relatively high number of narrow fracture spacings, suggesting a higher fracture density. The change in exponent with distance can be assessed for both the 060° transects and the 150° transects which measure different fracture sets. The 060° transects are more likely to measure fractures orientated perpendicular to the main fault trend, and the 150° transects are more likely to measure fractures orientated parallel to the main fault trend. Plots of exponent versus distance for both transect orientations are presented in **Figure 4.28**. The data points on the graphs represent the slopes of the lines from the graphs in **Figure 4.25**. The highest values of exponent (steepest slopes) in both plots in **Figure 4.28** occur close to the centre of the fault which suggests that this is where the closest spaced fracturing and highest fracture density occurs. The exponent values return to a background level of approximately 0.001 a few meters away from the centre of the fault, suggesting that the zone of dense fracturing is narrow.

The change in fracturing with distance can also be assessed by plotting the average fracture spacing from both the 060° and 150° transects (**Figure 4.29**). As expected the smallest average spacing values occur at the centre of HSF, in agreement with the exponent data.

The average spacing from transects measured every 30° across the outcrop photographs can be used to create ellipses. The shape of the ellipse represents the heterogeneity in fracture spacing and the size of the ellipse represents the density of fracturing (smaller ellipses represent higher fracture densities) (**Table 4.6**). The ellipses created for the HSF field photographs are presented in **Figure 4.30**, separated into localities north and south of the HSFP. The smallest ellipses occur at distances close to the fault, suggesting lower average spacing values in all transect orientations, and higher fracture densities. The shapes of the ellipses are varied. Most ellipses are elongate, with the minimum average spacing value occurring along either the 120° or 150° transect. Transects orientated 120°

Fault	Place		Locality	Total number fractures	Density	
					Area of average spacing ellipse (cm²)	Total number of fractures per cm²
VF	North of VFP	Reservoir Road	28a/164 (1)	175	not created	0.0072
			28a/164 (2)	215	not created	0.0108
			28c (1)	154	not created	0.0049
			28c (2)	175	not created	0.0201
			49	64	7436.74	0.0007
			133	105	not created	0.0012
			138	112	not created	0.0030
		720Road & Fjordside	46	323	not created	0.0112
			48i a	259	not created	0.0266
			48i g	72	not created	0.0078
			137	318	8.09	0.1203
		Verran Fault core	139 (1)	180	not created	0.0373
			139 (2)	85	not created	0.0200
	S of VFP		140	47	not created	0.0004
HSF	S of HSFP	Mefjellet	144	84	216.02	0.0081
			142	31	613.92	0.0012
			143	29	926.32	0.0015
	N of HSFP		108	93	494.74	0.0018
			145	199	4.55	0.1693
			158	38	447.00	0.0023
			159	50	468.83	0.0026
			160	48	763.14	0.0022
EF	Reservoir Road		132a	77	3687.26	0.0049
			132b	163	108.68	0.0097

Table 4.6 Fracture density values for all outcrop data sets

and 150° measure the spacings of fractures parallel and sub-parallel to the overall fault trend. Therefore the ellipses created for the HSF outcrop data set suggest that fractures parallel to the overall trend of the MTFC are closely spaced and have high densities.

As well as using average fracture spacing as a measure of fracture density for 1-dimensional sampling, fracture density can also be assessed in 2-dimensions by calculating the total number of fractures per unit area, which is directly related to fracture spacing (section 1.7.4.2) (**Table 4.6**). A plot of fracture densities from each locality against distance to HSF is presented in **Figure 4.31**. The highest value of fracture density occurs in the centre of HSF at locality 145 (0.17 fractures per cm^2), which corresponds to the locality with the smallest ellipse presented in **Figure 4.30**. The density values in **Figure 4.31** return to a background level of ~0.001 fractures / cm^2 within a few meters of HSF, suggesting that the zone of dense fracturing at outcrop scale is narrow.

4.2.3.2 VF

A total of 14 photographs of outcrop surfaces from 10 localities were selected to analyse fracture spacing data from the Verran Fault (VF) (**Table 4.1, Figure 4.9, Figure 4.10**). The localities chosen are at various distances north of the Verran Fault plane (VFP), with one locality south of the VFP (locality 140). A gneissose lithology is present at most of these localities, and most photographs used in this study are vertical or sub-vertical outcrop surfaces. Two photographs are of horizontal/sub-horizontal surfaces (localities 49 & 137) and at one locality (48i a) an amphibolitic lithology is present. At three localities (28b/164, 28c & 139) two photographs have been used, each of vertical outcrop surfaces, one perpendicular and one parallel to the main fault trend.

For the two localities where the photographs are of horizontal outcrop surfaces, fracture spacing data was collected by methods a) and b) outlined in section 4.2. For the rest of the photographs of vertical outcrop surfaces, two sets of 1-dimensional line transects were also carried out, a) one set of horizontal transects either perpendicular or parallel to the main fault trend (depending on the orientation of the outcrop surface), and b) one set of vertical transects. Ellipses were created for the horizontal outcrop data sets (localities 49 & 137) to analyse the change in fracture spacing with transect orientation but not created for the vertical outcrop data sets. This is because a fracture map created for a

vertical outcrop surface analyses the dip of the fractures and a fracture map created for a horizontal outcrop surface analyses the strike of the fractures. Horizontal outcrop surfaces are preferred, but limitations are imposed in the field due to the extent of exposure.

Spacing values from the 1-dimensional line transects from each locality are plotted in **Figure 4.32**. Within each graph, the two data sets correspond to the different transect orientations (horizontal or vertical). On most graphs the spacing data sets collected for vertical and horizontal transects plot as straight lines when the x-axis is plotted as a linear scale and the y-axis is plotted as a logarithmic scale, and therefore they are best described by an exponential distribution with a negative slope. This is confirmed when a Kolmogorov-Smirnov test (section 1.8.4.2) is carried out on each of the data sets. There are three data sets that do not appear to fit well to the exponential distribution, these are a) the horizontal transects (130°) from locality 28b/164 photograph 2 (**Figure 4.32b**), b) the horizontal transects (orientated 210°) from locality 133 (**Figure 4.32f**), and c) the horizontal transects (orientated 325°) from locality 139 photograph 2 (**Figure 4.32k**). For the horizontal data sets from localities 28b/164 (photograph 2) and 133, it is possible to fit two best-fit lines though the data sets (on log y-axis, linear x-axis), resulting in two exponent values for one data set.

In some data sets there are data points on the right hand side of the graph that do not fall onto the best fit lines. This is likely to be the result of either the under-representation of wide spacing values due to the limited size of the sample area, or over-representation of wide spacing values due to multi-line sampling (section 1.9.1).

A plot of mean spacing versus standard deviation for each of the localities (and distinguished for different transect orientations) is presented in **Figure 4.33**. As expected for exponential data, there is a good relationship between average spacing and standard deviation. However, two of the three data sets described above that are not best described by a single exponential equation do not show the same relationship.

The co-efficient of variation (Cv) is a measure of the degree of cluster within a data set (section 1.8.5.1) and is plotted in **Figure 4.34** for the HSF outcrop localities (with transect orientations distinguished) against distance. Most of the of Cv values for the VF outcrop data set plot close to Cv = 1, but unlike the HSF outcrop data set, the data from VF plot above and below the Cv = 1 line, so some of the data are clustered, and some are

anti-clustered. There does seem to be some correlation between Cv and distance to the VFP (**Figure 4.34**). The lower values of Cv occur close to the centre of the fault, suggesting that close to the VFP the fracture spacing data is anti-clustered (or regularly spaced). With increasing distance from the VFP the fracture spacing data appears to become clustered (Cv > 1) and then approaches the Cv = 1 line representing a random distribution of fracture spacings at large distances from VFP.

The change in fracture spacing with distance to the VFP can be assessed by plotting the exponents from the spacing graphs illustrated in **Figure 4.32** and **Table 4.5** because the exponent is a measure of the relative abundance of small and large spacings. A low exponent value suggests a low fracture density and corresponds to a shallow slope and a relatively high number of wide fracture spacings; whereas a high exponent value suggests a higher fracture density and corresponds to a steeper slope and a relatively high number of narrow fracture spacings. The change in exponent with distance can be assessed for the 1-dimensional transects orientated both perpendicular and parallel to the overall trend of the fault zone, and for the vertical transects, all of which are likely to measure the spacings of different fracture sets. Plots of exponent versus distance for the three different transect orientations are presented in **Figure 4.35**. (The graphs in **Figure 4.35** also include data collected from the Elvdalen Fault, which will be described in section 4.2.2.3.) The highest exponent values (steepest slopes) for all three transect orientations occur in the centre of VF, suggesting that this is where the closest spaced fracturing and highest fracture density occurs. Out of the three different data sets, the highest values of exponent occur for the transects orientated perpendicular to the overall fault trend, which measure the spacings and density of fault-parallel fractures. The lowest maximum exponent value occurs for the vertical transects, suggesting that sub-horizontal fractures have a relatively low fracture density. It is apparent in **Figure 4.35a** that the exponent from the fracture spacing data from the amphibolitic data set is significantly less than the exponent for the gneissose data set at the same distance for the fault, suggesting that lithology has an affect on fracture spacing. When the data from the three orientations is amalgamated (**Figure 4.35d**) it is apparent that the exponent values are above background level up to 500m away from the VFP, suggesting a wide zone of dense fracturing – wider than that observed for HSF (c.f. section 4.2.3.2, and **Figure 4.28**).

The change in fracture spacing with distance can also be assessed by plotting the average fracture spacing from each transect orientation (**Figure 4.36**). The smallest average spacing values occur at the centre of VF for all three data sets, and the range of spacing values at each locality increases with increasing distance away from the VFP.

The average spacing ellipses from transects measured every 30° across the two horizontal outcrop photographs (localities 49 and 137) are elongate in a NE/SW – NNE/SSW direction (**Figure 4.37**), suggesting that fractures perpendicular to the trend of the VF are relatively less dense than fractures orientated parallel to it. Locality 137 is 28m from the VF, and the ellipse from this locality is considerably smaller than the ellipse from locality 49, suggesting that fracture density increases towards VFP (**Table 4.6**).

As well as using average fracture spacing as a measure of fracture density for 1-dimensional sampling, fracture density can also be assessed in 2-dimensions by calculating the total number of fractures per unit area, which is directly related to fracture spacing (section 1.7.4.2) (**Table 4.6**). A plot of fracture densities from each locality against distance to VF is presented in **Figure 4.38**. The highest value of fracture density occurs in the centre of VF (0.012 fractures per cm^2). It is apparent that the density value from the amphibolitic data set is significantly less than the density value from the gneissose data set at the same distance from VF, suggesting that lithology has an affect on fracture density. The density values in **Figure 4.38** return to a background level of ~0.001 fractures / cm^2 over a distance of 500m from VF, suggesting that the zone of dense fracturing wider than HSF.

4.2.3.3 EF

Two localities were chosen to investigate fracture spacing adjacent to the Elvdalen Fault (**Table 4.1, Figure 4.9, Figure 4.10**), and also to compare this smaller, simpler fault to the data collected from the main structures in the MTFC (VF and HSF). The photographs used are of horizontal outcrop surfaces with a gneissose lithology. Fracture spacing data was collected from the two localities using the methods outlined in section 4.2. Locality 132a is approximately 10m away from the Elvdalen Fault plane and 1926m away from VFP; locality 132b is about 1m away from the EFP and 1936m away from the VFP.

Plots of spacing data from both localities collected along 1-dimensional line transects orientated both parallel (060°) and perpendicular (150°) to the main fault trend are presented in **Figure 4.39**. Within each graph the two data sets are for the two transect orientations. On each graph, the spacing data collected for both 060° and 150° transects plot as a straight line when the x-axis is plotted as a linear scale and the y-axis is plotted as a logarithmic scale, and therefore they are best described by an exponential distribution with a negative slope. This is confirmed when a Kolmogorov-Smirnov test (section 1.8.4.2) is carried out on each of the data sets. For each data set, some data points on the right hand side of the graphs do not fall onto the best fit lines. This is likely to be the result of the under-representation of wide spacing values due to the limited size of the sample area. To confirm that the data sets are best described by an exponential distribution, **Figure 4.40** shows the mean spacing from both transect orientations and both localities plotted against the standard deviation. As expected for exponential data sets, the mean and standard deviation values are very similar.

The coefficient of variation (Cv) for the EF data sets is plotted against distance from VF in **Figure 4.41**. Although there are few data points, the data sets from locality 132a plot close to the Cv = 1 line suggesting a random distribution of fracture spacings, but the data sets from locality 132b plot slightly below the Cv = 1 line, suggesting that close to the EFP the fracture spacing is relatively anti-clustered.

The exponents from the EF spacing graphs are presented on **Figure 4.39** and in **Table 4.5**, and are plotted against distance to VF in **Figure 4.35 a, b & d**. The exponents from locality 132b are higher than those from locality 132a for both transect orientations suggesting that fracture spacings at locality 132b (close to the EFP) are narrower and fracture density is higher due to the occurrence of EF.

The average spacing from both transect orientations from locality 132b (1m from EFP) are illustrated on **Figure 4.36a & c**, plotted against distance from VFP. For both transect orientations, the average spacing is decreased relative to background level.

Ellipses were created for both localities by measuring the average spacing from transects measured every 30° across the horizontal outcrop photographs (**Figure 4.42**). The ellipses can be used to assess both the heterogeneity in fracture spacing and the change in fracture density with distance from EF. The ellipses from both localities are elongate with

the minimum values of average spacing occurring in a NW-SE direction, along transects orientated 120°-150°. The transects in this orientation are likely to measure the spacings of fractures parallel to the overall fault trend, and therefore the data suggest that the density of fault-parallel fractures is highest. As well as the shape of the ellipses, their size can also be used to assess fracture density (**Table 4.6**). The ellipse from locality 132b, which lies 1m from EFP, is considerable smaller than the ellipse from locality 132a, which lies 10m from EFP. This suggests that the density of fracturing increases towards the EFP.

As well as using average fracture spacing as a measure of fracture density for 1-dimensional sampling, fracture density can also be assessed in 2-dimensions by calculating the total number of fractures per unit area, which is directly related to fracture spacing (section 1.7.4.2) (**Table 4.6**). Fracture densities from the two localities close to EF are plotted against distance to VF in **Figure 4.38**. Fracture density at the centre of EF (locality 132b) is increased above the background level to 0.01, but this value is significantly less than the values of density that occur at the centre of VF and HSF.

4.2.3.4 Summary of fracture spacing data from outcrop scale in 2-dimensions

A summary of fracture spacing data from outcrop, measured using 1-dimensional line transects across 2-dimensional photographs from all three faults (HSF, VF and EF), is presented in **Table 4.7**.

Fracture density has been measured for the outcrop data sets in two ways 1) average spacing ellipses, 2) number of fractures per cm^2. A power-law relationship is observed between these two measures of fracture density for the outcrop data set with an exponent value of -0.7344 (**Figure 4.43**).

	Fault		
	HSF	**VF**	**EF**
Outcrop photographs used	10	13	2
Data sets (different transect orientations)	20	22	4
Transect orientations used	1) parallel to main fault trend (060), 2) perpendicular to main fault trend (150)	1) parallel to main fault trend (~060), 2) perpendicular to main fault trend (~150) 3) vertical	1) parallel to main fault trend (060), 2) perpendicular to main fault trend (150)
Best-fitting spacing distribution	20 data sets = exponential with negative slope	19 data sets = exponential with negative slope 2 = exponential with 2 exponents 1 = poor fit to all distributions	4 data sets exponential with negative slope
Relationship between mean spacing and standard deviation	good, similar values	good, similar values for most data sets	good, similar values
Coefficient of variance (measure of clustering)	All data sets close to Cv = 1, but all data sets <1. No relationship between Cv and distance	Most data sets close to Cv = 1, some above some below. Possible correlation with distance, close to VFP Cv<1, medium distance Cv>1, large distance from VFP Cv~1.	Away from EFP Cv~1. Close to EFP Cv<1
Exponential exponents from spacing distribution against distance	Highest in centre of fault for both transect orientations. Max. values for parallel (0.0772) & perpendicular (0.0771) transects very similar. Background level <100m from HSFP.	Highest in centre of fault for all 3 transect orientations. Overall max. for perpendicular transects (0.0774) almost identical to max. from HSF. Lowest max. from vertical transects (0.0293). Background level ~500m from VFP.	Higher than VF background level for both transect orientations. Overall highest (0.0212) from perpendicular transects. Max. values not as high as max. from HSF or VF.
Mean spacing data against distance	Smallest in centre of fault, both transect orientations.	Smallest in centre of fault, all 3 transect orientations.	Decreased relative to VF background levels.
Ellipses (heterogeneity of spacing and density)	8 created. Locality closest to HSFP = smallest ellipse. Most ellipses elongate, minimum values av. spacing along 120/150 transects which measure fractures parallel to foliation + overall fault trend	2 created. Locality closest to VFP = smallest ellipse. Both ellipses elongate, minimum values av. spacing NW/SE orientated transects which measure fractures parallel to foliation + overall fault trend	2 created. Locality closest to EFP = smallest ellipse. Both ellipses elongate, minimum values av. spacing 120/150 transects which measure fractures parallel to foliation + overall fault trend.
Total number of fractures per cm² (fracture density) 'v' distance	Maximum value = 0.17 fractures per cm² in centre of HSF (8m from HSFP). Same locality as smallest ellipse. Density decreases to background level of 0.001 fractures/cm² a few meters from HSF = narrow zone high density.	Maximum value = 0.12 fractures per cm² in centre of VF (28m from VFP). Density decreases to background level of 0.001 fractures/cm² ~500m from VF = wide zone of dense fracturing. Amphibolitic data set has significantly (3x) less dense fracturing than gneissose data set at same distance from VF.	Max. value at EF is 0.01 fractures per cm², which is significantly (10x) higher than background level, but less than the max. values of density associated with VF and HSF.
Relationship between ellipse area and number of fractures per cm²	Good power-law relationship when plotted on logarithmic axes for all outcrop data points. There is some scatter in the data and one anomalous data point (from EF data), all likely to be due to errors involved in measuring the areas of ellipses.		

Table 4.7 Summary of fracture spacing data from outcrop scale measured using 1-dimensional line transects across 2-dimensional photographs

4.2.4 *Thin-section data*

Fracture spacing data measured from 1-dimensional line transects across 2-dimensional thin-sections created from hand specimens, are presented and discussed below to analyse fracture spacing and density at the thin-section (millimetre) scale. Data is presented for the two main faults in the MTFC, VF and HSF.

4.2.4.1 HSF

A total of 7 thin-sections were selected for the analysis of fracture spacing relative to HSF (**Table 4.2, Figure 4.11, Figure 4.12**). The thin-sections chosen are from hand specimens collected at various distances both north and south of the HSFP, close to the localities used for the analysis of fracture parameters at outcrop scale (section 4.2.3.1). All the thin-sections used are orientated and cut horizontally, and are composed of a quartzo-feldspathic (gneissose) lithology. Fracture spacing data were collected by the methods outlined in section 4.2 for all of the sections.

Plots of the spacing data from the 1-dimensional line transects orientated 060° (parallel to the overall fault zone trend) and 150° (perpendicular to the overall fault zone trend) from each thin-section are presented in **Figure 4.44**. Each graph represents a thin-section, and within each graph the two data sets are for the two transect orientations. Each data set plots as a straight line when the x-axis is plotted as a linear scale, and the y-axis is plotted as a logarithmic scale, and therefore the spacing data is best described by an exponential distribution with a negative slope. This is confirmed when a Kolmogorov-Smirnov test (section 1.8.4.2) is carried out on each of the data sets. Some data points on the right hand side of the graphs do not fall onto the best-fit lines. This is likely to be the result of either the under-representation of wide spacing values due to the limited size of the sample area, or over-representation of wide spacing values due to multi-line sampling (section 1.9.1).

A plot of mean versus standard deviation for each of the thin-section data sets is presented in **Figure 4.45**. There is a good correlation between the two parameters, confirming that the data show a good fit to an exponential distribution.

The values of Cv for the thin-sections collected from the HSF plot very close to the Cv = 1 line (maximum value of Cv = 1.19) which corresponds to the mean being equal to the standard deviation, the data sets being best described by an exponential distribution and neither clustered nor anti-clustered (**Figure 4.46**).

The exponents from the spacing graphs in **Figure 4.44** can be plotted and used to assess the change in fracture spacing with distance from HSFP (**Table 4.8**). Graphs of exponent versus distance for all thin-section data sets from HSF are presented in **Figure 4.47**, and are distinguished for the different transect orientations. The maximum exponent value for both transect orientations occurs at the centre of HSF, suggesting that this is where the highest fracture densities occur. However, the zone of high density is very narrow (<10m) in both orientations, marked by the sharp return to background level with increasing distance from the fault. The highest exponent value occurs in the data set collected from transects orientated perpendicular to the overall fault zone trend (150°) which measure the spacings of the fractures parallel to the overall trend, and are therefore the most dense.

The change in spacing around the HSF can also be assessed by plotting the range of spacing values, and the mean value from each section in each transect orientation (**Figure 4.48**). The lowest values of average fracture spacing for each transect orientation occur in the centre of HSF, suggesting that this is the area of highest fracture density, and supporting the exponent data.

Transects were carried out across the thin-section fracture maps every 30° and have been used to create ellipses from the average spacing in each orientation (**Table 4.9**). The ellipses created for the HSF thin-section data sets are presented in **Figure 4.49**, separated into localities north and south of the HSFP. The ellipses from all of the thin-section localities, both north and south of HSFP are elongate with the minimum values of average spacing occurring in a NW-SE direction, along transects orientated 150°. The transects in this orientation are likely to measure the spacings of fractures parallel to the overall fault trend, and therefore the data suggest that at this scale the set of fault-parallel fractures are most closely spaced both north and south of the HSFP. The smallest ellipses

Fault	Locality	Transect orientation	Statistical distribution	Exponent	R^2
HSF	HS3b	060	exponential	0.3818	0.98
	HS3b	150	exponential	0.8033	0.98
	HS13	060	exponential	1.6976	0.995
	HS13	150	exponential	2.1547	0.98
	HS16	060	exponential	0.4994	0.99
	HS16	150	exponential	0.8585	0.98
	HS19	060	exponential	0.4194	0.97
	HS19	150	exponential	0.5977	0.97
	HS21	060	exponential	0.4261	0.99
	HS21	150	exponential	0.5631	0.99
	HS42	060	exponential	0.5496	0.99
	HS42	150	exponential	1.163	0.99
	HS43	060	exponential	0.1862	0.99
	HS43	150	exponential	0.6641	0.98
VF	V99-17	060	exponential	0.5804	0.99
	V99-17	150	exponential	0.4521	0.98
	V99-24	060	exponential	0.5473	0.99
	V99-24	150	exponential	0.9926	0.98
	VM2	060	exponential	0.2699	0.97
	VM2	150	exponential	0.5656	0.97
	VPS2	060	exponential	1.1386	0.99
	VPS2	150	exponential	0.7784	0.99
	VMC7	060	exponential	1.035	0.99
	VMC7	150	power-law	0.797	0.99

Table 4.8 Best-fitting spacing distribution and exponent values from thin-section data sets (HSF VF EF)

Fault	Place		Section number	Total number fractures	Density	
					Area of average spacing ellipse (cm^2)	Total number of fractures per cm^2
VF	Reservoir Road		V99/17	91	0.1526	15.6095
			VM 2	62	0.1998	18.9238
	720 Road		VPS 2	296	0.0343	47.9601
	Fjordside		VMC 7	294	0.0360	28.2312
			V99/24	748	0.0544	25.6614
HSF	Mefjellet	North of HSFP	HS 21	119	0.0935	18.1030
			HS 19	139	0.1170	29.3255
			HS 3b	190	0.1169	30.9805
			HS 16	343	0.0617	44.0257
		South of HSFP	HS 13	964	0.0104	156.0376
			HS 42	91	0.0493	45.7412
			HS 43	89	0.1421	14.4539

Table 4.9 Fracture density values for all thin-section data sets

for both the north and south localities occur closest to the HSFP with the overall smallest ellipse occurring 4m north of the HSFP (**Table 4.9**). The ellipses from 6m south and 8m north of HSFP are similar in size suggesting similar fracture densities. The ellipse size increases with increasing distance from HSFP, suggesting a decrease in fracture density away from HSFP.

As well as using average fracture spacing as a measure of fracture density for 1-dimensional sampling, fracture density can also be assessed in 2-dimensions by calculating the total number of fractures per unit area, which is directly related to fracture spacing (section 1.7.4.2) (**Table 4.9**). A plot of fracture densities from each thin-section against distance to HSF is presented in **Figure 4.50**. The highest value of fracture density occurs in the centre of HSF from thin-section HS13 (156 fractures per cm^2), which corresponds to the thin-section with the smallest ellipse presented in **Figure 4.49**. The density values in **Figure 4.50** return to a background level of ~20 fractures / cm^2 within a few meters of HSF, suggesting that the zone of dense fracturing at thin-section scale is narrow.

4.2.4.2 VF

A total of 5 thin-sections were selected for the analysis of fracture spacing relative to VF (**Table 4.2, Figure 4.11, Figure 4.12**). The thin-sections chosen are from hand specimens collected at various distances north of the VFP, close to the localities used for the analysis of fracture parameters at outcrop scale (section 4.2.3.1). All the thin-sections used are orientated and cut horizontally, and are taken from a quartzo-feldspathic (gneissose) lithology. Fracture spacing data was collected by the methods outlined in section 4.2 for all of the sections.

Plots of the spacing data collected along 1-dimensional line transects orientated 060° (parallel to the overall fault zone trend) and 150° (perpendicular to the overall fault zone trend) from each thin-section are presented in **Figure 4.51**. Each graph represents a thin-section, and within each graph the two data sets are for the two transect orientations. The spacing data sets on the graphs from four out of the five localities (V99-17, V99-24, VM2, VPS2) all plot as a straight line for both transect orientations, when the x-axis is

plotted as a linear scale, and the y-axis is plotted as a logarithmic scale, i.e. an exponential distribution with a negative slope, confirmed by a Kolmogorov-Smirnov test (section 1.8.4.2). The spacing data collected from the thin-section at locality VMC7 (**Figure 4.51e**) do not show the same exponential relationship for both transect orientations. The data from transects orientated 150° fits to a straight line when the x-axis is plotted as a linear scale, and the y-axis is plotted as a logarithmic scale, and is therefore exponentially distributed like the other localities. However the spacing data from transects orientated 060° plot as a straight line when both the x-axis and y-axis are plotted as a logarithmic scale (**Figure 4.51f**). This relationship suggests that the data set of fracture spacings measured along transects orientated 060° from thin-section VMC7 is best described by a power-law distribution. Therefore this spacing data set is not randomly distributed (as is the case for exponentially distributed data), but instead there are relatively more small fracture spacings, and the fractures are clustered. Some data points on the graphs from each locality do not fall onto the best-fit lines. This is likely to be the result of the under-representation of wide spacing values due to the limited size of the sample area.

The mean and standard deviations of data sets that are best described by an exponential distribution should be similar, and this is the case for all but one of the data sets from the VF thin-section data (**Figure 4.52**). The only data point that does not show a good relationship is the transect data orientated 060° from section VMC7, for which the standard deviation value is larger than the mean spacing value. This data set is best described by a power-law distribution and not an exponential distribution; therefore the mean and standard deviation values are not expected to be similar.

The coefficient of variation can also be used to confirm the best-fit statistical distribution of a data set. A data set that is best described by an exponential distribution (i.e. all except one of the thin-section data sets from VF) is randomly distributed, and Cv should be close to 1. A data set that is best described by a power-law distribution is likely to be clustered and have a Cv>1. A plot of Cv versus distance for the thin-section data set from VF is presented in **Figure 4.53**. As expected, all of the data points plot close to the Cv = 1 line, except for the data set of spacing values from locality VMC7 (060° transect orientation), where Cv > 1 because the data is best described by a power-law distribution.

Graphs of exponent versus distance for all thin-section data sets from VF are presented in **Figure 4.54**, and are distinguished for the different transect orientations. The maximum exponent value for both transect orientations across the thin-sections occurs at the centre of VF, suggesting that this is where the closest spaced fracturing, and highest fracture density occurs (**Table 4.8**).

The change in fracturing with distance, as measured by average fracture spacing, is plotted for both each transect orientations in **Figure 4.55**. The smallest average spacing values occur at the centre of the VF for both transect orientations, supporting the observations from the exponent data, that the centre of the fault has the most dense fracturing.

Average spacing was measured along transects carried out every 30° across the thin-section data sets, and used to create ellipses for each locality north of VF (**Figure 4.56**). The ellipses from all 5 thin-section data sets are elongate in shape. Three sections (VM2, V99-24, VMC7) have their minimum average spacing along transects orientated 120°/150°. These transects are likely to measure spacings of fractures parallel to the overall fault zone trend, and therefore at these three localities the shape of the ellipse suggests that the set of fractures parallel to the overall fault trend have the lowest average spacing. The other two localities (V99-17 and VPS2) have their minimum average spacing along the transect orientated 090°. This is explained for thin-section V99-17 because the locality lies at the nose of the large antiform between the two main faults (VF and HSF), where the foliation is orientated N/S instead of parallel to the overall fault trend (060°). Therefore the foliation parallel fractures show the lowest average fracture spacing at locality V99-17, but the foliation is re-orientated due to the fold. Locality VPS2 is also elongate in a N-S direction with the minimum average spacing occurring along the 090° transect. This is explained due to the hand specimen (to make the thin-section) being collected adjacent to a N/S orientated fault. There is a larger than normal proportion of N/S fractures in this data set which are likely to be measured along the 090° transect. The size of the ellipses can also be used to assess the change in density with distance from VFP. The smallest ellipses occur closest to the VFP (VPS2, V99-24 and VMC7), and the largest ellipses occur at large distances from VF (VM2 and V99-17) (**Table 4.9**), suggesting a decrease in fracture density away from VFP.

As well as using average fracture spacing as a measure of fracture density for 1-dimensional sampling, fracture density can also be assessed in 2-dimensions by calculating the total number of fractures per unit area, which is directly related to fracture spacing (section 1.7.4.2) (**Table 4.9**). A plot of fracture densities from each thin-section against distance to VF is presented in **Figure 4.57**. The highest value of fracture density occurs near the centre of VF from thin-section VPS2 (48 fractures per cm^2), which corresponds to one of the thin-sections with the smallest ellipses presented in **Figure 4.52**. The density values in **Figure 4.57** return to a background level of ~20 fractures / cm^2 within 500m away from VF.

4.2.4.3 Summary of fracture spacing data from thin-section scale in 2-dimensions

Fracture spacing data from the thin-section data sets measured using 1-dimensional line transects across 2-dimensional photographs from VF and HSF, is summarised and presented in **Table 4.10**. Fracture density has been measured for the thin-section data sets in two ways: 1) average spacing ellipses (**Table 4.9**) and 2) number of fractures per cm^2. A good power-law relationship is observed between these two measures of fracture density for the thin-section data set when plotted on logarithmic axes (**Figure 4.58**). There is some scatter in the data, which is likely to be due to the errors involved in measuring the area of the ellipses.

4.2.5 *Comparison of fracture spacing data from four data scales in 2-dimensions*

A summary and comparison of spacing data collected using 1-dimensional line transects across 2-dimensional areas for four data scales is presented in **Table 4.11**.

Fracture density has been measured from the four data scales in two ways: 1) average spacing ellipses (**Table 4.3, Table 4.4, Table 4.6, Table 4.9**) and 2) number of fractures per cm^2. A good power-law relationship is observed between these two measures of fracture density on logarithmic axes over approximately 12 orders of magnitude (**Figure 4.59**). There is some scatter in the data, which is likely to be due to the errors involved in measuring the area of the ellipses.

	Fault	
	HSF	**VF**
Total thin sections used	7	5
Data sets (different transect orientations)	14	10
Transect orientations used	1) parallel to main fault trend (060), 2) perpendicular to main fault trend (150)	1) parallel to main fault trend (~060), 2) perpendicular to main fault trend (~150)
Best-fit spacing distribution	14 data sets = exponential with negative slope	9 data sets = exponential with negative slope 1 data set = power-law
Relationship between mean spacing and standard deviation	good, similar values	good, similar values for all data sets except power-law
Coefficient of variance (measure of clustering)	All data sets close to Cv = 1	All data sets close to Cv = 1 except power-law data set where Cv = 1.42 (clustered)
Exponential exponents from spacing distribution against distance	Maximum in centre of fault for both transect orientations. Narrow zone intense fracturing. Overall highest exponent from 150° orientated transects	Highest in centre of fault for both transect orientations
Mean spacing data against distance	Lowest in centre of fault, both transect orientations.	Lowest in centre of fault, both transect orientations.
Ellipses (heterogeneity of spacing and density)	7 created. All ellipses elongate, minimum values av. spacing along 150 transects which measure fractures parallel to overall fault trend + foliation. Localities closest to HSFP = smallest ellipse.	5 created. All ellipses elongate. 3 sections minimum value av. spacing = along 120/150 transects which measure fractures parallel to overall fault trend + foliation. 2 sections minimum value av. spacing = along 090 transect due to a) collection of specimen adjacent to NS fault, and b) re-orientation of foliation. Localities closest to VFP = smallest ellipse.
Total number of fractures per cm² (fracture density) 'v' distance	Maximum value = 156 fractures per cm² in centre of HSF (4m from HSFP). Same locality as smallest ellipse. Density decreases to background level of 20 fractures/cm² a few meters from HSF = narrow zone high density.	Maximum value = 48 fractures per cm² in centre of VF (50m from VFP). Density decreases to background level of 20 fractures/cm² ~500m from VF = wide zone of dense fracturing.
Relationship between ellipse area and number of fractures per cm²	Good power-law relationship when plotted on logarithmic axes for all thin section data points. There is some scatter in the data which is likely to be due to errors involved in measuring the areas of ellipses.	

Table 4.10 Summary of fracture spacing data from thin section scale using 1-dimensional line transects across 2-dimensional photographs

Data set	Landsat™	Air Photograph	Outcrop	Thin section
Data range (max. and min. spacing value measured)	max. 8786m min. 47.75m	max. 1262.9m min. 8.65m	max. 3.7m min. 1mm	max. 16.4mm min. 0.05mm
Size of data set (total number spacing values measured)	422	599	HSF = 748, 10 localities VF = 2250, 14 localities EF = 359, 2 localities TOTAL = 3357	HSF = 1398, 7 sections VF = 1145, 5 sections TOTAL = 2543
Transect orientations	060°, 150°	050°, 140°	060°, 150°, vertical	060°, 150°
Best-fit statistical distribution for spacing values	Exponential with negative slope for both transect orientations	Exponential with negative slope for both transect orientations	All data sets exponential with single negative slope except for 2 data sets that have 2 exponents, and 1 data set that does not fit well to any distribution	All data sets exponential with negative slope except for 1 data set that best fits to a power-law distribution.
Exponent from spacing data (**060°** transects likely to measure fractures perpendicular to fault zone trend + foliation. **150°** transects likely to measure fractures parallel to foliation and overall fault trend)	060° transects - highest exponent adjacent to VF 150° transects - exponent affected by N/S fault + antiform. max 150° exponent > max 060° exponent	050° transects – exponent generally decreases from VF 140° transects – exponent affected by N/S fault max 140° exponent > max 050° exponent	Highest for localities closest to centre of faults. Max. values for VF & HSF very similar. Zone of high exponent values narrower from HSF (<100m) than VF (~500m). Max. exponent from EF < max. exponents from VF & HSF.	Highest for sections closest to centre of VF & HSF. Max. exponents from HSF sections > max. exponents from VF sections.
Ellipse data (area = measure of density)	Elongate ellipse. Highest fracture density (lowest average spacing) occurs along 120° transect = fractures parallel to overall fault trend + foliation.	Elongate ellipse. Highest fracture density (lowest average spacing) occurs along 0° transect = fractures parallel & sub-parallel to overall trend + foliation.	Most ellipses elongate in NW/SE direction with min. mean spacing value along 120/150 transect. Smallest ellipses occur closest to the centre of VF & HSF	All ellipses elongate. Most have minimum mean spacing value along 120/150 transect except 2 sections which are affected by re-orientation of foliation and the occurrence of a NS fault. Smallest ellipses occur closest to centre of VF & HSF.
Total number of fractures per unit area (measure of density)	0.318 per km²	24.3 per km²	Highest for localities closest to centre of faults. Max. values for VF & HSF similar. Zone of high density narrower from HSF (<100m) than VF (~500m). Max. density from EF < max. density from VF & HSF.	Highest for sections closest to centre of VF & HSF. Max. density from HSF sections > max. density from VF section, but HSF locality is closer to the centre of the fault.
Total no. fractures per cm² 'v' area of ellipse (both measure density)	Good power-law relationship (logarithmic axes) over approx. 12 orders of magnitude. Exponent = 1. Scatter is likely to be due to errors involved in calculating the areas of ellipses.			

Table 4.11 Summary of fracture spacing data from all data scales, using 1-D transects across 2-D photographs

4.3 Fracture Length

Fracture trace lengths were measured by hand off the 2-dimensional data sets described in section 4.1. Fracture length measurements provide a direct estimate of fracture intensity, which can be represented by the *total fracture trace length per unit area* for 2-dimensional data (section 1.7.5.2), and will be discussed in the following sections.

4.3.1 *Landsat ™ data set*

The cumulative frequency distribution plot of fracture length measurements from the Landsat™ data set is presented in **Figure 4.60**. The central portion of the length data curve plots as a straight line when both the x-axis and the y-axis are plotted as a logarithmic scale, and therefore the length data is best described by a power-law distribution (section 1.8.2.4). This is confirmed when a Kolmogorov-Smirnov test (section 1.8.4.2) is carried out on the data set. The central segment determines the power-law exponent (slope of the best-fit line). The power-law exponent provides a measure of the relative importance of large and small objects. The larger (steeper) the exponent for a given length population, the more short fractures there are for every long fracture. The exponent value for the fracture length data set collected from the Landsat™ image is shown in the equation on **Figure 4.60** as -1.34.

Some of the data points do not fall onto the best-fit line. On the left hand side of the graph at the lower scale range (below ~1500m), the slope of the data curve is shallow and this is the result of incomplete observation of shorter fractures, known as the truncation effect (section 1.7.5.1 & section 1.8.2.4.5). On the right hand side of the graph at the upper scale range (above ~16000m), the slope of the data curve is steep and this is also the result of sampling as long fractures/faults often extend outside the sample area and their lengths are therefore undersampled. This bias effect is known as censoring (section 1.7.5.1 & section 1.8.2.4.5). Out of a total of 241 fracture length measurements, 189 data

points are used to calculate the best-fit line from the central portion of the curve, which extends over an order of magnitude.

Fracture/fault intensity from the Landsat™ data set can be quantified by calculating the fracture/fault length per unit area (section 1.7.5.2). For this data set, the total fracture/fault length in the sample area is 1078.5km, and the intensity is 0.000014 cm per cm^2 (**Table 4.12**) (centimetres are used as the unit of measurement so the value of intensity can be compared to other data scales).

Data set	Total fracture length in sample (km)	Intensity
		Total fracture length per cm^2
Landsat	1078.5	0.000014
Air photograph	259.5	0.000127

Table 4.12 Fracture intensity values for the Landsat and air photograph data sets

4.3.2 *Air photograph data set*

The cumulative frequency distribution plot of fracture length measurements from the air photograph data set is presented in **Figure 4.61**. The central portion of the length data curve plots as a straight line when both the x-axis and the y-axis are plotted as a logarithmic scale, and therefore the length data is best described by a power-law distribution (section 1.8.2.4). This is confirmed when a Kolmogorov-Smirnov test (section 1.8.4.2) is carried out on the data set. The central segment determines the power-law exponent (slope of the best-fit line). The power-law exponent value for the fracture length data set collected from the air photograph data set is shown in the equation on **Figure 4.61** as -1.62. This value is slightly steeper than the exponent from the Landsat™ data set, suggesting that at the air photograph scale, there are more shorter fractures/faults for every long fracture/fault.

Some of the data points do not fall onto the best-fit line as a result of the truncation effect (below ~ 300m) (section 1.7.5.1 & section 1.8.2.4.5), and censoring (above ~ 1300m)

(section 1.7.5.1 & section 1.8.2.4.5). Out of a total of 499 fracture length measurements, 286 data points are used to calculate the best-fit line from the central portion of the curve, which extends for approximately an order of magnitude.

Fracture/fault intensity from the air photograph data set can be quantified by calculating the fracture/fault length per unit area (section 1.7.5.2). For this data set, the total fracture/fault length in the sample area is 259.5km, and the intensity is 0.000127 cm per cm^2 (**Table 4.12**) (centimetres are used as the unit of measurement so the value of intensity can be compared to other data scales).

4.3.3 *Outcrop data set*

Fracture length data measured from 2-dimensional field photographs is presented and discussed below to analyse fracture length and intensity at the outcrop scale. Data is presented for the two main faults in the MTFC, the VF and HSF, and also for the Elvdalen fault (EF) which is parallel to the main structures, but has a shorter lateral extent and simpler kinematic history.

4.3.3.1 HSF

Fracture length was analysed from outcrop localities by selecting a total of 8 field photographs relative to the HSF. The localities chosen are at various distances both north and south of the HSFP, and are the same as the localities used for spacing analysis except for localities 86 and 117 which are not used for the length analysis (**Table 4.1, Figure 4.9, Figure 4.10**). All of the outcrop photographs are horizontal or sub-horizontal surfaces and exhibit a gneissose lithology. The fracture length values were measured by hand using a ruler and string.

Plots of length values from each outcrop photograph are presented in **Figure 4.62**, where each graph represents a locality, and in some cases there are two graphs for one locality. The graphs in **Figure 4.62** show that the fracture length data collected at outcrop scale from HSF are best described by one of two statistical distributions, or in some cases could be described by either distribution. The length data set shown on the graph for

locality 158 (**Figure 4.62h**) is best described by a power-law distribution because the data plot as a straight line when both the x and y axes are plotted as a logarithmic scale. The data sets for localities 142, 143, 145 and 159 (**Figures 4.62 c, d, g & k** respectively) are best described by an exponential distribution. Two graphs are presented for localities 108, 144 and 160 (**Figure 4.62 a, b, e, f, i, j**). These data sets can be described by either an exponential distribution or a power-law distribution, depending on the combination of axes on which the data is plotted. The distributions for each locality are confirmed when a Kolmogorov-Smirnov test (section 1.8.4.2) is carried out on each of the data sets. There appears to be no systematic change in statistical distribution with distance from the HSFP (**Figure 4.63**).

Some of the localities in **Figure 4.62** have data points that do not lie on the best-fit line. On the left-hand side of the graph, the slope of the curve is shallow and this is the result the truncation effect (section 1.7.5.1 & section 1.8.2.4.5). On the right hand side of the graph, the slope of the data curve is steep and this is the result of censoring (section 1.7.5.1 & section 1.8.2.4.5).

The exponents from the exponential length distribution graphs are a measure of the relative abundance of short and long fractures and can be used to analyse the changes in fracture length around the HSFP (**Table 4.13**). A plot of exponent versus distance for the HSF outcrop data set is presented in **Figure 4.64**. The highest value of exponent (0.0276) occurs in the centre of the fault, which suggests that in this area there are relatively more shorter fractures for every long fracture, and therefore the fracture intensity is highest. Exponential exponent values return to a background level of less than 0.005 a few meters away from the centre of the fault, suggesting that the zone of high intensity is narrow.

The values of power-law exponent from the HSF outcrop data have a narrow range from -0.78 to -1.2 (**Figure 4.65, Table 4.13**), and show no systematic change with distance to the HSFP.

Aside from the type of statistical distributions that can be fitted to data sets from the outcrop localities, the range of length values and average length can be plotted against the perpendicular distance to the HSFP (**Figure 4.66**). As expected, the lowest values of average fracture length occur close to the centre of the fault, along with the narrowest range of fracture length values.

Fault	Locality	Best-fit statistical distribution	Exponent (PL = power-law, E = exponential)	R^2
HSF	108	power-law or exponential	PL - 1.2149 E - 0.0029	0.995 0.99
	142	exponential	E - 0.0017	0.99
	143	exponential	E - 0.0016	0.98
	144	power-law or exponential	PL - 1.0 E - 0.0057	0.98 0.97
	145	exponential	E - 0.0276	0.98
	158	power-law	PL - 0.78	0.98
	159	exponential	E - 0.0036	0.99
	160	power-law or exponential	PL - 0.83 E - 0.0023	0.98 0.98
VF	28a/164 1	power-law	PL - 1.09	0.98
	28a/164 2	either	PL - 1.47 E - 0.0067	0.99 0.99
	28c 1	power-law	PL - 1.45	0.99
	28c 2	power-law	PL - 1.28	0.99
	46	exponential	E - 0.0055	0.995
	133	either	PL - 1.56 E - 0.0024	0.99 0.98
	137	power-law	PL - 1.51	0.997
	138	exponential	E - 0.0049	0.99
	48i a	power-law	PL - 0.99	0.99
	48i g	either	PL - 1.47 E - 0.01	0.98 0.99
	139 2	power-law	PL - 0.87	0.99
	139 1	exponential	E - 0.0128	0.996
	140	power-law	PL - 0.99	0.99
EF	132a	exponential	E - 0.0043	0.98
	132b	exponential	E - 0.0051	0.98

Table 4.13 Best-fitting statistical distributions and exponent values from outcrop data sets adjacent to the HSFP, VFP and EFP.

The intensity of fracturing in each 2-dimensional outcrop data set can be measured by calculating the total fracture length per unit area (cm per cm²) (section 1.7.5.2). The values of intensity can then be plotted against the perpendicular distance to the HSFP to analyse the change in intensity (**Figure 4.67, Table 4.14**). The longest total fracture length occurs in the centre of the fault, which suggests that this is the area of highest fracture intensity, and supports the observations from the exponent values from the exponential data sets. The intensity values return to a background level of approximately 0.1 (cm per cm²) within a few meters of the HSFP, suggesting that the area of high intensity is narrow, again supporting the exponential exponent data

Fault	Place		Locality	Total fracture length in sample (cm)	Intensity Total fracture length per cm²
VF	North of VFP	Reservoir Road	28a/164 (1)	3945.04	0.1627
			28a/164 (2)	4047.63	0.2036
			28c (1)	4216.67	0.1334
			28c (2)	2608.38	0.3000
			49	5810.13	0.0598
			133	5368.43	0.0605
			138	3291.17	0.0875
		720 road & fjordside	46	7268.07	0.2525
			48i a	1363.93	0.1486
			48i g	3615.42	0.3708
			137	2310.08	0.8739
		Verran Fault core	139 (1)	1934.12	0.4005
			139 (2)	1581.67	0.3730
	S of VFP		140	4260.75	0.0357
HSF	S of HSF	Mefjellet	144	1614.40	0.1564
			142	1799.50	0.0672
			143	1526.50	0.0801
	North of HSF	Mefjellet	108	4781.66	0.0948
			145	1157.41	0.9847
			158	1547.88	0.0955
			159	1533.78	0.0795
			160	1944.13	0.0889
EF	Reservoir Road		132a	2229.52	0.1425
			132b	3818.29	0.2291

Table 4.14 Fracture intensity values from outcrop data sets

4.3.3.2 VF

A total of 14 field photographs were selected to analyse fracture length at the outcrop scale relative to the VF. The localities chosen are at various distances north of the VFP, with one locality south of the VFP (locality 140) and are the same as the localities used for spacing analysis (**Table 4.1, Figure 4.9, Figure 4.10**). Most photographs used are vertical or sub-vertical outcrop surfaces, and most of the localities exhibit a gneissose lithology. Two of the photographs are horizontal/sub-horizontal surfaces (localities 49 & 137), and one locality (48ia) comprises an amphibolitic lithology. At three localities (28b/164, 28c & 139) two photographs are used, each of vertical outcrop surfaces, one is perpendicular to the main fault trend and one is parallel to the main fault trend. For the rest of the vertical data sets, the photographs were taken of surfaces parallel to the overall fault zone trend (i.e. foliation surfaces). The fracture length values were measured by hand using a ruler and string.

The length data from each locality and outcrop photograph are plotted in **Figure 4.68**, where each graph represents a locality, and in some cases there is more than one graph for one locality. The graphs in **Figure 4.68** show that the fracture length data collected at outcrop scale from VF can be best described by one of two statistical distributions, or in some cases by either of the two distributions. The length data sets shown on the graphs for 8 localities (140, 28b/164-1, 28c-1, 28c-2, 139-2, 137, 48i-a, 49) (**Figure 4.68 a, b, e, f, h, k, l, o**) are best described by a power-law distribution because the data sets plot as straight lines when both the x and y axes are plotted on a logarithmic scale. The length data sets shown on the graphs for 3 localities (139-1, 46, 138) (**Figure 4.68 g, p, q**) are best described by an exponential distribution as the data plot as straight lines when the x-axis is plotted as a linear scale, and the y-axis is plotted as a logarithmic scale. The remaining 3 localities (133, 28b/164-2, 48i-gn) each have two graphs (**Figure 4.68 c, d, i, j, m, n**) and can be described by either an exponential distribution or a power-law distribution, depending on the combination of axes on which the data is plotted. The distributions for each locality are confirmed when a Kolmogorov-Smirnov test (section 1.8.4.2) is carried out on each of the data sets. There appears to be no systematic change in statistical distribution with distance from the VFP (**Figure 4.69**).

The data sets in **Figure 4.68** have data points that do not lie on the best-fit line. At the lower scale range the slope of the data curve is relatively shallow and this is the result of the truncation effect (section 1.7.5.1 & section 1.8.2.4.5). At the upper scale range the slope of the data curve is relatively steep and this is the result of censoring (section 1.7.5.1 & section 1.8.2.4.5). As described in the previous section for the HSF outcrop data sets, the effects of censoring and truncation on a fracture length population can result in severe degradation of an underlying power-law distribution (section 1.8.3.2), and could explain some of the data sets being described by an exponential distribution. It is difficult to distinguish between censored and truncated power-law length data sets, and those that actually fit to a different distribution (i.e. exponential or lognormal).

The relative abundance of short and long fractures from each data set best described by an exponential distribution can be characterised by the exponent of the best-fit line (**Table 4.13**). A plot of exponent versus distance to the VFP for the outcrop data set is presented in **Figure 4.70**. The highest value of exponent (0.0128) occurs in the centre of the fault, which suggests that in this area there are relatively more shorter fractures for every long fracture, and therefore the fracture intensity is highest. The exponent values appear to decrease over a distance of approximately 500m, to a background level of less than 0.005. The values of power-law exponent from the VF outcrop data range from -0.61 to -1.56 (**Figure 4.71**), and show no systematic change with distance to the VFP.

The range of length values and the average length from each data set can be plotted against the perpendicular distance to the VFP (**Figure 4.72**) to assess the change in fracture length. As expected, the lowest values of average fracture length occur close to the centre of the fault, along with the narrowest range of fracture length values.

Fracture intensity can be measured by calculating the total fracture length per unit area (cm per cm^2) on each 2-dimensional outcrop data set (section 1.7.5.2). The values of intensity can then be plotted against the perpendicular distance to the VFP to analyse the change in intensity (**Figure 4.73, Table 4.14**). The longest total fracture length occurs in the centre of the fault (0.87 cm per cm^2), which suggests that this is the area of highest fracture intensity, and supports the observations from the exponent values from the exponential data sets. The intensity appears to decrease away from the VFP over a distance of approximately 500m, to a background level of approximately 0.1 (cm per

cm^2). It appears that lithology has an effect on fracture intensity, as on **Figure 4.73** the value from the amphibolitic data set (0.15cm per cm^2 at 150m from VFP) falls considerably below the value from the gneissose data point at the equivalent distance (0.37 cm per cm^2).

4.3.3.3 EF

Two localities (132a, 132b) were selected to analyse fracture length adjacent to the Elvdalen Fault. These were the same data sets as were used to analyse fracture spacing in section 4.2.2.3 (**Table 4.1, Figure 4.9, Figure 4.10**). The data sets used are photographs of horizontal outcrop surfaces comprising a gneissose lithology. Locality 132a is approximately 10m away from the Elvdalen Fault plane (EFP) and 1926m away from VFP. Locality 132b is approximately 1m away from EFP and 1936m away from the VFP. Cumulative frequency plots of fracture length from both localities are presented in **Figure 4.74**. In both cases, the data sets fit to straight lines when the x-axis is plotted as a linear scale and the y-axis is plotted as a logarithmic scale, suggesting that the data are best fitted to an exponential distribution with negative slope. This is confirmed by the Kolmogorov-Smirnov test. The values of exponent from the EF outcrop exponential graphs are plotted on **Figure 4.70** along with the VF data, and are presented in **Table 4.13**. The value of the exponent for locality 132b, the closest locality to EF, is higher than locality 132a, suggesting that close to the EFP there are relatively more shorter fractures for every long fracture. The exponent value from 132b is lower than the maximum exponential exponent from both the VF and HSF outcrop data sets.

The range of length values and the average length from both localities are plotted on **Figure 4.72**, against distance from VFP. The range of fracture length values and the average length value from locality 132b are lower than the background level relative to the VF outcrop data set.

The fracture intensity values for each locality, measured by fracture length per unit area, are plotted against distance with the VF outcrop data on **Figure 4.73** (**Table 4.14**). Both values from EF are increased relative to VF background level, suggesting that fracture intensity is increased due to the occurrence of EF.

4.3.3.4 Summary of fracture length from outcrop data set

A number of parameters have been plotted and described in the above sections for outcrop data sets collected adjacent to the HSFP, VFP and EFP. These results are summarised in **Table 4.15**.

There are also a number of plots that can be created for the whole outcrop data set to investigate relationships between length parameters, and to compare the data from the two main faults. These relationships are described below and summarised in **Table 4.15.**

If data sets are best described by an exponential distribution, then a relationship may be expected to exist between the mean values and the exponent values, since the mean is a defining aspect of an exponential distribution (section 1.8.2.3). Values of mean fracture length for data collected at outcrop scale adjacent to the HSFP, VFP and EFP data are plotted against their corresponding exponential exponent values on both logarithmic and linear axes (**Figure 4.75**). A good power-law relationship between these parameters is observed for data collected adjacent to the HSFP and the VFP, with an exponent value of -1.17. High values of exponential length exponents (which indicate steep slopes and relatively more short fractures for every long fracture) correlate with low mean length values and vice versa.

Secondly, the exponents from the exponentially distributed data sets are plotted against the values of fracture intensity (total fracture length per unit area (cm/cm^2) in **Figure 4.76**. A good positive relationship is observed between these two parameters, on linear axes, with high fracture intensities correlating to high exponent values (steep slopes).

Finally in **Figure 4.77**, the values of fracture intensity (total fracture length per unit area (cm/cm2) are plotted against fracture density for each data set from both faults. Fracture density is defined as the total number of fractures per unit area (section 1.7.4.2 and section 4.2) which is dependent on the spacing of the fractures. The data is plotted on both logarithmic and linear axes. A strong power-law relationship between fracture intensity and fracture density is observed for the outcrop data from both the VF and HSF, with an exponent value of 0.55.

	Fault		
	HSF	**VF**	**EF**
Outcrop photographs used	8	13	2
Orientation of data sets	8 horizontal	2 horizontal, 12 vertical (3 perpendicular to fault trend, 9 parallel to fault trend)	2 horizontal
Lithology of data sets	all gneissose	13 gneissose, 1 amphibolite	all gneissose
Best-fitting length distribution	1 data set = exponential 4 data sets = power-law 3 data sets = either power-law or exponential	3 data sets = exponential 8 data sets = power-law 3 data sets = either power-law or exponential	2 data sets = exponential
Exponents from length distribution versus distance	Exponential data – highest exponent (0.0276) at centre of fault. Values return to background level (0.005) within a few meters from HSFP. Power-law data – range of exponents = 0.78 to 1.2.	Exponential data – highest exponent (0.0128) at centre of VF, decreases over distance of ~500m from VFP to background level of ~0.003. Power-law data – range of exponents = 0.61 to 1.93	Exponential exponent at EFP increased above VF background level to 0.0051.
Length range and average length versus distance	Lowest average length & smallest range of length values occurs in centre of HSF.	Lowest average length & smallest range of length values occurs in centre of VF.	Lower average length and smaller range of length values than VF background.
Fracture intensity (total fracture length per unit area (cm/cm^2) versus distance	Highest intensity in centre of HSF (0.98), return to background level (0.1) within few m of HSFP.	Highest intensity in centre of VF (0.87), return to background level (0.1) over distance of ~ 500m from VF. Fracture intensity from amphibolitic data set (0.15) considerably lower than gneissose data set (0.37) at same distance from VF.	Fracture intensity at EF = 0.23, which is above background level for VF.
Exponential exponent versus average length	Strong inverse relationship, plotted on logarithmic axes		
Exponential exponent versus fracture intensity	Strong positive relationship, plotted on linear axes.		
Fracture intensity versus fracture density	Strong positive relationship, plotted on logarithmic axes		

Table 4.15 Summary of fracture length data from outcrop scale

4.3.4 *Thin-section data set*

Fracture length data were measured from thin-sections cut from hand specimens and are presented and discussed below to analyse fracture length and intensity at the thin-section (millimetre) scale. Data sets have been collected adjacent to the two main faults in the MTFC, the VF and the HSF.

4.3.4.1 HSF

A total of 7 thin-sections were selected to analyse fracture lengths adjacent to the HSFP. These were the same data sets that were used to analyse fracture spacing (**Table 4.2, Figure 4.11, Figure 4.12**). The sections chosen are at various distances from HSFP, both north and south. All the thin-sections used are orientated and cut horizontally, and are composed of a quartz-feldspathic (gneissose) lithology. To enable fracture lengths to be measured by hand, the data sets were enlarged (x10), but all values of fracture lengths presented here are plotted as actual measurements.

Cumulative frequency plots of fracture length from each of the thin-sections are presented in **Figure 4.78**. The graphs show that the fracture length data collected at thin-section scale adjacent to the HSFP are best described by either one or two statistical distributions. The length data sets from three of the sections (HS16, HS21, HS42, **Figure 4.78 c, d, k**) are best described by a power-law distribution only. The length data sets from the other four thin-section data sets (HS13, HS19, HS3b, HS43) are each plotted on two graphs. These data sets can be described by either an exponential distribution (**Figure 4.78 a, e, g, i**) or a power-law distribution (**Figure 4.78 b, f, h, j**). There appears to be no systematic change in statistical distribution with distance from HSFP. The distributions for each locality are confirmed when a Kolmogorov-Smirnov test (section 1.8.4.2) is carried out on each of the data sets.

The data sets in **Figure 4.78** have data points that do not lie on the best-fit line. On the left-hand side of the graph, the slope of the data curve is shallow and this is the result of the truncation effect (section 1.7.5.1 & section 1.8.2.4.5). On the right hand side of the

graph, the slope of the data curve is steep and this is the result of censoring (section 1.7.5.1 & section 1.8.2.4.5). The effects of censoring and truncation on a power-law fracture length population can result in severe degradation of an underlying power-law distribution (section 1.8.3.2), and could explain why some of the data sets can also be fitted to an exponential distribution. It is difficult to distinguish between censored and truncated power-law length data sets, and data sets that actually fit to a different distribution.

The exponents from the exponential length distribution graphs (**Table 4.16**) are a measure of the relative abundance of short and long fractures, and are plotted the perpendicular distance to the HSFP in **Figure 4.79**. Although there are few data points on the graph, the highest value of exponent (0.7275) occurs in the centre of the fault, which suggests that in this area there are relatively more shorter fractures for every long fracture, and therefore the fracture intensity is highest.

The exponents from the power-law length distributions are plotted against the perpendicular distance to the HSFP in **Figure 4.80**, and presented in **Table 4.16**. There is a large spread in the exponent values from the thin-section data (0.8 – 1.78), the highest exponent value occurs in the centre of the fault and the values decrease away from the fault. A larger data set is needed to further investigate the best-fitting statistical distributions and exponent values from this thin-section data set.

Aside from using the fitted statistical distribution, the change in fracture length from the thin-section data can be analysed by plotting the range of fracture length values and the average fracture length from each thin-section against the perpendicular distance to the HSFP (**Figure 4.81**). The lowest average length and smallest ranges of length values occur in the centre of the HSF. The average length values appear to return to a background level less than 100m away from the HSFP.

The intensity of fracturing in each 2-dimensional thin-section data set can be measured by calculating the total fracture length per unit area (cm per cm^2) (section 1.7.5.2). The values of intensity can then be plotted against the distance to the HSFP to analyse the change in intensity (**Figure 4.82, Table 4.17**). The highest value of total fracture length, $26cm/cm^2$ occurs in the centre of the fault. This suggests that this is the area of highest fracture intensity, and therefore supports the observations from the exponent values from

Fault	Section number	Statistical distribution	Exponent (PL = power-law, E = exponential)	R^2
HSF	HS3b	power-law or exponential	PL = 1.48 E = 0.412	0.98 0.98
	HS13	power-law or exponential	PL = 1.79 E = 0.773	0.99 0.99
	HS16	power-law	PL = 1.3	0.98
	HS19	power-law or exponential	PL = 1.47 E = 0.573	0.99 0.99
	HS21	power-law	PL = 0.972	0.99
	HS42	power-law	PL = 1.143	0.99
	HS43	power-law or exponential	PL = 0.816 E = 0.221	0.96 0.99
VF	V99-17	power-law or exponential	PL = 1.12 E = 0.273	0.99 0.99
	V99-24	power-law	PL = 1.25	0.98
	VM2	power-law	PL = 1.21	0.99
	VPS2	power-law or exponential	PL = 1.49 E = 0.446	0.98 0.99
	VMC7	power-law	PL = 0.98	0.996

Table 4.16 Best-fitting statistical distributions and exponent values for all thin section fracture length data sets

Fault	Place		Section number	Total fracture length in sample (cm)	Intensity Total fracture length per cm^2
VF	Reservoir Road		V99/17	40.21	6.8973
			VM 2	18.17	5.5459
	720 Road		VPS 2	88.06	14.2673
	Fjordside		VMC 7	126.37	12.1341
			V99/24	333.62	11.4454
HSF	Mefjellet	North of HSFP	HS 21	47.44	7.2169
			HS 19	34.64	7.3071
			HS 3b	56.11	9.1490
			HS 16	79.31	10.1798
		South of HSFP	HS 13	161.98	26.2180
			HS 42	82.53	10.9105
			HS 43	42.25	6.8607

Table 4.17 Fracture intensity values from thin section data sets

the exponential data sets. The intensity values return to a background level of approximately 7cm/cm² within a few meters of the HSFP, suggesting that the area of high intensity is narrow.

4.3.4.2 VF

A total of 5 thin-sections were selected for the analysis of fracture length adjacent to the VFP. These were the same data sets that were used to analyse fracture spacing (**Table 4.2, Figure 4.11, Figure 4.12**). The sections chosen are at various distances north of VF. All the thin-sections used are orientated and cut horizontally, and are composed of a quartz-feldspathic (gneissose) lithology. To enable fracture lengths to be measured by hand, the data sets were enlarged (x10), but all values of fracture lengths presented here are plotted as actual measurements.

Plots of fracture length versus cumulative frequency for each of the thin-section data sets are presented in **Figure 4.83**. Out of the 5 data sets, 3 are best fitted to a power-law distribution only (VM2, VMC7, V99-24, **Figure 4.83 d, g, c**). The remaining data sets (V99-17, VPS2) can be best described by either a power-law distribution or an exponential distribution, depending on the axes on which the data is plotted (**Figure 4.83 a, b, e, f**). There appears to be no systematic change in statistical distribution with distance from the VFP. The distributions for each locality are confirmed when a Kolmogorov-Smirnov test (section 1.8.4.2) is carried out on each of the data sets.

In all of the graphs in **Figure 4.83** there are some data points that do not fall onto the best fit line. This is due to censoring and truncation of the length data during sampling (section 1.7.5.1 & section 1.8.2.4.5). The effects of censoring and truncation on a power-law fracture length population can result in severe degradation of an underlying power-law distribution (section 1.8.3.2), and could explain why some of the data sets can also be fitted to an exponential distribution.

The exponent values from the statistical distributions are presented in **Table 4.16**. There are only two data sets that can be best described by an exponential distribution, which is insufficient for graphical representation. However, the highest value of exponent occurs from the thin-section that is closest to the VFP, suggesting that there are relatively more

shorter fractures near the centre of the VF, and a higher fracture intensity. The power-law exponents from the 5 the VF thin-section data sets are plotted against the perpendicular distance to the VFP in **Figure 4.84**. The exponent values range from -0.98 to -1.46, with both the highest and lowest exponent values occurring close to the centre of the VF.

The change in fracture length may be assessed by plotting the range of length values and the average length from each thin-section data set against distance to the VFP (**Figure 4.85**). There appears to be little change in the average length with distance from the VFP, although the range of values appears highest close to VF. This is possibly because the thin-sections closest to the VF contain infilled fractures (veins) that are laterally continuous.

The intensity of fracturing in each thin-section - measured by the total fracture length (cm) per unit area (cm^2) - is plotted against distance in **Figure 4.86** (**Table 4.17**). Although there are few data points, the maximum values occur in the centre of the fault (14.3 cm/cm^2), and decrease to a background level of approximately $6cm/cm^2$.

4.3.4.3 Summary of fracture length from thin-section data set

A number of parameters have been plotted and described in the above section for thin-section sets from the HSF and the VF. These results are summarised in **Table 4.18**.

Plots can also be created for the whole thin-section data set to investigate relationships between length parameters, and to compare the data from the two main faults. These relationships are described below and also summarised in **Table 4.18**.

In defining a data set that is best described by an exponential distribution, the mean value is used, and therefore a good relationship is expected between the mean fracture length values from the thin-section data set, and the corresponding exponents from exponentially distributed data sets (section 1.8.2.3) (**Figure 4.87**). A strong inverse relationship between these parameters is observed when the data are plotted on linear axes, with high exponent values correlate with low mean spacing and vice versa.

Secondly, fracture intensity (total fracture length (cm) per cm2) can be plotted against the exponents from the exponentially distributed data sets (**Figure 4.88**). Although there are few data points, a good relationship between these parameters is observed on linear axes,

	Fault	
	HSF	**VF**
Thin sections used	7	5
Orientation of data sets	all cut horizontal	all cut horizontal
Lithology of data sets	all gneissose	all gneissose
Best-fitting length distribution	3 data sets = power-law 4 data sets = either power-law or exponential	3 data sets = power-law 2 data sets = either power-law or exponential
Exponents from length distribution versus distance	Exponential data – highest exponent (0.7275) at centre of fault. Power-law data – range of exponents = 0.8 to 1.78.	Exponential data – only 2 data points, but highest exponent (0.446) occurs closest to VF Power-law data – range of exponents = 0.98 to 1.46
Length range and average length versus distance	Lowest average length & smallest range of length values occurs in centre of HSF. Average length returns to background level less than 100m from HSFP	Little change in average length, slightly higher values occur close to fault probably due to presence of laterally continuous veins
Fracture intensity (total fracture length per unit area (cm/cm^2) versus distance	Highest intensity in centre of HSF (26), return to background level (7) within few m of HSFP.	Highest intensity in centre of VF (14), decreases to background level (6)
Exponential exponent versus average length	Strong inverse relationship, plotted on linear axes.	
Exponential exponent versus fracture intensity	Good positive relationship, one anomalous data point (HS19), where the exponential exponent is anomalously high for the distance from HSF	
Fracture intensity versus fracture density	Good positive relationship. Two data points (VMC7, V99-24) have slightly lower fracture densities for their corresponding intensities, this is due to the sections containing laterally extensive veins.	

Table 4.18 Summary of fracture length data from thin section scale

with high fracture intensities correlating to high exponent values. There is one anomalous data point on the graph, HS19, which has a higher exponent value than would be expected for the corresponding fracture intensity.

Finally the values of fracture density (total number of fractures per unit area) from each data set (section 1.7.4.2 and section 4.2) can be plotted against fracture intensity (total fracture length per unit area) (**Figure 4.89**). A good power-law relationship between fracture intensity and fracture density is observed for the thin-section data sets collected adjacent to the VFP and HSFP, with an exponent value of 0.6. Two data points fall slightly below the rest of the values (VMC7 and V99-24). These data sets have a low fracture density for their corresponding intensity values and are the same data points that have anomalously high average length values close to VF. These two thin-sections contain laterally continuous veins, which would explain the high intensity value but a relatively low density value.

4.3.5 *Comparison of fracture length data from four data scales*

A summary and comparison of length values collected from 2-dimensional areas for four data scales is presented in **Table 4.19**.

A number of plots can be created for the four data scales, to investigate relationships between length parameters and to compare the data from the two main faults over a large range of magnitudes. These relationships are described below and also summarised in **Table 4.19**.

The exponent values from the length data sets that are exponentially distributed (thin-section and outcrop only) can be plotted against the average length values (**Figure 4.90**). A good relationship between these parameters is expected, as the mean value is a defining aspect of an exponential distribution (section 1.8.2.3). A strong inverse power-law relationship between these parameters is observed over 3 orders of magnitude by extrapolating the relationship between the data scales. The exponent value of the relationship is -1.0165.

	Data set			
	Landsat™	**Air Photograph**	**Outcrop**	**Thin section**
Data range (max. and min. length value measured)	max. 56918m min. 429.75m	max. 4947.8m min. 8.65m	max. 3919.5mm min. 5.7mm	max. 16.4mm min. 0.05mm
Size of data set (total number length values measured)	241	499	3094	3681
Data set orientations	horizontal	horizontal	horizontal & vertical	horizontal
Best-fit statistical distribution for length values	Power-law	Power-law	Data sets are either a) power-law only b) exponential only c) power-law or exponential	Data sets are either a) power-law only b) power-law or exponential
Exponents from length data	1.34	1.62	**Exponential exponent** - highest for localities closest to centre of faults. Zone of high exponent values narrower from HSF (<100m) than VF (~500m). Max. exponents from HSF localities > max. exponents from VF localities. **Power-law data** – range of exponents = 0.61 – 1.93	**Exponential exponent** - highest for sections closest to centre of fault. Max. exponents from HSF sections > max. exponents from VF sections. **Power-law data** – range of exponents = 0.8 – 1.78
Exponential exponent 'v' average length	n/a		Strong inverse **power-law** relationship between these parameters using all outcrop & thin section data points that are exponentially distributed. Exponent = 1.0165	
Exponential exponent 'v' Intensity (cm/cm2)	n/a		Strong positive **power-law** relationship between these parameters using all outcrop & thin section data points that are exponentially distributed. Exponent = 1.0401	
Length 'v' cumulative frequency	A **power-law** best fit line can be extrapolated between the four data scales, suggesting that fracture length is scale invariant over 8 orders of magnitude (exponent = 1.95). However, there are discrepancies between the exponent for the amalgamated data and the power-law exponents from the individual data scales.			
Intensity 'v' density	Strong positive **power-law** relationship between parameters over ~12 orders of magnitude. Exponent = 0.4875			
Intensity 'v' scale	Strong inverse **power-law** relationship between parameters over ~6 orders of magnitude. Exponent = 0.9802			
Modal length 'v' scale	Strong positive **power-law** relationship between parameters over ~6 orders of magnitude. Exponent = 1.0313			
Modal length 'v' box size	Strong positive **power-law** relationship between parameters over ~6 orders of magnitude. Exponent = 1.0229			

Table 4.19 Summary and comparison of fracture length data from four data scales

The values of fracture intensity from each locality (total fracture length per cm^2), can be plotted against the exponent values from the length data sets that are exponentially distributed (thin-section and outcrop only) (**Figure 4.91**). A strong positive power-law relationship is observed between the two parameters on logarithmic axes, which is extrapolated between the data scales. The relationship extends over 3 orders of magnitude, and has an exponent value of 1.0401.

Using data from all four scales, the values of fracture intensity from each data set can be plotted against the values of fracture density (total number of fractures per cm^2) (**Figure 4.92**). A strong positive relationship is observed between the parameters on logarithmic axes. By extrapolating between data scales, the relationship extends over approximately 12 orders of magnitude, and suggests that the parameters are scale invariant over this wide range of scales. The exponent for the power-law relationship is 0.4875.

It has been shown in the previous sections that the data sets of length values from thin-sections and outcrop localities can be best described by either an exponential distribution or a power-law distribution, whereas the data sets from both the Landsat™ and air photograph data sets are best described by a power-law distribution only. A power-law data set is said to be scale-invariant (section 1.8.2.4), and therefore the central portion of the curve can be extrapolated to predict the frequency of data points above and below the sampling limits. A plot of cumulative frequency against fracture length for all four data scales is presented in **Figure 4.93**. For each data scale, the y-axis (cumulative frequency) is normalised by dividing the frequency values by the area of the data set. The x and y axes are plotted on logarithmic scales due to the large range of data values present. The data have been plotted in three ways:

a) Firstly, fracture length values from all thin-section data sets and outcrop localities are plotted with the Landsat™ and air photograph data sets. In this case, as well as the data sets that are best described by a power-law distribution only, the data sets from thin-section and outcrop scale that can be best described by an exponential distribution are included in the plot, as are the data sets that can be described by either a power-law distribution or an exponential distribution (**Figure 4.93 a**).

b) Secondly, values of fracture length from Landsat™ and air photograph data sets are plotted with thin-section and outcrop data sets that are best described by a power-law

c) distribution, and the data sets that can be described by either a power-law distribution or an exponential distribution (**Figure 4.93 b**).

d) Thirdly, the data sets from outcrop localities and thin-sections that are best described by a power-law distribution only are plotted with the data sets from Landsat™ and air photograph scales (**Figure 4.93 c**).

In each plot only part of each data set is used to construct the best-fit line through the data scales (45.6%, 34.9%, 42.8%, respectively for **Figures 4.93 a, b, c**). The individual data sets all show a shallowing at the lower scale range and a steepening at the upper scale range due to truncation and censoring respectively (section 1.7.5.1 & section 1.8.2.4.5). In each plot, an inverse power-law relationship is observed, with the best fitting line extending over approximately 8 orders of magnitude. The power-law exponent from each of the plots are almost identical (-1.9448, -1.9483, -1.9486 respectively for **Figures 4.93 a, b, c**).

The exponent from all four data scales is close to 2, which has been explained in the literature in two ways (section 1.8.2.4.7). Yielding et al (1996) suggest that if the exponent from the combined data set is equal to 2, then it reflects the dimension of the sampling domain and does not reflect the overall length population (the fracture lengths were measured from 2-dimensional fracture maps). However, Odling (1997) suggests that a slope of 2 on a cumulative frequency plot indicates strict self-similarity and scale invariance.

The most accurate plot in **Figure 4.93** is assumed to be **(c)** for two reasons: 1) thin-section and outcrop data sets that are best-fitted to only a power-law distribution are used, 2) the best-fit line uses the highest percentage of total data values (45.6%). Using this plot, the power-law exponents from the individual data scales were calculated to compare to the overall power-law exponent of -1.9486 (**Figure 4.94**). For each individual data set the power-law exponent is less than the exponent for the best-fit line extrapolated between all data scales. The most significant difference occurs at the outcrop scale where the exponent is 0.9488. It is therefore possible that the data set of fracture length values

collected from the More-Trondelag Fault Complex (MTFC) is not scale invariant, but instead has a different power-law relationship at different data scales.

A scale invariant relationship extrapolated between scales is potentially a powerful tool in predicting the numbers of fractures with certain lengths at scales where no data is available. As well as extrapolating the power-law exponents, scale invariance and self-similarity can be tested in other ways (section 1.8.2.4.8).

Firstly, the modal length value from each power-law data set (normalised by dividing by the sample area) can be plotted against the scale of observation. Using data from all four data scales (**Figure 4.95 a**) a power-law relationship is observed between the parameters, with an exponent value of -0.9354. However, the scales of the thin-section data sets are all identical (0.1) and this may cause a distortion in the relationship. The graph is re-plotted in **Figure 4.95 b** without the thin-section data set. Again a strong power-law relationship is observed, with an exponent value of -1.0711 extending over 5 orders of magnitude.

Secondly, a strong positive power-law relationship is also observed if the modal length (normalised by dividing by sample area) is plotted against box size which is defined as the square root of the map area (**Figure 4.95 c**). The relationship extends over approximately 6 orders of magnitude with an exponent of -0.9613.

Thirdly, a plot of fracture intensity (fracture length per unit area, cm/cm^2) versus data scale shows a strong inverse power-law relationship using data from all scales (**Figure 4.95 d**). Here the relationship extends over 6 orders of magnitude, with an exponent value of -0.9802. For strictly self-similar/scale-invariant systems, the normalised modal length values and normalised intensity values should be constant with respect to scale, so the exponents on the graphs in **Figure 4.95** should be 1.

The exponents on the graphs in **Figure 4.95** from the fracture length data from the MTFC are all very close to 1, suggesting that the system is self-similar and scale-invariant over the range of scales presented.

4.4 Connectivity

Fracture connectivity (section 1.7.8) within 2-dimensional sample areas from four data scales has been assessed and will be described in the following sections.

Connectivity can be measured in two ways (section 1.7.8.4),

a) calculating parameters *within a cluster* (a group of interconnected fractures where the interconnections are referred to as nodes) (section 1.7.8.3)
b) *within a unit area* (cm^2).

4.4.1 *Landsat™ data set*

The connectivity of the fractures/faults observed on the Landsat™ image (**Figure 4.1** and **Figure 4.2**) have been assessed and the data is presented in **Table 4.20**. Out of a total of 241 fractures/faults observed, the majority (94%) are incorporated into a large cluster that touches all four sides of the rectangular sample area, with a total of 415 nodes. This large cluster that intersects all of the sample boundaries is known as a percolating cluster, and therefore for the Landsat™ data set the percolation threshold is reached ($p_c = 1$) (section 1.7.8.3). Only 6 unconnected fractures are present (single clusters), along with 3 small clusters. For a fracture data set to be considered well connected, it is suggested that 75% of the total fracture length in the sample area must contribute to the percolating cluster (section 1.7.8.4.5). For the Landsat™ data set the total fracture length that contributes to the percolating cluster is 95.9%. The connectivity of the Landsat™ data can also be expressed as the number of fracture interconnections (nodes) per unit area, which is equal to 0.556 nodes per km^2.

Data scale	Fault	Locality	Distance to fault (m)	Total number fractures	Percolation threshold (p_c)	number of nodes per cm^2	clusters								
							single	small (<15 nodes)				large (> 15 nodes)			
							no. of fractures & % total	number of clusters	no. of fractures & % total	number of nodes	total cluster length (mm)	number of clusters	no. of fractures & % total	number of nodes	total cluster length (mm)
Landsat				241	1	0.556 per km^2	6 (2.5%)	3	2,2,5 (3.7%)	1,1,4	4775, 3629, 22156 metres	1	226 (93.8%)	415	1034217 metres
Air Photo				499	1	43.41 per km^2	15 (3%)	4	2,2,2,2 (1.6%)	1,1,1,1	597,1090, 1868, 1047 metres	1	476 (95.4%)	876	249120 metres
Outcrop	HSF	108	125	93	1	0.00270	5 (5.3%)	1	3 (3.2%)	2	747	1	86 (91.5%)	134	45799
		142	375	31	1	0.00153	2 (6.5%)	0	-	-	-	1	29 (93.5%)	41	17527
		143	81	29	1	0.00173	3 (10%)	0	-	-	-	1	27 (90%)	33	14862
		144	12	84	1	0.00726	9 (10.7%)	5	2,2,2,4,3 (15.5%)	1,1,1,3,2	193, 30, 203, 700, 419	1	62 (73.8%)	67	13598
		145	8	199	1	0.2535	9 (4.6%)	3	2, 2, 3 (4%)	1, 2, 2	55, 91, 79	1	181 (91.4%)	293	11144
		158	100	38	1	0.00259	4 (10.5%)	2	1, 2 (13.2%)	3, 2	551, 407	1	29 (76.3%)	39	14149
		159	250	50	1	0.00249	7 (14%)	5	2,3,2,2,5 (28%)	1,2,1,1,4	573, 291	1	29 (58%)	39	11826
		160	215	48	1	0.00238	5 (10.4%)	1	3 (6.3%)	4	1299	1	40 (83.3%)	48	17301
	VF	28a/164-1	475	175	0.75	0.00928	15 (8.6%)	0	-	-	-	2	33, 127 (91.4%)	40, 185	8450 28907
		28a/164-2	475	215	1	0.00850	4 (1.9%)	2	4, 2 (2.8%)	3, 1	557, 269	1	205 (95.3%)	283	39003
		28c-1	600	154	1	0.00579	10 (6.5%)	3	2, 2, 2 (3.9%)	1, 1, 1	442, 331, 418	1	138 (89.6%)	180	39350
		28c-2	600	175	1	0.02818	2 (1.1%)	1	3 (1.7%)	2	147	1	170 (97.2%)	243	25730
		46	40	323	1	0.0176	2 (0.6%)	1	2 (0.6%)	1	215	1	319 (98.2%)	506	72357
		133	1300	105	1	0.00130	6 (5.7%)	1	2 (1.9%)	1	1150	2	48, 49 (92.4%)	53, 61	21910, 27888
		137	28	318	1	0.2047	2 (0.6%)	0	-	-	-	1	316 (99.4%)	541	23019
		138	2250	112	0.75	0.00274	19 (17%)	8	3,3,2,4,2, 2,5,3, 12 (47.3%)	2,2,1,3, 1,4,2, 12	510, 852, 336, 871, 510, 729, 633, 5635	1	59 (52.7%)	76	20041
		48i a	150	72	1	0.0109	2 (2.8%)	1	3 (4.2%)	2	293	1	67 (93%)	98	13238
		48i gn	150	259	1	0.0409	2 (0.8%)	0	-	-	-	1	257 (99.2%)	399	36073
		139-1	20	180	1	0.04473	8 (4.4%)	1	11 (6.1%)	12	1108	1	161 (89.5%)	204	17559
		139-2	20	85	1	0.02924	6 (7%)	0	-	-	-	1	79 (93%)	124	14629
		140	800	47	0.75	0.000435	5 (10.6%)	1	2 (4.3%)	1	897	1	40 (85.1%)	51	37295
	EF	132a	1926 (to VF)	77	1	0.00582	5 (6.5%)	1	9 (11.7%)	9	2568	1	63 (81.2%)	82	18878
		132b	1936 (to VF)	163	1	0.01386	11 (6.8%)	2	2, 3 (3%)	1, 2	138, 212	1	147 (90.2%)	228	36453

Table 4.20 Connectivity data from the Landsat™, air photograph and outcrop data sets, MTFC.

4.4.2 *Air photograph data set*

The air photograph data set interpretation (**Figure 4.7** and **Figure 4.8**) has been used to analyse the connectivity of fractures/faults over a portion of the MTFC, and the data is presented in **Table 4.20**. A total of 499 fractures/faults are observed, of which 95.4% are incorporated into a large cluster with 886 nodes, which touches all four sides of the rectangular sample area. This cluster is therefore the percolating cluster, and for this data set, the percolation threshold is reached (p_c = 1) (section 1.7.8.3). Within the 2-dimensional sample area there are also 15 unconnected fractures (single clusters) and 4 small clusters. The total fracture length that contributes to the percolating cluster for the air photograph data set is 96.0%. The connectivity of the air photograph data set can also be expressed as the number of fracture interconnections (nodes) per unit area, which is equal to 43.41 nodes per km².

4.4.3 *Outcrop data set*

The connectivity of fractures measured from 2-dimensional field photographs is presented and discussed. Data is presented for the two main faults in the MTFC, the Verran Fault (VF) and the Hitra-Snåsa Fault (HSF), and also for the Elvdalen fault (EF) which is parallel to the main structures but has a shorter lateral extent and simpler kinematic history.

4.4.3.1 HSF

A total of 8 field photographs were selected to analyse fracture connectivity relative to the Hitra-Snåsa Fault Plane (HSFP) at outcrop scale (**Table 4.1, Figure 4.9, Figure 4.10**). The selected data sets lie both north and south of HSFP and are the same localities used for the analysis of fracture spacing and length (section 4.3.3.1). All of the data sets

are photographs of horizontal or sub-horizontal surfaces and exhibit a gneissose lithology.

The connected fractures were recognised for each data set and divided into single, small and large clusters (section 1.7.8.3) depending on the number of nodes within the cluster. All of the outcrop data sets collected adjacent to the HSFP contain a large cluster which has more than 15 nodes. At each locality the large cluster is referred to as the percolating cluster because it intersects all four sides of the rectangular sample area and therefore the percolation threshold is reached for each data set ($p_c = 1$) (section 1.7.8.3.1) (**Table 4.20**). For the HSF outcrop data, the percentage of total fracture length from each data set that is contained within the percolating cluster is greater then 90% for most data sets, and greater than 75% for all data sets (**Table 4.21**), and may therefore be regarded as well connected (section 1.7.8.4.5).

Fault	locality	distance (m)	total fracture length (mm)	*pc* length (mm)	%
Verran Fault	28a/164 2	475	40476.32	39003.03	96.36
	28c 1	600	42166.71	39350.33	93.32
	28c 2	600	26083.79	25730.07	98.64
	49	1650	58101.32	55536.33	95.59
	46	40	72680.71	72357.05	99.55
	48i gneiss	150	36154.2	36073.15	99.78
	48i amphibolite	150	13639.3125	13237.69	97.06
	137	28	23100.83	23018.71	99.64
	139 1	20	19341.2	17599.23	90.99
	139 2	20	15816.67	14629.33	92.49
Elvdalen Fault	132a	1926	22295.16	18878.27	84.67
	132b	1936	38182.85	36452.99	95.47
Hitra-Snasa Fault	108	-125	47816.63158	45798.74	95.78
	142	375	17995	17526.61	97.40
	143	81	15265.03125	14860.78	97.35
	144	12	16144.04762	13598.19	84.23
	145	-8	11574.05	11143.61	96.28
	158	-100	15478.75	14148.61	91.40
	159	-250	15337.80303	11825.68	77.10
	160	-215	19441.29032	17301.37	88.99

Table 4.21 Percolating cluster data for outcrop data sets within the MTFC

The relative percentages of both the number of fractures and the fracture length contained in single, small and large clusters within each data set can be plotted against distance to the HSFP (**Figure 4.96, Figure 4.97**) (**Table 4.20**). There appears to be no systematic change in the percentage of total number of fractures within the different cluster sizes with distance to the HSFP (**Figure 4.96**). However, **Figure 4.97** illustrates that near the centre of the HSF the percentage of fracture length within large clusters is highest. With increasing distance from HSF on the northern side of the fault, the proportion of fracture length contained within small and single clusters increases suggesting that overall connectivity decreases away from the HSFP. It is likely that the percentage of fracture length composed of the large cluster in the data set collected 12m south of HSF is higher than the figure presented in **Figure 4.97** due to poor resolution, meaning that the data has been interpreted as a large cluster and a series of small clusters instead of a single large cluster.

For each cluster within each data set, the total number of fractures, total number of nodes and total cluster lengths (normalised for sample area) can be plotted against the perpendicular distance to the HSFP to analyse the change in connectivity around the fault (**Figure 4.98, Figure 4.99, Figure 4.100**). In all of the plots, the maximum value of fractures (181) and nodes (293) per cluster and total cluster length (0.95cm/cm^2) occurs at locality 145 close to the centre of HSF (8m from HSFP). The values then decrease away from HSF over a distance of approximately 100m to background levels of ~30 fractures per cluster, ~40 nodes per cluster and a total cluster length of <0.1cm/cm^2. The data therefore suggests that maximum fracture cluster connectivity occurs in the centre of HSF, and that the zone of high connectivity is less than 100m wide.

As well as dividing the fractures into clusters to analyse connectivity, the total number of nodes per unit area can be calculated for each data set and plotted against the perpendicular distance to HSF to analyse connectivity (**Figure 4.101**). The maximum number of nodes per cm^2 for the HSF outcrop data set is 0.25 and occurs close to the centre of HSF (8m from HSFP). The values decrease within 100m from HSFP to a background level of approximately 0.002 nodes per cm^2. This data therefore suggests that maximum fracture connectivity measured per 1 cm^2 area occurs in the centre of the HSF, which is in agreement with the observations from connectivity within clusters.

4.4.3.2 VF

Fracture connectivity has been analysed adjacent to the Verran Fault Plane (VFP) at outcrop scale by selecting a total of 13 field photographs (**Table 4.1, Figure 4.9, Figure 4.10**). The localities are chosen at various distances north of the VFP, with one locality south of the VFP (locality 140) and are the same data sets that have been used to analyse fracture spacing (section 4.2.2.2) and length (section 4.3.3.2).

For each of the outcrop data sets, the connected fractures were recognised and divided into single, small and large clusters depending on the number of nodes within the cluster (section 1.7.8.3). All of the outcrop data sets from VF contain at least one large cluster which has more than 15 nodes. Localities 28b/164-1 and 133 both have two large clusters within the sample area (**Table 4.20**). At the majority of the localities the large cluster is referred to as the percolating cluster because it intersects all four sides of the rectangular sample area and therefore the percolation threshold is reached ($p_c = 1$) (section 1.7.8.3.1). However, for four of the data sets (localities 28b/164-1, 133, 138, 140) the largest cluster only intersects with three sides of the rectangular sample area and therefore these data sets are below the percolation threshold ($p_c = 0.75$) (**Table 4.20**).

In the outcrop data set from VF, the percentage of total fracture length that is contained within the percolating cluster is greater then 90% for all data sets (**Table 4.21**) and therefore all of the data sets may be considered well-connected (section 1.7.8.4.5).

The relative percentages of both the number of fractures and the fracture length contained in single, small and large clusters within each data set can be plotted against perpendicular distance to VF for the data sets that are parallel to the overall fault trend (**Figure 4.102, Figure 4.103**) (**Table 4.20**). For both plots, the data north of VF illustrate a systematic change with distance. The percentage of total number of fractures and the percentage of total fracture length contained within large clusters decreases away from VF, and the proportion of fractures and fracture length contained within small and single fractures increases away from VF. This suggests that connectivity decreases away from VFP. However, the locality closest to VF is anomalous in that it has a higher proportion of fractures contained within small clusters. This is possibly the result of poor data resolution; i.e. the data has been interpreted as a series of small clusters and a large cluster instead of a single large cluster.

Within each data set, the total number of fractures and total number of nodes per cluster and the total cluster lengths (normalised for sample area) can be plotted against the perpendicular distance to VF to analyse the change in connectivity around the fault (**Figure 4.104, Figure 4.105, Figure 4.106**). In all of the plots, the maximum value of nodes (541) and fractures (349) per cluster and total cluster length (0.87cm/cm^2) all occur close to the centre of VF. The values then decrease away from VF over a distance of approximately 500m to a background levels of ~80 nodes per cluster, ~60 fractures per cluster, and a total cluster length of <0.1 cm/cm^2. The data therefore suggests that maximum fracture cluster connectivity occurs near to the centre of VF, and that the zone of high connectivity is approximately 500m wide.

As well as dividing the fractures into clusters to analyse connectivity, the total number of nodes per unit area can be calculated for each data set and plotted against the perpendicular distance to VF to analyse connectivity (**Figure 4.107**). The maximum value of number of nodes per cm^2 for the VF outcrop data set is 0.2 and occurs close to the centre of VF (20m from VFP). The values decrease over approximately 500m to a background level of 0.01 nodes per cm^2. This data therefore suggests that maximum fracture connectivity measured in a cm^2 occurs near to the centre of VF, which is in agreement with the observations from connectivity within clusters.

4.4.3.3 EF

Two data sets were selected for the analysis of fracture connectivity relative to EF (132a, 132b), and are the same data sets used to analyse fracture spacing and length (**Table 4.1, Figure 4.9, Figure 4.10**). Both data sets are photographs of horizontal outcrop surfaces and exhibit a gneissose lithology. Locality 132a is approximately 10m away from the Elvdalen Fault plane and 1926m away from VFP; locality 132b is approximately 1m away from the EFP and 1936m away from the VP.

For each data set, the connected fractures were recognised and divided into single, small and large clusters depending on the number of nodes within the cluster (section 1.7.8.3). The fracture maps from both localities contain a large cluster that spans the sample area and intersects all four sides of the rectangular fracture map. These clusters are known as

percolating clusters and the data sets are said to have reached the percolation threshold ($p_c = 1$) (section 1.7.8.3.1) (**Table 4.20**). In both data sets the percentage of total fracture length that contributes to the percolating cluster is above 75% which suggests that both data sets are well-connected (section 1.7.8.4.5) (**Table 4.21**).

The total number of fractures and nodes for both data sets and the total fracture cluster lengths are plotted in **Figure 4.104**, **Figure 4.105** and **Figure 4.106** against perpendicular distance to the VFP along with the outcrop data sets from VF. The values from the data set at locality 132b (1m from EFP) are above background level in each plot, but the values are not as high as the maximum values observed at the centre of VF or HSF. The values from locality 132a (10m from EFP) are similar to the background levels observed away from VF. The data therefore suggests that fracture cluster connectivity is increased adjacent to EF, but that connectivity is not as high as in the centre or HSF or VF.

The total number of nodes per unit area can also be used as a measure of connectivity. The values of nodes per cm^2 for the data sets collected near EF are presented in **Figure 4.107** with the data from VF, and plotted against the perpendicular distance to the VFP. The value of the total number of nodes per cm^2 is 0.014 at a distance of 1m from EFP, which is slightly increased above background level (0.01 nodes per cm^2), and suggests that the connectivity of fractures adjacent to EF is increased, but not as high as the connectivity at the centre of VF or HSF.

4.4.3.4 Analysis of connectivity from whole outcrop data set

A number of connectivity parameters have been plotted and described in the above sections for outcrop data sets against the perpendicular distance from the HSFP, the VFP and the EFP. These results are summarised in **Table 4.22**.

There are also a number of plots that can be created for the whole outcrop data set to investigate relationships between connectivity parameters, and to compare the data from the two main faults. These relationships are described below and summarised in **Table 4.22** with respect to measurements within clusters and with respect to measurements within a unit area.

		Fault		
		HSF	VF	EF
	Outcrop photographs used *(table 4.1, figures 4.9 & 4.10)*	8	13	2
	Orientation of data sets	8 horizontal	2 horizontal, 12 vertical (3 perpendicular to fault trend, 9 parallel to fault trend)	2 horizontal
	Lithology of data sets	all gneissose	13 gneissose, 1 amphibolite	all gneissose
connectivity measured within clusters	Percolation threshold (p_c) reached?	$p_c = 1$ for all data sets	$p_c = 1$ for all but 4 data sets where $p_c = 0.75$	$p_c = 1$ for both data sets
	Percentage of fracture length within percolating cluster	all data sets >77%	all data sets > 90%	both data sets > 84%
	Percentage of fractures within single, small and large clusters 'v' distance	no systematic change	increased percentage of fractures contained in small and single clusters with increasing distance to VF	-
	Percentage of total fracture length within single, small and large clusters 'v' distance	increased percentage of fracture length contained in small & single clusters with increasing distance to HSF	increased percentage of fracture length contained in small and single clusters with increasing distance to VF	-
	Number of fractures per cluster 'v' distance	Max. value occurs in centre of HSF = 181 fractures per cluster. Decrease to background level (~30) over ~100m.	Max. value occurs near centre of VF = 349 fractures per cluster. Decrease to background level (~60) over ~500m.	Increased above background level to 148 fractures per cluster.
	Number of nodes per cluster 'v' distance	Max. value occurs in centre of HSF = 293 nodes per cluster. Decrease to background level (~40) over ~100m.	Max. value occurs near centre of VF = 541 nodes per cluster. Decrease to background level (~75) over ~500m.	Increased above background level to 227 nodes per cluster.
	Total cluster length 'v' distance	Max. length occurs in centre of HSF = 0.95 cm/cm². Decrease to background level (~0.07) over ~100m.	Max. length occurs near centre of VF = 0.87 cm/cm². Decrease to background level (~0.05) over ~500m.	Increased above background level to 0.33 cm/cm².
	Total fractures per cluster 'v' Total nodes per cluster	Strong positive relationship on linear axes. Connectivity less than 1%.		
	Total fractures per cluster 'v' total cluster length (per area)	No apparent relationship.		
	Total nodes per cluster 'v' total cluster length (per area)	No apparent relationship.		
	Total nodes per fracture in a cluster	Most frequent value is 0.5, rest of data is approximately normally distributed, with mean value of 1.34.		
	Total fractures per node in a cluster	Most frequent value is 2, rest of data is approximately normally distributed, with mean value of 0.76.		
connectivity measured within a unit area (cm²)	Total number nodes per cm² 'v' distance	Max. value occurs in centre of HSF = 0.25 nodes per cm² Decrease to background level (~0.002) over ~100m.	Max. value occurs near centre of VF = 0.2 nodes per cm². Decrease to background level (~0.001) over ~500m.	Increased above background level to 0.014 nodes per cm².
	Total nodes per cm² 'v' total fractures per cm²	Strong positive power-law relationship on logarithmic axes, exponent = 1.0547		
	Total nodes per cm² 'v' total fracture length per cm²	Strong positive power-law relationship on logarithmic axes, exponent = 1.9104		
	Total nodes per fracture in a cm²	Approximately normally distributed with mean value of 1.25		
	Total fractures per node in a cm²	Approximately normally distributed with mean value of 0.83		
	Total nodes per cm² 'v' exponent from exponential length distribution	Good positive power-law relationship, exponent = 0.4839		
	Power-law exponent & relationship to connectivity	No obvious relationship between nodes per cm² and power-law exponent, although the spread of power-law exponent values is highest when the values of nodes per cm² are low. Values of exponent all < 2 suggesting that large fractures control the connectivity of the data sets.		

Table 4.22 Summary of fracture connectivity data from outcrop scale

Firstly, the total number of fractures from each cluster in each data set can be plotted against the total number of nodes in the same cluster, for all outcrop data (**Figure 4.108**). A strong positive relationship is observed between these parameters on linear axes for the outcrop data sets from all three faults. When planar fractures are connected in a cluster, maximum and minimum values of connectivity can be calculated (section 1.7.8.3.3); connectivity decreases exponentially between maximum and minimum values. These extremes are plotted on **Figure 4.108**, along with the relationship for 1% connectivity. It is evident that although large clusters (i.e. containing >100 fractures and nodes) occur adjacent to the faults, the connectivity of the fractures within clusters in 2-dimensions at outcrop scale is very low (< 1%) for all three fault data sets.

Secondly, the values of cluster length (normalised for sample area) can be plotted against both the total number of fractures per cluster and the total number of nodes per cluster (**Figure 4.109** and **Figure 4.110**). There are no obvious strong relationships on either of these plots, although both exhibit a weak positive correlation.

Thirdly, both the total number of nodes per fracture and the number of fractures per node within each cluster from all outcrop data sets can be assessed and plotted as histograms (**Figure 4.111** and **Figure 4.112**) (section 1.7.8.4.4). The graphs are approximately mirror images of each other. The most frequent value of fractures per node is 2, and the most frequent value of nodes per fracture is 0.5. These values correspond to small clusters with 2 fracture and 1 node. Similarly, the values of fractures per node equal to 1.5 and the values of nodes per fracture equal to 0.67 correspond to small clusters with 3 fractures and 3 nodes. The total number of fractures per node in a cluster between 0.6 and 1, and the total number of nodes per fracture in a cluster between 1 and 1.8 appear to be approximately normally distributed with mean values of 0.76 and 1.34 respectively. These values mean that on average within fracture clusters observed at outcrop scale, there are more nodes than fractures and therefore connectivity is relatively good (section 1.7.8.4.4).

Aside from connectivity measurements within clusters, parameters can also be calculated within a unit area (cm^2). Firstly the total number of fractures per cm^2 (fracture density) (section 1.7.4.2, section 4.2) from each 2-dimensional outcrop data set can be plotted against the total number of nodes per cm^2 (a measure of connectivity, section 1.7.8.4.3)

(**Figure 4.113**). A strong positive power-law relationship is observed between fracture density and fracture connectivity when the outcrop data are plotted on both logarithmic axes and linear axes, with an exponent value of 1.06.

Secondly the total number of nodes per cm^2 can be plotted against the total fracture length per cm^2 (fracture intensity) (section 1.7.5.2, section 4.3) (**Figure 4.114**). The parameters are plotted on both logarithmic and linear axes, and a strong positive power-law relationship is observed for the outcrop data from all three faults with an exponent value of 1.91.

Thirdly both the total number of nodes per fracture and the number of fractures per node within a cm^2 from all outcrop data sets can be assessed and plotted as histograms (**Figure 4.115** and **Figure 4.116**) (section 1.7.8.4.4). Both plots are approximately normally distributed with mean values of 1.25 nodes per fracture and 0.83 fracture per node. Again, these values mean that on average within fracture clusters observed at outcrop scale, there are more nodes than fractures and therefore connectivity is relatively good (section 1.7.8.4.4).

Finally, the exponent data from the fracture length distribution from each data set can be plotted against the total number of nodes per cm^2. As illustrated previously, the fracture length data from the selected outcrop localities can be best fitted to either an exponential distribution or a power-law distribution (section 4.3.3). Here, a good positive power-law relationship is observed, on both linear and logarithmic axes, between the exponent from the length data sets that are exponentially distributed and the total number of nodes per cm^2, with a power-law exponent of 0.4839 (**Figure 4.117**). No obvious relationship is observed between the values of the power-law length exponents and the numbers of nodes per cm^2, although the spread of the power-law exponent values is highest when the values of nodes per cm^2 are low (**Figure 4.118**).

The power-law exponent has been used to characterise the abundance of large and small fractures with respect to the size of the sample area (large fractures are longer than the dimensions of the sample area) (section 1.7.8.5). Power-law exponents less than 1 suggest that connectivity is controlled by a small number of large fractures, and the number of nodes is low; whereas power-law exponents between 1 and 3 suggest that connectivity is controlled by both large and small clusters (section 1.7.8.5). When the

exponent is equal to 2 the relative contribution to connectivity of large and small fractures is identical, above 3 the connectivity is controlled by small fractures (section 1.7.8.5). The 15 values of fracture length power-law exponent from the outcrop data sets range from 0.61 to 1.56 (**Table 4.13**); with 40% of the values being less than 1, and the remaining 60% of values being between 1 and 2 (**Figure 4.119**). This suggests that for all of the data sets the connectivity is controlled by relatively large fractures.

4.4.4 *Thin-section data set*

The connectivity of fractures measured by hand from 2-dimensional thin-sections is presented and discussed. Data is presented for the two main faults in the MTFC, the VF and HSF.

4.4.4.1 HSF

Fracture connectivity has been analysed from a total of 7 thin-sections relative to HSF, the same data sets that were used to analyse fracture spacing and length (**Table 4.2, Figure 4.11, Figure 4.12**). The sections chosen are at various distances from HSFP, both north and south. All the thin-sections used are orientated and cut horizontally, and are composed of a quartz-feldspathic (gneissose) lithology. To enable fracture lengths to be measured by hand, the data sets were enlarged (x10), but all values of fracture lengths presented here are plotted as actual measurements.

For each of the 7 data sets, the connected fractures were divided into single, small and large clusters (section 1.7.8.3) depending on the number of nodes within the cluster. All of the data sets contain at least one large cluster which has more than 15 nodes, sections HS3b and HS43 have two large clusters (**Table 4.23**). For the majority of the thin-sections, all four sides of the rectangular sample area are intersected by the largest cluster, and therefore these clusters are referred to as percolation clusters and the percolation threshold is reached (p_c = 1) (section 1.7.8.3.1). Only one of the data sets (HS19) does not contain a percolating cluster, instead the largest cluster intersects only 3 sides of the sample area, and the percolation threshold is not reached (p_c = 0.75).

Data scale	Fault	Locality	Distance to fault (m)	Total number fractures	Percolation threshold (p_c)	number of nodes per cm^2	clusters								
							single	small				large			
							no. of fractures & % total	number of clusters	no. of fractures & % total	number of nodes	total cluster length (mm)	number of clusters	no. of fractures & % total	number of nodes	total cluster length (mm)
Thin section	HSF	HS3b	45	190	1	33.263	18 (9.5%)	7	2, 4, 2, 2, 7, 2, (10%)	1,3, 1, 1, 6, 1	13, 16, 4, 3, 20, 3,	2	15, 138 (80.5%)	18, 173	39, 421
		HS13	4	964	1	208.32	31 (3.2%)	8	2, 2, 2, 2, 6, 2, 3, 2 (2.2%)	1, 1, 1, 1, 5, 1, 2, 1	3, 2, 2, 2, 7, 1, 3, 2	1	912 (94.6%)	1275	1563
		HS16	6	343	1	47.106	40 (11.7%)	7	2,3,9,7, 3,4,3 (9%)	1,2,8,6, 2, 4,2	5, 6, 16, 15, 5, 11, 4	1	272 (79.3%)	342	678
		HS19	180	139	0.75	21.73	33 (23.8%)	11	5,2,2,5, 2,2,3,2, 8,12,10 (38.1%)	6,1,1,4, 1,1,2,1, 7,11,10	15, 3, 4, 10, 5, 2, 6, 3, 18, 57, 31	1	53 (38.1%)	58	124
		HS21	430	119	1	18.711	21 (17.6%)	3	3,5,2 (18.4%)	2,5,1	8, 8, 2	1	88 (74%)	115	421
		HS42	8	346	1	51.955	38 (11%)	11	2,2,2,15, 2,2,2,4, 2,5,5 (12.4%)	1,1,1,16, 1,1,3,1, 7,4	2, 4, 4, 38, 2, 3, 3, 6, 1, 11, 10	1	265 (76.6%)	356	678
		HS43	25	89	1	12.505	12 (13.5%)	9	3,2,3,2, 4,2,8,4,3 (34.8%)	2,1,2,1, 4,1,9,3,2	7, 8, 6, 2, 10, 12, 55, 11, 15	2	31, 15 (51.7%)	33, 19	137, 125
	VF	V99-17	2800	91	1	18.869	11 (12.1%)	1	5 (5.5%)	4	27	1	75 (82.4%)	106	348
		V99-24	25	748	1	41.786	20 (2.7%)	6	2,7,2,2,3,2 (2.4%)	1,6,1,1, 2,1	6, 31, 3, 8, 4, 3	1	710 (94.9%)	1206	3228
		VM2	550	62	0.5	13.43	18 (29%)	6	4,2,3,2,2,2 (24.2%)	3,1,2,1, 1,1	8,4,5,3,4,3	1	29 (46.8%)	35	109.8
		VPS2	50	296	1	61.408	16 (5.4%)	5	2,2,2,2,2 (3.4%)	1,1,1,1,1	5,4,4,2,4	1	270 (91.2%)	374	835
		VMC7	30	294	1	46.764	6 (2%)	1	2 (0.7%)	1	4	1	286 (97.3%)	486	1251

Table 4.23 Connectivity data from all thin section data sets.

For the majority of thin-section data sets from HSF, the percentage of total fracture length that is contained within the percolating cluster is greater than 80%, and may be regarded as well-connected (section 1.7.8.4.5) (**Table 4.24**). One data set (HS43) has only 61.9% of the total fracture length contained within the percolating cluster and is relatively poorly connected (section 1.7.8.4.5) (**Table 4.24**).

Fault	section	distance (m)	total fracture length (mm)	*pc* length (mm)	%
Hitra-Snasa Fault	HS43	25	422.45	261.85	61.98
	HS42	8	825.3	678.4	82.20
	HS13	4	1619.75	1562.7	96.48
	HS16	6	793.1	675.65	85.19
	HS3b	45	561.1	460.35	82.04
	HS21	430	474.4	421.2	88.79
Verran Fault	V99/24	25	3336.21	3228.27	96.76
	VMC7	30	1263.65	1250.55	98.96
	VPS2	50	880.55	835	94.83
	V99/17	2800	402.1	347.45	86.41

Table 4.24 Percolating cluster data for thin-section data sets within the MTFC

The relative percentages of both the number of fractures and the fracture length contained in single, small and large clusters within each thin-section data set are plotted against the perpendicular distance to the HSFP to analyse the change in connectivity away from the HSFP (**Figure 4.120, Figure 4.121**) (**Table 4.23**). Both plots illustrate a systematic change in clustering with distance to the HSFP. Near the centre of HSF the percentage of the total number of fractures and total fracture length contained within large clusters is highest. The values for the large clusters systematically decrease with increasing distance away from the HSFP, suggesting that overall fracture connectivity decreases away from the HSFP.

For each thin-section data set the total number of fractures, and total number of nodes within each cluster and the total cluster lengths (normalised for sample area) can be plotted against the perpendicular distance to HSF to analyse the change in connectivity around the fault (**Figure 4.122, Figure 4.123, Figure 4.124**). The maximum values of

fractures (912) and nodes (1274) per cluster and total cluster length (25.3cm/cm²) all occur 4m north of the HSFP from section HS13. The values then decrease to background levels within 100m from the HSFP. The thin-section data therefore suggests that maximum fracture cluster connectivity occurs in the centre of HSF, and that the zone of high connectivity is less than 100m wide.

Instead of using fracture clusters to analyse connectivity, the total number of nodes per unit area can be calculated for each data set and plotted against the perpendicular distance to HSF (**Figure 4.125**). The maximum number of nodes per cm² for the HSF thin-section data set is occurs 4m north of the HSFP (208 nodes per cm²). The values decrease within 100m from HSFP to a background level of approximately 20 nodes per cm². This data therefore suggests that maximum fracture connectivity measured in a cm² occurs in the centre of HSF, and supports the observations from connectivity within clusters.

4.4.4.2 VF

The analysis of fracture connectivity has been carried out for a total of 5 thin-sections adjacent to the VFP, the same data sets that were used to analyse fracture spacing (section 4.2.4.2) and fracture length section 4.3.4.2) (**Table 4.2, Figure 4.11, Figure 4.12**). To enable fracture lengths to be measured by hand, the data sets were enlarged (x10), but all values of fracture lengths presented here are plotted as actual measurements.

For each of the 5 thin-sections, the connected fractures were divided into single, small and large clusters (section 1.7.8.3) depending on the number of nodes within the cluster. All of the data sets contain one large cluster which has more than 15 nodes (**Table 4.23**). For the majority of the thin-sections, all four sides of the rectangular sample area are intersected by the largest cluster, and therefore these clusters are referred to as percolation clusters and the percolation threshold is reached (p_c = 1) (section 1.7.8.3.1). Only one of the data sets (VM2) does not contain a percolating cluster, instead the largest cluster intersects only 2 sides of the sample area, and the percolation threshold is not reached (p_c = 0.5). The largest cluster from this data intersects two opposite sides of the sample area, and the fracture network is connected parallel to the overall trend of the MTFC (section 1.7.8.4.1).

For the thin-section data sets collected adjacent to the VFP, the 85% of total fracture length that is contained within the percolating cluster for all data sets, suggesting that they are all well connected (section 1.7.8.4.5) (**Table 4.24**).

For each thin-section data set, the relative percentages of both the number of fractures and the fracture length contained in single, small and large clusters can be plotted against the perpendicular distance to the VFP (**Figure 4.126, Figure 4.127**) (**Table 4.23**). No systematic change in clustering is observed on either plot, but the relative percentages of fractures and fracture lengths that are contained in the large clusters appear to broadly decrease away from the VFP suggesting that overall fracture connectivity decreases away from the VFP.

The total number of fractures, and total number of nodes within each cluster and the total cluster lengths (normalised for sample area) for each data set can be plotted against the perpendicular distance to the VFP to analyse the change in connectivity around the fault (**Figure 4.128, Figure 4.129, Figure 4.130**). The maximum values of nodes (1206) and fractures (710) per cluster and total cluster length (13.5cm/cm^2) all occur close to the VFP. The values then decrease to background levels within 500m from the VFP. The thin-section data therefore suggests that maximum fracture cluster connectivity occurs in the centre of the VF.

The total number of nodes per unit area, which is independent of the size and amount of fracture clusters, can be calculated for each data set and plotted against the perpendicular distance to the VFP (**Figure 4.131**). The maximum number of nodes per cm^2 (61.4) occurs close to the centre of the VF. The values decrease within 500m from the VFP to a background level of approximately 15 nodes per cm^2. This data therefore suggests that maximum fracture connectivity measured in a cm^2 occurs in the centre of the VF, and supports the observations from connectivity within clusters.

4.4.4.3 Analysis of connectivity from whole thin-section data set

A number of connectivity parameters measured from the thin-section data sets have been plotted against the perpendicular distance from the HSFP and the VFP and are described in the above sections. These results are summarised in **Table 4.25**.

		Fault	
		HSF	VF
	Thin sections used	7	5
	Orientation of data sets	all cut horizontal	all cut horizontal
	Lithology of data sets	all gneissose	all gneissose
connectivity measured within clusters	Percolation threshold (p_c) reached?	p_c = 1 for 6 data sets, p_c = 0.75 for 1 data set	p_c = 1 for 4 data sets, p_c = 0.5 for 1 data set
	Percentage of fracture length within percolating cluster	6 data sets >80% 1 data set = 62%	all data sets > 85%
	Percentage of fractures within single, small and large clusters 'v' distance	increased percentage of fractures contained in small and single clusters with increasing distance to HSF	broad decrease away from VF in percentage of fractures contained in large cluster
	Percentage of total fracture length within single, small and large clusters 'v' distance	increased percentage of fracture length contained in small & single clusters with increasing distance to HSF	broad decrease away from VF in percentage of fracture length contained in large cluster
	Number of fractures per cluster 'v' distance	Max. value occurs in centre of HSF = 912 fractures per cluster. Decrease to background level (~50) over ~100m.	Max. value occurs near centre of VF = 710 fractures per cluster. Decrease to background level (~50) within ~500m.
	Number of nodes per cluster 'v' distance	Max. value occurs in centre of HSF = 1274 nodes per cluster. Decrease to background level (~50) over ~100m.	Max. value occurs near centre of VF = 1206 nodes per cluster. Decrease to background level (~50) within ~500m.
	Total cluster length 'v' distance	Max. length occurs in centre of HSF = 25.3 cm/cm². Decrease to background level (~5) over ~100m.	Max. length occurs near centre of VF = 13.5 cm/cm². Decrease to background level (~5) within ~500m.
	Total fractures per cluster 'v' Total nodes per cluster	Strong positive relationship on linear axes. Connectivity less than 1%	
	Total fractures per cluster 'v' total cluster length (per area)	No apparent relationship.	
	Total nodes per cluster 'v' total cluster length (per area)	No apparent relationship.	
	Total nodes per fracture in a cluster	Most frequent value is 0.5, rest of data is unevenly distributed, with mean value of 1.08.	
	Total fractures per node in a cluster	Most frequent value is 2, rest of data is unevenly distributed, with mean value of 0.98.	
connectivity measured within a unit area (cm²)	Total number nodes per cm² 'v' distance	Max. value occurs in centre of HSF = 208 nodes per cm² Decrease to background level (~20) over ~100m.	Max. value occurs near centre of VF = 61.4 nodes per cm². Decrease to background level (~15) over ~500m.
	Total nodes per cm² 'v' total fractures per cm²	Strong positive power-law relationship on linear axes.	
	Total nodes per cm² 'v' total fracture length per cm²	Good positive relationship on linear axes, slightly different slopes for data from HSF & VF data.	
	Total nodes per fracture in a cm²	Wide distribution of values, mean = 1.15	
	Total fractures per node in a cm²	Wide distribution of values, mean = 0.93	
	Total nodes per cm² 'v' exponent from exponential length distribution	Good positive power-law relationship, exponent = 0.4144	
	Power-law exponent & relationship to connectivity	No obvious relationship between nodes per cm² and power-law exponent. Values of exponent all < 2 suggesting that large fractures control the connectivity of the data sets.	

Table 4.25 Summary of fracture connectivity data from thin section scale

There are also a number of plots that can be created for the whole thin-section data set to investigate relationships between connectivity parameters, and to compare the data from the two main faults. These relationships are described below and summarised in **Table 4.25** with respect to measurements within clusters and with respect to measurements within a unit area.

Firstly, the total number of fractures from each cluster in each data set can be plotted against the total number of nodes in the same cluster, for all thin-section data (**Figure 4.132**). A strong positive relationship is observed between these parameters on linear axes using the thin-section data sets from both faults. When planar fractures are connected in a cluster, maximum and minimum values of connectivity can be calculated (section 1.7.8.3.3); connectivity decreases exponentially between maximum and minimum values.

These extremes are plotted on **Figure 4.132**, along with the relationship for 1% connectivity. It is evident that although large clusters (i.e. containing >200 fractures and nodes) occur adjacent to the faults the connectivity of the fractures within clusters in 2-dimensions at thin-section scale is very low (< 1%) for all three fault data sets.

Secondly both the total number of fractures per cluster and the total number of nodes per cluster for each data set can be plotted against values of cluster length (normalised for sample area) (**Figure 4.133** and **Figure 4.134**). In both plots there is scatter in the data, and there are a large number of small values, but there does appear to be a positive relationship between the parameters on linear axes.

Thirdly both the total number of nodes per fracture and the number of fractures per node within each cluster from all thin-section data sets can be assessed and plotted as histograms (**Figure 4.135** and **Figure 4.136**) (section 1.7.8.4.4). The graphs are approximately mirror images of each other. The most frequent value of fractures per node is 2, and the most frequent value of nodes per fracture is 0.5. These values correspond to small clusters with 2 fractures and 1 node. Similarly, the values of fractures per node equal to 1.5 and the values of nodes per fracture equal to 0.67 correspond to small clusters with 3 fractures and 3 nodes, and these values also have a high frequency. The values of fractures per node in a cluster between 0.6 and 1.5, and the values of nodes per

fracture in a cluster between 0.8 and 1.7 are distributed unevenly, with mean values of 0.98 and 1.08 respectively. These values mean that on average within fracture clusters observed at thin-section scale, there are slightly more nodes than fractures and therefore connectivity can be considered relatively good (section 1.7.8.4.4).

As well as measuring connectivity within clusters, parameters can also be calculated within a unit area (cm^2) for each 2-dimensional thin-section data set. Firstly the total number of fractures per cm^2 (fracture density) (section 1.7.4.2, section 4.2) from each data set can be plotted against the total number of nodes per cm^2 (a measure of connectivity, section 1.7.8.4.3) (**Figure 4.137**. A strong positive relationship is observed between fracture density and fracture connectivity when the thin-section data are plotted on linear axes.

Secondly, the total number of nodes per cm^2 can be plotted against the total fracture length per cm^2 (fracture intensity) (section 1.7.5.2, section 4.3) (**Figure 4.138**). Good positive relationships are observed for both fault data sets on linear axes. Although there are few data points for each fault, it appears that the thin-section data from the VF and HSF have different relationships between connectivity and intensity. For the same value of fracture length within a cm^2, the connectivity (number of nodes) is higher for the HSF thin-section data.

Thirdly, both the total number of nodes per fracture and the number of fractures per node within a cm^2 from the thin-section data sets from both faults can be plotted as histograms (**Figure 4.139** and **Figure 4.140**) (section 1.7.8.4.4). Both plots show a wide distribution of values probably due to the small number of data points. The mean value for the total number of fractures per node per cm^2 is 0.93; the mean value of nodes per fracture in a cm^2 is 1.15. These values mean that on average within fracture clusters observed at thin-section scale, there are slightly more nodes than fractures and therefore connectivity is relatively good (section 1.7.8.4.4).

Finally, from each thin-section data set, the total number of nodes per cm^2 can be plotted against the exponent from the fracture length distributions. The fracture length data from the thin-section data sets localities can be best fitted to either an exponential distribution or a power-law distribution (section 4.3.4).

Although there are few data points, a good positive power-law relationship is observed, on both linear and logarithmic axes, between the exponent from the length data sets that are exponentially distributed and the total number of nodes per cm^2, with a power-law exponent of 0.4144 (**Figure 4.141**). There is one anomalous data point on the plot, HS19, which has a higher exponent value than is expected for the exponential exponent from the data set. No obvious relationship is observed between the values of exponent from the power-law length distributions and the total number of nodes per cm from each data set (**Figure 4.142**). However, the power-law exponent has been used to characterise the abundance of large and small fractures with respect to the size of the sample area (large fractures are longer than the dimensions of the sample area) (section 1.7.8.5). The 12 values of fracture length power-law exponent from the thin-section data sets range from 0.8 to 1.78 (**Table 4.16**); with 25% of the values being less than 1, and the remaining 75% of values being between 1 and 2 (**Figure 4.143**). This suggests that for all of the data sets the connectivity is controlled by large fractures.

4.4.5 *Comparison of connectivity data from four data scales*

A number of plots can be created by amalgamating data from the four data scales, to investigate fracture connectivity over a large range of magnitudes. These relationships are described below and also summarised in **Table 4.26**.

The total number of fractures per cluster and nodes per cluster measured from all four data scales are plotted against each other in **Figure 4.144**. A good positive relationship is observed for all of the data scales. The curves for maximum and minimum connectivity for planar fractures that are connected in a cluster are plotted on the graph (section 1.7.8.3.3), along with the curve for 1% cluster connectivity. It is apparent that although large clusters occur, the fracture connectivity within the MTFC, measured in clusters from a variety of data scales, is less than 1%. Both the total number of nodes per fracture in a cluster and the total number of fractures per node in a cluster can be plotted for data from all four scales (**Figure 4.145, Figure 4.146**). Their most frequent values are 2 and 0.5 respectively. The values of fractures per node in

		Data set			
		Landsat™	**Air Photograph**	**Outcrop**	**Thin section**
	Connectivity range (max. and min. nodes per cm² measured)	42.93 / km²	0.556 / km²	min. - 0.0013 max. - 0.2535	min. - 12.5 max. - 208.3
	Size of data set (total number nodes measured)	421	880	23 photographs 4110 nodes	12 sections 4792 nodes
	Data set orientations	horizontal	horizontal	horizontal & vertical	horizontal
connectivity measured within clusters	p_c	$p_c = 1$	$p_c = 1$	$p_c = 1$ for all but 4 data sets where $p_c = 0.75$	$p_c = 1$ for all but 2 data sets where $p_c = 0.75$ & $p_c = 0.5$
	% length in pc	95.9	96.0	all > 77%	all > 80% except one data set = 62%
	no. fractures / cluster 'v' number of nodes / cluster	Good positive relationship on linear axes for all data. Connectivity < 1%			
	number of nodes per fracture in a cluster	Most frequent value = 0.5. Values between 1.2 & 1.8 approx. normally distributed mean value 1.41			
	number of fractures per node in a cluster	Most frequent value = 2. Values between 0.5 & 1.0 approx. normally distributed mean value 0.77			
connectivity measured within a unit area (cm²)	**total number of nodes / cm2 'v' total number fractures / cm2**	Strong power-law relationship for all data scales, exponent = 0.9869			
	total number of nodes / cm2 'v' total fracture length / cm2	Strong power-law relationship for all data scales, exponent = 2.0211			
	number of nodes per fracture in a cm2	Values approx. normally distributed, mean value 1.28.			
	number of fractures per node in a cm2	Values approx. normally distributed, mean value 0.83.			
	total number of nodes / cm2 'v' exponential length exponent	n/a	n/a	Good positive power-law relationship, exponent = 0.5052	
	total number of nodes / cm2 'v' power-law length exponent	No apparent relationship, although all power-law exponent are less than 2 suggesting that the connectivity at all scales is controlled by 'large' fractures			

Table 4.26 Summary and comparison of fracture connectivity data from four data scales

a cluster between 0.5 and 1.0 are approximately normally distributed with a mean value of 0.77. Likewise, the values of nodes per fracture in a cluster between 0.2 and 1.8 are also approximately normally distributed, with a mean value of 1.41. These values mean that on average within fracture clusters observed at all scales, there are more nodes than fractures and therefore connectivity is relatively good (section 1.7.8.4.4).

Connectivity can also be assessed within a unit area (e.g. cm^2) instead of assessing within a cluster. The total number of nodes per cm^2 is plotted against the total number of fractures per cm^2 (a measure of fracture density) in **Figure 4.147**. A strong power-law relationship is observed for the data from all scales, with a power-law exponent of 0.9869. The total number of nodes per cm^2 is then plotted against the total fracture length per cm^2 (a measure of fracture intensity) in **Figure 4.148**. Again a strong positive power-law relationship is observed with a power-law exponent of 2.0211.

Both the total number of nodes per fracture in a cm^2 and the total number of fractures per node in a cm^2 can be plotted for data from all four scales (**Figure 4.149, Figure 4.150**). The data in both plots are approximately normally distributed with mean values of 1.28 and 0.83 respectively. These values mean that on average within fracture clusters observed at all scales, there are more nodes than fractures and therefore connectivity is relatively good (section 1.7.8.4.4).

The best-fitting statistical distribution for each data set of length values at all four scales has been determined and discussed (section 4.3). Two distributions can be used to describe fracture length at outcrop and thin-section scales (exponential and power-law). The air photograph and Landsat™ data sets are best described by a power-law distribution only. The exponents from the outcrop and thin-section length data sets that are best described by an exponential distribution can be plotted against the total number of nodes per cm^2 for each data set (thin-section and outcrop scales only) (**Figure 4.151**). A good positive relationship is observed with a power-law exponent of 0.5052.

No apparent relationship is observed between the total number of nodes per cm^2 and the power-law exponents from the length distributions (**Figure 4.152**). However, the power-law exponents from all data scales are all less than 2, with 69% between 1 and 2, suggesting that the connectivity at all scales is dominated by large fractures (section 1.7.8.5) (**Figure 4.153**).

4.5 Summary of fracture parameters collected from 2-D data sets within the MTFC

4.5.1 *Spacing, length and connectivity characteristics at Landsat ™& air photo scales*

Fracture *spacing* data sets measured from both the Landsat™ and air photograph data sets (along transects orientated both parallel and perpendicular to the MTFC trend) are best-described by an *exponential distribution* with a negative slope. Fracture density ellipses from both the Landsat™ and air photograph data sets show the highest values of density occurring along transects orientated approximately perpendicular to the MTFC trend, which are likely to measure fractures parallel to the overall fault and foliation trends.

Fracture *length* data sets measured from both the air photograph and Landsat™ data sets are best described by a *power-law distribution* with exponents of -1.62 for the air photo and -1.34 for the Landsat™.

Both data sets possess a percolating cluster of fractures, and therefore at both Landsat™ and air photo scales, the percolation threshold is reached.

4.5.2 *Spacing, length and connectivity characteristics at outcrop & thin section scales*

A number of fracture attributes collected at outcrop and thin-section scales from the MTFC, can be used to illustrate the differences between the two main bounding faults within the MTFC – the VF and the HSF, and also to compare smaller faults such as the EF (**Figures 4.154, 4.155, 4.156**).

Each of the fracture attributes described in this chapter possesses a background level of values, above which the VF, HSF and EF can be recognised as perturbations in the data. Both the absolute values of fracture attributes, and the width of the perturbation differs for all three faults presented.

Using spacing, length and connectivity characteristics, it can be seen that the VF is associated with a wider zone of fracturing above background levels than the HSF or the

EF. The maximum values of the different attributes occur either at the centre of the VF or the centre of the HSF. It is important to note however, that due to a lack of exposure in the field, data collected at the centre of the HSF is closer to the fault plane than data collected at the centre of the VF, for all plots of fracture attributes presented in **Figures 4.154, 4.155, 4.156**. Therefore, in the case of the VF, if data was collected closer to the centre of the fault, higher values of fracture attributes may occur for the VF compared to the HSF. For all characteristics plotted in **Figures 4.154, 4.155, 4.156**, the maximum values observed at the location of the EF are lower than the maximum values associated with the HSF and the VF.

4.5.2 *Relationships between fracture density, intensity and connectivity*

- A strong power-law relationship is observed between values of fracture *density* (total number of fractures per cm^2) and fracture *intensity* (total fracture length per cm^2), for data collected adjacent to all faults from all data scales, with a power-law exponent of 0.4875 (**Figure 4.92**).
- A strong power-law relationship is also observed between values of fracture *density* and *connectivity* (total number of nodes per cm^2), with a power-law exponent of 0.9869 (**Figure 4.147**).
- A strong power-law relationship is also observed between fracture *intensity* and *connectivity*, with a power-law relationship of 2.0211 (**Figure 1.148**).

CHAPTER 5 - THE WALLS BOUNDARY FAULT SYSTEM

The Walls Boundary Fault System (WBFS) is a crustal-scale, N-S-trending, transcurrent fault system that transects the Shetland Isles and the adjacent Shetland Platform offshore (**Figure 5.1**). The Shetland Isles lie 300km to the west of Bergen, Norway, and 300km to the north of Aberdeen, Scotland. There are over 100 islands that together stretch north-south over a distance of 100km, and stretch 50km east-west at their widest point. The Islands rise out of the North Sea and form part of the Shetland platform. The West Shetland Basin and the Faroe-Shetland Basin lie to the west of the Shetland platform, with the Viking Graben to the east (Ziegler 1981, Johnson et al., 1993) (**Figure 5.1**).

Offshore, E-W orientated, deep seismic profiles to the north and south of the Shetland Isles, show a steeply dipping structure that extends through the entire crust and offsets the Moho. It is suggested that this structure is the offshore continuation of the WBF (McGeary 1989, McBride 1994). It has been suggested by several authors that the WBF may be extrapolated offshore to join with the Møre-Trøndelag Fault Complex in Central Norway (chapter 2) (Norton et al., 1987, Ziegler 1985, Grønlie and Roberts 1989, Séranne 1992, Blystad 1995), therefore suggesting that the two fault systems were linked at some stage during their development. Conroy (1996) suggested that the fault systems may have been linked in pre-Devonian times, but this correlation would require linkage of two structures intersecting Baltican and Laurentian basement complexes that were originally on opposite sides of the Iapetus Ocean, and therefore conflicts with traditional Caledonian models (Doré et al., 1997, Watts 2001). It is more reasonable to suggest that either the WBF and the MTFC may have become linked during Mesozoic times or in Early Devonian times (e.g. Grønlie and Roberts 1989, Watts 2001), or that the correlation could be based on the chance alignment of the structures (Watts 2001). It has also been suggested in the literature that the WBF is a continuation of the Great-Glen Fault in Scotland (Flinn 1961, 1977, 1985, 1992, Roddom et al., 1989).

The following sections describe the regional setting of the WBFS, the various lithologies that outcrop on Shetland, the main structural components of the fault system, key fault zone exposures, and the kinematic history of the WBFS.

5.1 Geological setting and protolith lithologies of the WBFS

Three main faults constitute the WBFS, the Walls Boundary Fault, the Nestings Fault (NF) and the Melby Fault (MF). The WBF is the most significant, having the largest displacement and being most laterally continuous (**Figure 5.2**). The WBF juxtaposes a segment of the Caledonian front to the west against Moine-Dalradian rocks to the east. The numerous lithologies present east and west of the WBF are briefly described below. For a more detailed description, the reader is referred to Mykura 1976 and Flinn 1985, and references therein.

5.1.1 *West of the WBF*

To the west of the WBF, rocks of the Caledonian front (consisting of alternating slices of basement and cover rocks) are unconformably overlain by Devonian sedimentary and volcanic rocks, and are cut by later granites (Mykura 1976, Flinn 1985). Two types of basement gneisses occur - Western and Eastern, along with 3 types of cover rocks – the Sand Voe, Hillswick and Queyfirth groups (Flinn 1985) (**Figure 5.3, Table 5.1**).

The Western Gneisses are banded orthogneisses and are cut by foliated pegmatites. The Eastern Gneisses are described by Flinn (1985) as Lewisian inlier-like, blasto-mylonitised hornblende-banded orthogneisses. The *Sand Voe group* cover rocks are generally highly schistose, dominantly siliceous, psammites with some garnet-mica psammites and pelites. The *Hillswick group* cover rocks are lithologically similar to the Sand Voe cover rocks, but differ in the frequent presence of units rich in graphite and pyrite (Flinn 1985). Both the Sand Voe and Hillswick groups are regarded as part of the Moine Supergroup (Flinn 1988). The *Queyfirth* group cover rocks are a series of interbanded calcareous and non-calcareous pelitic schists, and quartzite beds. The sequence has been tentatively correlated with the Dalradian Supergroup of Scotland (Flinn 1988). A further group of rocks of uncertain origin known as the *Walls Metamorphic Series* are also exposed west of the WBF on the southern shore of St. Magnus Bay (**Figure 5.4**). The series consists of quartzo-feldspathic and hornblende-rich gneisses, limestones, calc-silicate rocks and semi-pelites, and is unlike any of the other rocks exposed west of the WBF (Flinn 1985).

Relative geographical position and age	Components and lithology	Phemister's series	Groups in Pringle's Eastern Series	Possible correlation with Scottish mainland
East (younger) ↑ West (older)	6. Banded quartz- & muscovite schist 5. Calcareous Group, (ranges from quartzose schist to siliceous limestone) 4. Greenschist group 3. Banded quartz- and muscovite schist	Ollaberry Series	Queyfirth Group	Dalradian Supergroup (Flinn 1988)
	2. Muscovite-schist with garnet & chloritoid in parts 1. Banded hornblendic gneiss with granulitic gneiss & bands of impure quartzite	Fethaland Series	Sand Voe and Hillswick Groups	Moine Supergroup (Flinn 1988)

Table 5.1 The metasediments of north-west Shetland, to the west of the Walls-Boundary Fault. (Adapted from Mykura 1976)

Divisions of the East Mainland succession	Sub groups (*with significant units in brackets*)	Possible correlation with Scottish mainland	
Clift Hills Division (~ 3km thick)	Dunrossness Spilitic Group Dunrossness Phyllite Clift Hills Phyllitic Group (*Dales Voe Grit*) Asta Spilitic Group	Upper Dalradian	young ↑
Whiteness Division (~ 6km thick)	Laxfirth Limestone Wadbister Ness Group Girlsta Limestone Colla Firth Group (*East Burra Pelite, Whiteness Limestone*) Weisdale Limestone	Middle & Lower Dalradian	
Scatsta Division (~ 4km thick)	Scatsta Quartzitic Group Scatsta Pelitic Group		
Yell Sound Division (9-14 km thick)		Moine	old

Table 5.2 Divisions of the East Mainland Succession, Shetland (Adapted from Mykura 1976, and Johnson 1991)

5.1.2 *East of the WBF*

To the east of the WBF, lies a succession of Moine-Dalradian sedimentary rocks that were metamorphosed during the Caledonian orogeny, overthrust by an ophiolite complex, intruded by Early Devonian granites and unconformably overlain by Devonian Sandstones (Mykura 1976, Flinn 1985). Together the rocks are known as the Eastern Mainland Succession, and the sequence has been divided into four main units that are lithologically different – the Yell Sound Division, the Scatsta Division, the Whiteness Division and the Clift Hills Division (Flinn et al., 1972, Mykura 1976, Flinn 1985) (**Figure 5.4, Table 5.2**).

The *Yell Sound Division*, the westernmost unit, is composed almost entirely of well-laminated feldspathic psammites, together with several quartzitic horizons, conformable hornblende schists and belts of gneiss (possibly tectonized early granite intrusions) (Mykura 1976, Flinn 1985). This division has been equated with the Moine of Scotland (Flinn et al., 1972). The *Scatsta Division* is composed of quartzites with interbanded semi-pelitic schists, the relative proportions of which are variable, but generally quartzite is dominant (Flinn et al., 1972, Mykura 1976, Flinn 1985). The Scatsta Division is suggested to be the equivalent of the Lower Dalradian Supergroup in Scotland (Flinn 1985). The *Whiteness Division* lies to the east of the Scatsta division and comprises mostly micaceous psammite, interbedded with crystalline limestone units, semipelites, mica schists, calc-silicate granulites, thin marbles and hornblende schists (Flinn et al., 1972, Mykura 1976). The Whiteness Division has also been correlated with the Dalradian Supergroup (Flinn 1985). Finally the *Clift Hills Division* occurs conformably east of the Whiteness Division, and consists of metavolcaniclastic bands, semipelitic pelites, impure limestones and quartzite bands (Mykura 1976, Flinn 1985). This division has been correlated with the Upper Dalradian Supergroup (Flinn 1985).

5.1.3 The Ophiolite Complex

An ophiolite complex is exposed in Northeast Shetland, on the islands of Unst and Fetlar. The main unit is 6km wide and over 20km long, and is composed of a standard ophiolite sequence - peridotite, dunite, pyroxenite, gabbro, a sheeted dyke complex

and metavolcanic cap rocks. For a more detailed description the reader is referred to Flinn (1985).

5.1.4 Devonian Rocks

Old Red Sandstone deposits of Devonian age outcrop on Shetland both to the east and west of the WBF, and lie unconformably on the basement. This thick Devonian sequence is believed to represent remnants of the Devonian Orcadian basin that extended from northern Scotland possibly as far north as western Norway (Norton et al., 1987). The Devonian sandstones have been divided into three main groups based on geographical distribution and lithological differences, known as the Eastern, Central and Western groups (Mykura 1976, Flinn 1985) (**Figure 5.5**). Each group is situated within a different fault-bounded block, lying unconformably on basement rocks. The *Eastern Group* outcrops to the east of the Nestings Fault extending in a narrow strip from Lerwick to Sumburgh Head on the mainland, and on the islands of Bressay and Noss (**Figure 5.5**). The group is composed mainly of flaggy sandstones commonly containing pebbles, lenses of conglomerate and localised calcareous units with fish remains, which provide ages from Middle to Upper Devonian (Mykura 1976). The *Central Group* outcrops on Shetland between the Walls Boundary Fault and the Melby Fault (**Figure 5.5**). This group is also known as the Walls Sandstone, and is further separated into the lower Sandness and upper Walls formations. The Central Group is composed of frequently cross-bedded and/or laminated sandstones, interbedded with silts and shales, with conglomerates and breccias near the unconformable base. Within the succession, a group of basic and intermediate lavas agglomerates, and tuffs, ignimbrites and felsic intrusions are interleaved with the sandstones (Flinn 1985). The age of the Walls Sandstone is possibly Lower to Middle Devonian (Mykura 1976). The *Western Group* lies to the west of the Melby Fault, on the mainland, and the islands of Papa Stour and Foula (**Figure 5.5**). The outcrops to the west of the Melby Fault on the mainland are known as the Melby Formation (Mykura 1976). The Western Group is comprised of red sandstones and volcanic rocks of Middle Devonian age (Mykura 1976). Sandstones lie unconformably on metamorphic rocks on the island of Foula; on the mainland at Melby these sandstones pass up into volcanic rocks which are well developed on the island of Papa Stour. The

volcanics range in composition from basalt to rhyolite, and include lavas, agglomerates and ignimbrites (Flinn 1985).

5.1.5 Plutonic complexes

Plutonic complexes exposed on Shetland are divided into two groups, those that lie to the east and west of the WBF respectively (**Figure 5.5**). Complexes to the east are all cut by the WBF and the NF, and have yielded ages of ~400Ma; the Eastern Group of Devonian sandstones are not cut by these complexes (Flinn 1985). West of the WBF, the plutonic complexes yield ages of ~350Ma, and their associated dykes cross-cut the Devonian Central Group (Flinn 1985). There are three recognised complexes to the east of the WBF – the Graven, Brae and Spiggie complexes, and two to the west of the WBF – the Northmaven and the Sandsting complexes (Flinn 1985). In this study, fracture characteristics have been collected from two of these plutons, the Graven and the Spiggie complexes, both lying to the east of the WBF. The Graven complex is a hornblende-rich granodiorite with common enclaves of the Yell Sound Division (see above). The main unit within the Spiggie complex is a quartz-epidote granodiorite (Flinn 1985).

5.2 Structural components and key exposures of the WFBS

The Walls Boundary Fault System (WBFS) consists of 3 main structures, the Walls Boundary Fault (WBF), the Nestings Fault (NF) and the Melby Fault (MF) (**Figure 5.2**). Both the WBF and the NF are N-S trending sub-vertical structures; the MF (part of the St. Magnus Bay Fault) trends NE-SW and is also sub-vertical (Flinn 1977). Fracture data has been collected adjacent to all 3 of the main structures, within a variety of lithological units. Data has also been collected adjacent to the Aith Voe Fault (AVF), a N-S trending reverse fault that lies within the WBFZ (**Figure 5.6**). The AVF is thought to be part of a 'positive' flower structure that links into the WBF farther to the north and at depth (Watts 2001).

The WBFS has been studied in detail by Flinn (e.g. 1977), Conroy (1996), and most recently by Watts (2001).

In the following sections the WBF (including the AVF), NF and MF will be described briefly along with their key exposures and associated fault rocks.

5.2.1 *The Walls Boundary Fault (including the Aith Voe Fault)*

The Walls Boundary Fault Zone (WBFZ) refers to a zone of rocks that have been intensely deformed as a result of movement along the WBF. The WBFZ contains the Walls Boundary Fault Plane (WBFP), which is defined as the most significant and most recent movement plane (Watts 2001), and is used in this thesis as a central reference line for this fault zone. The Aith Voe Fault Plane (AVFP) also lies within the WBFZ. Fracture data for this study has been collected within a variety of lithologies at 3 sections across the WBF – Ollaberry, Sullom and Bixter, and adjacent to the AVF at Sand (**Figure 5.6**).

5.2.1.1 Ollaberry

The headland at Ollaberry provides 2 cross-sections through the WBFZ, the northern section is known as the Back Sand section, and the southern section is known as the Moo Wick section (**Figure 5.6 b**). The northern section is composed of high cliffs surrounding a sandy bay (**Figure 5.7**), and the southern section is composed of a rocky shoreline with inlets and low cliffs. The most obvious, and most significant, movement plane within the WBFZ is exposed at the Back Sand section. This is defined as the Walls Boundary Fault Plane (WBFP) and is orientated 012/ 84 E (**Figure 5.8**).

At Ollaberry, rocks belonging to the Queyfirth group (section 5.1, **Table 5.1**) are juxtaposed by the WBF against granite of the Devonian Graven Complex (section 5.1) (**Figure 5.6 b**). The Queyfirth group lies to the west of the WBFP, and comprises pelites and flaggy, finely laminated psammites which are interbanded (layers 15-70cm in thickness), and probably represent the original bedding. The granite lies to the east of the WBFP, and is red/pink in colour, course-medium grained with phenocrysts up to 1cm in length (Watts 2001).

The WBFZ at Ollaberry is at least 300m wide (~100m to the east and ~200m to the west) (Watts 2001). To the west of the WBFP, the WBFZ comprises mainly anastomosing fault gouges, which increase in thickness towards the fault plane. The gouges surround slivers of cataclasite and intensely fractured protolith material. At the centre of the WBFZ (within the WBF core), cataclastically deformed rocks derived from psammites/pelites grade into, and are overprinted by, an 8m-wide blue-coloured incohesive fault gouge (Watts 2001). To the east of the WBFP, N-S trending anastomosing cataclasites derived from granite surround blocks of fractured protolith. Both the cataclasites and the protolith are cross-cut by faults containing red-coloured gouges, which in places are mineralised by hematite (Watts 2001). Within the core of the WBF to the east of the WBFP, 2m of red-coloured gouge is observed. The cataclasites and the gouges at Ollaberry all preserve good evidence for dextral strike-slip movements (Watts 2001). Faults that display dip-slip reverse movements are also observed to the west of the WBFP, usually within pelitic horizons, and are considered to be coeval with strike-slip faulting, with deformation partitioned into contractional and strike-slip dominated domains formed during dextral transpression deformation (Watts 2001). It is not clear in the field whether the cataclasites and gouges were developed during 2 successive periods of dextral transpression along the WBF, or if they were formed during the same kinematic event, during fault zone exhumation (Watts 2001).

At Ollaberry, fracture data has been collected to the west of the WBFP within psammites and pelites.

5.2.1.2 Sullom

Along the western side of Sullom Voe, a N-S coastal section of low cliffs and beaches extends from Sullom to the Ness of Haggrister (**Figure 5.6 c**). Two E-W trending sections at the Ness of Haggrister expose the WBFZ and the WBFP, which is orientated 004/ 87 W, and forms a narrow inlet on the southern section (**Figure 5.9**).

On the southern side of the Ness of Haggrister, the WBFP juxtaposes granite belonging to the Devonian Graven Complex (section 5.1) to the east, against metasedimentary rocks of the Queyfirth group (section 5.1, **Table 5.1**) to the west. To the north of the Ness of Haggrister, the WBF bifurcates into a series of fault strands which bound slivers of banded gneiss, mylonite and cataclasite to the west of the WBFP (Watts 2001). The granite to the east of the WBFP is coarse-medium grained,

pink in colour (weathering to green) with feldspar phenocrysts up to 0.75cm in size, and possesses no obvious magmatic fabric. Metasedimentary rocks from the Queyfirth group on the west of the WBFP comprises calcareous schists, crystalline limestones and quartz-mica schists, which possess a strong schistosity trending N-S within the WBFZ and NW-SE outside the WBFZ.

At Sullom, the WBFZ varies in thickness from 300m to >500m, and is described by Watts (2001) as a kilometre-scale, braided network of sub-vertical faults associated with cataclasis and the development of fault gouge, that resembles a positive flower structure formed as a result of dextral strike-slip movement along the WBF.

The rocks either side of the WBFP at Sullom record different kinematic events. The earliest recognised fault rocks are mylonites and coeval 'early' cataclasites, which were formed during a period of sinistral strike-slip movement. These rocks are preserved in an uplifted fault-bounded block to the west of the WBFP, and are overprinted by all other structures and fault rocks within the WBFZ (Watts 2001). This ductile sinistral event is not preserved to the east of the WBFP within the granite, suggesting that either the granite may not have been adjacent to the WBF at that time, or that the granite had not been intruded when left-lateral movements occurred (Watts 2001).

Two phases of dextral strike-slip movements are observed within the WBFZ, and both overprint the mylonitic rocks. A major phase of dextral strike-slip faulting which led to the development of widespread cataclasis and gouge formation, and also led to the formation of the present day fault geometry, overprints a dextral strike-slip ductile event (Watts 2001). It is possible that these two phases of dextral strike-slip movement are part of the same kinematic event, developing from ductile to brittle as the fault zone was being exhumed (Watts 2001).

To the east of the WBFP, the granite is poorly exposed, but, the brittle dextral event is evidenced by cataclasites that contain subhorizontal stepping slickenfibres on fractures and fault surfaces that suggest dextral strike-slip movements and epidote/quartz-filled fractures which show dextral strike-slip displacements across them. To the west of the WBFP, good evidence of dextral strike slip movements are observed with the Queyfirth group (dextrally verging folds, sub-horizontal stepping slickenfibres, fracture offsets) and within blue gouge adjacent to the WBFP (dextral shear bands).

Within the WBF core, the 2m thick blue gouge derived from the Queyfirth group to the west of the WBFP displays a series of west-dipping shears which cross-cut the dextral shear fabric, and suggest that a period of minor dip-slip movement may post-date the dextral strike-slip events (Watts 2001).

The most recent movement event along the WBFP observed at this locality is recorded by stepping quartz slickenfibres on the WBFP itself. The slickenfibres display evidence for sinistral strike-slip movements (Watts 2001).

At Sullom, fracture data has been collected to the east of the WBFP within granite, and to the west of the WBFP within calcareous metasediments.

5.2.1.3 Bixter

The southern coast of the Ness of Bixter, a small headland extending into Sandsound Voe, provides an E-W cross-section across the WBFZ, and exposes the WBFP (**Figure 5.6 d**). The WBFP is orientated 002/ 85 W and defines a narrow inlet.

To the west of the WBFP sandstones from the Middle Devonian Walls Formation (section 5.1) are exposed. To the east of the WBFP, fault-bounded slivers of cataclasite and calcareous schist are juxtaposed against granite belonging to the Late Devonian Spiggie Complex to the east. The sandstones to the east of the WBFP are grey coloured and finely laminated, with occasional interbeds of mudstone. Bedding outside the WBFZ trends NW-SW, inside the WBFZ bedding trends N-S. Grey-coloured calcareous schists exposed in a fault-bounded block are similar in appearance to those belonging to the Queyfirth Group at the Ness of Haggrister (section 5.2.1.2). The granite to the east is red/pink in colour, medium-coarse grained, and contains phenocrysts of feldspar up to 3cm in length. The granite displays no obvious magmatic foliation.

At Bixter, the WBFZ is ~500m wide, comprising a narrow fault core (~50m wide and containing the WBFP), flanked by wide zones of cataclasis. Fault-related deformation is strongly asymmetric, extending ~350m into Devonian sandstones to the west, and <150m into calcareous schists and granite to the east (Watts 2001). Fault gouge, breccia and cataclasite increase in volume towards the WBFP. The WBFZ comprises a braided network of faults containing gouge and/or breccia, which appear to bifurcate from the WBF core (Watts 2001). These anastomosing faults bound slivers of fault rock and protolith, and display either dextral strike-slip or dip-slip normal movements both sides of the WBFP (evidence for dextral and dip-slip kinematics – dextral shear

bands, slickenside indicators, dextral verging folds, R-type Riedel shears and tension gashes) (Watts 2001). The dip-slip and dextral strike-slip faults are inferred to be the same age, as they contain the same generation of fault rocks and display no consistent cross-cutting relationships, and therefore appear to represent strain partitioning on an outcrop scale (Watts 2001). The geometry of the WBFZ at Bixter is likened to that of a transtensional negative flower structure by Watts (2001), that developed during dextral strike-slip movement along a releasing bend of the WBF. It is suggested by Watts (2001) that the presence of a negative flower structure explains why older fault rocks are not exposed at Bixter (cf. section 5.2.1.2, Sullom locality).

Fracture data has been collected within Devonian sandstones that crop out to the west of the WBFP at Bixter.

5.2.1.4 Sand

The coastal sections around the shores of Seli Voe and Sand Voe provide exposures of the WBFZ. The sections are dominated by cliffs (5-40m high), beaches and a rocky shoreline (**Figure 5.6 e**). The WBFP is not exposed at this locality, but can be extrapolated from the Ness of Bixter (section 5.2.1.3), to lie through Seli Voe. Inland, the WBF trace is marked by a flat-bottomed valley. Within the WBFZ at this locality, a large-scale dip-slip (reverse) fault is exposed, known as the Aith Voe Fault (AVF) (**Figure 5.10**).

To the west of the WBFP at this locality, sandstones belonging to the Middle Devonian Walls Formation (section 5.1) are exposed, intruded by granite belonging to the Late Devonian Sandsting Complex (**Figure 5.5**). The sandstones to the west of the WBFP are grey in colour, fine-medium grained, and are occasionally interbedded with mudstones.

To the east of the WBFP, a thin sliver of cataclasite is exposed adjacent to a succession of pelites and psammites. The origin of the pelite/psammites succession to the east of the WBFP is unclear, but the rocks are noted by Watts (2001) as being lithologically and structurally similar to those exposed to the west of the WBFP at Ollaberry locality (section 5.2.1.1), which are interpreted to be part of the Queyfirth Group (section 5.1, **Table 5.1**). To the east of the pelites and psammites, a fault-bounded block of blastomylonite, cataclasite and foliated cataclasite is exposed, adjacent to granodiorite belonging to the Late Devonian Spiggie complex (section 5.1) (**Figure 5.6 e**). The granodiorite exposed to the east of the WBFP (east of the

fault bounded block containing blastomylonites etc.) is grey in colour, coarse-grained, and contains phenocrysts of feldspar up to 1cm in size. In places the rock displays a weak magmatic foliation, trending N-S (Watts 2001). The boundary between the fault-bounded block of blastomylonites etc. and the granodiorite is marked by the Aith Voe Fault (AVF) which is orientated 177/ 54 W (**Figure 5.6 e, Figure 5.10**).

At Sand, the WBFZ is 1.5km wide. Fault-related deformation is strongly asymmetric, extending 200m to the west of the WBFP into Devonian sandstone and granite, and approximately 1.3km to the east of the WBFP into pelites, psammites and granodiorites (Watts 2001) (**Figure 5.6 e**). The rocks exposed either side of the WBFP record different kinematic events.

The earliest recognised fault rocks are blastomylonites and coeval isotropic cataclasites and quartz and epidote veins, that are exposed in a fault-bounded block to the east of the WBFP, and show good evidence for formation during a sinistral strike-slip event (Watts 2001). Within the fault-bounded block, the early blastomylonites and isotropic cataclasites are overprinted by foliated cataclasites that show evidence for dextral strike-slip (Watts 2001).

A major phase of dextral, brittle, strike-slip faulting appears to overprint the dextral foliated cataclasites observed within the fault-bounded block (Watts 2001). This phase of dextral movement along the WBFP led to the development of widespread cataclasis and fault-gouges both east and west of the WBFP, resulting in the present day geometry of the fault network (Watts 2001). Within sandstones to the west of the WBFP cataclastic deformation, associated with dextral strike-slip movements, increases towards the WBFP, with the development of N-S trending gouge-filled faults surrounding zones of breccia and intensely fractured protolith. Directly to the east of the WBFP, a succession of psammites and pelites is overprinted by broad zones of cataclastic deformation and the development of gouge-filled faults. Dextral kinematic indicators within the psammites/pelites include centimetre-scale shear bands and kink bands, and fractures and faults with subhorizontal lineations and dextral offsets (Watts 2001). Granodiorite to the east of the AVF is intensely fractured and cross cut by zones of incohesive breccia and gouge-filled faults. Good evidence for dextral strike-slip kinematics within the granodiorite include fractures and faults with subhorizontal slickenside lineations displaying dextral offsets, and centimetre-scale shear bands (Watts 2001). Adjacent to the AVFP, steeply dipping gouge-filled faults and fractures display reverse dip-slip movements based on the stepping of

quartz fibres. Reverse dip-slip slickenside lineations are also observed on the actual AVFP.

It is suggested by Watts (2001), that the AVF is part of a kilometre-scale 'positive' flower structure, which links into the WBFP farther north and at depth, which formed as a result of dextral strike-slip movements along the WBFP. An initial curve in the WBF trace led to a local region of transpression during dextral strike-slip along the WBF. Continued movement produced a braided network of faults to the east of the WBFP and resulted in the exhumation of a fault-bounded block of early fault rocks (blastomylonites etc.) in the hanging wall of the reverse dip-slip AVF.

Fracture data has been collected within granodiorite belonging to the Devonian Spiggie Complex, to the east of the AVFP.

5.2.2 *The Nestings Fault*

The Nestings Fault Zone (NFZ) refers to a zone of rocks that are intensely deformed as a result of movement along the Nestings Fault. The NFZ contains the Nestings Fault Plane, which is defined as the most significant and most recent movement plane (Watts 2001), and used here as a central reference line for this fault zone. The Nestings Fault is interpreted to be a splay off the WBF (section 5.2.1), which accommodated some displacement as the WBF changed strike (Flinn 1977, 1992, Watts 2001).

Fracture data has been collected within 2 lithologies adjacent to the Nestings Fault along the shores of Wadbister Voe (**Figure 5.11**). The northern coast of Wadbister Voe provides the best and most complete cross-section through the NFZ on Shetland (Watts 2001). The coast comprises a rocky shoreline with narrow inlets and low cliffs (<5m high).

The NFP itself is exposed within a narrow inlet, orientated 016/ 85 E. To the west of the NFP limestones, hornblende schists and calc-silicates belonging to the Whiteness Division are exposed, and to the east of the NFP, psammites and semi-pelites from the Whiteness Division are exposed (section 5.1, **Table 5.2**). Both to the east and west of the NFP the rocks display a strong, N-S, near-vertical foliation. Directly to the east of the NFP, a fault-bounded sliver of intensely cataclastically deformed limestone of uncertain origin is present.

At Wadbister Voe, the NFZ is approximately 600m wide and is strongly asymmetric, extending 550m to the west of the NFP and 50m to the east of the NFP

To the west, a braided network of gouge-filled faults with sub-horizontal slickenside lineations, display shear banding and steeply plunging folds consistent with dextral shear. Locally, N-S trending contractional faults, which link into dextral strike-slip faults, are present.

To the east, within 50m of the NFP, the rocks are characterised by intense fracturing and millimetre-scale networks of calcite veins, which overprint protolith lithologies (Watts 2001). Gouge-filled faults are rare, but where present, the gouges are associated with subhorizontal slickenside lineations and centimetre-scale shear bands indicating a dextral sense of shear (Watts 2001).

To summarise, only one phase of movement along the NFP is observed at Wadbister Voe. The NFZ is characterised by a wide (asymmetrical) zone of brecciation, subsidiary faulting, and the development of fault gouge, which are all consistent with dextral transpression (Watts 2001). The Nestings Fault is interpreted to have formed as a result of dextral strike-slip movement along a large-scale restraining bend along the WBF (Flinn 1977, Watts 2001).

Fracture data has been collected within psammites to the east of the NFP, and within calcareous schists to the west of the NFP.

5.2.3 *The Melby Fault*

The Melby Fault Zone (MFZ) refers to a zone of rocks that are intensely deformed as a result of movements along the Melby Fault. The MFZ includes the most recent, and most significant, plane of movement known as the Melby Fault Plane (MFP) (Watts 2001) which is used as a central reference line in this thesis for this fault zone. The Melby Fault (Mykura and Phemister 1976) has also been named as the St. Magnus Bay Fault by Flinn (1977).

The MFZ is poorly exposed along one coastal section, on the southern side of the Sound of Papa, where the MF trace intersects a 500m long sandy beach known as The Crook (**Figure 5.11**). The actual MFP is not exposed, but the fault trace trends NE-

SW. The Melby Fault also intersects the coastline of Shetland at Hesti Geo, but is inaccessible except by boat.

On the western side of the MF trace, as it intersects the sandy bay known as The Crook, a series of sandstones, conglomerates and rhyolites belonging to the Middle Devonian Western Group (section 5.1.4) are exposed. To the east of the MF trace, basement rocks of uncertain origin are exposed, known as the Walls Metamorphic Series (section 5.1.1). These rocks consist of interlayered hornblende schists, amphibolites, quartzo-feldspathic semi-pelites and marbles. To the south of The Crook, sandstones and conglomerates belonging to the Sandness Formation, part of the Devonian Central Group (section 5.1.4), unconformably overlie the basement rocks and occur adjacent to the MFP at Hesti Geo.

To the east of the MFP, the basement rocks exposed at the Neap of Norby possess a foliation orientated parallel to the MF trace, trending NE-SW and dipping steeply to the SE, with subhorizontal lineations, and contain evidence for dextral shear (Watts 2001). It is unclear whether the dextral shear event is associated with movements along the MF, or whether the structures represent regional deformation. These rocks are cross-cut by several poorly exposed phyllonitic shear zones with sub-horizontal lineations. The sense of shear could not be determined due to the lack of exposure (Watts 2001). The basement rocks and the phyllonitic shear zones are overprinted by a series of gouge-filled faults, orientated NE-SW, parallel to the MF trace, which are associated with dip-slip reverse movements (Watts 2001) (**Figure 5.11 d**).

To the east of the MF trace, interbedded sedimentary rocks and rhyolites are intensely fractured, but no faults were observed within the outcrops available. The rocks contain bedding surfaces trending NE-SW and dipping to the NW. Along some bedding surfaces subhorizontal lineations occur (Watts 2001).

Therefore the only kinematic indicators that can be related with some certainty to movements along the MF are reverse dip-slip.

Fracture data has been collected either side of the MF trace, within sandstones to the west and within hornblende schists to the east.

5.3 The kinematic history of the WBFS

The kinematic history of the WBFS has been investigated by many authors (e.g. Flinn 1977, 1992, Mykura and Phemister 1976, Conroy 1996, Watts 2001). The earliest phase of movement within the WBFS is suggested by Watts (2001) to be sinistral strike-slip movements along the WBFZ, which led to the development of mylonites (section 5.2.1.2, Sullom locality) and blastomylonites (section 5.2.1.4, Sand locality). Flinn (1977) also recognised slices of mylonite occurring sporadically along the trace of the WBF, and attributed these to an earlier phase of movement related to the Great Glen Fault in Scotland.

The second main movement phase recognised along the WBF consists of a major dextral strike slip event, associated with the production of cataclasites and fault gouges (sections 5.1.2.1, 5.1.2.2, 5.1.2.3, 5.1.2.4, Ollaberry, Sullom, Bixter, Sand localities, and other localities along the WBF trace, described by Flinn (1977), in part by Conroy (1996) and in detail by Watts (2001)). It is during this dextral phase of movement along the WBF, that the Nestings Fault formed as a linking structure, due to the development of a 10's of kilometre-scale left-stepping restraining bend to the east of the WBFZ. Along the WBF trace during this event, a series of kilometre-scale positive flower structures formed, exposing deeply exhumed early mylonites (e.g. Sullom locality, and the formation of the Aith Voe Fault at Sand locality), and locally negative flower structures (e.g. Bixter locality). This dextral event therefore led to the formation of the present day geometry and fault rock distribution of the WBFS (Watts 2001). The age of this movement is constrained by offshore observations (McGeary 1989). In the Sandwick Basin to the southwest of the Shetland Isles, the WBF clearly cuts Permo-Triassic sedimentary rocks, and in the West Fair Isle Basin also to the southwest of Shetland, Permo-Triassic successions show no evidence of thickening towards the WBF (McGeary 1989). It is therefore suggested that the dextral strike-slip event is post-Triassic (McGeary 1989), probably Mesozoic, related to Late Jurassic to Early Cretaceous rifting in the North Sea.

Watts (2001) recognised an earlier, possible ductile, dextral strike-slip event based on field observations, which pre-dates the main phase of dextral movement described above. It is possible that the two phases of dextral strike-slip movement (i.e. brittle

and ductile) are formed during the same kinematic event, as the fault zone was being exhumed (Watts 2001).

Coward et al., (1989) also suggest pre-Mesozoic dextral strike-slip movements along the WBFZ, associated with Variscan (Permo-Carboniferous) deformation.

Two later phases of movement, that post-date both dextral events, are recognised by Watts (2001). A dip-slip event based on the observation of steeply dipping shears within gouge at Sullom locality (section 5.1.2.2) and the most recent event recognised by Watts (2001) is a sinistral strike-slip event based on the stepping of quartz slickenfibres on the WBFP exposed at Sullom (section 5.1.2.2), and Brae, and also fracture offsets observed on the island of Papa Little.

The kinematic history of the Melby Fault is more difficult to constrain due to the lack of exposure and offshore data. It has long been considered to be a strike-slip fault (e.g. Mykura 1976, Mykura and Phemister 1976, Mykura 1991, Donovan et al., 1976, Séranne 1992). Donovan et al., (1976) proposed a dextral strike-slip offset of 'considerable amount', based upon the reconstruction of Devonian palaeogeography. Rogers et al., (1989) suggested that the fault is an inverted syn-depositional normal fault. Séranne (1992) also suggested a major dextral strike-slip displacement, based upon field observations and mapping. In the study by Watts (2001) reverse movements along NE-SW trending gouge-filled faults were observed within outcrops adjacent to the MF trace. This is consistent with observations by Flinn (1977, 1992), who observed reverse slickenfibres on the MFP exposed at Hesti Geo. Watts (2001) and Conroy (1996) observed evidence for dextral shear within outcrops to the east of the MF, but it is unclear whether they are related to regional deformation, or early movements along the MFZ. It is also unclear whether the MF is in any way linked to the WBF, or is part of the WBFS.

The relative kinematic histories of the WBF, NF, and MF are presented in **Figure 5.12**, along with possible timings for the kinematic events.

The actual magnitudes of displacement along the WBF and the NF has been suggested by many authors (e.g. Flinn 1969, 1977, 1985, 1992, Donovan et al., 1976, Mykura and Phemister 1976, Rogers et al., 1989, Watts 2001).

A 65km dextral strike-slip offset along the WBF, of Mesozoic age, was first proposed by Flinn (1969). This was based on the matching and restoration of aeromagnetic anomalies to the south and west of Shetland associated with Devonian granites on either side of the WBF trace. Evidence for this dextral strike-slip offset has also been

presented by Mykura and Phemister (1976), who noted similarities between the Fair Isle sandstones to the east of the WBF, and the Walls sandstones to the west of the WBF, which are brought into proximity after restoration of 65km dextral offset. The same authors also noted that a suite of scapolite veins exposed to the west of the WBF would be restored to the only recognised scapolite veining to the east of the WBF by ~65km of dextral offset. A larger dextral displacement of 95km was suggested by Rogers et al., (1989) based on restoring the palaeogeography of Devonian basins and the distribution of later sedimentary rocks on Shetland.

However, even after restoring a 65km dextral offset along the WBF trace to match Devonian features, an earlier sinistral movement along the WBF is required by the lack of matching between the crystalline rocks exposed either side of the WBF trace (Flinn 1977, 1985, 1992). A ductile thrust exposed in the north west of Shetland (the Western Keolka shear zone (Pringle, 1970)) is thought to be the along-strike equivalent of the Moine Thrust that outcrops in northern Scotland. The ductile thrust outcrops ~1km to the west of the WBF trace and must therefore intersect the WBFP at depth. No trace of the thrust is found in Shetland on the eastern side of the WBF, suggesting that a sinistral displacement of the order of 100-200km must pre-date the dextral event (Flinn 1985, 1992).

A dextral strike-slip offset of 16km is recognised across the Nestings Fault by Flinn (1969, 1977), based on the restoration of the Devonian age Graven complex (section 5.1) and metamorphic rocks farther south. However, restoration of 16km does not provide a perfect match across the fault, and it is therefore probable that the displacement along the NF was oblique (Flinn 1985).

The magnitude of reverse movement along the Melby Fault is unknown.

CHAPTER 6 - FRACTURE CHARACTERISTICS FROM 1-D OUTCROP DATA, WBFS, SHETLAND, SCOTLAND

Fracture parameters have been collected along a series of 1-dimensional (1-D) line transects (section 1.9.1) from outcrops adjacent to four faults within the Walls Boundary Fault System (WBFS) – the Walls Boundary Fault (WBF) (**Figure 5.6**), the Aith Voe Fault (AVF) (**Figure 5.6**), the Nestings Fault (NF) (**Figure 5.11**) and the Melby Fault (MF) (**Figure 5.11**) (section 5.2). Where possible, vertical and horizontal line transects were measured on surfaces both parallel and perpendicular to the overall trend of the WBFS (N-S for WBF, NF and AVF, NE-SW for the MF) to measure all possible fracture orientations.

6.1 The Walls Boundary Fault

The following sections describe in detail the fracture orientations, infills, kinematics and spacing values measured from a number of localities (and various lithologies) adjacent to the Walls Boundary Fault Plane (WBFP) (section 5.2.1, **Figure 5.6**).

6.1.1 *Fracture orientation data*

Fracture orientations have been measured at a number of localities adjacent to the WBFP within a total of 5 different lithologies and are described below.

Psammite

Psammite is exposed interbedded with pelite along a coastal section at Ollaberry, to the west of the WBFP (section 5.2.1.1). A total of 5 stereographic projections (section 1.7.2) have been plotted to illustrate the change in fracture orientation within psammite with decreasing distance to the WBFP (**Figure 6.1**). The data are plotted as poles to fracture planes, and for each cluster of orientation values the mean girdle is shown which represents the mean fracture plane for that cluster.

In general, the number of fracture orientation clusters increases towards the WBFP. The two localities which lie closest to the WBFP (OL24 & OL22, stereonets D & E) both show a similar pattern of fracture orientations. The foliation at both of these localities strikes N-S parallel to the WBFP, but dips moderately to the E at locality OL24 and steeply to the W at locality OL22. The poles to fracture planes of fractures orientated NE-SW to NNE-SSW and SE-NW to ESE-WNW (green girdles on stereonets D & E) lie on the mean girdle of fractures which are parallel to the WBFP (red girdle). The intersection points of these 3 mean girdles (red and green) correspond approximately to the position of the clusters of fracture poles. The data sets collected closest to the WBFP (locality OL22) shows an additional set of mean fracture orientations, striking N-S and dipping shallowly to the E.

Pelite

Pelite is exposed interbedded with psammite, west of the WBFP, along a coastal section at Ollaberry (section 5.2.1.1). A total of 5 stereographic projections illustrating poles to fracture planes and mean fracture cluster girdles (section 1.7.2) have been plotted to analyse the change in fracture orientation within pelite with decreasing distance to the WBFP (**Figure 6.2**).

Only one cluster of fracture orientations is recognised, from the data set which was collected furthest from the WBFP (OL30). The cluster of fracture orientations is parallel to the strike and dip of the foliation at that locality. The rest of the stereonets show a scatter of fracture orientations and no strongly defined clusters.

Sandstone

Sandstone is exposed to the west of the WBFP at the Ness of Bixter, along a coastal section (section 5.2.1.3). Three stereographic projections are plotted in **Figure 6.3** to illustrate the change in fracture orientations adjacent to the WBFP within psammite. Fracture orientations are plotted as poles to fracture planes. No strong clusters are recognised on any of the data sets.

Calcareous metasediments

Calcareous metasediments are exposed at the Ness of Haggrister to the west of the WBFP, along the coast of Sullom Voe (section 5.2.1.2). Fracture orientations from three localities are plotted as poles to fracture planes with mean cluster girdles on

stereographic projections in **Figure 6.4**. Localities SU3 and SU4 have 2 common fracture orientation clusters striking NW-SE (parallel to the rock foliation) and NE-SW. Locality SU3 also has a cluster of fracture orientations striking N-S, parallel to the WBFP. The data set collected closest to the WBFP (SU12) shows a wide scatter of fracture orientations and no strongly defined clusters.

Granite .

Pink-coloured granite is exposed to the east of the WBFP at the Ness of Haggrister and along the coast of Sullom Voe. Three stereographic projections have been plotted to illustrate the change in fracture orientations with distance to the WBFP (**Figure 6.5**). Data collected furthest from the WBFP at locality SU21 shows a cluster of fracture orientations which strike parallel to the trend of the WBFP. The two data sets collected closer to the WBFP (SU17, SU18) both show a wide scatter of fracture orientations and no strongly defined clusters.

6.1.2 *Fracture infills and kinematic data*

Out of more than 2000 fractures measured within 5 lithologies adjacent to the WBFP, 223 filled fractures were recorded (11% of total) (**Figure 6.6**). The lithology with the most filled-fractures is granite (33% of measured fractures are filled). Overall, 6 different infills were observed – quartz, iron, epidote, albite, calcite and cataclasite, examples of which are illustrated in **Figure 6.7**. Some infills occur only within certain lithologies (e.g. epidote-filled fractures in granite, and calcite-filled fractures within calcareous metasediments), whereas other infills were observed within fractures from multiple lithologies (e.g. iron-filled fractures in pelite, psammite, granite and calcareous metasediments). Where multiple infills are observed within a single lithology, the different infills do not appear to occupy separate fracture orientations (e.g. quartz- and iron-filled fractures within psammite occupy the same fracture orientations), but multiple infills within individual fractures were not observed in the field. The percentage of filled fractures from each lithology are plotted against distance to the WBFP in **Figure 6.6 f – j**. Although there are few data points for each lithology, the sandstone and calcareous metasediments data sets show an increase in

filled fractures towards the WBFP. The other data sets show the peak of filled-fractures to be away from the fault plane.

Apparent offsets along fracture planes were occasionally recorded in the field, but lineations within fractures (i.e. slickenlines, slickenfibres (section 1.5.1.2)) were rarely observed, hence no kinematic data is presented here.

6.1.3 *Fracture spacing data*

Fracture spacing data sets have been collected at 20 localities, from 5 lithologies that lie adjacent to the WBFP (**Table 6.1**). Data has been collected along 1-dimensional line transects orientated parallel and perpendicular to the trend of the WBFP (N-S).

The sections below describe in detail fracture spacing parameters analysed from localities adjacent to the WBF.

6.1.3.1 Cumulative frequency 'v' spacing

Plots of spacing values measured from 1-dimensional line transects 'v' cumulative frequency are presented in **Figure 6.8**. Each graph represents a locality, and within each graph different data sets represent different transect orientations (see legends on graphs). The spacing values collected for all data sets plot as a straight line when the x-axis is plotted as a linear scale and the y-axis is plotted as a logarithmic scale, and therefore they are best described by an exponential distribution with a negative slope. This is confirmed when a Kolmogorov-Smirnov test (section 1.8.4.2) is carried out on each of the data sets. In some data sets there are data points that do not fall onto the best fit lines (on the right hand side of the graph). This is likely to be the result of under-representation of wide spacing values due to the limited size of the outcrops.

6.1.3.2 Mean spacing 'v' standard deviation

The mean and standard deviation values from data sets that are best fitted by an exponential distribution are expected to be similar. A plot of mean spacing versus standard deviation for data collected adjacent to the WBFP from 5 lithologies is presented in **Figure 6.9**. The majority of data points fall close to the x=y line suggesting that the data sets are best fitted to an exponential distribution.

Place	lithology	locality	~ distance to VFP (m)	transect name & orientation (degrees)	no. fractures measured	transect length (mm)	mean spacing (mm)	exponent from exponential spacing graph
Ollaberry	psammite	OL15	-170	T1 – 090	43	1430	33.26	0.0324
		OL22	-20	T1 98, T2 99 – 180	132	1379.5	10.45	0.0901
				T1 99 – 077	27	681	25.22	0.0473
				T2 98, T3 99 – vertical	69	652	9.45	0.1125
		OL24	-50	T6 98 – 270	88	147.7	1.68	0.9837
				T4 T5 98, T3 T4 99 - 180	88	2525	28.69	0.0374
		OL25	-130	T1 98 – 358	44	528	12.00	0.0755
				T2 99 – 270	58	353	6.09	0.1835
				T2 98, T1 99 – vertical	130	1058	11.60	0.1049
		OL28	-45	T2 – 340	62	2515	40.56	0.0314
				T1 – 061	30	1151	38.37	0.0321
		OL30	-1300	T5 T6 98, T2 T3 99 – 180	63	4343	68.94	0.0140
				T3 T4 98, T1 99 - 280	59	4688	79.46	0.0138
	pelite	OL24	-50	T1 98, T1 99 – 001	60	4213	70.22	0.0166
				T3 98, T2 99 – 093	31	2079	67.06	0.0163
		OL25	-130	T4 98 – 178	18	2420	134.44	0.0075
				T3 98, T3 99 – vertical	21	1715	81.67	0.0119
		OL27	-30	T2 – 022	25	929	37.16	0.0280
				T1 – 300	25	1505	60.20	0.0179
				T3 - vertical	13	686	52.77	0.0267
		OL29	-170	T1 T2 – 004	43	9119	212.07	0.0053
		OL30	-1300	T2 98, T2 99 – 100	51	3674	72.04	0.0168
				T1 98, T1 99 – 012	35	6697	191.34	0.0053

Table 6.1 Details of 1-dimensional line transects adjacent to the WBFP used to analyse fracture spacing.
Negative distances represent localities west of the WBFP, positive distances represent localities east of the WBFP.
(continued on next page)

Place	lithology	locality	~ distance to VFP (m)	transect name & orientation (degrees)	no. fractures measured	transect length (mm)	mean spacing (mm)	exponent from exponential spacing graph
Sullom	calcareous metasediments	SU3	-245	T1 – 169	32	1971	61.59	0.0219
				T2 – vertical	21	1032	49.14	0.0217
		SU4	-150	T1 – 160	44	1542	35.05	0.0214
				T2 – vertical	21	1095	52.14	0.0199
		SU12	-15	T1 T4 – 000	97	2466	25.42	0.0407
				T2 – 085	26	866	33.31	0.0396
				T3 – vertical	19	364	19.21	0.0444
	granite	SU17	225	T4 T5 - 180	32	1542	48.19	0.0297
				T1 T2 T3 - 270	40	1131	28.28	0.0394
				T6 – vertical	7	118	16.86	0.0517
		SU18	15	T3 – 354	24	331	13.67	0.0666
				T1 T4 - 261	77	1488	19.32	0.0637
				T2 – vertical	24	520	21.67	0.0477
		SU21	280	T1 T3 – 090	42	1688	40.19	0.0229
				T4 – 340	39	1969	50.49	0.0271
Bixter	sandstone	BI1	-400	T1 – 150	84	885.5	10.54	0.1018
				T2 vertical	15	423	28.20	0.0345
		BI2	-535	T1 – 170	50	710	14.20	0.0674
				T2 - 077	26	527	20.05	0.0748
		BI9	-100	T1 – 185	77	341.5	4.44	0.1926
				T2 – 275	49	354	7.22	0.1509

Table 6.1 Details of 1-dimensional line transects adjacent to the WBFP used to analyse fracture spacing.
Negative distances represent localities west of the WBFP, positive distances represent localities east of the WBFP.
(continued from previous page)

6.1.3.3 Co-efficient of variation

The co-efficient of variation (Cv) is a measure of the degree of clustering within a data set (section 1.8.5.1). For data sets that are best described by an exponential distribution, the Cv values are expected to be close to 1 which represents a random distribution of data values. Values of Cv are plotted in **Figure 6.10**, and are distinguished for different lithologies (**Figure 6.10 a, b**) and different transect orientations (**Figure 6.10 c**). The majority of Cv values appear to be <1, suggesting that the data sets are slightly anti-clustered (**Figure 6.10 a**). Both the highest and lowest values of Cv (highest Cv = 1.52, lowest Cv = 0.54) occur in the centre of the fault and are measured from fractures contained within a psammitic lithology. Away from the centre of the fault, data sets from all lithologies show a narrower range of Cv values (**Figure 6.10 b**). Transects measured parallel to the WBFP, which measure attributes of fractures that are perpendicular to the WBFP, record the only values of Cv that are >1, suggesting that along these transects some clustering of fractures occurs (**Figure 6.10 c**). Data sets collected from transects measured both vertically and perpendicular to the WBFP all record Cv values <1. The highest value of Cv measured from all transects is 1.52, which is observed near to the centre of the WBFP, recorded from a transect orientated parallel to the WBFP within psammite.

6.1.3.4 Cumulative frequency exponent 'v' distance to WBFP

The change in fracture spacing adjacent to the WBFP can be assessed by plotting the exponent (slope) values from the spacing graphs plotted in **Figure 6.8** (**Table 6.1**). High exponent values represent a relatively large number of narrow spacings, and suggest a higher fracture density. Exponent values from the three transect orientations (fault parallel, fault perpendicular and vertical) are plotted against the perpendicular distance to the WBFP in **Figure 6.11**, and are distinguished for different lithologies. Each lithological data set collected both parallel and perpendicular to the WBFP illustrates an increase in exponent value towards the centre of the WBF. For data sets collected from vertical transects, little/no change in exponent value is observed towards the centre of the WBF. From transects measured perpendicular to the WBFP (**Figure 6.11 a, b**) and vertically (**Figure 6.11 d**) the highest exponent values are observed from fractures within psammite. The highest exponent values measured from transects orientated parallel to the WBFP (**Figure 6.11 b**) are observed for the

sandstone data set. At the centre of the WBF, the lowest values of exponent from each transect orientation is observed from the pelitic data set.

6.1.3.5 Mean spacing 'v' distance to WBFP

The change in fracture spacing with distance can also be assessed by plotting the mean fracture spacing from each lithology (**Figure 6.12 a**) and each transect orientation (**Figure 6.12 b**) against the perpendicular distance to the WBFP (**Table 6.1**). For each lithological data set, the values of mean spacing decrease towards the centre of the fault (**Figure 6.12 a**). The lowest values of mean spacing (i.e. most densely fractured data sets) occur at the centre of the WBFP, and are measured within psammite and sandstone. Mean spacing values from the pelitic data sets show the highest values of mean spacing and therefore fracturing within this lithology is suggested to be less dense (**Figure 6.12 a**). The highest values of mean spacing are measured from transects orientated parallel to the WBFP (**Figure 6.12 b**).

6.1.3.6 Mean spacing 'v' cumulative frequency exponent

The mean value is a defining aspect of an exponential distribution, and therefore a good relationship between the mean values and exponents from exponentially distributed data sets is expected (section 1.8.2.3). The spacing data collected adjacent to the WBFP along 1-dimensional line transects show a good power-law relationship between mean and exponent values, with a power-law exponent value of -0.9992 (**Figure 6.13**).

6.1.3.7 "Step" plots of fracture spacing 'v' distance along 1-dimensional transects

To analyse the change in fracture spacing and the density of fracturing along a 1-dimensional transect, the cumulative fracture frequency can be plotted against the distance along the transect (cumulative fracture spacing) (section 1.8.5.2). The 1-dimensional line transects must be of sufficient length (defined as greater than approximately 2m in this study except for very dense fracturing where shorter transects are sufficient) to illustrate the change in fracturing. A total of 32 line transects (16 parallel and 16 perpendicular to the WBF trend) from 5 lithologies have been selected and plotted (**Figure 6.14**), each measured at varying distances to the WBFP.

Psammite

For transects measured parallel to the WBFP, localities closest to the centre of the fault show the steepest slopes, and the slope decreases with increasing distance to the WBFP (**Figure 6.14 a**). This suggests that fracture density is highest at the WBFP, and decreases away from the centre of the fault. For transects measured perpendicular to the WBFP, two localities show very steep slopes (OL24, OL25), even though these localities are not closest to the centre of the fault (**Figure 6.14 b**). These are the same data sets that record very high values of exponential spacing exponent (**Figure 6.11 a**, **Table 6.1**) adjacent to the WBFP. Transects orientated perpendicular to the WBF trend measure the attributes of fractures that are parallel to the WBFP and therefore parallel to the rock bedding/foliation/lamination. There are 2 possible explanations for these abnormally steep slopes, either 1) the data sets were collected in high strain zones which occur parallel to the WBFP, or 2) differences in grainsize of the psammite, lithology may lead to a more finely bedded rock, and later fracturing has preferentially used these closely spaced surfaces (**Figure 6.15**), i.e. bed thickness has a control on fracture spacings (section 1.7.4.3.1). The other data sets that are plotted on **Figure 6.14** do not show such a high fracture density, but instead the slope (and therefore fracture density) decreases with increasing distance to the WBFP.

All of the data sets collected from psammite show relatively straight-line plots in **Figure 6.14 a, b**. This suggests that little/no clustering of fractures occurs over the scale of observation.

Pelite

The two localities closest to the WBFP (OL24 & OL27) show the steepest slopes from transect orientated parallel to the WBFP (**Figure 6.14 c**), suggesting that fracture density is highest at these localities. The slope of the data sets then decreases away from the centre of the fault, suggesting that fracture density also decreases. From transects measured perpendicular to the WBFP, all 3 data sets show very similar slopes. This suggests that the density of fractures parallel to the WBF trend within pelite does not change significantly with increasing distance from the WBFP.

Again, all of the data sets do not show any significant "stepping" in either **Figure 6.14 c** or **d**, suggesting that at this scale of observation, little or no clustering of fractures occurs.

Sandstone

The transects carried out within sandstone adjacent to the WBFP are shorter than the preferred length (~2m) for plotting cumulative fracture frequency 'v' cumulative fracture spacing plots, which is due to insufficient amounts of exposure. However, although the data may not be as reliable as if longer transects were carried out, they show results that are consistent with those from other lithologies. For transects measured both parallel and perpendicular to the WBFP, steeper slopes are observed from data sets that have been collected closest to the centre of the fault (**Figure 6.14 e, f**). This suggests that fractures both parallel and perpendicular to the WBFP show an increase in density towards the WBFP.

Calcareous metasediments

Transects measured within calcareous metasediments orientated both parallel and perpendicular to the WBF trend show little/no change in slope with increasing distance to the WBFP (**Figure 6.14 g, h**). This suggests that there is little change in fracture density towards the centre of the WBFP for fractures measured within calcareous metasediments. Little/no clustering of fractures within calcareous metasediments is suggested by the straight-line nature of the data sets.

Granite

For both transects measured parallel and perpendicular to the WBF trend within granite, steeper slopes are observed from data sets collected closest to the WBFP, and a decrease in slope is observed with increasing distance from the centre of the fault (**Figure 6.14 g, h**). This suggests that the density of fractures orientated both parallel and perpendicular to the WBF trend increases towards the centre of the fault. Little stepping is observed from the data sets collected within granite, suggesting that there is little clustering of fractures.

6.1.4 *Summary of fracture data from 1-d line transects (WBF).*

A summary of fracture data collected within 5 lithologies adjacent to the WBFP along 1-dimensional line transects is presented in **Table 6.2**.

Place			Ollaberry		Bixter	Sullom	
Lithology			Psammite	Pelite	Sandstone	Calcareous metasediments	Granite
Data sets used			893 fractures measured from 6 localities, 13 1-D transects	322 fractures measured from 5 localities, 10 1-D transects	301 fractures measured from 3 localities, 6 1-D transects	260 fractures measured from 3 localities, 7 1-D transects	285 fractures measured from 3 localities, 8 1-D transects
Orientation			Overall increase in fracture orientation clusters towards WBFP. Localities closest to WBFP show 3 main clusters 1) N-S strike, parallel to WBFP, 2) NE-SW striking set, 3) NW-SE striking set. Poles to sets 2 & 3 lie on the mean girdle to set 1.	Only recognisable cluster occurs in data set collected furthest from WBFP. Data sets collected close to WBF show scatter of fracture orientations & no recognisable clusters.	No clusters of fracture orientations were recognised in any of the data sets.	Data sets collected at 245m and 150m from WBFP show 2 common fracture orientation clusters 1) NW-SE striking set, parallel to rock foliation, 2) NE-SW striking set. The data set collected closest to the WBFP shows no recognisable clusters	The data set collected furthest from the WBFP shows a cluster of fracture orientations striking parallel to the WBFP. Data sets collected closest to the WBFP show a scatter of orientations and no recognisable clusters.
Infill			Out of >2000 fractures, 223 filled-fractures were observed. Granite had most filled-fractures (33% of all fractures were filled). Overall 6 different infills observed – quartz, iron, epidote, albite, calcite and cataclasite. Some infills are only observed within 1 lithology (e.g. epidote in fractures in granite), other infills are observed within fractures in multiple lithologies. Where >1 infill is observed within a lithology, the infills do not appear to occupy separate fracture orientations. No individual fractures with multiple infills were observed.				
Spacing	Cumulative freq 'v' spacing		All data sets are best described by an exponential distribution.				
	mean 'v' standard deviation		Good linear relationship close to x = y line.				
	Coefficient of variation (Cv)		Majority of Cv values are slightly <1. Both highest (1.52) and lowest (0.54) values occur in the centre of the fault and are measured within psammite. Transects measured parallel to the WBFP record the only Cv values >1, suggesting slight clustering.				
	exponent 'v' distance to WBF		Each lithological data set from transects collected both parallel and perpendicular to the WBFP show an increase in exponent value towards the centre of the fault. Little/no change in exponent is observed towards the WBFP from vertical transects. Highest exponent values measured along perpendicular and vertical transects are from psammite, and along parallel transects is from sandstone. Lowest values of exponent from each transect orientation are observed from the pelitic data set.				
	mean spacing 'v' distance to WBF		Mean spacing values from each lithological data set decrease towards the centre of the fault. Lowest values of men spacing at the WBFP are observed from psammite and sandstone data sets, and highest values from the pelitic data set.				
	exponent 'v' mean spacing		Good power-law relationship using data from all lithologies, exponent value = 0.9992.				
	Cumulative frequency 'v' distance along transect	Transects parallel to WBF trend	Localities closest to the WBFP show steepest slopes, slope decreases away from the WBFP	Localities closest to the WBFP show steepest slopes, slope decreases away from the WBFP	Localities closest to the WBFP show steepest slopes, slope decreases away from the WBFP	Transects show little/no change in slope from various distances to the WBFP.	Localities closest to the WBFP show steepest slopes, slope decreases away from the WBFP
		Transects perp. to WBF trend	2 localities show very steep slopes due to the very small spacings between fractures. Other localities show a decrease in slope away from the WBFP	All 3 data sets collected at various distances to WBFP show similar slopes.	Localities closest to the WBFP show steepest slopes, slope decreases away from the WBFP	Transects show little/no change in slope from various distances to the WBFP.	Localities closest to the WBFP show steepest slopes, slope decreases away from the WBFP

Table 6.2 Summary of fracture data collected and analysed along 1-dimensional line transects adjacent to the WBFP.

6.2 The Aith Voe Fault

The following sections describe in detail the fracture orientations, infills, kinematics and spacing values measured within granite at 3 localities adjacent to the Aith Voe Fault Plane (AVFP). The AVF is a N-S-striking, W-dipping reverse fault which is part of the Walls Boundary Fault System (WBFS), and links into the WBFP (section 5.2.1.4).

6.2.1 *Fracture orientation data*

Three stereographic projections of fracture orientations collected at different distances from the AVFP are presented in **Figure 6.16**. The data are plotted as poles to fracture planes, and for clusters of orientation values the mean girdle is shown which represents the mean fracture plane for that cluster. Data collected 400m and 240m from the AVFP both show a cluster of fractures orientated E-W, and dipping steeply to the S at locality SA3 and steeply to the N at locality SA6. The data sets collected furthest from the AVFP also shows a cluster of fracture orientation striking NE-SW and dipping steeply to the SE. The data set of fracture orientations collected closest to the AVFP (locality SA7, 15m from fault) does not show any obvious clusters. Instead, the poles to fracture planes lie along an E-W-striking girdle, which dips moderately to the south (084/ 50 S). The pole to this girdle (the beta-axis, 40/ 354) represents the intersection of the fracture planes, and could represent the transport direction within the WBFS at this locality.

6.2.2 *Fracture infills and kinematic data*

Out of the 277 fractures recorded in the field from the 3 localities, a total of 39 (14%) filled-fractures were observed. No filled fractures were recorded from locality SA3 (400m from WBFP). At locality SA6 (240m from WBFP), 23 zeolite and/or calcite-filled fractures were observed orientated mostly E-W (**Figure 6.17 b, c**). From the data set collected closest to the AVFP (locality SA7, 15m) 3 different fracture infills

were recorded, zeolite and/or calcite mineralisation being the most common, also observed were 3 gouge-filled fractures and 1 fracture with both zeolite and gouge (**Figure 6.17 a, c**). The filled-fractures at locality SA7 are mostly orientated NW-SE. Examples of zeolite-filled fractures from locality SA7 are presented in **Figure 6.18**. Apparent offsets along fracture planes were occasionally recorded in the field, but lineations within fractures (i.e. slickenlines, slickenfibres (section 1.5.1.2)) were rarely observed, hence no kinematic data is presented here.

6.2.3 *Fracture spacing data*

Fracture spacing data has been collected within granite from 3 localities adjacent to the AVFP, by carrying out a series of 1-dimensional line transects orientated parallel and perpendicular to the trend of the AVFP (N-S), and vertically.

6.2.3.1 Cumulative frequency 'v' spacing

Plots of cumulative frequency 'v' fracture spacing are presented in **Figure 6.19**. Each graph represents a locality, and within each graph different transect orientations are represented by different data sets (see legends on graphs). All of the data sets plot as straight lines when the x-axis is plotted as a linear scale and the y-axis is plotted as a logarithmic scale, and therefore they are best described by an exponential distribution. A Kolmogorov-Smirnov test (section 1.8.4.2) has been carried out on each of the data sets and confirms that the data are best described by an exponential distribution. Some data points do not fall onto the best-fit lines. This is likely to be the result of either the under-representation of wide spacing values due to the limited size of the outcrops (on the right hand side of the graph), or the under-representation of small spacing values due to the limits of resolution (on the left-hand side of the graph, e.g. locality SA7 T1)

6.2.3.2 Mean spacing 'v' standard deviation

For data sets that are best-fitted to an exponential distribution, the mean and standard deviation values are expected to be similar. A plot of mean 'v' standard deviation values from localities adjacent to the AVF is presented in **Figure 6.20** (**Table 6.3**). A good linear relationship is observed, with the data points lying close to the x = y line.

lithology	locality	distance to AVFP (m)	transect name & orientation (degrees)	number of fractures measured	transect length (mm)	mean spacing (mm)	exponent from exponential spacing graph
granite	SA3	400	T1 - 180	54	2241	41.50	0.0245
	SA3		T2 - 274	21	1456	69.33	0.0136
	SA6	240	T1 - 335	46	1048	22.78	0.0369
	SA6		T2 T3 vertical	24	1509	85.38	0.0182
	SA7	15	T1 - vertical	62	1098	17.71	0.0975
	SA7		T2 - 075	49	1257	25.65	0.0411
	SA7		T3 - 340	15	466	31.07	0.0402

Table 6.3 Details of 1-dimensional line transects adjacent to the AVFP used to analyse fracture spacing

6.2.3.3 Co-efficient of variation

To measure the amount of clustering within a data set, the co-efficient of variation may be calculated (section 1.8.5.1). For data sets that are best described by an exponential distribution, the Cv values are expected to be close to 1 which represents a random distribution of data values. Although there are few data points, the values of Cv from each transect orientation are very close to 1 for the 2 localities collected away from the AVFP, and appear to decrease towards the AVFP at locality SA7 (**Figure 6.21**). This suggests that close to the AVFP, the fractures are slightly anti-clustered (more regular) than would be expected for a perfect exponential distribution.

6.2.3.4 Cumulative frequency exponent 'v' distance to AVFP

Values of exponent calculated from best-fitting exponential distributions (**Figure 6.19**, **Table 6.3**) can be used to assess the change in fracture spacing adjacent to the AVFP, as high exponent values (steep slopes) represent a relatively large number of narrow spacings, and suggest a higher fracture density. Exponent values from the three transect orientations carried out at various distances to the AVFP are plotted against the perpendicular distance to the AVFP in **Figure 6.22**. Although there are few data points, each transect orientation shows an increase in exponent towards the AVFP, suggesting that fracture density within the granite is highest at the centre of the fault. Overall, the highest value of exponent (0.0975) recorded adjacent to the AVFP is from a vertical transect, suggesting that the density of sub-horizontal fractures is highest.

6.2.3.5 Mean spacing 'v' distance to AVFP

The mean spacing along 1-dimensional line transects can also be used as a measure of fracture density, and can be used to assess the change in fracture spacing when plotted against the perpendicular distance to the AVFP (**Figure 6.23**). Again, although there are few data points, the lowest values of mean spacing (and therefore the most dense fracturing) occur close to the centre of the AVFP for all transect orientations.

6.2.3.6 Mean spacing 'v' cumulative frequency exponent

A good relationship between the mean values and exponents from exponentially distributed data sets is expected, as the mean value is a defining aspect of an exponential distribution (section 1.8.2.3). Spacing data collected adjacent to the AVFP show a good power-law relationship between mean and exponent values, with a power-law exponent of -1.0076. (**Figure 6.24**).

6.2.3.7 "Step" plots of fracture spacing 'v' distance along 1-dimensional transects

Cumulative fracture frequency can be plotted against the distance along a 1-dimensional line transect (cumulative fracture spacing) to analyse the change in fracture spacing and the density of fracturing adjacent to the AVFP (section 1.8.5.2). The 1-dimensional line transects must be of sufficient length (defined as greater than approximately 2m in this study except for very dense fracturing where shorter transects are sufficient) to illustrate the change in fracturing. A total of 6 transects carried out within granite adjacent to the AVFP are between 1m & 2m in length, and are plotted in **Figure 6.25**, 2 from each transect orientation.

For each transect orientation, the steepest slopes are observed from the data sets that are closest to the AVFP, suggesting that the density of fractures that are both parallel and perpendicular to the AVFP and sub-horizontal, all increase towards the AVFP. The data sets show no obvious stepping patterns, suggesting that little/no clustering of fractures is observed at this scale of observation.

6.2.4 *Summary of fracture data from 1-d line transects (AVF).*

A summary of fracture data collected within granite adjacent to the AVFP along 1-dimensional line transects is presented in **Table 6.4**.

Place		Sand
Lithology		granite
Data sets used		>270 fractures measured from 3 localities, 7 1-dimensional line transects
Orientation		2 data sets collected furthest from AVFP (240m & 400m) show a cluster of fracture orientations striking E-W. Poles to fracture planes collected closest to the AVFP (15m) lie on a girdle (084/ 50 S), the beta axis (40/ 354) to which may represent the transport direction in the WBFS at this locality
Infill		14% of observed fractures at the 2 localities closest to the AVFP were filled. The data set collected furthest from the AVFP had no filled-fractures. Most common infill is zeolite/calcite mineralisation
Spacing	Cumulative frequency 'v' spacing	All data sets are best described by an exponential distribution.
	mean 'v' standard deviation	Good linear relationship close to x = y line.
	Coefficient of variation (Cv)	The 2 data sets collected furthest from the AVFP show Cv values very close to 1. Cv values from the data set closest to the AVFP are <1, suggesting anti-clustering.
	exponent 'v' distance to AVFP	Exponent values from each transect orientation increase towards the centre of the AVFP. Highest overall exponent collected from a vertical transect 15m from the AVFP.
	mean spacing 'v' distance to AVFP	Mean spacing values from each transect orientation decrease towards the centre of the AVFP.
	exponent 'v' mean spacing	Good power-law relationship, exponent value = 1.0076.
	Cumulative frequency 'v' distance along transect	Steepest slopes are observed closest to the centre of the fault for each transect orientation.

Table 6.4 Summary of fracture data collected and analysed along 1-dimensional line transects adjacent to the AVFP.

6.3 The Nestings Fault

The following sections describe in detail the fracture orientations, infills, kinematics and spacing values measured adjacent to the Nestings Fault Plane (AVFP), a N-S striking, strike-slip fault which is part of the Walls Boundary Fault System (WBFS), and links into the WBFP (section 5.2.2). Along the shores of Wadbister Voe, psammitic rocks are exposed to the east of the NFP and to the west of the NFP calcareous metasediments are exposed.

6.3.1 *Fracture orientation data*

Five stereographic projections of fracture orientations collected adjacent to the NFP are presented in **Figure 6.26**. Three are from data sets collected to the west of the NFP within calcareous metasediments, and two are from data sets collected to the east of the NFP within psammite. The data are plotted as poles to fracture planes, and for clusters of orientation values the mean girdle is shown which represents the mean fracture plane for that cluster.

Calcareous metasediments

The three data sets plotted in **Figure 6.26 a, b, c** are collected within calcareous metasediments at varying distances west of the NFP. All of the data sets show 2 main clusters of fracture orientations which are steeply dipping and trend N-S (parallel to the NFP) and ~E-W.

Psammite

Both data sets collected within psammite to the east of the NFP show 2 clusters of fracture orientations (**Figure 6.26 d, e**) which are moderately dipping, and trend NE-SW (parallel to the rock foliation), and E-W to ESE-WNW.

6.3.2 *Fracture infills and kinematic data*

No filled-fractures were recorded from transects carried out to the east of the NFP within psammite. To the west of the NFP, out of the 236 fractures recorded within calcareous metasediments from 3 localities, a total of 30 (13%) filled fractures were observed (**Figure 6.27 a**). Two different fracture infills occur, a set of steeply-dipping calcite-filled fractures trending ENE-WSW, and a set of N-S trending (fault parallel) quartz-filled fractures. The percentage of filled fractures increases towards the NFP for both types of fracture-fill (**Figure 6.27 b**). Examples of both types of filled fractures are presented in **Figure 6.27 c & d**. The relative ages of the infills is unclear. Kinematic indicators such as lineations on fracture planes (i.e. slickenlines, slickenfibres (section 1.5.1.2)) were rarely observed, although the NE-SW trending fractures (occasionally filled with calcite) were associated in the field with apparent dextral strike-slip movements, whereas the fractures orientated ENE-WSW and filled with calcite appear to be tensional.

6.3.3 *Fracture spacing data*

Fracture spacing data has been collected along a series of 1-dimensional line transects from both lithologies adjacent to the NFP (**Table 6.5**). Where possible, the line transects are orientated both parallel and perpendicular to the trend of the NFP (N-S), and vertically.

6.3.3.1 Cumulative frequency 'v' spacing

Spacing values measured from 1-dimensional line transects have been plotted against cumulative frequency, and are presented in **Figure 6.28**. Each locality is represented by one graph, and within each graph different data sets represent different transect orientations (see legends on graphs). The spacing values collected for all data sets are best described by an exponential distribution with a negative slope. This is confirmed when a Kolmogorov-Smirnov test (section 1.8.4.2) is carried out on each of the data sets. In some data sets there are data points that do not fall onto the best fit lines (on the right hand side of the graph). This is likely to be the result of under-representation of wide spacing values due to the limited size of the outcrops.

Place	lithology	locality	~ distance to NFP (m)	transect name & orientation (degrees)	number of fractures measured	transect length (mm)	mean spacing (mm)	exponent from exponential spacing graph
Wadbister Voe	calcareous metasediments	WA2	-520	T1 190	33	1924	58.30	0.0197
				T2 vertical	11	900	83.45	0.0113
				T3 275	24	1463	60.96	0.0174
		WA16	-235	T1 090	50	812	16.24	0.0646
				T2 T3 190	41	2558	62.39	0.0150
		WA17	-70	T1 189	45	1118	24.84	0.0358
				T2 101	24	554	23.08	0.0472
	psammite	WA19	50	T1 040	23	1867	81.17	0.0112
				T3 290	25	837	33.48	0.0385
		WA20	150	T1 vertical	15	1417	94.47	0.0093
				T2 T3 160	28	1883	67.25	0.0173
		WA18	25	T1 280	15	591	39.40	0.0520
				T2 190	9	159	17.56	0.0427

Table 6.5 Details of 1-dimensional line transects adjacent to the NFP used to analyse fracture spacing. Negative distances represent localities to the west of the NFP, positive distances represent localities east of the NFP.

6.3.3.2 Mean spacing 'v' standard deviation

The mean and standard deviation values of data sets that are best described by an exponential distribution are expected to be similar due to the random nature of the data. A plot of mean and standard deviation values measured from localities adjacent to the NFP is presented in **Figure 6.29** (**Table 6.5**). A good linear relationship is observed between the two parameters, with the values lying close to the x = y line.

6.3.3.3 Co-efficient of variation

The co-efficient of variation (Cv) is a measure of the degree of clustering within a data set (section 1.8.5.1). For data sets that are best described by an exponential distribution, Cv values are expected to be close to 1 which represents no clustering within that data. Cv values from transects carried out at localities adjacent to the NFP are plotted in **Figure 6.30**. The data are distinguished for lithology (psammite values lie to the east of the NFP and are plotted as circles, calcareous metasediments lie to the west of the NFP and are plotted as squares), and for transect orientation. Although there are few data points, the majority of Cv values lie below the Cv = 1 line suggesting that the data sets are slightly more regular (i.e. anti-clustered) than would be expected for a perfectly random (and therefore exponential) data set.

Transects carried out to the west of the NFP within calcareous metasediments show little change in Cv value towards the centre of the NF. However, although there are few data points, Cv values collected from transects orientated both parallel and perpendicular to the NFP carried out within psammite show an increase in Cv value towards the centre of the fault. This suggests that within psammite, fracture spacing becomes slightly more clustered towards the centre of the NFP.

6.3.3.4 Cumulative frequency exponent 'v' distance to NFP

The change in fracture spacing adjacent to the NFP can be assessed by plotting the exponent values calculated from the best-fitting exponential distributions (**Figure 6.28, Table 6.5**) against the distance to the NFP. Exponent values from both lithologies adjacent to the NFP are plotted against distance to the NFP in **Figure 6.31**, and are distinguished for transect orientation. Although there are few data points, the values of exponent from both lithologies generally increase towards the NFP

suggesting that fracture density is highest at the centre of the fault. The apparently high value of exponent that occurs 235m to the west of the NFP within calcareous metasediments may represent a local increase in fracture density due to the occurrence of a metre-scale fault, not observed in the field due to poor exposure.

6.3.3.5 Mean spacing 'v' distance to NFP

Fracture density can also be assessed by plotting the mean spacing values calculated from 1-dimensional line transects against the perpendicular distance to the NFP (**Figure 6.32**). Again, although there are few data points, the lowest values of mean spacing (and therefore the most dense fracturing) occur close to the centre of the NFP for all transect orientations, except for an anomalously low value 235m to the west of the NFP.

6.3.3.6 Mean spacing 'v' cumulative frequency exponent

A good relationship between the mean values and exponents from exponentially distributed data sets is expected, as the mean value forms part of the definition of an exponential distribution (section 1.8.2.3). Spacing data collected adjacent to the NFP show a good power-law relationship between mean and exponent values, with a power-law exponent of -1.002. (**Figure 6.33**).

6.3.3.7 "Step" plots of fracture spacing 'v' distance along 1-dimensional transects

Cumulative fracture frequency can be plotted against the distance along a 1-dimensional line transect (cumulative fracture spacing) to analyse the change in fracture spacing and the density of fracturing adjacent to the NFP (section 1.8.5.2). The 1-dimensional line transects must be of sufficient length (defined as greater than approximately 2m in this study except for very dense fracturing where shorter transects are sufficient) to illustrate the change in fracturing. No vertical transects are long enough to be plotted, but transects orientated parallel and perpendicular to the NFP within psammite and calcareous metasediments are plotted in **Figure 6.34**.

Calcareous metasediments

For each transect orientation, the steepest slopes are observed from the data sets that are closest to the NFP, suggesting that the density of fractures that are both parallel and perpendicular to the NFP increases towards the NFP (**Figure 6.34**). The data sets

show no obvious stepping patterns, suggesting that little/no clustering of fractures is observed at this scale of observation.

Psammite

Some of the transects carried out within psammite and plotted in **Figure 6.34** are shorter than the preferred length (~2m) for plotting cumulative fracture frequency 'v' cumulative fracture spacing plots, which is due to insufficient exposure. However, transects orientated both parallel and perpendicular to the NFP are plotted in **Figure 6.34** and show little change in slope with increasing distance to the NFP from either transect orientation. This suggests that the density of fractures both parallel and perpendicular to the NF trend within psammite does not change significantly with increasing distance from the NFP, but may be due to the insufficient length of the transects.

6.3.4 *Summary of fracture data from 1-d line transects (NF).*

A summary of fracture data collected within psammite and calcareous metasediments adjacent to the NFP along 1-dimensional line transects is presented in **Table 6.6**.

6.4 The Melby Fault

The following sections describe the fracture orientations, infills, kinematics and spacing values measured within basement rocks and volcani-clastic rocks adjacent to the Melby Fault Plane (MFP). The MF is a NE-SW-striking, NW-dipping, dip-slip fault that is considered to be part of the Walls Boundary Fault System (WBFS) (section 5.2.3).

		Wadbister Voe	Wadbister Voe
Lithology		Calcareous metasediments	Psammite
Data sets used		>220 fractures measured from 3 localities & 7 1-dimensional line transects	>110 fractures measured from 3 localities & 6 1-dimensional line transects
Orientation		All 3 data sets collected at varying distances to NFP show 2 main clusters of fracture orientations striking N-S and ~E-W, both are steeply dipping,	Data sets collected 150m and 50m from NFP both show 2 clusters of fracture orientations striking NE-SW and E-W to ESE-WNW, both are moderately dipping.
Infill		13% of observed fractures at the 3 localities were filled. Two different infills occur a) calcite which fills steeply dipping ENE-WSW trending fractures, and b) quartz which fills N-S trending fractures.	No filled fractures were recorded.
Spacing	Cumulative frequency 'v' spacing	All data sets are best described by an exponential distribution.	
	mean 'v' standard deviation	Good linear relationship close to x = y line.	Good linear relationship close to x = y line.
	Coefficient of variation (Cv)	Cv values are all at or slightly below 1. Little change in Cv value is observed with increasing distance to the NFP.	Cv values from transects parallel and perpendicular to the NFP both increase towards the centre of the NF (few data points)
	exponent 'v' distance to AVFP	Few data points, but exponent values from both lithologies generally increase towards the centre of the fault. One anomalously high value 235m to west of NFP (in calc. metaseds.).	
	mean spacing 'v' distance to AVFP	Few data points, but mean spacing values from both lithologies generally decrease towards the centre of the fault. One anomalously low value 235m to west of NFP (in calc. metaseds.).	
	exponent 'v' mean spacing	Good power-law relationship, exponent value = 1.002.	
	Cumulative frequency 'v' distance along transect	Steepest slopes are observed closest to the centre of the fault for transects orientated both parallel and perpendicular to the NFP.	Little change in slope observed towards the centre of the fault for transects orientated both parallel and perpendicular to the NFP. (transect lines are relatively short)

Table 6.6 Summary of fracture data collected and analysed along 1-dimensional line transects adjacent to the NFP.

6.4.1 *Fracture orientation data*

Stereographic projections of fracture orientations collected adjacent to the MFP are presented in **Figure 6.35**. Three stereonets are from data sets collected to the west of the MFP within volcani-clastic rocks, and three are from data sets collected to the east of the MFP within undifferentiated basement rocks. The data are plotted as poles to fracture planes, and for clusters of orientation values the mean girdle is shown which represents the mean fracture plane for that cluster.

Volcani-clastic rocks

Two clusters of fracture orientations are identified from data sets collected within volcani-clastic rocks exposed to the west of the MFP. A set of fractures that strike parallel to the MFP (NE-SW) are observed at localities closest to the MFP (ME2 & ME3); a set of fractures striking NNW-SSW is also observed at locality ME3 (closest to the MFP) and at locality ME8.

Undifferentiated basement rocks

The data set of fracture orientations collected closest to the MFP (ME5) shows the only cluster observed within data sets collected in basement rocks. The cluster of fractures is parallel to the trend of the MFP (NE-SW). The poles to the other fracture planes collected at locality ME5, lie on a girdle parallel to the MFP, trending NE-SW, and dipping to the SE. Data sets collected farther from the MFP (ME4, ME10 & ME11) show no obvious clustering of fracture orientations.

6.4.2 *Fracture infills and kinematic data*

No filled-fractures were recorded from transects carried out to the west of the MFP within volcani-clastic rocks. To the east of the MFP, out of the 302 fractures recorded within basement rocks, a total of only 13 (4%) filled fractures were observed. Three different fracture infills occur - calcite, quartz and iron mineralisation. The individual infills do not correspond to separate fracture orientations, and no clusters are

recognised for any of the infills. The percentage of fractures filled with calcite and quartz increases towards the centre of the MF (**Figure 6.36**)

Kinematic indicators such as lineations on fracture planes (i.e. slickenlines, slickenfibres (section 1.5.1.2)) were rarely observed from either lithology.

6.4.3 *Fracture spacing data*

Fracture spacings have been measured along a series of 1-dimensional line transects from both lithologies adjacent to the MFP. Where possible, depending on exposure, the line transects are orientated both parallel and perpendicular to the trend of the MFP (NE-SW), and vertically.

6.4.3.1 Cumulative frequency 'v' spacing

Fracture spacing values collected from 7 localities adjacent to the MFP are plotted against cumulative frequency in **Figure 6.37**. Each locality is represented by an individual graph, and within each graph, the different coloured data sets represent different transect orientations (see legends on graphs). All of the fracture spacing data sets collected both east and west of the MFP are best described by an exponential distribution, plotting as straight lines on when the x-axis is plotted as a linear scale and the y-axis is plotted as a logarithmic scale. This is confirmed when a Kolmogorov-Smirnov test (section 1.8.4.2) is carried out on each of the data sets. Some data points do not fall onto the best-fit lines. This is likely to be the result of the under-representation of wide spacing values due to the limited size of the outcrops.

6.4.3.2 Mean spacing 'v' standard deviation

Data sets that are best-described by an exponential distribution are expected to have similar values of mean and standard deviation (section 1.8.2.3). A plot of mean and standard deviation values measured from localities adjacent to the MFP is presented in **Figure 6.38** (**Table 6.7**). A good linear relationship is observed between the two parameters, with the values lying close to the x = y line.

Place	lithology	locality	~ distance to MFP (m)	transect name & orientation (degrees)	number of fractures measured	transect length (mm)	mean spacing (mm)	exponent from exponential spacing graph
Melby	volcani-clastic rocks	ME2	-225	T1 - 305	42	871	20.74	0.0472
				T2 - 010	42	1706	40.62	0.0320
		ME3	-150	T1 - 060	62	1682	27.13	0.0488
				T2 - 310	43	1802	41.91	0.0256
		ME8	-660	T1 - 250	43	5574	129.63	0.0071
				T2 - vert	11	1284	116.82	0.0106
	undifferentiated basement rocks	ME4	140	T1 - 035	29	1167	40.24	0.0306
				T2 T3 - ~100	46	1511	32.85	0.0333
		ME5	70	T1 - 030	39	1266	32.46	0.0321
				T2 - vert	34	864	25.41	0.0540
		ME10	1470	T1 - 220	52	3901	75.02	0.0147
				T2 - 313	22	3999	182.68	0.0045
				T3 - vert	8	1010	126.25	0.0174
		ME11	1600	T1 - 040	44	3161	71.84	0.0156

Table 6.7 Details of 1-dimensional line transects adjacent to the MFP used to analyse fracture spacing. Negative distances represent localities to the west of the MFP, positive distances represent localities to the east of the MFP.

6.4.3.3 Co-efficient of variation

The co-efficient of variation (section 1.8.5.1) may be calculated to assess the amount of clustering within a data set. For data sets that are best described by an exponential distribution, the Cv values are expected to be close to 1 which represents a random distribution of data values. Values of Cv measured from transects carried out adjacent to the MFP are plotted against the perpendicular distance to the MFP in **Figure 6.39**. The values are divided by lithology (different symbols), and into the different transect orientations (different colours). Although there are few data points the majority of values are < 1, which suggests that fracturing adjacent to the MFP is slightly more regular than would be expected for perfectly exponential data sets. There are no obvious changes in Cv value with distance from the MFP, although the highest variation in Cv values is displayed by data collected from vertical transects.

6.4.3.4 Cumulative frequency exponent 'v' distance to MFP

The exponent values (slopes) calculated by plotting cumulative frequency graphs (**Figure 6.37, Table 6.7**) can be used as a measure of fracture density, as the higher exponents (steeper slopes) correspond to relatively more small fracture spacings (and therefore higher fracture densities). The exponent values from spacings measured adjacent to the MFP are plotted in **Figure 6.40** against the perpendicular distance to the MFP. Again the data points are distinguished for both lithology (by symbol) and transect orientation (by colour). Although there are few data points, the highest values of exponents from each lithology occur closest to the centre of the fault, suggesting that, as expected, this is where fracture density is highest.

6.4.3.5 Mean spacing 'v' distance to MFP

The mean spacing along 1-dimensional line transects can also be used as a measure of fracture density, and can be used to assess the change in fracture spacing when plotted against the perpendicular distance to the MFP (**Figure 6.41, Table 6.7**). Again, although there are few data points, the lowest values of mean spacing (and therefore the most dense fracturing) occur close to the centre of the MFP for lithologies.

6.4.3.6 Mean spacing 'v' cumulative frequency exponent

The mean value is used as part of the definition of an exponential data set, and so a good relationship between the exponent values and mean values from data best-

described by an exponential data set is expected. The values of mean spacing from localities adjacent to the MFP are plotted against exponential exponent values in **Figure 6.42**, shown on both logarithmic-logarithmic and linear-linear axes. A good power-law relationship is observed with an exponent value of -1.009.

6.4.3.7 "Step" plots of fracture spacing 'v' distance along 1-dimensional transects

Cumulative fracture frequency can be plotted against the distance along a 1-dimensional line transect (cumulative fracture spacing) to analyse the change in fracture spacing and the density of fracturing adjacent to the MFP (section 1.8.5.2). The 1-dimensional line transects must be of sufficient length (defined as greater than approximately 2m in this study except for very dense fracturing where shorter transects are sufficient) to illustrate the change in fracturing.

Transects orientated both parallel and perpendicular to the MF, and collected at varying distances from the MFP, are plotted in **Figure 6.43** from both lithologies. For each transect orientation, and for each lithological data set, the steepest slopes are observed from the data sets that are closest to the MFP, suggesting that the density of fractures that are both parallel and perpendicular to the MFP increases towards the centre of the fault. The data sets show no well-defined or predominant stepping patterns, suggesting that little/no significant clustering of fractures is observed at this scale of observation.

6.4.4 *Summary of fracture data from 1-d line transects (MF).*

A summary of fracture data collected from basement and volcani-clastic lithologies adjacent to the MFP along 1-dimensional line transects is presented in **Table 6.8**.

		Melby	Melby
Lithology		Undifferentiated basement	Volcani-clastics
Data sets used		>300 fractures measured from 4 localities & 8 1-dimensional line transects	>240 fractures measured from 3 localities & 6 1-dimensional line transects
Orientation		2 clusters of fracture orientations identified, striking NE-SW (parallel to MFP) and NNW-SSE. Locality closest to MFP shows both clusters	1 cluster observed striking NE-SW (parallel to MFP) from data set collected closest to MFP. Data sets collected further from MFP show no obvious clusters.
Infill		4% of observed fractures at the 4 localities were filled. 3 different infills occur – calcite, quartz & iron mineralisation, no predominant orientations	No filled fractures were recorded.
Spacing	Cumulative frequency 'v' spacing	All data sets are best described by an exponential distribution.	
	mean 'v' standard deviation	Good linear relationship close to x = y line.	Good linear relationship close to x = y line.
	Coefficient of variation (Cv)	Most of values are slightly <1. No obvious changes in Cv with increasing distance from MFP.	Most of values are slightly <1. No obvious changes in Cv with increasing distance from MFP.
	exponent 'v' distance to AVFP	Few data points, but exponent values from both lithologies generally increase towards the centre of the fault.	
	mean spacing 'v' distance to AVFP	Few data points, but mean spacing values from both lithologies generally decrease towards the centre of the fault.	
	exponent 'v' mean spacing	Good power-law relationship, exponent value = 1.009.	
	Cumulative frequency 'v' distance along transect	Steepest slopes are observed closest to the centre of the fault for transects orientated both parallel and perpendicular to the MFP.	Steepest slopes are observed closest to the centre of the fault for transects orientated both parallel and perpendicular to the MFP.

Table 6.8 Summary of fracture data collected and analysed along 1-dimensional line transects adjacent to the MFP.

6.5 Summary of 1-dimensional fracture data from the WBFS

6.5.1 *Fracture orientation and infill data*

6.5.1.1 The Walls Boundary Fault Zone (including the Aith Voe Fault)

Patterns of fracture orientations observed adjacent to the WBF are variable, depending on the lithology in which the fracturing occurs. The psammitic data set shows the strongest degree of clustering of fracture orientations from data sets collected at 5 different distances from the WBFP. A strong foliation-parallel cluster of fractures is observed, striking N-S adjacent to the WBFP and NE-SW at distances >1km from the WBFP. At distances less than ~200m from the WBFP within psammite, other fracture orientations occur, the poles of which lie on the mean girdle of fractures parallel to the rock foliation (and WBF trend). Clusters of fracture orientations that lie parallel to the rock foliation also occur within calcareous metasediments at distances >150m from the fault plane. The data set of fractures collected closest to the WBFP within calcareous metasediments shows no obvious clustering of fracture orientations. Data sets of fracture orientations collected within other lithologies adjacent to the WBFP (granite, pelite, and sandstone) all show a large degree of scatter, with little/no clustering. The poles to fracture orientations measured 15m from the AVFP (a N-S trending, kilometre-scale reverse fault, that lies within the WBFZ, section 5.2.1.4) lie on a girdle that trends ~E-W, the pole to which lies close to the girdle corresponding to the AVFP (and WBFP). The pole may represent the transport direction at this locality and suggests an overall strike-slip movement.

Overall, six different types of fracture-fills were observed within rocks adjacent to the WBFP (quartz, iron, calcite, epidote, albite and cataclasite). Two infills are confined to a single lithology (epidote within granite and calcite within calcareous metasediments), whereas the other infills were observed within multiple lithologies. There is little data for each infill within individual lithologies, but the overall percentage of filled-fractures appears to increase towards the WBFP for both

sandstone and calcareous metasediment data sets. The data sets of filled-fractures collected within pelite and psammite adjacent to the WBFP, and within granite adjacent to the WBFP and the AVFP show a higher percentage of filled fractures ~200m from the fault planes. This may be a real feature of the data, but may also be attributed to insufficient information.

6.5.1.2 The Nestings Fault

Fracture orientations measured within both lithologies adjacent to the NFP show some degree of clustering. To the west within calcareous metasediments, 2 main fracture orientations are observed, trending N-S (parallel to the rock foliation and the trend of the NFP), and E-W to ESE-WNW. To the east within psammite, both data sets collected also show 2 main clusters, trending NE-SW (parallel to the rock foliation) and E-W to ESE-WNW.

No filled fractures were observed within psammite to the east of the NFP. To the west of the NFP, fractures filled with calcite and quartz were observed. The frequency of both types of filled-fractures increases towards the NFP. Their relative ages are unclear.

6.5.1.3 The Melby Fault

All data sets of fracture orientations collected adjacent to the MFP show a NE-SW trending cluster, parallel to the trend of the MFP, dipping to the SE within volcaniclastic rocks west of the MFP, and dipping to the NW within basement rocks to the east of the MFP. The data set of fracture orientations collected closest to the MFP within basement rocks (east of the MFP, locality ME5) shows a strong cluster of fractures orientated NE-SW, with numerous other poles to fracture planes lying on the NE-SW girdle.

No filled fractures were observed to the west of the MFP. To the east of the MFP, fractures filled with calcite, quartz and iron were observed. Although there are few data points, the percentage of fractures filled with quartz and calcite increases towards the MFP, whereas the percentage of iron-filled fractures decreases.

6.5.2 *Fracture kinematic data*

Very few kinematic indicators were observed in the field within lithologies adjacent to the WBFP, AVFP, MFP and NFP, therefore no kinematic data is presented.

6.5.3 *Fracture spacing data*

Cumulative frequency plots of fracture spacing values for all 1-dimensional line transects carried out adjacent to the WBF, AVF, MF and NF, within all lithologies, are all best described by an exponential distribution. As expected for exponentially distributed data, when mean spacing values are plotted against their corresponding standard deviation values, the data lie close to the x=y line (**Figure 6.44**). Some points lie below the x=y line suggesting that the fracture spacing data is slightly anit-clustered, which is supported by values of Cv being <1 for some data sets. Data collected adjacent to all faults, within all lithologies, show no consistent relationship between Cv (i.e. clustering) and distance to the fault planes. Some data sets show an increase in Cv towards the fault, others show a decrease, but most show no consistent change.

Values of exponent measured from the exponential spacing graphs for each lithology and adjacent to each fault, all increase towards the centre of the faults (**Figure 6.45**).

Mean fracture spacing values show an inverse relationship to the exponential exponent date, and decrease towards the centre of each fault, for each lithology.

A good relationship is observed between the mean spacing values and the exponential exponent values for all data sets, which is expected for exponential distributed data (**Figure 6.46**).

Finally, cumulative fracture frequency can be plotted against cumulative fracture spacing to investigate the distribution of fractures both parallel and perpendicular the fault trends, for each lithology. No obvious stepping was observed on any of the plots, suggesting that no significant clustering of fractures is observed at this scale. Most lithological data sets show an increase in slope towards the centre of the faults, suggesting an increase in fracture density towards each fault plane.

CHAPTER 7 - FRACTURE CHARACTERISTICS FROM 2-D OUTCROP DATA, WBFS, SHETLAND, SCOTLAND

Data sets for the analysis of fracture characteristics in 2-dimensions (2-D) were selected from localities adjacent to four faults within the Walls Boundary Fault System (WBFS), the main Walls Boundary Fault (WBF), the Nestings Fault (NF), the Aith Voe Fault (AVF) and the Melby Fault (MF) (section 5.2). Fracture spacing, length, and connectivity data are described and interpreted for each data set.

7.1 Data sets available for 2-dimensional analysis

In total, 23 field photographs from outcrop localities have been used to analyse fracture characteristics adjacent to four faults within the WBFS at outcrop scale (metre scale). A total of 7 different lithologies are present. The localities were chosen based on a) the quality and resolution of the photographs and b) varying distances to the fault planes, in order to represent a range of fracture densities and intensities (**Figure 7.1, Figure 7.2, Table 7.1**). Only outcrop data sets have been used, as inland the extensive peat cover means that faults and fractures cannot be traced on air photographs and Landsat images. Thin section data sets were also of insufficient quality to analyse fracture attributes. The fracture attributes in the following sections (spacing, length and connectivity) are analysed for each individual lithology, and then compared between lithologies and between fault data sets.

7.2 Fracture spacing

Fracture spacing data was collected from the data sets by using four methods (section 1.9.1), the same methods that were used to collect spacing data relative to the main faults from the MTFC, Norway (section 4.2)

	Fault	Place		Locality	Approx. perpendicular distance to fault plane (m)	lithology	photo area (cm²)	total number of fractures
Walls Boundary Fault System (WBFS)	WBF	Sullom	E of WBFP	SU13	18.75	granite	3421.49	270
				SU21	281	granite	16742.97	174
		Ollaberry .	W of WBFP	OL24 -1	51	pelite	44963.27	200
				OL29	172	pelite	9259.42	67
				OL30 –1 (fol. surface)	1333	psammite	4115.30	100
				OL30 –2 (fol. perp.)	1333	psammite	2500.11	79
				OL25	131	psammite	9251.32	491
				OL24 -2	51	psammite	1401.82	109
		Bixter	W of WBFP	BI2	535	sandstone	1883.33	277
				BI6	167	sandstone	9861.06	410
	NF	Wadbister Voe	W of NFP	WA16	235	calc-silicates	2347.12	117
				WA17	77	calc-silicates	1999.91	94
			E of NFP	WA19	153	psammite	13519.39	152
				WA20	51	psammite	14976.93	78
	AVF	Sand	E of AVF	SA3	407	granite	21680.26	205
				SA6	242	granite	23256.50	237
				SA7	16	granite	14467.84	332
	MF	Melby	W of MF	ME2	225	volcanics	12715.88	249
				ME8	663	volcanics	11843.29	71
			E of MF	ME4	138	basement	3854.08	211
				ME5	71	basement	9154.50	161
				ME10	1475	basement	69535.32	91
				ME11	1590	basement	57215.60	151

Table 7.1 Data sets used for analysis of fracture characteristics from WBFS

a) a set of 1-dimensional line transects parallel to the main fault trend (~N-S for WBF, NF & AVF and ~NE-SW for MF) to analyse the spacing population of fractures perpendicular to the main trend,
b) a set of 1-dimensional line transects perpendicular to the main fault trend (~E-W for WBF, NF, AVF and ~NW-SE for MF) to analyse the spacing population of fractures parallel to the main trend,
c) for data sets where the photographs are taken of vertical surfaces, a set of 1-dimensional line transects vertically across the photograph to analyse the spacing population of horizontal / sub-horizontal fractures,
d) for horizontal data sets, a transect every 30° across the data set to enable the creation of ellipses from the average fracture spacing in each orientation, and a comparison of fracture density between localities (section 1.7.4.2.2).

Methods a), b) and c) all involve six 1-dimensional line transects (i.e. multi-line sampling, section 1.9.1) in the same orientation to provide a data set large enough to analyse the spacing population. Method d) is only carried out on horizontal data sets. This is because a fracture map created for a vertical outcrop surface analyses the dip of the fractures and a fracture map created for a horizontal outcrop surface analyses the strike of the fractures.

Fracture spacing can be used to calculate fracture density, which is defined in this thesis as the total number of fractures (or spacings) per unit length along a 1-dimensional line transect, or the total number of fractures per unit area for a 2-dimensional data set (section 1.7.4.2). Fracture density is directly related to average spacing along 1-dimensional line transects. Fracture density in 2-dimensions is also directly related to fracture spacing, as the wider the spacing of the fractures the fewer fractures per unit area and vice versa.

Spacing values from 1-dimensional line transects carried out relative to all four faults are plotted against cumulative frequency in **Figure 7.3**. Each graph represents a locality, and within each graph the two data sets represent different transect orientations (see legend on graphs). On each graph, for each data set, the spacing data plot as straight lines when the x-axis is plotted as a linear scale and the y-axis is plotted as a logarithmic scale, and therefore they are best described by an exponential distribution with a negative slope. This is confirmed when a Kolmogorov-Smirnov test (section 1.8.4.2) is carried out on each of the data sets.

In some data sets there are data points that do not fall onto the best fit lines (on the right hand side of the graph). This is likely to be the result of either the under-representation of wide spacing values due to the limited size of the sample area, or over-representation of wide spacing values due to multi-line sampling (section 1.9.1). The mean and standard deviation values of a data set that is best described by an exponential distribution are expected to be similar. These parameters are plotted against each other in **Figure 7.4** for each data set from each fault within the WBFS and for all lithologies. As expected for exponential data, there is a good relationship between average spacing and standard deviation.

Also, if a data set is best described by an exponential distribution, the values are randomly distributed, that is neither clustered nor anti-clustered (regular). The degree of cluster within a data set can be measured by calculating the co-efficient of variation (Cv) (section 1.8.5.1) which is plotted in **Figure 7.5** for all data sets. The values of Cv are separated into different faults and different lithologies. The majority of Cv values lie close to, or slightly below the Cv = 1 line, suggesting random or slightly anti-clustered data sets. The highest value of Cv occurs within WBF psammite data set (Cv = 1.58), from locality OL30, ~1300m from the WBFP, and suggests clustering of fractures at this locality.

The exponents from the spacing graphs illustrated in **Figure 7.3** and **Table 7.2** are a relative measure of the abundance of small and large spacings, and can be used to assess the change in fracture spacing with distance to the faults, and also to investigate the effects of lithology on fracture spacing. The change in exponent with distance can be assessed for the three different transect orientations – vertical, fault parallel (horizontal transects) and fault perpendicular (horizontal transects), which all measure different fracture sets (**Figure 7.6**).

Although there are few data points for each data set (each fault and each lithology), some general relationships can be recognised. For each data set plotted in **Figure 7.6a** (transects perpendicular to the fault trend), the values of exponent are highest at the centre of the 3 faults for all 4 lithologies present, with the highest exponent value (correlating with the closest spaced fracturing and highest fracture density) occurring within the psammite data set collected adjacent to the WBF. Data sets plotted in **Figure 7.6b** (vertical transects), also show an increase in exponent towards the centre of the faults for each lithology except the psammite data set collected from the NF.

Walls Boundary Fault System (WBFS)	Fault	Place		Lithology	Locality	Transect orientation	Statistical distribution	Exponent	R^2
	WBF	Sullom	E of WBFP	Granite	SU13	horiz – 075 vertical	exponential exponential	0.05 0.0456	0.99 0.99
					SU21	horiz N-S horiz E-W	exponential exponential	0.0176 0.0236	0.99 0.99
		Ollaberry	W of WBFP	Pelite	OL24 -1	horiz N-S horiz E-W	exponential exponential	0.0081 0.0181	0.98 0.99
					OL29	horiz N-S horiz E-W	exponential exponential	0.0075 0.0122	0.98 0.98
				Psammite	OL30 -1	horiz – 036 vertical	exponential exponential	0.0278 0.025	0.99 0.99
					OL30 -2	horiz N-S horiz E-W	exponential exponential	0.0273 0.0342	0.98 0.98
					OL25	horiz N-S vertical	exponential exponential	0.0522 0.0468	0.99 0.99
					OL24 -2	horiz N-S horiz E-W	exponential exponential	0.0221 00277, 0.0925	0.99 0.97, 0.99
		Bixter	W of WBFP	Sandstone	BI2	horiz N-S vertical	exponential exponential	0.0649 0.0445	0.997 0.99
					BI6	horiz N-S horiz E-W	exponential exponential	0.0357 0.0538	0.99 0.98
	NF	Wadbister Voe	W of NFP	Calc-silicates	WA16	horiz – 190	exponential	0.0368	0.98
					WA17	horiz – 190	exponential	0.0495	0.99
			E of NFP	Psammite	WA19	horiz – 040 vertical	exponential exponential	0.0114 0:0251	0.99 0.99
					WA20	horiz – 040 vertical	exponential exponential	0.0121 0.0123	0.99 0.99
	AVF	Sand	E of AVF	Granite	SA3	horiz N-S horiz E-W	exponential exponential	0.0187 0.0164	0.98 0.99
					SA6	horiz – 335 vertical	exponential exponential	0.0169 0.0293	0.99 0.99
					SA7	horiz – 075 vertical	exponential exponential	0.0264 0.0383	0.99 0.99
	MF	Melby	W of MF	Volcani-clastics	ME2	horiz – 010 horiz 305	exponential exponential	0.025 0.0257	0.99 0.99
					ME8	horiz – 070 horiz – 160	exponential exponential	0.016 0.0154	0.99 0.98
			E of MF	Basement	ME4	horiz – 298 horiz – 035	exponential exponential	0.0381 0.0329	0.99 0.98
					ME5	horiz – 030 vertical	exponential exponential	0.0159 0.0175	0.99 0.995
					ME10	horiz – 045 vertical	exponential exponential	0.0043 0.0047	0.99 0.99
					ME11	horiz – 040	exponential	0.0067	0.99

Table 7.2 Best-fitting statistical distributions and exponent values for fracture spacings adjacent to faults within the WBFS.

The highest exponent value from the vertical transects occurs within the WBF psammite data set, as was the case for the fault perpendicular transects. The exponents from transects carried out parallel to the fault trends are plotted in **Figure 7.6c**. Out of a total of 8 data sets present (7 lithologies and 4 faults), the exponents from 3 data sets stay approximately the same with increasing distance to the centre of the faults (AVF granite, NF psammite, WBF pelite). A further 4 data sets (MF basement, MF volcani-clastics, NF calc-silicates, WBF psammite) all show an increase in exponent towards the centre of the faults, with the highest exponent again occurring within the WBF psammite data set. The exponent values from the remaining data set (WBF sandstone) decrease towards the centre of the fault.

The mean spacing values from each 1-dimensional transect can be also be used as an indicator of the change in spacing around faults, and although there are few data points for each fault and each lithology, some general relationships can be suggested. The mean spacing values are plotted in **Figure 7.7** for each fault and lithology, separated into the three transect orientations (perpendicular to the fault trend and parallel to the fault trend (both horizontal transects) and vertical transects). The values of mean spacing from each data set in **Figure 7.7a** (transects perpendicular to the overall fault trends) all decrease towards the centre of the faults. The lowest mean spacing is observed within the WBF psammite data set. The mean spacings from the vertical transects are plotted in **Figure 7.7b**, and again the values decrease towards the centre of the fault, except the data set from NF psammite. Again the lowest mean spacing is observed within the WBF psammite data set. Finally in **Figure 7.7c**, the mean spacings from transects orientated parallel to the overall fault trends are plotted against distance to the faults. For a total of 5 out of the 8 data sets (AVF granite, NF calc-silicates, NF psammite, WBF psammite and WBF sandstone) the mean spacing values do not change significantly with distance to the faults. The mean spacings from 2 of the data sets (MF basement and MF volcani-clastics) both decrease towards the centre of the fault, and for one data set (WBF pelite) the mean spacing slightly increases towards the centre of the fault.

If data sets are best described by an exponential distribution, then a relationship may be expected to exist between the mean spacing and the exponent values, since the mean is a defining aspect of an exponential distribution (section 1.8.2.3). The values of mean spacing and exponent from the WBFS illustrate a strong power-law

relationship when the data is plotted on both logarithmic and linear scales, with a power-law exponent of 0.91 (**Figure 7.8**).

The density of fracturing within a 2-dimensional area is dependent on the spacing of the fractures (section 1.7.4.2) and can be quantified in two ways a) by calculating an the area of an ellipse from the mean fracture spacings measured from transects carried out every 30° across the sample (only horizontal data sets), and b) by calculating the total number of fractures per unit area.

Out of the 23 data sets used to analyse spacing (**Figure 7.1, Figure 7.2, Table 7.1**), 10 data sets are photographs of horizontal/sub-horizontal outcrop surfaces of different lithologies, and have been used to create ellipses from mean spacing values (**Figure 7.9, Table 7.3**). Although there are few data sets for each lithology, some general observations can be made.

The ellipses presented in **Figure 7.9a** are created from two localities at different distances adjacent to the WBF that exhibit a pelitic lithology. Both ellipse sizes are similar suggesting that fracture density is approximately equal at both localities and does not change with distance to the fault for a pelitic lithology. Both ellipses are elongate in approximately a N-S direction suggesting that the mean spacing of fractures parallel to the overall fault trend is lowest (measured along the E-W transects) for a pelitic lithology.

The two ellipses plotted in **Figure 7.9b** are created from localities exhibiting a psammitic lithology at different distances adjacent to the WBF. Both ellipses are elongate in a N-S orientation, again suggesting that the mean spacing of fractures parallel to the overall fault trend is lowest for a psammitic lithology. The smallest ellipse out of the two data sets occurs closest to the fault (51m) suggesting that fracture density is higher close to the centre of the fault for a psammitic lithology.

Only one ellipse is created for sandstone adjacent to the WBF (**Figure 7.9c**). The ellipse is elongate in a N-S to NE-SW orientation, suggesting that the mean spacing of fractures orientated parallel to the WBF within sandstone is lowest.

Two ellipses are created for a granitic lithology (**Figure 7.9d**), one data set is collected adjacent to the WBF and the other data set is collected adjacent to the AVF. Both ellipses are elongate in a N-S to NE-SW orientation, suggesting that for a granitic lithology adjacent to both faults the mean spacing of fractures parallel to the faults are lowest. The ellipses in **Figure 7.9d** are approximately the same size suggesting that the fracture density in the granite is similar at both localities.

	Fault	Place		Locality	total number of fractures	Density	
						Area of average spacing ellipse (mm²)	Total number of fractures per cm²
Walls Boundary Fault System (WBFS)	WBF	Sullom	E of WBFP	SU13	270	not created	0.0789
				SU21	174	11418.12	0.0104
		Ollaberry	W of WBFP	OL24 -1	200	21088.18	0.0044
				OL29	67	19077.26	0.0072
				OL30 –1 (fol. surface)	100	not created	0.0243
				OL30 –2 (fol. perp.)	79	4989.56	0.0316
				OL25	491	not created	0.0531
				OL24 -2	109	1854.68	0.0778
		Bixter	W of WBFP	BI2	277	not created	0.1471
				BI6	410	2746.02	0.0416
	NF	Wadbister Voe	W of NFP	WA16	117	not created	0.0498
				WA17	94	not created	0.0470
			E of NFP	WA19	152	not created	0.0112
				WA20	78	not created	0.0052
	AVF	Sand	E of AVF	SA3	205	12722.92	0.0095
				SA6	237	not created	0.0102
				SA7	332	not created	0.0229
	MF	Melby	W of MF	ME2	249	7507.22	0.0196
				ME8	71	31231.88	0.0060
			E of MF	ME4	211	1763.94	0.0547
				ME5	161	not created	0.0176
				ME10	91	not created	0.0013
				ME11	151	not created	0.0026

Table 7.3 Fracture density values calculated from data sets adjacent to faults within the WBFS.

Two ellipses are created in **Figure 7.9e** for a volcani-clastic lithology adjacent to the MF. The locality closest to the fault is smallest suggesting a higher fracture density. The smallest ellipse is elongate in a NE-SW orientation, suggesting that fractures parallel to the MF trend have the smallest mean spacing. The larger ellipse is elongate in both N-S and NE-SW orientations, suggesting that the fractures orientated N-S (parallel to the overall WBFS) and NE-SW (parallel to the trend of the MF) have the lowest mean spacing values. The final ellipse (**Figure 7.9f**) represents a data set collected from a basement lithology adjacent to the MF. The ellipse is elongate in a N-S to NE-SW orientation, parallel to the trend of the MF and the overall trend of the WBFS.

Fracture density can also be assessed by calculating the total number of fractures per unit area for each data set. Plots of total number of fractures per cm^2 'v' distance are created for each fault in **Figure 7.10**. The data sets from the AVF (granite lithology, **Figure 7.10a**) and MF (basement and volcani-clastic lithologies, **Figure 7.10b**) show an increase in fracture density towards the centre of the faults for each lithology. Some of the data sets from the WBF (granite and psammite lithologies, **Figure 7.10c**) also show an increase in fracture density towards the centre of the fault. The values of density from the pelitic lithology do not change significantly with distance to WBF, whereas the density values from the sandstone data set decrease towards the centre of the fault. Finally in **Figure 7.10d** density values are plotted for calc-silicate and psammite lithologies adjacent to the NF. Both lithologies show little change in density with distance to the centre of the fault, although the density values for the calc-silicate lithology are a lot higher than the density values from the psammitic lithology.

The two parameters that have been used to quantify fracture density – the area of mean spacing ellipse and the total number of fractures per cm^2 - are plotted against each other in **Figure 7.11**. A strong power-law relationship is observed between the two measures of fracture density when the values are plotted on both logarithmic and linear scales. The power-law exponent of the relationship is 0.95.

A summary and comparison of fracture spacing data from each of the four faults analysed within the WBFS is presented in **Table 7.4**. Spacing parameters from each of the lithologies that are adjacent to the faults are summarised and compared in **Table 7.5**.

		Faults within Walls Boundary Fault System (WBFS)			
		AVF	MF	NF	WBF
	Fault orientation	N-S	NE-SW	N-S	N-S
	Data sets & orientation of outcrop surface	3 localities – 1 horizontal, 2 vertical	6 localities - 3 horizontal, 3 vertical	4 localities - 4 vertical	10 localities - 6 horizontal, 4 vertical
	Size of data set (spacing values measured)	906	1027	2364	557
	lithologies present	1 (granite)	2 (basement, volcani-clastic.)	2 (calc-silicate, psammite)	4 (psammite, pelite, sandstone, granite)
	best-fit stat distribution	exponential	exponential	exponential	exponential
	standard deviation 'v' mean spacing	good positive relationship, close to y = x line	good positive relationship, close to y = x line	good positive relationship, close to y = x line	good positive relationship, close to y = x line
	Cv	range from 0.78 to 1.06	range from 0.86 to 1.16	range from 0.79 to 1.00	range from 0.68 to 1.58
	exponent 'v' distance	Exponents from vertical and fault perpendicular transects increase towards centre of fault. exponents from fault parallel transects stay approx. same with distance. Highest exponent value = 0.0383 (from vertical transect)	Exponent values increase towards centre of fault for all lithologies and all transect orientations. Exponent values similar for both lithologies. Max. value = 0.0329 from fault parallel transect in basement lithology	No transects perp. to fault trend. Values of exponent from fault parallel transects increase towards centre of fault for calc-sil. lithology, and stay approx. same for psammitic lithology Exponent values from vertical transects in psammite appear to decrease towards centre of fault.	Exponent values from all transect orientations and lithologies increase to centre of fault except for WBF sandstone measured along fault parallel transects where values decrease towards centre. Highest exponent value = 0.0898 measured from fault perpendicular transects in psammite.
	mean spacing 'v' distance	Mean spacing decreases towards centre of fault for fault perp. and vertical transects. Stays approx. same with distance for fault parallel transects.	Mean spacing from both lithologies and along all transect orientations decreases towards centre of fault.	Mean spacing along fault parallel transects for both lithologies stays approx. same with distance to fault. Mean spacing of psammite along vertical transects increases towards centre of fault	Mean spacing values decrease towards centre of fault for all lithologies and transect orientations except for the pelite and sandstone data sets from fault parallel transects which increase to centre of fault.
	exponent 'v' mean spacing	Good power-law relationship. Exponent = 0.8026	Good power-law relationship. Exponent = 0.9748	Good power-law relationship. Exponent = 0.9131	Good power-law relationship. Exponent = 0.8228
Density	Ellipses	1 created. Elongate in a N-S to NE-SW direction.	3 created. 2 are elongate in N-S to NE-SW direction, 1 has 2 points of maxima (N-S and WNW-ESE). Ellipses closest to fault are smaller.	None created.	6 created. All are elongate N-S to NE-SW except OL29 (pelitic lithology). Smaller ellipses occur closest to fault, except pelite ellipses which stay same.
	total number of fractures per cm^2	Increases towards centre of fault. Max. value = 0.0229.	Increases towards centre of fault. Max. value = 0.0547 (basement).	No apparent change with distance to fault. Calc-sil. values > psammite.	All lithologies increase to centre except sandstone which decreases. Max value at centre = 0.0789 (granite).
	ellipse area 'v' fractures / cm^2	Only one data point but lies along same trend as rest of data.	Only 3 data points but power-law relationship observed.	N/A	Power-law relationship observed.

Table 7.4 Comparison of spacing parameters between faults within the Walls Boundary Fault System

		Lithology adjacent to faults within Walls Boundary Fault System (WBFS)						
		granite	calc-silicate	psammite	pelite	sandstone	basement	volcani-clastic
	Adjacent to faults?	AVF, WBF	NF	WBF, NF	WBF	WBF	MF	MF
	Data sets & outcrop surface orientation	5 localities - 2 horizontal, 3 vertical	2 localities - 2 vertical	6 localities - 2 horizontal, 4 vertical	2 localities - 2 horizontal .	2 localities - 1 horizontal, 1 vertical	4 localities - 1 horizontal, 3 vertical	2 localities - 2 horizontal
	size of data set	1441	202	1072	477	635	648	379
	best fit statistical distribution	exponential	exponential	exponential	exponential	exponential	exponential	exponential
	standard deviation 'v' mean spacing	good positive relationship close to y = x line	good positive relationship close to y = x line	good positive relationship close to y = x line	good positive relationship close to y = x line	good positive relationship close to y = x line	good positive relationship close to y = x line	good positive relationship close to y = x line
	Cv	WBF data has smaller range than AVF data, majority of Cv values from both faults < 1	2 data points very similar and both < 1	wider range values from WBF than NF data, majority of Cv values from both faults <1	narrow range 0.8 to 1.09.	narrow range 0.79 to 0.98.	narrow range 0.87 to 1.05.	narrow range 0.86 to 1.16.
	exponent 'v' distance	Exponent values increase towards centre of faults except for AVF data along fault parallel transects where values stay ~ same with distance. Values of exponent from WBF generally higher than AVF. Max. value = 0.05 from fault perpendicular transects to WBF.	Exponent values increase towards NF. Max. value = 0.0495 from fault parallel transects.	Exponent values for WBF data increase towards centre of fault for all transect orientations. NF values from fault parallel transects stay same with distance, values from vertical transects decrease towards centre of fault. Exponents from WBF > NF. Max. value = 0.0898 measured from WBF perp. transects.	Exponent values increase towards centre of fault along fault perpendicular transects, and stay approx. same along fault parallel transects. Max. value = 0.0181 from fault perp. transects.	Decrease of exponent values towards centre of fault along fault parallel transects. Only one data point each for fault perp. and vertical transects.	Exponent values increase to centre of fault for both fault parallel and vertical transects. Max. value = 0.0329 from fault parallel transects.	Exponent values increase to centre of fault for both fault parallel and fault perpendicular transects. Very similar values for both orientations. Max. value = 0.0257 from fault perp. transects.
	mean spacing 'v' distance	Mean values decrease towards centre of faults except from vertical transects where values do not change.	Mean values decrease slightly towards fault from fault parallel transects.	Mean values decrease towards centre of fault or stay approx. same except for data from NF vertical transects where values increase.	Mean values decrease towards centre of fault along fault perpendicular transects, but increase along fault parallel transects.	Mean spacing slightly increases towards centre of fault along fault parallel transects.	Large decrease in mean spacing towards centre of fault along both vertical and fault parallel transects.	Large decrease in mean spacing towards centre of fault along both fault parallel and fault perpendicular transects.
	exponent 'v' mean spacing	Good power-law relationship.	Only 2 data points but both lie along same trend as rest of data.	Good power-law relationship, 1 anomalous data points.	Good power-law relationship.	Good power-law relationship.	Good power-law relationship.	Power-law relationship, 2 anomalous data points
Density	Ellipses	2 created. Both elongate in NNE-SSW direction and similar size.	None created.	2 created. Both elongate NS to NNE-SSW direction. Smaller ellipse lies closest to centre of fault.	2 created. Both similar size even though one locality is a lot closer to centre of fault.	1 created. Elongate in a NNE-SSW direction.	1 created. Elongate in a NNE-SSW direction.	2 created. Both elongate in a NE-SW direction, smaller ellipse occurs closest to centre of fault
	total number of fractures per cm²	Increases towards centre of faults. Max value = 0.0789 (WBF)	No change with distance to fault.	Increases to centre of fault for WBF data, no change for NF data. Max = 0.0778	Stays approx. same with distance to fault. Values very low. Max = 0.007	Decreases to centre of fault.	Increases to centre of fault. Max. = 0.0547	Increases to centre of fault. Max. = 0.0196
	ellipse area 'v' fractures / cm²	Too few data points for each lithology to make any observations. Whole data set (all lithologies together) fits to a power-law distribution with an exponent of 0.9484.						

Table 7.5 Comparison of spacing parameters between lithologies adjacent to faults within the Walls Boundary Fault System

7.3 Fracture length

Fracture trace lengths were measured by hand using a ruler and string off the 2-dimensional data sets described in section 7.1, the same data sets that were used for spacing analysis (section 7.2). Fracture length measurements provide a direct estimate of fracture intensity which can be represented by the *total fracture trace length per unit area* for 2-dimensional data (section 1.7.5.2), and will be discussed in the following sections.

Plots of fracture length values versus cumulative frequency are plotted for each data set in **Figure 7.12**, in some cases two graphs are shown for one locality. The graphs illustrate that the fracture length data can be best fitted to one of two statistical distributions (exponential or power-law) or in some cases could be described by either distribution (**Table 7.6**). The data sets illustrated in **Figure 7.12 a, d, i, k, p, w, x, y, ab, ac** are all best described by a power-law distribution. The data sets illustrated in **Figure 7.12 b, c, j** are all best described by an exponential distribution with a negative slope. Two plots are presented for 8 localities (**Figure 7.12 e, f, g, h, n, o, q, r, s, t, u, v, z, aa, ad, ae**) as the data sets can be described by either a power-law distribution or an exponential distribution. The best-fit distributions for each locality are confirmed when a Kolmogorov-Smirnov test (section 1.8.4.2) is carried out on each of the data sets.

Some of the plots in **Figure 7.12** have data points that do not lie on the best-fit line. On the left hand side of the graph, the slope of the curve is shallow and this is the result the truncation effect (section 1.7.5.1 & section 1.8.2.4.5). On the right hand side of the graph, when the slope of the data curve is steep this is the result of censoring (section 1.7.5.1 & section 1.8.2.4.5).

The exponents from the cumulative frequency 'v' length graphs that are best described by an exponential distribution can be plotted against distance to analyse the change in fracturing adjacent to each fault and within each lithology (**Figure 7.13**). For the data sets with more than one data point, the highest exponent values occur at the centre of the faults suggesting that this is the area of highest intensity. The values from the psammite data set adjacent to the WBF are higher than the values from the granite data set adjacent to the AVF.

	Fault	Place		Locality	Best fit statistical distribution	Exponent (PL = power-law E = exponential)	R^2
Walls Boundary Fault System (WBFS)	WBF	Sullom	E of WBFP	SU13	power-law	1.7093	0.99
				SU21	power-law	1.4897	0.99
		Ollaberry	W of WBFP	OL24 –1	power-law	1.2899	0.99
				OL29	either	PL – 1.1327 E – 0.006	0.98 0.98
				OL30 –1 (fol. surface)	either	PL – 1.8534 PL – 0.8806 E – 0.009	0.99 0.99 0.98
				OL30 –2 (fol. perp.)	either	PL – 0.8613 E – 0.0076	0.99 0.99
				OL25	power-law	2.0872	0.98
				OL24 -2	either	PL – 0.8319 E – 0.0188	0.98 0.98
		Bixter	W of WBFP	BI2	either	PL – 1.6123 E – 0.0225	0.97 0.99
				BI6	power-law	2.0711	0.99
	NF	Wadbister Voe	W of NFP	WA16	power-law	0.9866	0.99
				WA17	exponential	0.0097	0.99
			E of NFP	WA19	exponential	0.0053	0.97
				WA20	power-law	1.1219	0.97
	AVF	Sand	E of AVF	SA3	either	PL - 1.1367 E – 0.0052	0.99 0.99
				SA6	power-law	1.5846	0.98
				SA7	either	PL – 2.2489 E – 0.007	0.99 0.99
	MF	Melby	W of MF	ME2	exponential	0.0086	0.99
				ME8	exponential	1.1955	0.99
			E of MF	ME4	power-law	1.909	0.99
				ME5	exponential	1.6188	0.99
				ME10	either	PL - 1.5319 E – 0.0025	0.99 0.98
				ME11	power-law	1.1236	0.996

Table 7.6 Best-fitting statistical distributions and exponent values for fracture length data collected adjacent to faults within the WBFS.

The exponents from the data sets that are best described by a power-law distribution range from 0.8319 to 2.2489 (**Figure 7.12, Figure 7.13, Table 7.6**). Although the range of exponent values does not appear to change with distance to the faults in **Figure 7.13**, the values of power-law exponent from 4 of the data sets (WBF granite, WBF pelite, WBF sandstone, AVF granite) appear to increase towards the centre of the fault.

The change in fracture length adjacent to the faults within each lithology can be assessed by plotting the mean fracture length versus perpendicular distance to the fault (**Figure 7.14**). Firstly for the WBF (**Figure 7.14a**) although for each data set there are few data points, the granitic data illustrates a decrease in average length towards the fault, the pelitic and sandstone data sets both show an increase in mean fracture length towards the centre of the fault, and the psammitic data show little change in mean fracture length with distance. Secondly both data sets from the NF show little change in mean fracture length with distance. Thirdly the granitic data set from the AVF also show little change in mean length with distance, and finally both data sets from the MF illustrate a decrease in average fracture length towards the centre of MF.

If data sets are best described by an exponential distribution, then a relationship be to between the mean spacing and the exponent values may be expected, since the mean is a defining aspect of an exponential distribution (section 1.8.2.3) (**Figure 7.15**). A good power-law relationship is observed when the exponential exponents are plotted against the mean fracture length values (exponent = 1.0395), but there appears to be no relationship between the mean fracture length and the exponents from the power-law length distributions.

The intensity of fracturing can be assessed from each data set by calculating the total fracture length per unit area (cm per cm^2) (section 1.7.5.2). These values can then be plotted for each data set against the perpendicular distance to the fault (**Figure 7.16, Table 7.7**). Although there are few data points for each lithology, some general relationships can be suggested. Firstly for the WBF, the values of intensity from the psammite, granite and pelite data sets all increase towards the centre of the fault; whereas the values of intensity from the WBF sandstone data set slightly decrease towards the centre of the fault. Secondly for the NF, both data sets show little change in intensity with a change in distance. Thirdly the values of intensity from the granitic

	Fault	Place		Locality	Total fracture length (cm)	Intensity: Total fracture length per cm²
Walls Boundary Fault System (WBFS)	WBF	Sullom	E of WBFP	SU13	2282.52	0.6671
				SU21	4303.46	0.2570
		Ollaberry	W of WBFP	OL24 -1	7254.52	0.1613
				OL29	1240.96	0.1340
				OL30 –1 (fol. surface)	1234.13	0.2999
				OL30 –2 (fol. perp.)	1012.64	0.4050
				OL25	5921.50	0.6401
				OL24 -2	1007.91	0.7190
		Bixter	W of WBFP	BI2	1577.83	0.8378
				BI6	5021.38	0.5092
	NF	Wadbister Voe	W of NFP	WA16	1420.52	0.6052
				WA17	1152.27	0.5762
			E of NFP	WA19	3287.83	0.2432
				WA20	2208.26	0.1474
	AVF	Sand	E of AVF	SA3	4849.54	0.2237
				SA6	6262.71	0.2693
				SA7	6312.80	0.4363
	MF	Melby	W of MF	ME2	4143.00	0.3258
				ME8	1500.82	0.1267
			E of MF	ME4	2139.05	0.5550
				ME5	3239.40	0.3539
				ME10	4613.49	0.0663
				ME11	6326.09	0.1106

Table 7.7 . Fracture intensity values calculated from data sets adjacent to faults within the WBFS.

data set adjacent to the AVF increase towards the centre of the fault, and lastly both data sets adjacent to the MF show an increase in fracture intensity towards the centre of the fault.

The values of fracture intensity can be plotted against parameters such as exponent values from best-fitting length distributions, mean fracture length values and fracture density values (section 1.7.4.2, section 7.2). Exponent values from data that are best-fitted to an exponential distribution are plotted against equivalent values of fracture intensity in **Figure 7.17 a, b**. A good power-law relationship is observed both on linear and logarithmic axes, with a power-law exponent of 0.7404. No apparent relationship is observed between the exponents of best-fitting power-law length distributions and values of fracture intensity (**Figure 7.17 c**). The values of intensity from each data set are plotted against the mean fracture length values in **Figure 7.18** and although there is scatter in the data, a power-law relationship is suggested with an exponent of 1.1484. The values of fracture density (calculated as the total number of fractures per cm^2 in section 7.2) from each data set are plotted against the values of fracture intensity in **Figure 7.19**. A strong positive relationship is observed on both linear and logarithmic axes, with an exponent of 0.5663.

A summary and comparison of fracture length data from each of the four faults analysed within the WBFS is presented in **Table 7.8**. Length parameters from each of the lithologies that are adjacent to the faults are summarised in **Table 7.9**.

7.4 Connectivity

Fracture connectivity (section 1.7.8) within 2-dimensional sample areas from the data sets described in section 7.1 (the same data sets used for spacing and length analyses) is described in the following sections.

Connectivity can be measured in two ways (section 1.7.8.4),

a) calculating parameters *within a cluster* (a group of interconnected fractures where the interconnections are referred to as nodes) (section 1.7.8.3)
b) calculating parameters *within a unit area* (cm^2) (section 1.7.8.4.4).

		Faults within Walls Boundary Fault System (WBFS)			
		AVF	**MF**	**NF**	**WBF**
	Fault orientation	N-S	NE-SW	N-S	N-S
	Data sets & orientation of outcrop surface	3 localities – 1 horizontal, 2 vertical	6 localities - 3 horizontal, 3 vertical	4 localities - 4 vertical	10 localities - 6 horizontal, 4 vertical
	Data range (max. & min. lengths, cm)	max. – 181.56 min. – 2.0	max. – 213.97 min – 1.5	max. – 122.19 min. – 1.45	max. – 249.06 min. – 0.43
	lithologies present	1 (granite)	2 (basement, volcani-clastic.)	2 (calc-silicate, psammite)	4 (psammite, pelite, sandstone, granite)
	best-fit stat distribution (PL = power-law E = exponential)	2 data sets = either PL or E 1 data set = PL	1 data set = either PL or E 4 data sets = PL 1 data set = E	2 data sets = PL 2 data sets = E	5 data sets = either PL or E 5 data sets = PL
	exponent 'v' distance (PL = power-law E = exponential)	PL – increases to centre of fault max = 2.25. E – slight increase to centre of fault max. = 0.007.	PL – (basement) little change with distance.	Only 1 value of each distribution for each lithology, therefore no relationships can be established.	PL – granite, pelite & sandstone data sets all have increase in exponent to centre of fault. Highest value from sandstone (=2). Psammite stays ~ same. E – psammite data increase to centre of fault max. = 0.0188
	mean length 'v' distance	Values stay approx. same with distance.	Both lithologies show decrease in mean length to centre of fault.	Both lithologies show little change with distance.	Granite – decrease in mean length to centre of fault. Pelite & sandstone – increase in mean length to centre. Psammite – little change to centre.
	exponential exponent 'v' mean length	PL – no relationship for all data sets E – good power-law relationship using data from all faults and lithologies, exponent = 1.0395 (Too few data points to investigate each fault individually)			
Intensity	**Intensity (total fracture length (cm) per cm²) 'v' distance**	Increase in intensity towards centre of fault. Max. = 0.437 cm/cm²	Both lithologies show an increase in intensity towards centre of fault. Values from basement (max. = 0.555) > volc. values (max. = 0.326)	Little change in intensity towards centre of fault from both lithologies.	Pelite, psammite & granite all show an increase in intensity towards centre of fault (max. = psammite, 0.719). Sandstone shows a decrease towards centre of fault.
	Intensity 'v' exponent	No relationship between power-law exponents and intensity. A power-law relationship exists between the exponential exponents and intensity, with exponent of 0.7404. (Too few data points to investigate each fault individually)			
	Intensity 'v' mean fracture length	Scatter exists in data, but possible power-law relationship between intensity & mean, with exponent of 1.1484 (Too few data points to investigate each fault individually)			
	Intensity 'v' density	Good power-law relationship between intensity (total fracture length per cm²) and density (total number of fractures per cm²), exponent = 0.5663 (Too few data points to investigate each fault individually)			

Table 7.8 Comparison of length parameters between faults within the Walls Boundary Fault System

		Lithology adjacent to faults within Walls Boundary Fault System (WBFS)						
		granite	**calc-silicate**	**psammite**	**pelite**	**sandstone**	**basement**	**volcani-clastic**
	Adjacent to faults?	AVF, WBF	NF	WBF, NF	WBF	WBF	MF	MF
	Data sets & outcrop surface orientation	5 localities - 2 horizontal, 3 vertical	2 localities - 2 vertical	6 localities - 2 horizontal, 4 vertical	2 localities - 2 horizontal	2 localities - 1 horizontal, 1 vertical	4 localities - 1 horizontal, 3 vertical	2 localities - 2 horizontal
	Data range (max. & min. lengths cm)	max. – 181.56 min – 1.17	max. – 52.52 min. – 1.45	max. – 122.19 min. – 0.75	max. – 249.06 min. – 2.56	max. – 64.41 min. – 0.43	max. – 213.97 min. – 2.07	max. – 113.64 min. – 1.5
	best fit stat. dist. (PL = power-law, E = exponential)	2 data sets = PL or E 3 data sets = PL	1 data set = PL 1 data set = E	3 data sets = PL or E 2 data sets = PL 1 data set = E	1 data set = either 1 data set = PL	1 data set = either 1 data set = PL	1 data set = PL or E 3 data sets = PL	1 data set = PL 1 data set = E
	exponent 'v' distance	PL and E data sets from AVF and PL data sets from WBF all show an increase in exponent towards centre of fault.	Not enough data points from each distribution.	Not enough data from NF. WBF data show an increase in exponential exponent to centre of fault, more complex relationship.	Only 2 data points but show an increase in PL exponent to centre of fault.	Only 2 data points but WBF PL data show an increase in exponent to centre of fault.	Slight increase in PL exponent to centre of fault.	Not enough data points from each distribution.
	mean length 'v' distance	WBF data set shows decrease to centre of fault, AVF data set values stay ~ same with distance to fault.	Only 2 data points but values stay same with distance to fault.	Only 2 data points from NF but show increase in mean length to centre of fault. WBF data show little change with distance.	Only 2 data points but show an increase in mean length to centre of fault.	Only 2 data points but show an increase in mean length to centre of fault.	Decrease in mean length towards centre of fault.	Only 2 data points but show a decrease in mean length to centre of fault.
	exponential exponent 'v' mean length	E – too few data points to analyse each lithology separately, but all data points show a good power-law relationship with exponent of 1.0395 PL – no relationship between exponent and mean length for any lithology.						
Intensity	**Intensity (total fracture length (cm) per cm²) 'v' distance**	Both data sets (AVF and WBF) show an increase in intensity towards centre of fault.	Only 2 data points but values stay same with distance to fault.	Only 2 data points from NF but values stay ~ same with distance. WBF data show increase in intensity to centre of fault.	Only 2 data points but show a slight increase in intensity to centre of fault.	Only 2 data points but show a decrease in intensity to centre of fault.	Increase in intensity towards centre of fault.	Increase in intensity towards centre of fault.
	Intensity 'v' exponent	E – too few data points to analyse each lithology separately, but all data points show a good power-law relationship with exponent of 0.7404 PL – no relationship between exponent and intensity for any lithology.						
	Intensity 'v' mean fracture length	Too few data points to analyse each lithology separately, but all data points show a power-law relationship with exponent of 1.1484						
	Intensity 'v' density	Too few data points to analyse each lithology separately, but all data points show a power-law relationship with exponent of 0.5663						

Table 7.9 Comparison of length parameters between lithologies adjacent to faults within the Walls Boundary Fault System

7.4.1 *Connectivity parameters calculated within clusters*

All of the 2-dimensional data sets collected from the WBFS contain a large cluster that has more than 15 nodes (**Table 7.10**). The large cluster is referred to as the percolating cluster (p_c) when all four sides of the rectangular sample area are intersected and therefore the percolation threshold is reached (p_c = 1) (section 1.7.8.3.1). The percolation threshold is reached for all but one data set collected from the WBFS (**Table 7.11**). The largest cluster from locality OL24 (pelitic lithology) only intersects 3 sides of the sample area, therefore p_c = 0.75 and the percolation threshold is not reached (**Table 7.11**). For a set of fractures to be considered well connected, it is suggested that 75% of the total fracture length in the sample area must contribute to the percolating cluster (section 1.7.8.4.5). The percentage of total fracture length that is contained within the percolating cluster for all of the data sets from the WBFS is greater than 87% (**Table 7.11**).

The total number of fractures and nodes per cluster and the total cluster lengths (normalised for sample area) can be calculated from each data set and plotted against the perpendicular distance to the individual faults within the WBFS to analyse the change in connectivity around the faults within different lithologies (**Table 7.10, Figure 7.20, Figure 7.21, Figure 7.22**). Although there are few data points for each lithology and each fault, some general conclusions can be drawn. The total numbers of nodes and fractures per cluster for lithologies adjacent to the WBF, MF and AVF all increase towards the centre of the faults. The cluster lengths (normalised for sample area) for lithologies adjacent to the WBF, MF and AVF also increase towards the centre of the faults. This suggests that within lithologies adjacent to these three faults, connectivity increases towards the centre of the faults. Overall the highest values of fractures and nodes per cluster and the longest cluster length occur adjacent to the WBF from the psammitic lithology (484 fractures and 1079 nodes per cluster, 0.72cm/cm^2 cluster length). The data collected adjacent to the NF do not show the same trend. The total number of fractures per cluster and total number of nodes per cluster both appear to decrease towards the centre of the fault, and the cluster length (normalised for sample area) decreases towards the centre. These relationships may be due insufficient data.

Fault	Locality	Lithology	Distance to fault (m)	Total number fractures	Percolation threshold (p_c)	number of nodes per cm^2	clusters								
							single	small (<15 nodes)				large (> 15 nodes)			
							no. of fractures & % total	number of clusters	no. of fractures	number of nodes	total cluster length (mm)	number of clusters	no. of fractures	number of nodes	total cluster length (mm)
WBF	SU13	granite	18.75	270	1	0.1184	1	2	2, 2	1, 1	194.52, 142	1	265	403	22422.50
	SU21	granite	281	174	1	0.0199	3	1	2	1	271.09	1	169	333	42501.03
	OL24 -1	pelite	51	200	0.75	0.0070	7	4	2, 4, 2, 3	1, 3, 1, 2	2730.5, 3598.33, 239.89, 804.33	1	182	305	63126.10
	OL29	pelite	172	67	1	0.0071	5	4	2, 3, 2, 2	1, 2, 1, 1	176, 489.6, 278.4, 288	1	53	61	10838.40
	OL30 –1 (fol. surface)	psammite	1333	100	1	0.0323	7	3	2, 4, 3	1, 3, 2	285.87, 168.53, 192	1	84	127	11146.67
	OL30 –2 (fol. perp.)	psammite	1333	79	1	0.0444	1	0	-	-	-	1	79	111	10063.21
	OL25	psammite	131	491	1	0.1170	3	1	4	3	195.84	1	484	1079	58870.87
	OL24 -2	psammite	51	109	1	0.1441	0	0	-	-	-	1	109	202	10079.07
	BI2	sandstone	535	277	1	0.2565	0	2	2, 8	1, 8	89.48, 386.77	1	267	474	15302.06
	BI6	sandstone	167	410	1	0.0774	3	1	4	4	556.40	1	403	759	49451.74
NF	WA16	calc-silicates	235	117	1	0.0988	0	0	-	-	-	1	117	232	14205.17
	WA17	calc-silicates	77	94	1	0.0780	3	2	4, 5	3, 4	318.26, 304.87	1	82	149	10573.85
	WA19	psammite	153	152	1	0.0189	1	2	3, 2	3, 1	320.93, 259.07	1	146	252	32228.67
	WA20	psammite	51	78	1	0.0061	5	1	6	7	960.47	1	66	85	20385.47
AVF	SA3	granite	407	205	1	0.0146	6	1	2	1	357.45	1	197	315	47315.38
	SA6	granite	242	237	1	0.0186	3	1	2	1	390.5	1	232	431	61795.36
	SA7	granite	16	332	1	0.0441	5	1	2	1	304	1	325	637	63128.00
MF	ME2	volcanics	225	249	1	0.0344	3	0	-	-	-	1	246	437	41182.50
	ME8	volcanics	663	71	1	0.0090	3	0	-	-	-	1	68	107	14566.67
	ME4	basement	138	211	1	0.0942	5	1	2	1	61.93	1	204	362	21020.90
	ME5	basement	71	161	1	0.0267	5	0	-	-	-	1	156	244	32074.46
	ME10	basement	1475	91	1	0.0017	0	2	2, 2	1, 1	710.31, 613.85	1	87	114	44810.77
	ME11	basement	1590	151	1	0.0041	3	1	2	1	1089.77	1	146	236	61248.41

Table 7.10 Connectivity data from 2-D data sets within the WBFS.

	Fault	Place		Locality	p_c value (1 = all 4 sides of sample area intersected)	Total fracture length (cm)	p_c length (cm)	%
Walls Boundary Fault System (WBFS)	WBF	Sullom	E of WBFP	SU13	1	2282.52	2242.25	98.24
				SU21	1	4303.46	4250.10	98.76
		Ollaberry	W of WBFP	OL24 -1	0.75	7254.52	-	-
				OL29	1	1240.96	1083.84	87.34
				OL30 –1 (fol. surface)	1	1234.13	1114.67	90.32
				OL30 –2 (fol. perp.)	1	1012.64	1006.32	99.38
				OL25	1	5921.50	5887.09	99.42
				OL24 -2	1	1007.91	1007.91	100.00
		Bixter	W of WBFP	BI2	1	1577.83	1530.21	96.98
				BI6	1	5021.38	4945.17	98.48
	NF	Wadbister Voe	W of NFP	WA16	1	1420.52	1420.52	100.00
				WA17	1	1152.27	1057.38	91.77
			E of NFP	WA19	1	3287.83	3222.87	98.02
				WA20	1	2208.26	2038.55	92.31
	AVF	Sand	E of AVF	SA3	1	4849.54	4731.54	97.57
				SA6	1	6262.71	6179.54	98.67
				SA7	1	6312.80	6312.80	100.00
	MF	Melby	W of MF	ME2	1	4143.00	4118.25	99.40
				ME8	1	1500.82	1456.67	97.06
			E of MF	ME4	1	2139.05	2102.09	98.27
				ME5	1	3239.40	3207.45	99.01
				ME10	1	4613.49	4481.08	97.13
				ME11	1	6326.09	6124.84	96.82

Table 7. 11 Percolation threshold data from fracture data sets collected adjacent to faults within the WBFS.

To analyse the connectivity of the whole outcrop data set from the WBFS, the total number of fractures from each cluster in each data set can be plotted against the total number of nodes in the same cluster (**Table 7.10, Figure 7.23**). As expected, a strong positive relationship is observed between these parameters on linear axes for the data sets from all faults and all lithologies, but it is the nature (i.e. slope) of this relationship that is useful and can be used to compare data sets between faults, lithologies etc. Values of maximum and minimum connectivity can be calculated for planar fractures that are connected in a cluster, (section 1.7.8.3.3); connectivity decreases exponentially between maximum and minimum values. These extremes are plotted on **Figure 7.23**, along with the curve for 1% connectivity. It is apparent that for clusters with up to ~400 nodes and ~200 fractures, the connectivity is approximately 1%, clusters with more than 400 nodes appear to be connected by less than 1%.

The values of cluster length (normalised for sample area) from each data set can be plotted against both the total number of fractures per cluster and the total number of nodes per cluster (**Figure 7.24** and **Figure 7.25**). There are no obvious strong relationships, although the data points on both of the plots do seem to be constrained by maximum and minimum envelopes, and show a general positive relationship.

Both the total number of nodes per fracture and the number of fractures per node within each cluster from all data sets can be assessed and plotted as histograms (**Figure 7.26**) (section 1.7.8.4.4). The most frequent value of fractures per node is 2, and the most frequent value of nodes per fracture is 0.5. These values correspond to small clusters with 2 fracture and 1 node. The values of fractures per node in a cluster between 0.45 and 0.8 appear to be approximately normally distributed with a mean value of 0.61. The modal value of nodes per fracture in a cluster is 0.5, and the rest of the values are spread approximately evenly over a wide range from 1.2 to 1.9, with no approximation to a normal distribution.

7.4.2 *Connectivity parameters calculated within a unit area (cm^2)*

As well as dividing the fractures into clusters to analyse connectivity, parameters can be calculated with respect to a unit area. The total number of nodes per unit area can

be calculated for each data set and plotted against the perpendicular distance to each fault to analyse connectivity (**Table 7.10, Figure 7.27**). Although there are few data points for each lithology and each fault, some general conclusions can be drawn.

The total number of nodes per cm^2 for lithologies adjacent to the MF and AVF all increase towards the centre of the faults. This suggests that within lithologies adjacent to these faults connectivity increases towards the centre of the faults, which is in agreement with the cluster connectivity data (section 7.4.1). The values of nodes per cm^2 from the lithologies adjacent WBF also increase towards the centre of the fault with the exception of the sandstone data set. The lithologies adjacent to the NF however, both show a slight decrease in the number of nodes per cm^2 approaching the centre of the fault. The highest value of nodes per cm^2 from the centre of the faults is highest within the psammitic lithology adjacent to the WBF (0.144 nodes per cm^2)

To analyse the connectivity of the whole WBFS outcrop data set, the total number of fractures per cm^2 (fracture density) (section 1.7.4.2) can be plotted against the total number of nodes per cm^2 (a measure of connectivity, section 1.7.8.4.3) from each data set (**Figure 7.28**). A strong positive power-law relationship is observed between fracture density and fracture connectivity when the data are plotted on both logarithmic and linear axes with an exponent value of 1.08.

Also, the total number of nodes per cm^2 (a measure of fracture connectivity) can be plotted against the total fracture length per cm^2 (fracture intensity) (section 1.7.5.2,) (**Figure 7.29**). The data are plotted on both logarithmic and linear axes, and a strong positive power-law relationship is observed with an exponent value of 1.86.

The total number of fractures per node and the number of nodes per fracture within a cm^2 from all of the data sets can be assessed and plotted as histograms (**Figure 7.30**) (section 1.7.8.4.4). Both plots are approximately normally distributed between 0.5 - 1.1 and 1 – 2.4 with mean values of 0.64 fractures per node and 1.63 nodes per fracture.

Fracture connectivity can be related to fracture length by plotting the mean length against the total number of nodes per unit area (**Figure 7.31**). A good power-law relationship is observed when the data are plotted on both logarithmic and linear axes, with a power-law exponent of 2.22.

The fracture length data analysed from the WBFS (section 7.3) can be best described by either an exponential distribution or a power-law distribution The exponents calculated from the best-fit fracture length statistical distributions can be plotted

against the total number of nodes per unit area, again to relate connectivity to fracture length. A good positive power-law relationship is observed between the exponent from the length data sets that are exponentially distributed and the total number of nodes per cm^2 (**Figure 7.32**). No obvious relationship is observed between the values of power-law length exponents and the numbers of nodes per cm^2 (**Figure 7.33**). However, the power-law exponent has been used to characterise the abundance of large and small fractures with respect to the size of the sample area (large fractures are longer than the dimensions of the sample area) (section 1.7.8.5). Power-law exponents less than 1 suggest that connectivity is controlled by a small number of large fractures and the number of nodes is low; whereas power-law exponents between 1 and 3 suggest that connectivity is controlled by both large and small fractures (section 1.7.8.5). When the exponent is equal to 2 the relative contribution to connectivity of large and small fractures is identical. Exponent values between 2 and 3 suggest that connectivity is controlled by mostly small fractures but with a small proportion of large fractures, and exponent values above 3 suggest that the connectivity is controlled by small fractures. The values of power-law exponent from the WBFS fracture length distributions range from 0.83 to 2.25 (**Table 7.6, Figure 7.34**). 85.7% of the exponent values lie between 0 and 2 and this suggests that for the majority of data sets from the WBFS the connectivity is controlled by large fractures. 14.3% of the power-law exponent values lie between 2 and 3 suggesting that for these data sets small fractures control connectivity.

7.4.3 *Summary of connectivity data*

A summary and comparison of fracture connectivity data from each of the four faults analysed in 2-dimensions within the WBFS is presented in **Table 7.12**. Connectivity parameters from each of the lithologies adjacent to the faults are summarised and compared in **Table 7.13**.

		Faults within Walls Boundary Fault System (WBFS)			
		AVF	**MF**	**NF**	**WBF**
	Fault orientation	N-S	NE-SW	N-S	N-S
	Data sets & orientation of outcrop surface	3 localities – 1 horizontal, 2 vertical	6 localities - 3 horizontal, 3 vertical	4 localities - 4 vertical	10 localities - 6 horizontal, 4 vertical
	Size of data set (total number nodes measured)	1386	1504	736	3891
	lithologies present	1 (granite)	2 (basement, volcani-clastic.)	2 (calc-silicate, psammite)	4 (psammite, pelite, sandstone, granite)
connectivity measured within clusters	**Percolation threshold (p_c) reached?**	$p_c = 1$ for all data sets	$p_c = 1$ for all data sets	$p_c = 1$ for all data sets	$p_c = 1$ for all data sets except 1 pelitic locality where $p_c = 0.75$
	% length in pc	all data sets > 97%	all data sets > 96%	all data sets > 92%	all data sets > 87%
	Number of fractures per cluster 'v' distance	increases to centre of fault	increases to centre of fault	decreases to centre of fault	increases to centre of fault
	Number of nodes per cluster 'v' distance	increases to centre of fault	increases to centre of fault	decreases to centre of fault	increases to centre of fault
	Total cluster length 'v' distance	increases to centre of fault	increases to centre of fault	decreases to centre of fault	increases to centre of fault for all except sandstone data set which decreases.
	Total fractures per cluster 'v' total nodes per cluster	Good positive relationship on linear axes for all data points. Clusters with up to 200 nodes = ~1% connectivity. Clusters > 200 nodes connectivity <1% (Too few data points to investigate each fault individually)			
	Total fractures per cluster 'v' total cluster length (per area)	No apparent relationship.			
	Total nodes per cluster 'v' total cluster length (per area)	No apparent relationship.			
	Total nodes per fracture in a cluster	Most frequent value is 0.5. Large spread of values.			
	Total fractures per node in a cluster	Most frequent value is 2. Values between 0.45 & 0.8 are approximately normally distributed, with mean value of 0.61.			
connectivity measured within a unit area (cm^2)	**Total number nodes per cm^2 'v' distance**	increases to centre of fault	increases to centre of fault	decreases to centre of fault	increases to centre of fault for all except sandstone data set which decreases.
	Total nodes per cm^2 'v' total fractures per cm^2	Good positive power-law relationship using data from all faults, exponent = 1.0758. (Too few data points to investigate each fault individually)			
	Total nodes per cm^2 'v' total fracture length per cm^2	Good positive power-law relationship using data from all faults, exponent = 1.8549. (Too few data points to investigate each fault individually)			
	Total nodes per fracture in a cm^2	Values are approx. normally distributed between 0.5 & 1.1, with mean value of 0.64. (Too few data points to investigate each fault individually)			
	Total fractures per node in a cm^2	Values are approx. normally distributed between 1.0 & 2.4, with mean value of 1.63. (Too few data points to investigate each fault individually)			
	Mean fracture length v nodes per cm^2	Good power-law relationship using data from all faults, exponent = 2.2216. (Too few data points to investigate each fault individually)			
	Total nodes per cm^2 'v' exponent from exponential length distribution	Good power-law relationship using data from all faults, exponent = 2.1698. (Too few data points to investigate each fault individually)			
	Power-law exponent v nodes per cm^2 & exponent relationship to connectivity	No relationship between power-law exponent and nodes per cm^2. Majority of exponent values (87%) lie between 0 & 2 which suggests that large fractures control connectivity. Remaining 14.3% of values lie between 2 & 3 and suggests that for these data sets connectivity is controlled by small fractures.			

Table 7.12 Comparison of connectivity parameters between faults within the Walls Boundary Fault System

		Lithology adjacent to faults within Walls Boundary Fault System (WBFS)						
		granite	calc-silicate	psammite	pelite	sandstone	basement	volcani-clastic
	Adjacent to faults?	AVF, WBF	NF	WBF, NF	WBF	WBF	MF	MF
	Data sets & outcrop surface orientation	5 localities - 2 horizontal, 3 vertical	2 localities - 2 vertical	6 localities - 2 horizontal, 4 vertical	2 localities - 2 horizontal	2 localities - 1 horizontal, 1 vertical	4 localities - 1 horizontal, 3 vertical	2 localities - 2 horizontal
	Size of data set (total number nodes measured)	2125	388	1876	378	1246	960	544
	Percolation threshold (p_c) reached?	p_c = 1 for all data sets	p_c = 1 for all data sets	p_c = 1 for all data sets	p_c = 1 for 1 data set, p_c = 0.75 for 1 data set,	p_c = 1 for all data sets	p_c = 1 for all data sets	p_c = 1 for all data sets
	% length in p_c	>97% all localities	>91% all localities	>90% all localities	>87% for p_c = 1 locality	>96% all localities	>96% all localities	>97% all localities
connectivity measured within clusters	Number of fractures per cluster 'v' distance	increases to centre, AVF max. (325) > WBF max. (265)	decreases to centre	inc. to centre of WBF (max. = 484). dec. to centre of NF.	increases to centre, max. = 182	increases to centre, max. = 403	increases to centre, max. = 204	increases to centre, max. = 246
	Number of nodes per cluster 'v' distance	increases to centre, AVF max. (637) > WBF max. (403)	decreases to centre	inc. to centre of WBF (max.= 1079). dec. to centre of NF.	increases to centre, max. = 305	increases to centre, max. = 759	increases to centre, max. = 362	increases to centre, max. = 437
	Total cluster length 'v' distance	increases to centre, WBF max. (0.66) > AVF max. (0.44)	decreases to centre	WBF perp. & para. data sets increase to centre (max. = 0.72) NF data decreases.	increases to centre, max. = 0.14	decreases to centre	increases to centre, max. = 0.55	increases to centre, max. = 0.32
	Total fractures per cluster 'v' total nodes per cluster	Good positive relationship on linear axes for all data points. Clusters with up to 200 nodes = ~1% connectivity. Clusters > 200 nodes connectivity <1% (Too few data points to investigate each lithology individually)						
	Total fractures per cluster 'v' total cluster length (per area)	No apparent relationship.						
	Total nodes per cluster 'v' total cluster length (per area)	No apparent relationship.						
	Total nodes per fracture in a cluster	Most frequent value is 0.5. Large spread of values.						
	Total fractures per node in a cluster	Most frequent value is 2. Values between 0.45 & 0.8 are approximately normally distributed, with mean value of 0.61.						
connectivity measured within a unit area (cm^2)	Total number nodes per cm^2 'v' distance	increases to centre both faults. WBF max. (0.12) > AVF max. (0.045)	decreases to centre	WBF perp. & para. data sets increase to centre (max. = 0.14) NF data decreases.	No change with distance (0.007)	decreases to centre	increases to centre, max. = 0.094	increases to centre, max. = 0.034
	Total nodes per cm^2 'v' total fractures per cm^2	Good positive power-law relationship using data from all faults, exponent = 1.0758. (Too few data points to investigate each lithology individually)						
	Total nodes per cm^2 'v' total fracture length per cm^2	Good positive power-law relationship using data from all faults, exponent = 1.8549. (Too few data points to investigate each lithology individually)						
	Total nodes per fracture in a cm^2	Values are approx. normally distributed between 0.5 & 1.1, with mean value of 0.64. (Too few data points to investigate each lithology individually)						
	Total fractures per node in a cm^2	Values are approx. normally distributed between 1.0 & 2.4, with mean value of 1.63. (Too few data points to investigate each lithology individually)						
	Mean fracture length v nodes / cm^2	Good power-law relationship using data from all faults, exponent = 2.2216. (Too few data points to investigate each lithology individually)						
	Total nodes per cm^2 'v' exponent from exponential length distribution	Good power-law relationship using data from all faults, exponent = 2.1698. (Too few data points to investigate each lithology individually)						
	Power-law exponent & relationship to connectivity	No relationship between power-law exponent and nodes per cm^2. Majority of exponent values (87%) lie between 0 & 2 which suggests that large fractures control connectivity. Remaining 14.3% of values lie between 2 & 3 and suggests that for these data sets connectivity is controlled by small fractures.						

Table 7.13 Comparison of connectivity parameters between lithologies adjacent to faults within the Walls Boundary Fault System

7.5 Summary of fracture characteristics from WBFS 2-D outcrop data set

A detailed summary of each fracture characteristic (spacing, length and connectivity) for each fault is provided in **Tables 7.4, 7.8 and 7.12**. Fracture spacing, length and connectivity data are compared in detail between each lithology observed adjacent to the faults in **Tables 7.5, 7.9 and 7.13**. The following section provides a more general summary of fracture characteristics observed from 2-dimensional (photograph) data sets within the WBFS.

7.5.1 *Fracture spacing*

Three main spacing parameters have been used to analyse how the spacing of fractures (measured along 1-D line transects across 2-D data sets) changes with distance to each fault, and for each lithological data set. These parameters are exponent, mean spacing and density, and are described below.

a) *Exponent.* All data sets of fracture spacing values are best described by an exponential distribution with a negative slope. Although there are few data points, the exponent values from the best-fitting distributions increase towards the centre of each fault for all except 2 (out of 17) data sets. These two are a spacing data set measured along parallel transects within sandstone adjacent to the WBF, and a data set measured along vertical transects within psammite adjacent to the NF, which both show a decrease (**Figure 7.6**)

b) *Mean spacing.* Mean spacing values measured along 1-D transects across 2-D photographs show an inverse relationship to the exponential exponent values. The majority of the lithology data sets show either a decrease in mean spacing, or little change, towards the centre of the faults (**Figure 7.7**).

c) *Fracture density.* Fracture density, defined as the total number of fractures in a cm^2, increases towards the centre of the WBF, MF and NF, for all lithologies except sandstone which decreases. Fracture density measured within lithologies adjacent to the NF show little change towards the centre of the fault (**Figure 7.10**).

7.5.2 *Fracture length*

Three main parameters have also been used to analyse how fracture length changes in 2-D with distance to each fault, and within each lithology. These parameters are exponent, mean length and intensity, and are described below.

a) *Exponent.* The best-fitting statistical distribution for fracture length data sets was found to be either power-law or exponential. For some data sets, both distributions could be applied. The majority of data sets can be fitted to a power-law distribution. Few data sets are best described by an exponential distribution only. Where >1 data point exists for a lithological data set adjacent to each fault, an increase in exponential exponent towards the centre of the fault is observed. (**Figure 7.13 a**). Fracture length data sets best described by a power-law distribution also show an increase in exponent towards the centre of each fault (**Figure 7.13 b**).

b) *Mean length.* No consistent relationship is observed between mean fracture length and distance to the centre of the faults. For some lithologies fracture length increases towards the fault plane (WBF, pelite & sandstone), whereas others show a decrease (WBF granite, MF both lithologies), and some show little change (WBF & AVF granite, NF both lithologies) (**Figure 7.14**).

c) *Fracture intensity.* The majority of data sets show an increase in fracture intensity, total fracture length per cm^2, towards the centre of the faults (WBF psammite, granite, pelite, AVF granite, MF both lithologies), but the sandstone data set from the WBF shows a decrease, and both lithologies adjacent to the NF show little change in intensity with distance to the fault. A good power-law relationship is observed between fracture intensity and the exponential exponent values from fracture length data sets (**Figure 7.17 a**), but no consistent relationship is observed between power-law exponent values and fracture intensity (**Figure 7.17 b**). A good power-law relationship is also observed between mean fracture length and fracture intensity (**Figure 7.18**).

7.5.3 *Fracture connectivity*

A variety of parameters have been plotted from data sets collected within the WBFS to assess how fracture connectivity changes with distance to each fault and within each lithology, in 2-D.

All except one data sets (WBF pelite) possess a large percolating cluster of interconnected fractures which intersects all 4 sides of the sample area. For all of these data sets, the percentage of fracture length contained in the percolating cluster is >87%, suggesting that the data sets are well-connected.

For each lithological data set collected adjacent to the AVF, MF and WBF (except the sandstone data set), the total number of fractures and nodes per cluster increases towards the centre of the faults (**Figures 7.20, 7.21**). Data sets analysed from the NF show a decrease in nodes and fractures per cluster towards the faults. For all data sets the number of fractures is greater than the number of nodes in large clusters, and a good relationship is observed for the two parameters (**Figure 7.23**).

As well as analysing fracture clusters, connectivity can be described by the total number of nodes per cm^2. Using this parameter, connectivity increases towards the centre of the AVF, MF and WBF for all except the sandstone lithology. Lithologies adjacent to the NF show a slight decrease in connectivity towards the centre of the fault (**Figure 7.26**).

7.5.4 *Relationships between fracture density, intensity and connectivity*

- A strong power-law relationship is observed between values of fracture *density* (total number of fractures per cm^2) and fracture *intensity* (total fracture length per cm^2), for data collected adjacent to all faults and within all lithologies, with a power-law exponent of 0.5663 (**Figure 7.19**).
- A strong power-law relationship is also observed between values of fracture *density* and *connectivity* (total number of nodes per cm^2), with a power-law exponent of 1.08.
- A strong power-law relationship is also observed between fracture *intensity* and *connectivity*, with a power-law relationship of 1.86.

CHAPTER 8 – DISCUSSION AND CONCLUSIONS

Detailed analyses of fracture parameters, collected within and outside the damage zones associated with two, crustal-scale faults (chapters 3, 4, 6 & 7), have enabled the development and evolution of the fracture system geometry to be documented and described quantitatively. As far as the author is aware, this comprehensive study of fracture parameters associated with strike-slip reactivated basement structures is unique to date. The findings of this study show that although reactivated structures possess complex kinematic histories, which are often difficult to unravel, intricate studies of their associated fractures may potentially be used to fingerprint reactivation and enable recognition in the subsurface.

The aims of this chapter are as follows:

- To discuss the statistical analyses of fracture spacing and length carried out in this study, in relation to published literature (section 8.1)
- To synthesise and compare fracture characterisation results from the two fault zones studied (sections 8.2, 8.3)
- To compare and contrast studies of fracture attributes from other fault systems (section 8.4)
- To present potential signatures for distinguishing between relatively highly reactivated and little reactivated faults (section 8.5)
- To suggest future work to develop the findings discussed here (section 8.6)

8.1 Statistical analysis of fracture attributes

In the following sections, the best-fit statistical distributions for fracture spacing and length distributions will be discussed, along with the relationship between the best-fit spacing distribution and other methods of characterising fracture clustering (Cv values, and 'step plots'). Fracture spacing data collected in the field along 1-D line transects across outcrop surfaces will also be compared to fracture spacing data collected using 1-D transects across 2-D photographs.

8.1.1 *Best-fitting statistical distribution for fracture spacing*

There are numerous published studies of discontinuity spacing in the literature (see **Table 1.4**), with no consensus on whether there is one best-fit statistical distribution, nor what that distribution should be. The majority of studies to date have focused on the analyses of jointed rock bodies (e.g. Priest and Hudson 1976, Hudson and Priest 1979, 1983, Narr and Suppe, 1991, Rives et al., 1992, Wu and Pollard 1992), with relatively few studies of spacings within faulted/fractured rock bodies (e.g. Gillespie et al., 1993, Brookes et al., 1996). By plotting the spacing values in descending order against cumulative frequency (known as the spacing population technique, Gillespie et al., 1993), the range of spacing values in a data set can be analysed. This method does not relate to the spatial analysis of the data, as the values are not analysed 'in situ', and therefore one cannot deduce whether a distribution is fractal or not. To analyse whether a spacing data set has a fractal nature, a different technique must be used to analyse the data 'in situ', such as the interval counting technique (the 1-D equivalent of the 2-D box-counting technique, e.g. Gillespie et al., 1999, Brookes et al., 1996), the use of which was beyond the time frame of this study.

When using the cumulative frequency method to investigate the best-fit distribution, it is imperative to always objectively select whichever distribution best fits the data, and never force the data to fit to a preferred distribution. The cumulative frequency method is often used to investigate scale-invariant properties. If a data set follows a power-law distribution, then the relationship may be extrapolated above and below the sampling limits. However, as shown in **Table 1.4** and **Figure 1.41**, the majority of the spacing data sets reported in the literature are best-fitted by either exponential or log-normal distributions.

Fracture spacing data sets collected in this study adjacent to faults within the MTFC and the WBFS, at a variety of scales and within a variety of lithologies, are all found to be best described by an exponential distribution, with a negative slope (sections 3.1.4, 3.2.4, 3.3.4, 3.4.4, 4.2, 6.1.3, 6.2.3, 6.3.3, 6.4.3, 7.2). This observation is based on cumulative frequency plots of fracture spacing values, and the good relationship observed between the exponent from exponential graphs and mean spacing values, which is expected for exponentially distributed data (**Figure 8.1**). Spacing data sets from both the MTFC and WBFS have been collected in two ways, 1) by carrying out

a series of 1-D line transects across outcrop surfaces, and 2) by carrying out 1-D multi-line transects across 2-D data sets (thin sections, photographs taken in the field, an air photograph and a Landsat data set). Spacing data sets collected both in the field and from 2-D data sets are best described by exponential distributions, and show similar exponent values (**Figure 8.2**). Data sets collected in the field are likely to be more reliable, as data collected from 2-D data sets involves multi-line sampling which can distort population plots as some large spacing values may be multiply sampled (e.g. Marrett 1994). The data sets of fracture spacing collected in the field are also more consistent, in that the resolution of all data sets is identical (i.e. equal to the resolution of the human eye, ~0.5mm). The resolution of photographic data sets is dependent on the scale of the image (photographs taken closer to the outcrop surface will have better resolution than those taken further away), and the quality of processing of the photographic film.

When data is interpreted as being best-described by any distribution other than a power-law, little further analysis of the spacing parameters has been reported in the literature, giving the impression that non-power-law spacing data is less useful than power-law spacing data. The adherence of a data set to an exponential distribution implies that a characteristic spacing value (the mean spacing) is a defining property of the rock mass, and therefore suggests that discontinuities are not spaced self-similarly. The mean spacing of an exponential distribution is inversely related to the exponent (slope) of the relationship, and may therefore be used to compare data sets from, for example, different lithologies, or from different parts of a fault zone. The exponent and mean spacing values from data collected within the MTFC and WBFS in this study have successfully been used to characterise fracture spacing at different distances to the main faults, and between different lithologies, thus proving that non-power-law spacing data is useful and well worth investigating!

A number of explanations have been put forward as to why spacing data sets may be best-described by an exponential distribution. The first is that in a homogeneous, pristine rock mass, fractures/faults may not be initially spatially correlated, but with increasing deformation, interaction between structures increases, which changes the distribution of the discontinuities. Modelling by Rives et al., (1992) and Belfield (1998) has simulated the development of the spacing distribution through changing the magnitude and spatial distribution of strain respectively. It was found that spacing values are best described by an exponential distribution when the system of

discontinuities is immature (low fracture density and low fracture interaction) and the strain is homogeneous. With increasing deformation the best-fit spacing distribution was found to evolve from exponential to lognormal to normal as fracture interaction increases. In the case of the data sets collected in this study, within the MTFC and the WBFS, it is difficult to see how fracture sets developed within these complex multiply reactivated fault zones can be considered as representing immature systems.

A second explanation, put forward by Brookes et al., (1996), is that tectonic fractures/faults may simply re-activate pre-existing discontinuities, such as cooling joints related to the intrusion of magmatic bodies which follow an exponential distribution. Fractures and faults measured within the MTFC and WBFZ have been collected from a number of lithological units, including some granitic bodies. In each case, data sets from each lithology are best-described by an exponential distribution, and no pre-existing, non-tectonic joint sets have been recognised in the field, suggesting that the exponential spacing distributions must have some other explanation.

It has been widely documented that errors involved in sampling fracture attributes, can result in severe degradation of a power-law distribution so that the data appears to be either log-normal or exponentially distributed (e.g. Castaing et al., 1996, Bonnet et al., 2001). This degradation of a power-law distribution has been most recognised when measuring and analysing fracture length distributions (see section 1.8.3.2), but may also affect the analysis of fracture spacing, due to limited field exposures (Gillespie et al., 1993). The effects of sampling on data collected in this study are thought to be limited. Exposures on which to measure attributes of faults and fractures in both the MTFC and the WBFS were chosen with care, to avoid as much as possible the effects of truncation (i.e. where large spaces are inadequately sampled due to small outcrops). The lower limit of fracture spacing resolution in the field is only limited by the resolution of the human eye; the smallest spacing measured at outcrop scale was 0.5mm. Every spacing data set collected from both fault zones in this study, from a variety of lithologies, and over a wide range of scales is best described by an exponential distribution. If the data are exponential due to degrading of a power-law distribution, one may expect at least some of the data sets to show some power-law tendencies, but even the largest data sets of fractures (more than 100 values in an individual spacing data set) show a strong tendency to an exponential distribution,

therefore suggesting that the effects of sampling is limited, and that the exponential fit is real.

All the data sets collected in this study lie in the vicinity of large-scale multiply reactivated faults. If during each individual episode of brittle faulting, new fractures are produced, then it is possible that the superimposition of different fracture networks could produce an exponential distribution, regardless of the best-fit distributions for each individual fracture set (Priest and Hudson, 1976, Hudson and Priest 1979, Brookes et al., 1996). In the case of the MTFC data set, it is apparent in the field that the present day fracture network was largely produced during the initial faulting event, and that during later reactivations, the 'old' fracture network was re-used, as well as new fractures being created (c.f. section 3.1.2). This combination of superimposition and re-use is probably the most plausible explanation as to why the fracture/fault spacing distributions are best-described by an exponential distribution. By analogy with the work of Brooks et al., (1995), it is possible that the resulting exponential distribution for fracture spacing may be related to the ratio of birth (nucleation) rate and growth rate of fractures. For example, the birth of a new fracture within a rock volume creates new fracture spaces (e.g. by superposition of fracture sets during successive reactivation events), whereas growth of existing fractures (e.g. by re-use of 'old' fractures during successive reactivation events) results in no new fractures being formed, and consequently no change in fracture spacing. However, the work of Brooks et al., (1995) concentrated on the birth and growth rates of vein thickness, which may increase indefinitely and is effectively an open-ended system. Fracture spacing on the other hand, is effectively a closed system, where spacing values in a rock can only decrease if new fractures are inserted into a rock volume. The relationship between the ratio of fracture birth rate and growth rate and the resulting statistical distribution for fracture spacing requires further investigation by computer-based modelling which is beyond the scope of this project.

8.1.2 *Relationship between best-fit spacing distribution, 'step plots' and co-efficient of variation values*

An exponentially distributed data set of values strictly means that the data are neither clustered (which would be equated to a power-law distribution) nor anti-clustered (i.e.

regular, equated to a normal distribution) but are instead randomly distributed (section 1.8.2.3). However, some degree of clustering is observed from exponentially distributed spacing data collected up to ~500m from the VF within the MTFC. The clustering of fractures is based on field observations and 'step plots' created for 1-D transects such as that at locality 157 (section 3.1.4.7, **Figure 3.18 b, c**). Also, a systematic increase in exponential exponent values is observed towards major faults within the MTFC and WBFS, suggesting that at the centre of faults, the data sets are dominated by small spaces relative to large spaces, and suggests that fractures may be more clustered adjacent to the faults than away from them. Values of Cv also vary significantly within the data sets collected from the MTFC and the WBFS (overall values range from 0.43 to 1.58), suggesting that the data are not strictly random (expected Cv = 1) as is the case for truly exponential data sets. There is therefore no systematic relationship between data sets that are best-described by an exponential distribution, 'step plots' and Cv values. It is suggested that adjacent to some faults (VF, MTFC), fracture clustering may be present, yet the data set is still best-fitted to an exponential distribution, because the clustering is not strong enough to yield a power-law distribution of fracture spacing values (McCaffrey et al., (in preparation)). Co-efficient of variation is a bulk parameter that is insensitive to different scales of observation. Therefore, as well as using cumulative frequency plots to determine the best-fitting statistical distribution for fracture spacings, other parameters and techniques, such as 'step plots' should be used to assess the 'in situ' degree of clustering within the data sets, as clustered exponential data sets appear to occur in nature. More investigation is needed into how close to the Cv = 1 line do values of Cv have to be, in order for the data set to be best-described by an exponential distribution.

8.1.3 *Best-fitting statistical distribution for fracture length and its relationship to connectivity*

As was the case with fracture spacing (section 8.1.1), there have been numerous studies on the statistical properties of fracture/fault length populations (see **Table 1.4**). The majority of studies carried out to date suggest that fracture/fault length data sets are generally best-described by a power-law distribution (**Figure 1.44**), although the exact nature of the relationship, defined by the power-law exponent, has no overall

consensus, and a wide range of exponent values have been reported (**Table 1.4, Figure 1.45**). Fracture length data sets that are best described by a power-law distribution are scale-invariant, and potentially allow the prediction of fracture lengths beyond the sampled data range. However, the term 'power-law exponent' has often been used synonymously, and erroneously, in the literature, with 'fractal dimension' (e.g. Marret & Allmendinger 1991, Walsh et al., 1994, Brooks et al., 1996, Needham et al., 1996, Schultz & Fori 1996, Yielding et al., 1996, Belfield 1998, Beacom, 1999, Poulimenos, 2000, Gillespie et al., 2001). When analysing data sets of fracture length, the values are sorted into descending order and plotted against cumulative frequency to investigate the best-fit statistical distribution, hence the data is not analysed 'in situ'. The term 'fractal' defines how an object fills space, for example a fracture network exposed on an outcrop surface partially fills 2-D space, and the term should only be used to describe the spatial, in situ, properties of the fracture network, and not individual fracture attributes (Bonnet et al., 2001). Power-law length distributions may form part of, but do not necessarily equate to, fractal data sets. The fractal dimension of a fracture network can be analysed by using the box-counting technique (section 1.8.2.4.3), but it has been concluded in the literature (Gillespie et al., 1993, Bonnet et al., 2001) that 2-dimensional box-counting techniques are too insensitive to characterise the many attributes of most fracture arrays, and that instead, parameters that compose the fracture geometry should be characterised individually, which is the methodology that has been followed in this study.

In this study, fracture length data sets have been measured from 2-D data sets, at outcrop scale within the WBFS, and from four data scales within the MTFC. Based on cumulative frequency plots, it has been shown that fracture length values are best described by either exponential or power-law distributions (for some data sets, both distributions may be applicable).

There are essentially two possible explanations for this observation of both exponential and power-law length distributions. The first is that the observed exponential distributions are real facets of the data, and that in both study areas, two best-fitting statistical distributions for fracture length are observed. The second is that all of the length data sets collected are samples from underlying power-law distributions that have been degraded to appear exponential through sampling errors.

Taking the first scenario, that the exponential data sets are real, it has actually been suggested in the literature that a common ambiguity in interpreting fault/fracture

length data arises when a power-law distribution is fitted to data sets that are actually exponential (Borgos et al., 2000). Although power-law length distributions are most common in the literature, other distributions, including exponential, have also been reported (**Table 1.4**). Of utmost importance in interpreting any cumulative frequency 'v' length plot is to always fit a distribution to the data set, and never fit the data set to a distribution, i.e. never over interpret the data.

It has been suggested by Cowie et al., (1993), based on numerical modelling, that the best-fit fracture length distribution may evolve from an exponential distribution to power-law as the interaction of fractures increases. An exponential distribution would therefore indicate an immature fracture system, and as the system evolves fracture linkage increases and results in a power-law distribution of fracture lengths. As suggested for the best-fitting fracture spacing distributions (section 8.1.1), it is unlikely that the fracture systems observed within the MTFC and the WBFS are immature due to the complex reactivation histories of the two fault systems.

Another explanation for exponentially distributed fracture lengths may be provided for data sets that possess a strong mechanical anisotropy. In layered, bedded or strongly foliated rocks, the growth of fractures orientated perpendicular to the foliation/bedding/layering may be restricted, thus resulting in a non-power-law fracture length distribution (section 1.8.3.2). Most of the data sets of fracture lengths collected in this study are from lithologies that possess a mechanical anisotropy. For example fractures collected within psammite adjacent to the WBFS, appear to have preferentially concentrated along pre-existing bedding surfaces, creating laterally continuous fractures parallel to the rock fabric, these are accompanied by a series of shorter, perpendicular and sub-perpendicular, fractures which have restricted growth (see photograph in **Figure 6.15 a**). The data set of fracture lengths collected from the MTFC may also be affected by the pre-existing foliation (parallel to the fault trend) which has been preferentially re-used by later brittle fracturing, acting as a mechanical anisotropy and restricting fracture growth perpendicular to the foliation trend. On a more general note, it is also possible that in complex reactivated systems such as those studied here, pre-existing fractures and faults created during early kinematic events may also act as mechanical boundaries across which the growth of later fractures and faults is restricted, and therefore a power-law distribution may not exist.

The second possible explanation for the observation of exponential length distributions in the study area is related to sampling and data collection, and can be

divided into two: a) *insufficient data quantity*, i.e. the data set is not large enough to be representative of the population, or b) *insufficient data quality*, i.e. the occurrence of sampling errors such as truncation and censoring of fracture/fault length measurements (see section 1.7.5.1), which can cause the frequency distribution of a power-law population to degrade and deviate from a perfect straight line that would be observed for an infinitely large system (see section 1.8.2.4.5). On one hand, insufficient data quality seems a plausible explanation for some data sets collected in this study, where an equally good fit is observed for both a power-law distribution and an exponential distribution, suggesting that possibly these data sets are on the border-line between recognisable power-law distributions, and those that are degraded due to sampling errors. With reference to data quantity, it has been suggested by Bonnet et al., (2001) that a minimum of 200 fractures should be sampled to provide an accurate sample of fracture/fault lengths. Therefore it may be expected that data sets in this study which possess more than 200 fractures are more reliable. Out of 53 2-D data sets analysed in this study (from both fault zones and a variety of data scales), 22 contain more than 200 fractures. Of these 22 data sets, 12 are best-fitted to a power-law distribution, 7 can be best-described by either a power-law or exponential distribution, and 3 are best described by an exponential distribution, suggesting that even data sets of more than 200 fractures still show no consistent fracture length population. It is interesting to note that out of all the data sets measured, the one with the most fractures, and therefore the largest sample (thin section data set HS13, MTFC, 964 fractures), can be either described by an exponential or a power-law distribution. This all suggests that although the effects of data quality and quantity on best-fit length distributions cannot be disregarded in this study, it is plausible that for some data sets, the effects of sampling are not significant, and that the exponential data sets are real.

Many authors have related the exponent values from power-law length data sets to the connectivity of the fracture network (Bour and Davy, 1997, 1998, Odling et al., 1999, Renshaw, 1999). It is suggested that, when sampling from 2-D data sets, the exponent of the power-law length distribution is indicative of the relative importance of 'large' and 'small' fractures to the connectivity of the network (where large fractures are longer than the sample area, small fractures are contained within the sample area) (see section 1.7.8.5). However, the fact that exponentially distributed length data sets may be misinterpreted as power-law data sets, and the wide range of power-law length

exponents reported in the literature may question the validity of characterising connectivity using the exponent of the power-law length distribution. In this study, fracture length from each data set has been characterised using the total fracture length per unit area (fracture intensity), which is independent of the best-fit statistical length distribution, and has been shown to have a good relationship with fracture network connectivity (defined as the total number of nodes per unit area) (see section 8.4). Using this independent measure of fracture length for 2-D data sets is likely to be more robust than using the exponents of best-fitting distributions, which are often ambiguous.

8.2 Synthesis and discussion of fracture characteristics from the MTFC, Central Norway

8.2.1 *Fracture orientation data*

All fracture orientations measured in the field are plotted on stereographic projections (as poles to fracture planes) in **Figure 8.3**, separated into data collected adjacent to faults within the VFS (which includes the VF, the EF and the RF) (**Figure 8.3 a**), and data collected adjacent to the HSFP (**Figure 8.3 b**). All fracture orientation data are plotted together on the stereonets shown in **Figure 8.3 c** and **d**. Although there is scatter in the data, three, possibly four, clusters of fracture orientations are evident. There are two clusters striking ~ENE-WSW, dipping to the NW and SE, and a large spread of steeply dipping values ranging in strike from NW-SE to N-S, which may encompass two clusters. This pattern of fracture orientations observed from outcrop-scale data is also present at air photograph scale, as illustrated by the rose diagram in **Figure 8.3 e**. On the rose diagram, the most prominent trend is ENE-WSW, with clusters also occurring trending N-S and NW-SE. An extra cluster of orientations is present trending E-W, which could represent an additional set of fractures/faults, but may also be attributed to non-tectonic lineaments observed on the air photograph, such as streams or rivers.

The arrangement of the 3 (or 4) main clusters of fracture orientations observed within the MTFC, together with the earliest recognised fracture-fill (epidote-rich cataclasite), and kinematic observations in the field, all suggest that the present day fracture network was initiated during a period of sinistral transtensional movements along the MTFC (**Figure 8.4**). Brittle sinistral transtensional movements along the MTFC, which localised along two pre-existing shear zones and are associated with the production of epidote-rich cataclasites and pseudotachylites, have been recognised in the field and dated by Watts (2001) at 291 Ma (see chapter 2) (**Figure 8.4**). Subsequent reactivation events during the Mesozoic and later times, which concentrated along the VF whilst the HSF remained largely inactive (Watts 2001), appear to have largely re-used this initial fracture network (**Figure 8.4**) (based on field evidence such as multiple fracture infills, section 3.1.2), whilst also creating new fractures (note the difference in scatter between VFS and HSF stereonets, **Figure 8.3 a, b**).

It has been suggested in the literature (e.g. Beacom et al., 2001 and references therein) that pre-existing compositional and structural heterogeneities in basement rocks, such as foliation, exert a significant control on fracture development. Foliation measurements from the NW and SE limbs of the regional antiform that lies between the two bounding structures of the MTFC (section 2.2) have been collected by Watts (2001). Visual inspection suggests that there is a close correspondence between clusters A and B on the stereonet of poles to fracture planes, and the clusters of foliation readings (**Figure 8.5**). Beacom et al., (2001) suggest that these qualitative assessments of correspondence can be quantitatively tested using the eigenvector ratios, C (strength of the cluster) and K (shape of the cluster) (Woodcock and Naylor 1983). The C and K values for MTFC foliation clusters are plotted against the C and K values for their corresponding fracture clusters in **Figure 8.6**. On the graph of C values (**Figure 8.6 a**), both data points lie close to the 1:1 line, suggesting that the strength of clustering is similar for the fracture and foliation data sets. On the graph of K values (**Figure 8.6 b**) the HSF data point lies close to the 1:1 line, suggesting that the shape of the fracture cluster is similar to that of the foliation cluster. The VF data point however, does not lie close to the 1:1 line, suggesting that for this data set the shape of the fracture cluster is different to the shape of the foliation cluster. This departure from a direct correspondence may be explained by the VF experiencing a more complex reactivation history than the HSF (Watts 2001), resulting in a greater

scatter of fracture orientations. Visual inspection shows that the scatter on VF stereonet is greater than scatter on the HSF stereonet **Figure 8.3 a, b**, due to the creation of new fractures and possibly local re-orientation of pre-existing fractures during multiple brittle faulting events.

It is concluded by Beacom et al., (2001) that data points that lie close to the 1:1 line confirm that the foliation and fault/fracture data are geometrically co-incident, and therefore suggest that the pre-existing foliation has a significant control on the location of later faulting/fracturing. However, when positive correlations of *C* and *K* values between fracture/fault and foliation data sets are observed, the only conclusion that can be drawn is that the shape and strength of the clusters are similar. Eigenvector ratios do not show that two clusters are geometrically co-incident. Two clusters with similar shapes and strength that lie in opposite portions of a stereonet can provide good *C* and *K* correlations, but are not geometrically co-incident.

In fact, when the data sets of foliation and fractures collected from the MTFC are superimposed, it can be seen that although the *C* values from the foliation and fracture clusters plotted close to the 1:1 line for both faults, the clusters of foliation and fractures are not geometrically co-incident for either fault data set (**Figure 8.7**). Both foliation clusters lie 5-10° clockwise of the fracture clusters. The fracture clusters are instead parallel to the trend of the two major brittle structures (VF and HSF, measured in the field), which are slightly oblique to the pre-existing ductile foliation (Watts 2001) (**Figure 8.8**). Therefore it is the orientation of the brittle faults that has the strongest control on fracture zone development, rather than the pre-existing ductile foliation, although the foliation is also likely to have been exploited by later fracturing due to there only being a difference of 5-10° in the orientation of the later faults and the foliation.

It is possible that the small, but consistent, difference in observed foliation and fracture orientations may be due to human error. The fractures were measured by the author, whereas the foliation values were measured by Watts (2001), albeit at the same time in the field. If the compass declinations were set differently, then a consistent difference in readings would occur. However, this is considered to be extremely unlikely, as the foliation measurements were made using three different compasses over the duration of field work (due to breakage!), and each time a new compass was used the declination was re-set and compared between the author's compass and Watts (2001). It is considered more likely that the reason the fracture

clusters are 5-10° *anti-clockwise* of the foliation clusters is a product of the initial sinistral brittle faulting event. Conversely, if the fracture clusters were *clockwise* of the foliation clusters, then this may instead be consistent with dextral strike-slip movements.

It is therefore important, when analysing the effect of pre-existing anisotropies on later fracture development, to first determine that the clusters of fractures/faults and the pre-existing anisotropy are co-incident, before testing whether the clusters have similar shape and strength parameters. Testing whether the clusters are geometrically co-incident can be done either by superimposing the data, or more accurately by comparing the mean girdles from each cluster, instead of relying on visual inspection.

8.2.2 *Fracture infill data*

The earliest fracture-fills observed within the MTFC are coeval epidote-rich cataclasite and pseudotachylite which formed during sinistral transtensional movements along the VF and the HSF, and are coeval with the initiation of the present day fracture network (see chapter 2, and Watts 2001). Later infills of zeolite and calcite mineralisation are observed within fractures adjacent to the VF, HSF, RF and EF, in different proportions. This infill is thought to be associated with dip-slip and dextral Mesozoic movements along the MTFC (see chapter 2 and Watts 2001). The common observation of early epidote and later zeolite/calcite within the same fracture suggests that the fracture network created during sinistral transtension was re-utilised during later reactivation events. The youngest observed fracture-fill is incohesive gouge, and this is also observed to be re-using the 'old' fracture network.

The distribution of fracture-fill types differs for the four faults studied (HSF, VF, EF and RF). Fractures observed adjacent to the VFP contain all 3 types of fracture fill, suggesting that the VF was active during all 3 events. Zeolite/calcite-filled fractures are more common than both epidote and gouge-filled fractures. Gouge-filled fractures are observed within 10m of the VFP only, whereas zeolite/calcite and epidote-filled fractures are observed up to ~500m NW of the VFP.

Both epidote-cataclasite and zeolite/calcite mineralisation are observed within fractures adjacent to the EF and RF, although the proportion of epidote-filled fractures adjacent to the EFP is very small, suggesting that the major phase of movement along

the EFP probably occurred during Mesozoic times. The absence of gouge-filled fractures adjacent to the EF or the RF, suggests that neither of these structures were active during the latest phases of movement along the MTFC observed by Watts (2001) (see chapter 2).

The distribution of filled-fractures is observed to change along strike of the HSF. Towards the NE (Mefjellet localities), epidote/pseudotachylite-filled fractures are most common, with minor zeolite/calcite infills observed. Farther to the SW along the strike of the HSF (Hammardalen quarry and 719 road localities) zeolite/calcite filled fractures are more common than epidote/pseudotachylite-filled fractures. This change in dominant fracture infill along strike of the HSF, may suggest that only parts of the HSF were reactivated during the Mesozoic (i.e. that localised reactivation occurred). No gouge-filled fractures are observed adjacent to the HSFP, suggesting that the structure was inactive after Mesozoic times.

In essence, the geometry of fractures, distribution of fracture-fills and kinematic observations are all consistent with the kinematic history of the MTFC described by Watts (2001).

8.2.3 *Fracture spacing, length and connectivity parameters*

A number of different fracture parameters described in this study collected at outcrop scale indicate different signatures for the two main faults, VF and HSF, and also for the EF. These parameters are:

1. exponential spacing exponent
2. mean spacing values
3. fracture density
4. exponential length exponent
5. mean fracture length
6. fracture intensity
7. fracture connectivity (defined by the numbers of fractures and nodes per cluster, fracture cluster length and the number of nodes per unit area)

   (where 1 & 2 are 1-D measurements, 3-7 are all 2-D measurements)

All of the above parameters show the following signatures:

- The VF is characterised by a *tall* peak in values (or trough for measurements such as mean length and spacing), with a *wide* zone of ~500m to the NW of the VFP over which values decrease to background levels.
- The HSF is characterised by a *tall* and *narrow* zone of above-background values (or below for mean spacing and length parameters). Values decrease to background levels within 100m, either side of the HSFP.
- The EF is also characterised by a *narrow* but *shorter* peak in above-back ground values, where the height of the peak is less than half that associated with the VF and HSF.

Graphical representations of these signatures are presented in **Figures 3.63, 4.154, 4.155** and **4.156**.

A series of thin section data sets have also been used to analyse the change in fracture parameters around faults within the MTFC. An individual thin section of rock measuring 3 x 2cm (approximately) is unlikely to be 100% representative of the surrounding area, therefore the thin section data sets are not as reliable as the outcrop data sets. However, the fracture parameters listed above measured from thin section data sets show the same signatures for the VF and the HSF as the outcrop data set (no thin section data sets have been analysed adjacent to the EFP).

The reason that the fracture parameters listed above (from outcrop and thin section scales) provide the different signatures for the three faults is most likely to be related to the different kinematic histories observed for the three structures. The VF is a relatively large, laterally continuous structure that has been multiply reactivated, and is associated with a wide zone of intense fracturing. The HSF is also a large, laterally continuous structure, but has experienced less reactivation. The EF is a relatively small structure, less laterally continuous, and has probably only experienced one major phase of fault movement during Mesozoic times (although this phase encompasses both dip-slip and dextral strike-slip movements). These differences in kinematic history and 'size' between the three faults are recognised by the fracture parameters listed above.

Fracture data sets have also been collected adjacent to the RFP, a ~N-S trending fault within the VFS. Due to the nature of the exposure (the RF outcrops in a steep-sided narrow gorge), it was not possible to measure fracture parameters at different

perpendicular distances to the RFP. Instead fracture parameters have been collected along strike, within ~5m of the RFP. The exponent values measured from exponential spacing graphs change along strike of the RF (section 3.4.4.4, **Figure 3.37 b**). Exponent values measure the relative abundance of small and large fracture spaces; they are inversely proportional to mean spacing values and are therefore a measure of fracture density. The exponent values slightly increase to the north along the strike of the RFP, and suggest that fracture density increases away from the intersection of the RFP and the VFP. The RF initiated as a dip-slip normal fault during sinistral transtensional movements along the VFP (and HSFP). It is possible that fracture density increases along the RFP, away from the intersection with the VFP, because the centre of the RFP, corresponding to the area of maximum displacement is further north, as illustrated in **Figure 8.9**, and that the data sets collected nearest to the VFP are within the tip zones of the RFP.

8.3 Synthesis and discussion of fracture characteristics from the WBFS, Shetland Isles.

The data set of fracture parameters collected and analysed from rocks adjacent to faults within the WBFS is complicated by three main features:

1) The wide variety of lithologies present means that fracture data sets collected in the field from each lithology are small, compared to the data set collected from the MTFC which was within only one lithology

2) Different kinematic events are preserved within fault-bounded blocks along the strike of the WBF, because the magnitude of displacement along the WBFS is 10's – 100's km, and early fault rocks and structures are often cut out. However, the magnitude of displacement along the MTFC is likely to be no more than a few 10's km (Watts 2001), and therefore fault rocks and structures are generally not cut out, but instead are preserved in sequence within the wall rocks adjacent to the fault core.

3) The four faults studied (WBF, NF, MF and AVF) all have different kinematic histories (see chapter 5).

However, some general conclusions can be drawn from the analysis of fracture orientations and fracture-fills. Different patterns of fracture orientations were

observed for all lithological data sets. The data set that displays the strongest clustering is the data set of fractures collected within psammite at Ollaberry locality (section 6.1.1), which in the field also corresponds with the lithology that displays the strongest and most persistent foliation. The lithologies that display the least clustering of fracture orientations are the data sets collected within pelite adjacent to the WBFP, which displays a weak foliation in the field, and granite also adjacent to the WBFP, which displays no obvious magmatic or tectonic foliation in the field. Most of the other lithologies display clustering of fracture orientations close to the fault planes, orientated parallel to the rock foliation. This all suggests that lithologies containing a strong/persistent foliation are most likely to contain fractures with preferred orientations, parallel to the rock foliation trend.

A variety of fracture-fills occur within a small percentage of fractures observed adjacent to faults within the WBFS. Some fracture-fills are only observed within individual lithologies (e.g. epidote-filled fractures within granite at Sullom), suggesting a possible local source of fluids. The relative percentage of filled-fractures observed adjacent to the faults increases towards the fault planes for some lithologies, but for others the peak percentage of filled fractures occurs away from the fault plane. This observation could be the result of insufficient data collected from fractures within these lithologies close to the fault planes, or may represent a real difference in the distribution of fluids between different lithologies. More data from each lithology at different distances to each fault plane are needed to investigate this further.

Little kinematic data were available to collect in the field, but the observations made correlate well with the kinematic history of the WBFS described from a detailed field and microstructural study by Watts (2001) (see chapter 5).

It is difficult to make any robust statements regarding the change in fracture spacing, length and connectivity parameters for each fault and each lithology due to the limited nature of the data sets. However, some fracture attributes display common trends. Exponential spacing exponent values, fracture density, fracture intensity, and fracture connectivity (defined by the total number of nodes and fractures per cluster, and the total number of nodes per cm^2) all increase towards the centre of the MF, AVF and WBF for all lithologies except the Devonian sandstone data set collected at Bixter. These general trends are consistent with the changes in fracture attributes observed adjacent to faults within the MTFC (section 8.2.3).

As well as the sandstone data set, fracture parameters collected within psammite and calcareous metasediments adjacent to the NF also do not show the same increases towards the centre of the fault. The lithological data sets that do not show the general trends described above need to be investigated further by collecting more fracture data from each lithology, as the differences could either be due to insufficient data, or could represent real differences in fracture attributes between lithologies adjacent to the faults.

8.4 Comparison of fracture characteristics from the MTFC and the WBFS

8.4.1 *Size of the data sets*

Fracture characteristics from the MTFC were measured within one dominant lithology – namely acid gneissose rocks. Therefore each data set of fracture characteristics is directly comparable. Fracture characteristics from the WBFS however, have been collected within seven different lithological units. The fracture attributes of each lithology must then be considered separately, meaning that the data set for each lithology is relatively small compared to the data set collected from gneisses within the MTFC. Therefore, compared to the WBFS data set, the fracture parameters collected from the MTFC form a more reliable and robust data set on which to base observations of the changes in fracture attributes around faults.

8.4.2 *Scales of observation*

Four scales of observation have been used to analyse fracture and fault characteristics from the MTFC, ranging from a kilometre-scale Landsat image, to a series of millimetre-scale thin section data sets. From Shetland, data sets have only been collected at outcrop scale within the WBFS. The lack of inland exposure on Shetland (due to extensive peat cover) means that no faults/fractures can be observed on air photographs (**Figure 8.10**), or Landsat images along the trace of the WBFS. Therefore

fracture characteristics have been analysed over a larger range of magnitudes from the MTFC than from the WBFS.

8.4.3 *Structural architecture of the fault systems*

The MTFC has a better-constrained kinematic history than the WBFS, based on the work of Watts (2001) (and references therein). Displacement magnitudes across the MTFC are thought to be on a kilometre-scale, as the same lithologies are observed either side of the main structures. The two bounding structures of the MTFC, and other smaller faults within the fault complex, possess different reactivation histories but all cross-cut the same gneissose lithology. Therefore comparisons can be made between non-reactivated and highly reactivated structures, and those which have experienced little reactivation, without the added complexity of lithological variations. On the other hand, the WBFS contains three main faults, each of which possess a different magnitude of displacement and different kinematic history. Overall, displacements along the WBFS have been estimated at up to 100's km (see chapter 5), meaning that this fault system is significantly larger than the MTFC. This fact, combined with the large variety of lithologies present within the WBFS, makes inferences of the effects of reactivation on fracture attributes difficult.

8.4.4 *Fracture attributes*

Although there are major differences between the data sets of fracture characteristics collected from the two fault systems, a number of similar trends have been observed (sections 8.2.3 and 8.3). In order to compare the fracture data sets from the two fault systems, four plots can be created. In each case, a good relationship between the fracture parameters plotted may be expected, for example, data sets with higher densities (i.e. more fractures) are likely to possess higher intensities (i.e. a longer total fracture length), and similarly, data sets with higher densities and intensities may be expected to show higher connectivity values, due to more interaction between fractures present. However, the exact nature of the relationships can be compared between the two fault systems:

- *Fracture density 'v' fracture intensity.* Data collected at all four scales from the MTFC, and at outcrop scale from the WBFS are plotted in **Figure 8.11a**. A good, positive, power-law relationship between these two parameters is observed for both fault data sets, extending over a large range of magnitudes. The data sets collected at outcrop scale from the two faults lie in the same portion of the graph, and are plotted together on **Figure 8.11b** and **c**. Both data sets show good power-law relationships, on both linear and logarithmic axes. The exponent values are similar for both data sets, suggesting that the relationship between fracture density and intensity is comparable for the two fault systems. Both exponent values are less than 1, suggesting that there is relatively little variation in fracture intensity values as fracture density values change (**Figure 8.12**).

- *Fracture density 'v' fracture connectivity.* Data sets collected from the WBFS (outcrop scale) and the MTFC (four data scales) are plotted together on **Figure 8.13a**. A good, positive, power-law relationship is observed for both fault data sets, with the values lying in the same portion of the graph and extending over a large range of magnitudes. The outcrop data sets from the MTFC and the WBFS are plotted together in **Figure 8.13b** and **c**. A good power-law relationship is observed for both data sets on logarithmic axes, but on linear axes, a linear relationship may also be appropriate. Both data sets have similar power-law exponent values (close to 1), suggesting that the relationship between fracture density and connectivity is comparable for the two systems, and that the parameters are directly proportional to each other (i.e. a 1:1 relationship (**Figure 8.12**)) for both fault systems.

- *Fracture intensity 'v' fracture connectivity.* All data collected within the MTFC and the WBFS are plotted on **Figure 8.14a**. Both data sets show a good, positive, power-law relationship. Data collected at outcrop scale only are plotted in **Figure 8.14b** and **c** for both fault systems, and show good power-law relationships on both linear and logarithmic axes. Both data sets show similar exponent values, close to 2, suggesting that the relationship between fracture intensity and connectivity is comparable for the two fault systems. The exponent values suggest

that fracture intensity values change significantly with respect to changes in fracture connectivity (**Figure 8.12**) for both fault complexes.

- *Total number of fractures and nodes per cluster.* Finally, the total numbers of fractures and nodes per cluster are plotted in **Figure 8.15a** for both the MTFC and WBFS data sets. These parameters can be constrained by maximum and minimum envelopes shown on the graph, as all fractures must be connected to at least one other fracture. Maximum connectivity refers to every fracture intersecting every other fracture within a cluster, in 2-D. This is in contrast to the calculations of fracture density and connectivity detailed above, where parameters are measured within a unit area, and all fractures do not have to be connected. A good relationship between these parameters is observed on **Figure 8.15a**, as expected for both fault data sets. Clusters containing less than 60 fractures plot close to the minimum connectivity line (**Figure 8.15b**). The change in relative cluster connectivity, from minimum to maximum, is not linear, but is instead an exponential change. Therefore although clusters with greater than ~60 fractures appear to depart from the minimum connectivity line, the actual cluster connectivity is still very low (around 1%) (**Figure 8.15**). Visual inspection of the data points from both fault systems suggests that the WBFS data set may be slightly better connected than the MTFC data set (i.e. the WBFS data points lie slightly above and to the left of the MTFC data points). However, this may be misleading as the WBFS data set is composed of fracture data sets from a number of lithologies, whereas fracture data sets collected within the MTFC are all measured from the same lithology. The WBFS data set may appear to be better connected due to the different lithologies being present. The lithologies are distinguished in **Figure 7.22b**, and no consistent relationship is observed between cluster connectivity and lithology, although more data is needed to investigate this further.

8.5 Comparison of fracture attributes from other fault systems

8.5.1 *Scaling of fracture length values*

Best-fitting power-law relationships from fracture length data sets (discussed in section 8.1.3) may be extrapolated between scales to potentially allow interpolation of values between sampling limits. This relationship is especially useful in the petroleum industry where the most common forms of data are seismic (10's metres- to kilometre-scale) and core (millimetre- to centimetre scale), and it is important to know what occurs in between these scales to accurately model sub-surface fracture geometries.

A number of studies have been carried out that have collected length data from 2-D data sets at different scales, and a wide range of power-law exponents have been reported (Heffer and Bevan, 1990, Castaing et al., 1996, Knott et al., 1996, Yielding et al., 1996, Line et al., 1997, Odling 1997) (**Figure 8.16**). In this study, data sets have been collected from four different data scales over the MTFC, with power-law length relationships observed for some data sets (section 8.1.3), and the extrapolation of the power-law relationship between scales extends over 12 orders of magnitude (**Figure 4.93**). The plots in **Figure 4.93** have been created using a number of different data sets, i.e. all data sets collected within the MTFC, irrespective of whether the fracture length distribution is power-law (**Figure 4.93 a**), through to individual data sets that are strictly only best-fitted to a power-law distribution (**Figure 4.93 c**). In each case, the power-law exponent of the overall relationship is 1.95, and does not appear to be sensitive to variations in the type of data that is plotted.

The exponent value for the MTFC data set is comparable to exponent values reported in the literature from Castaing et al., 1996 (exp. = 2.34) and Odling 1997 (exp. = 2.1) but is significantly different to exponents reported by other authors (e.g. Knott et al., 1996 (exp. = 1.29)) (see **Figure 8.16**).

Odling (1997) has suggested that a slope of 2 on a power-law cumulative frequency graph (c.f. MTFC data set) is indicative of a self-similar and scale invariant system. However, further analysis of the MTFC data set suggests that the reliability of the power-law exponent collected from data at different scales may be questioned. When analysed separately, the data sets at each individual scale in the MTFC show

significantly different power-law exponents to the exponent extrapolated over all scales (**Figure 4.94**). It is therefore questionable whether the exponent of 1.95 accurately represents the scaling law for the whole MTFC data set, considering that the individual exponents are so different. Questions may also be asked about the reliability of the individual power-law exponents for single data scales. For example, individual thin-section data sets, or similarly subsurface core data sets, are unlikely to accurately represent the surrounding rock mass, and this may explain why a variety of power-law exponents were observed at thin section scale over the MTFC (**Table 4.16**), instead of one consistent exponent value for that data scale. It has also been suggested that the power-law exponent for individual data sets could be sensitive to geological variables such as lithology, layer thickness, grainsize and rock competency (e.g. Gauthier and Lake 1993, Knott et al., 1996). In addition, the value of the power-law exponent may decrease as a fault system evolves due to progressive concentrations of strain onto larger structures (Nicol et al., 1996, Bonnet et al., 2001). It is therefore suggested that more investigation is needed into the validity of single power-law exponents at each individual data scale, before the extrapolated exponent can be used as the scaling factor for the fracture data set, and used to predict the frequency of fracture attributes beyond sampling limits.

A more reasonable explanation for a power-law exponent of ~2 (observed from the MTFC) has been proposed by Yielding et al., (1996), who suggest that if the exponent of the combined data set is ~2 then it simply reflects the dimension of the sampling domain (i.e. 2-D data sets), and does not reflect the scaling parameter for the whole length population. Each individual sample may reflect the true population slope (which may be the same or different for the different data scales), but the overall slope will be 2 (**Figure 8.17**). The reason that the slope is 2 is because successive sample lines from the individual populations are offset from each other, because fracture data sets are rarely collected in areas of very low fracture density.

8.5.2 Fracture connectivity

The connectivity of a fracture/fault network is a fundamental property, particularly in terms of its implications for fluid flow. There have been numerous investigations of fracture network connectivity published in the literature within the field of percolation

theory (e.g. Robinson 1983, Berkowitz & Balberg, 1993, Stauffer & Aharmony 1994, Berkowitz 1995, Odling 1997, Bour & Davy 1997, Odling et al 1999). Based on this theory, a fracture network is considered to be connected when it reaches percolation threshold, i.e. the largest fracture cluster present reaches all sides of the sample area. Two-dimensional fracture networks can therefore be characterised into those above and below percolation threshold. This method of quantifying connectivity is not very specific. The majority of 2-D data sets analysed in this study, from both fault zones and over a wide range of scales, are above the percolation threshold, and therefore a more detailed way of characterising connectivity between data sets is necessary.

As discussed in section 8.1.3, the connectivity of fracture systems has also been quantified by using the power-law exponent from the fracture length distribution (Bour and Davy, 1997, 1998, Odling et al., 1999, Renshaw, 1999). Although this is a more detailed scheme of characterising fracture connectivity, it is not thought to be robust. This is because, as discussed in section 8.1.3, measurements of power-law exponents from fracture length distributions are often ambiguous. Power-law fracture length data sets are also often misinterpreted, and may actually be best-fitted to a different statistical distribution. When fracture lengths are not found to be power-law, the quantification of connectivity must be carried out using other methods.

It is suggested in this thesis that connectivity from individual 2-D fracture networks may be easily quantified by calculating parameters such as the total number of nodes (fracture intersections) per unit area and the total number of nodes per cluster. Both of these methods allow accurate characterisation of individual data sets, regardless of the best-fit distribution for fracture length.

In this study, the total number of nodes per unit area (a measure of connectivity) has been found to have a strong correlation with other important fracture network parameters such as fracture density and intensity, for both fault zones studied (section 8.4.4, **Figure 8.13, Figure 8.14**) potentially allowing the prediction of network connectivity from density and/or intensity measurements.

A data set of fault characteristics collected adjacent to the Ninety Fathom Fault in Northumberland, England, published by Knipe et al., (1998), enables the relationship of fracture density and connectivity to be assessed for an additional fault system.

The E-W trending Maryport – Stublick - Ninety Fathom fault system (MSNFFS) is a major structural feature in North East England, exposed on the coast at Cullercoats Bay (**Figure 8.18**). The fault system comprises the southern bounding structure for

the Northumberland Basin, and is thought to have formed in early Carboniferous times by extensional reactivation of a major basement thrust zone (Kimbell et al., 1989, Chadwick and Holliday 1991, Chadwick et al., 1993). The faults within the MSNFFS are sub-planar, with a present-day throw (at base Carboniferous) of less than 4km. Extensional reactivation, with a minor dextral strike-slip component, during Permo-Mesozoic times has been suggested (Collier 1989, Skamvetsaki 1994), associated with 90m of normal displacement at the base of the Permian sequence. Overall the dominant displacements along the fault system appear to have been dip-slip. On the coast of North East England, the main host lithology cross-cut in the hanging wall of the Ninety Fathom fault are aeolian sandstones belonging to the Yellow Sands of Lower Permian age.

Knipe et al., (1998) presents two graphs of fault attributes collected from the Ninety Fathom fault system (NFF) (**Figure 8.19**). One shows the total number of faults per m^2 (fault density) against distance to the fault, and the other shows the total number of nodes per m^2 (fault connectivity) against distance to the fault. Data points were measured from the two graphs, and the values were converted to fault density and connectivity per cm^2 in order to be able to directly compare the data to the MTFC and WBFS data sets collected in this study.

Values of fracture/fault density are plotted against fracture/fault connectivity in **Figure 8.20 a**, for data sets collected from the MTFC, WBFS and the NFF system at all data scales. A good, positive, power-law relationship is observed for all data sets, which all lie in the same portion of the graph. Data sets collected at outcrop scale only from all three fault systems are plotted in **Figure 8.20 b**. The data sets are plotted on logarithmic axes, and all show a good power-law relationship with similar exponent values (close to 1). Power-law exponents close to unity suggest that the parameters are directly proportional to each other (**Figure 8.12**). However, when the data sets plotted in **Figure 8.20 b** (collected at outcrop scale) are re-plotted on linear axes, different relationships between density and connectivity are observed between the different fault/fracture data sets (**Figure 8.20 c, d**). The data set collected adjacent to the NFF suggests that fractures/faults are slightly better connected here compared to the other fault data sets. This difference is not observed on the logarithmic plot (**Figure 8.20 b**), and it is therefore important to plots parameters on both logarithmic and linear axes where possible, as logarithmic axes may 'disguise' small differences,

and obscure small changes in parameters between data sets. In other words, linear axes are more sensitive to small changes in parameters than logarithmic axes.

There are a number of explanations as to why the data set collected from the NFF system may be better connected than those collected from the MTFC and the WBFS. Firstly as the raw data was not available, human errors may be involved in measuring the values of fault density and connectivity from **Figure 8.19**. Secondly, the data presented by Knipe et al., (1998) is described as *fault* data, whereas the parameters collected from the MTFC and WBFS are *fracture* data sets. This may imply a scale difference in the structures measured (i.e. >metre-scale for faults, >centimetre-scale for fractures) and may affect the connectivity and density values. Following on from this difference in terminology between data sets, having visited the likely location where density and connectivity data was collected from the NFF, it is evident in the field that the dominant discontinuity observed within the Yellow Sands adjacent to the fault are deformation bands, i.e. narrow localised bands of cataclastic fracturing, grain-size reduction and displacement of grains, resulting in strain hardening with increasing communition (Main et al., 2001), as opposed to the formation of tectonic fractures by pervasive dilatant microcracking (c.f. MTFC and WBFS data). It is therefore possible that although the data set collected from the NFF is described as fault data, measurements of density and connectivity may have been collected from deformation bands, which have been initiated by different mechanical processes than the fractures measured from the MTFC and WBFS, and may also explain why different density and connectivity relationships are observed. Thirdly, the data collected from the NFF were measured within aeolian sandstones, whereas the MTFC data sets are from gneiss and the WBFS data set comprises a number of lithologies. Different lithologies may possess different density-connectivity relationships due to, for example, the presence of mechanical anisotropy's such as bedding planes. Finally, there is a major kinematic difference between the NFF system, and the WBFS and MTFC fault systems. All three fault systems are large (km-scale), laterally extensive, and have experienced reactivation. However, the dominant type of displacements along both the WBFS and the MTFC are *strike-slip*, and the dominant movement along the Ninety Fathom fault system is *dip-slip*. It is therefore possible that rocks that have experienced different kinematic histories may display fracture systems with different density-connectivity relationships. This suggestion needs to be investigated further using more robust dip-slip data sets.

8.6 Characterising faults and their reactivation histories

8.6.1 *The importance of recognising reactivation*

Reactivation of pre-existing structures is a well-known phenomenon in many geological settings. However, in the absence of direct field evidence, and/or other reliable criteria (see section 1.6, and Holdsworth et al, 1997), the reactivation of pre-existing structures, in preference to the formation of new ones, is difficult to recognise in the subsurface. This is especially true when successive reactivation events are kinematically similar (e.g. two phases of dip-slip normal movement). Many times in the literature, reactivation has been wrongly assumed on the basis of geometric similarity between structures in the subsurface, in the absence of direct evidence (Holdsworth et al., 1997). More accurate techniques for the detection of reactivation in the subsurface, where direct field evidence is unavailable, are therefore needed.

On a large scale, pre-existing structures are known to influence the location and architecture of numerous geological features, such as sedimentary basins and orogenic belts (e.g. Dewey et al., 1986). On a smaller scale (i.e. hydrocarbon reservoir scale), there are at least two fundamental reasons why recognition of reactivated faults in the subsurface is imperative:

a) As shown in this study, more highly reactivated faults are more likely to be associated with wider damage zones, compared to less reactivated structures. Within the damage zone, the density, intensity and connectivity of micro- and macro-scale fractures/faults will be significantly above background levels. This wider damage zone can be either beneficial or detrimental to the flow and extraction of fluids, for example, hydrocarbons in the subsurface. Fluid flow may be prohibited through compartmentalisation of the reservoir, or, in impermeable rocks, fluid flow and storage may be enhanced through the creation of a wider zone of fracture/fault porosity (**Figure 8.21**).

b) Reactivation of pre-existing faults that act as seals for the accumulation of hydrocarbons could promote leakage from the reservoir, if the timing of migration was before reactivation of the fault (**Figure 8.22**).

The findings of this study have led to the development of a methodology to potentially characterise individual faults, and gain an insight into their reactivation histories, as detailed in the following section.

8.6.2 *Using fracture attributes to potentially fingerprint reactivated structures*

The following suggestions are based mostly on field observations and the characterisation of detailed fracture attributes from the MTFC, as this is considered to be a more robust data set than that collected from the WBFS. The MTFC also has a better-constrained kinematic history, based on the work of Watts (2001). The MTFC contains two parallel bounding structures, which display heterogeneous kinematic histories (see **Figure 2.12**). Both structures (VF and HSF) broadly initiated as ductile shear zones, and were both reactivated during a phase of sinistral transtension, during which the initial fracture network was created on each fault. Subsequent to this, the HSF remained largely inactive in the study area, whereas the VF suffered intense, polyphase reactivation (involving dextral strike-slip and dip-slip movements) (see **Figure 2.12**). A smaller, less laterally extensive fault, parallel to the main structures has also been studied, and is likely to have only experienced one major phase of movement. All three structures (HSF, VF and EF) all have the same trend, and are all contained within banded gneiss. Therefore the effects of structural trend and lithology on the fracture network may be discounted, and direct comparisons of the fracture attributes associated with each structure can be made.

- More reactivated structures may be associated with wider zones of filled-fractures, and an overall higher percentage of filled-fractures than less reactivated structures, suggesting that more reactivated structures may be more efficient fluid conduits.
- If individual fracture-fills can be tied to specific kinematic events, then the presence/absence of fracture fills, and the relative proportions of infill-types observed, may help to constrain different reactivation histories, either between faults or along strike of a single fault.
- Highly reactivated structures may be associated with a tall peak and a wider damage zone of above-background values of fracture *density*, and other fracture *spacing* parameters such as the exponent from exponentially distributed data, and lower mean spacings, than less reactivated and non-reactivated structures.

- Similarly, highly reactivated structures may be associated with a tall peak and a wider damage zone of above-background values of fracture *intensity*, and other fracture *length* parameters such as the exponent from exponentially distributed data, and lower mean lengths, than less reactivated and non-reactivated structures
- Also, highly reactivated structures may be associated with a tall peak and a wider damage zone of above-background values of fracture *connectivity*, defined by parameters such as the total number of nodes per unit area, or the total number of fractures and nodes per cluster, than less reactivated and non-reactivated structures
- The previous three points refer to identified changes in fracture attributes with distance to faults. It has also been shown in this study, that the relationships between fracture parameters, such as connectivity and density, connectivity and intensity, density and intensity, may also change for different fault systems, although the reasons for the different relationships observed remains unclear (sections 8.4.4, 8.5.2)

All of these suggestions are preliminary, and the methodology presented here remains to be tested on other substantial and detailed data sets of fracture attributes from faults with different kinematic histories.

8.6.3 *Controls on fault reactivation*

There has been much discussion recently in the literature regarding the significance of 'weak' crustal-scale faults, and the fault rocks they contain, on controlling fault reactivation (e.g. Rutter et al., 2001, and references therein). It is suggested by some authors (e.g. Imber 1997, Stewart et al., 1999, 2000, Holdsworth et al., 2001, Imber et al., 2001), that long term weakening mechanisms, operative within fault rocks at the core of long-lived structures, may affect the strongest part of the crust or lithosphere. These mechanisms are thought to shallow and narrow the frictional-viscous transition within the fault zone, leading to weakening, and making pre-existing structures susceptible to reactivation and localisation in the long term. Conversely, Walsh et al., (2001) suggest that it is the geometrical properties of pre-existing structures, such as size, orientation and connectivity, that are the dominant control on fault system evolution, and therefore determines whether an old fault is reactivated, or a new fault is produced. Numerical modelling has also shown that, if the fault is of sufficient size,

localisation (i.e. reactivation) can occur along faults that contain relatively 'strong' fault rocks (Walsh et al., 2001).

Observations and results from this study from the MTFC may be used to investigate this further, by comparing a highly reactivated fault (VF) and a similar-scale fault that has experienced little reactivation (HSF) within a comparable lithological and structural setting. The initial fracture network is coeval along both faults, and was associated with the production of epidote-rich cataclasite and pseudotachylite during sinistral transtension (see chapter 3). The extent of this 'early' fracture network, may be examined by analysing the width of the damage zone where fractures filled with epidote-cataclasite occur (c.f. **Figure 3.4b** (VF) and **Figure 3.47e** (HSF)). Although there is some variety in the amount of filled fracture observed along the strike of the HSF, it is apparent from the detailed analysis of fracture attributes and field observations, that the initial fracture network was up to five times wider on the VF than the HSF. Within the damage zones, increased fracture density, intensity and connectivity occur. Subsequent multiple reactivations along the VF have re-used this extensive, pre-existing fracture network, as well as creating new structures, whilst the HSF remained largely inactive. It is therefore possible then, that the reason why the VF has been significantly reactivated and the HSF has not, is due to the initial size differences between the two faults (i.e. width of fracture network/damage zone), and not necessarily due to the presence/absence of 'weak' rocks in the fault cores. However, it is most likely that the size and connectivity of the initial fracture network, and the rheology of the fault rocks within the fault core go 'hand-in-hand', and both fundamentally control reactivation.

8.7 Recommendations for further work

- The relationship between the ratio of fracture birth rate and growth rate, and the resulting statistical distribution for fracture spacing, requires further investigation by computer-based modelling.
- The relationships between the best-fitting statistical distributions for fracture spacing data sets, Cv values and 'step' spacing plots needs to be investigated further, to establish, for example, whether clustered exponential distributions are represented by characteristic Cv values. A full analysis of this problem requires a modelling solution, as suggested in McCaffrey et al., (in preparation).
- A larger data set of fracture characteristics is needed from individual lithologies adjacent to faults within the WBFS, in order to fully assess, and to be able to make more robust statements about, the change in fracture attributes around the faults, and between different lithologies.
- The relationships between fracture density, intensity and connectivity (as discussed in section 8.4.4) could be investigated for other tectonic settings (e.g. reactivated and non-reactivated dip-slip faults) and other lithologies. The relationships between these parameters can then be compared to assess how geological/tectonic setting affects fracture attributes measured in 2-D.
- The fracture connectivity maps presented here (chapters 4 and 7), may be used as an input into computer based models, to assess in more detail how fracture connectivity from real geological data sets changes around faults
- Finally, the onshore fracture and fault data collected in this study (especially the MTFC data set as it covers a wider range of scale observations) may be converted to digital form, and compared to offshore data sets such as 2-D and 3-D fault maps derived from offshore seismic data, to investigate how fracture/fault parameters observed onshore, can be used to predict offshore fracture/fault attributes

REFERENCES

Aarseth, E. S., Bourgine, B., Castaing, C., Chiles, J. P., Christensen, N. P., Eeles, M., Fillion, E., Genter, A., Gillespie, P. A., Hakansson, E., Zinck Jorgensen, K., Lindgaard, H. F., Madsen, L., Odling, N. E., Olsen, C., Reffstrup, J., Trice, R., Walsh, J. J. & Watterson, J. 1997. Interim guide to fracture interpretation and flow modeling in fractured reservoirs. European Commission report, Joule II, Contract number CT93-0334.

Acuna, J. A. & Yortos, Y. C. 1995. Application of fractal geometry to the study of networks of fractures and their pressure transient. *Water resources research* **31**(3), 527-540.

Aguilera, R. 1995. *Naturally fractured reservoirs*. Penwell Books, Tusla, Oklahoma.

Ameen, M. S. 1995. Fractography and fracture characterization in the Permo-Triassic sandstones and the Lower Palaeozoic Basement, West Cumbria, UK. In: *Fractography: fracture topography as a tool in fracture mechanics and stress analysis* (edited by Ameen, M. S.). *special publications* **92**. Geological society, London, 97-147.

Antonelli, M. & Aydin, A. 1995. Effect of faulting on fluid flow in porous sandstones: geometry and spatial distribution. *AAPG Bulletin* **79**(5), 642-671.

Arnesen, L. 1995. Damage zones around large faults. Unpublished undergraduate thesis, University of Trondheim, Norway.

Atkinson, B. K. 1987. Introduction to fracture mechanics and its geophysical applications. In: *Fracture mechanics of rock* (edited by Atkinson, B. K.). Academic Press.

Baecher, G. B. 1983. Statistical Analysis of Rock Mass Fracturing. *Mathematical Geology* **15**(2), 329-348.

Barnett, J. A., Mortimer, J., Rippon, J. H., Walsh, J. J. & Watterson, J. 1987. Displacement geometry in the volume containing a single normal fault. *AAPG Bulletin* **71**(8), 925-937.

Barton, N. 1978. International society for rock mechanics commission on standardization of laboratory and field tests. *International Journal of Rock Mechanics and Mining Sciences* **15**, 319-368.

Barton, C. C. & La Pointe, P. R. 1995. Fractals in petroleum geology and earth processes. Plenum Press, New York, London.

Beach, A. 1975. The geometry of en-echelon vein arrays. *Tectonophysics* **28**, 245-263.

Beacom, L. E. 1999. The kinematic evolution of reactivated and non-reactivated faults in basement rocks, NW Scotland. Unpublished PhD thesis, Queen's University, Belfast.

Beacom, L. E., Holdsworth, R. E., McCaffrey, K. J. W. & Anderson, T. B. 2001. A quantitative study of the influence of pre-existing compositional and fabric heterogeneities upon fracture-zone development during basement reactivation. In: *The nature and tectonic*

significance of fault zone weakening. (edited by Holdsworth, R. E., Strachan, R. A., Magloughlin, J. F. & Knipe, R. J.). *Special Publications* **186**. Geological Society, London, 195-211.

Belfield, W. C. 1998. Incorporating spatial distribution into stochastic modeling of fractures: multifractals and Levy-stable statistics. *Journal of Structural Geology* **20**(4), 473-486.

Bergman, S. C. & Woodroof, P. B. 2001. Cenozoic and Mesozoic Igneous Hydrocarbon Reservoirs in Southern Vietnam. In: *Hydrocarbons in crystalline rocks*, (Geol. Soc. conference proceedings), London.

Bering, D. 1992. The orientation of minor fault plane stirrer and the associated deviator stress tensor as a key to the fault geometry in part of the Møre-Trøndelag Fault Zone, on-shore, central Norway. In: *Structural and Tectonic Modeling and its application to Petroleum Geology* (edited by Larsen, R. M., Brekke, H., Larsen, B. T. & Talleras, E.). *NPF Special Publication* **1**. Elsevier, Amsterdam, 83-90.

Berkowitz, B. & Balberg, I. 1993. Percolation theory and its application to groundwater hydrology. *Water resources research* **29**(4), 775-794.

Berkowitz, B. 1995. Analysis of fracture network connectivity using percolation theory. *Mathematical geology* **27**(4), 467-483.

Berkowitz, B. & Adler, P. M. 1998. Stereological analysis of fracture network structure in geological formations. *Journal of Geophysical research* **103**(B7), 15339-15360.

Bloomfield, J. 1996. Characterisation of hydrogeologically significant fracture distributions in the chalk: an example from the Upper Chalk of southern England. *Journal of Hydrology* **184**, 355-379.

Blystad, P. 1995. Structural elements of the Norwegian continental shelf. *Norwegian Petroleum Directorate Bulletin* **8**.

Bøe, R. & Bjerkli, K. 1989. Mesozoic Sedimentary-Rocks in Edøyfjorden and Beitstadfjorden, Central Norway, Implications for the Structural History of the Møre-Trøndelag Fault Zone. *Marine Geology* **87**(2-4), 287-299.

Bøe, R. & Skilbrei, J. R. 1998. Structure and seismic stratigraphy of the Griptane area, Møre Basin margin, mid-Norway continental shelf. *Marine Geology* **147**, 85-107.

Bonnet, E., Bour, O., Odling, N. E., Davy, P., Main, I., Cowie, P. & Berkowitz, B. 2001. Scaling of fracture systems in geological media. *Reviews of geophysics* **39**(3), 347-384.

Borgos, H. G., Cowie, P. A. & Dawers, N. H. 2000. Practicalities of extrapolating one-dimensional fault and fracture size-frequency distributions to higher-dimensional samples. *Journal of geophysical research* **105**(B12), 28377-28391.

Bour, O. & Davy, P. 1997. Connectivity of random fault networks following a power law fault length distribution. *Water resources research* **33**(7), 1567-1583.

Bour, O. & Davy, P. 1998. On the connectivity of three-dimensional fault networks. *Water resources research* **34**(10), 2611-2622.

Bour, O. & Davy, P. 1999. Clustering and size distributions of fault patterns: theory and measurements. *Geophysical research letters* **26**(13), 2001-2004.

Brooks, C. M., Brantley, S. L. & Fisher, D. M. 1995. Power-law vein-thickness distributions and positive feedback in vein growth. *Geology* **23**(11), 975-978.

Brooks, B. A., Allmendinger, R. W. & Garrido de la Barra, I. 1996. Fault spacing in the El Teniente Mine, central Chile: evidence for nonfractal fault geometry. *Journal of geophysical research* **101**(B6), 13633-13653.

Bukovics, C. & Ziegler, P. A. 1984. Tectonic development of the Mid-Norway continental margin. *Marine and Petroleum Geology* **2**, 1-22.

Caine, J. S., Evans, J. P. & Forster, C. B. 1996. Fault zone architecture and permeability structure. *Geology* **24**(11), 1025-1028.

Caselli, F. 1987. Oblique-slip tectonics, mid-Norway shelf. In: *Petroleum geology of north west Europe* (edited by Brooks, J. & Glennie, K. W.). Graham & Trotman, London.

Castaing, C., Halawani, M. A., Gervais, F., Chiles, J. P., Genter, A., Bourgine, B., Ouillon, G., Brosse, J. M., Martin, P., Genna, A. & Janjou, D. 1996. Scaling relationships in intraplate fracture systems related to Red Sea rifting. *Tectonophysics* **261**, 291-314.

Castaing, C., Genter, A., Chiles, J. P., Bourgine, B. & Ouillon, G. 1997. Scale effects in natural fracture networks. *International Journal of Rock Mechanics and Mining Sciences* **34**(3/4), 389.

Cello, G., Gambini, R., Mazzoli, S., Read, A., Tondi, E. & Zucconi, V. 2000. Fault zone characteristics and scaling properties of the Val d'Agri fault system (Southern Apennines, Italy). *Journal of Geodynamics* **29**, 293-307.

Chadwick, R. A. & Holliday, D. W. 1991. Deep crustal structure and Carboniferous basin development within the Iapetus convergence zone, northern England. *Journal of the Geological Society* **148**, 41-53.

Chadwick, R. A., Holliday, D. W., Holloway, S. & Hulbert, A. G. 1993. The evolution and hydrocarbon potential of the Northumberland-Solway basin. In: *Petroleum geology of northwest europe: proceedings of the 4th conference* (edited by Parker, J. R.). Geological Society, London, 717-726.

Childs, C., Walsh, J. J. & Watterson, J. 1990. A method for estimation of the density of fault displacements below the limits of seismic resolution in reservoir formations. In: *North Sea oil and gas reservoirs* **3**. Kluwer Academic publishers, 309-318.

Childs, C., Watterson, J. & Walsh, J. J. 1996. A model for the structure and development of fault zones. *Journal of the Geological Society* **153**, 337-340.

Cladouhos, T. T. & Marrett, R. 1996. Are fault growth and linkage models consistent with power-law distributions of fault lengths? *Journal of structural geology* **18**(2/3), 281-293.

Collier, R. E. 1989. Tectonic evolution of the Northumberland Basin: the effects of renewed extension upon an inverted extensional basin. *Journal of the Geological Society of London* **146**, 981-989.

Coney, D., Fyfe, T. B., Retail, P. & Smith, P. J. 1993. Clair appraisal: the benefits of a co-operative approach. In: *Petroleum geology of northwest Europe: Proceedings of the 4th conference* (edited by Parker, J. R.). Geological society, London.

Conroy, D. A. 1996. The kinematic history of the Walls Boundary fault system, Shetland Islands. Unpublished PhD thesis, Queen's University, Belfast.

Coward, M. P., Enfield, M. A. & Fischer, M. W. 1989. Devonian basins of Northern Scotland: extension and inversion related to Late Caledonian - Variscan tectonics. In: *Inversion tectonics* (edited by Cooper, M. A. & Williams, G. D.). *Special publications* **44**. Geological Society, London, 275-308.

Cowie, P. A., Sornette, D. & Vanneste, C. 1993. Statistical physical model for the spatio-temporal evolution of faults. *Journal of Geophysical research* **98**, 21809-21821.

Cowie, P. A., Knipe, R. J. & Main, I. G. 1996. Introduction to the special issue. *Journal of structural geology* **18**(2/3), v-xi.

Daly, M. C., Chorowicz, J. & Fairhead, J. D. 1989. Rift basin evolution in Africa: the influence of reactivated steep basement shear zones. In: *Inversion tectonics* (edited by Cooper, M. A. & Williams, G. D.). *Special publications* **44**. Geological Society, London, 309-344.

Davis, J. C. 1986. *Statistics and data analysis in geology*. J. Wiley & Sons, New York.

Davy, P. 1993. On the frequency-length distributions of the San Andreas fault system. *Journal of Geophysical research* **98**(B7), 12141-12151.

Dershowitz, W. S. & Herda, H. H. 1992. Interpretation of fracture spacing and intensity. In: *Rock mechanics* (edited by Tillerson, J. R. & Wawersik, W. R.). *Proceedings of the 33rd U.S. symposium Proceedings - Symposium on Rock Mechanics* **33**. Balkema, 757-766.

Dershowitz, W., Lee, G., Geier, J., Foxford, T., LaPointe, P. & Thomas, A. 1995. FRACMAN user documentation manual. Golder Associates, Seattle, Washington.

Dewey, J. F., Hempton, M. R., Kidd, W. S. F., Saroglu, F. & Sengor, A. M. C. 1986. Shortening of Continental lithosphere: the neotectonics of Eastern Anatolia - a young collision zone. In: *Collision tectonics* (edited by Coward, M. P. & Ries, A. C.). *Special publications* **19**. Geological Society, London, 3-36.

Donovan, R. N., Archer, R., Turner, P. & Tarling, D. H. 1976. Devonian palaeogeography of the Orcadian Basin and the Great Glen Fault. *Nature* **259**, 550-551.

Doré, A. G. & Lundin, E. R. 1996. Cenozoic compressional structures on the NE Atlantic margin: Nature, origin and potential significance for hydrocarbon exploration. *Petroleum Geoscience* **2**(4), 299-311.

Doré, A. G., Lundin, E. R., Birkeland, O., Eliassen, P. E. & Jensen, L. N. 1997. The NE Atlantic Margin: implications of late Mesozoic and Cenozoic events for hydrocarbon prospectivity. *Petroleum Geoscience* **3**(2), 117-131.

Doré, A. G., Lundin, E. R., Fichler, C. & Olesen, O. 1997. Patterns of basement structure and reactivation along the NE Atlantic margin. *Journal of the Geological Society* **154**, 85-92.

Ehlen, J. 1999. Fracture characteristics in weathered granite. *Geomorphology* **31**, 29-45.

Einstein, H. H. & Baecher, G. B. 1983. Probabilistic and Statistical Methods in Engineering Geology - Specific Methods and Examples Part 1: Exploration. *Rock Mechanics and Rock Engineering* **16**(1), 39-72.

Engelder, T. 1987. Joints and shear fractures in rock. In: *Fracture mechanics of rock* (edited by Atkinson, B. K.), 27-69.

Evans, J. P., Chester, F. M. & Li, G. 1994. Characterization of exhumed faults of the San Andreas fault system, southern California. In: *Fault populations*, (TSG conference proceedings) 79-81.

Feder, J. 1988. *Fractals*. Plenum.

Flinn, D. 1961. Continuation of the Great Glen Fault beyond the Moray Firth. *Nature* **191**, 589-591.

Flinn, D. 1967. The Metamorphic Rocks of the Southern Part of the Mainland of Shetland. *Journal of Geology* **5**(2), 251-290.

Flinn, D. 1969. A geological interpretation of the aeromagnetic maps of the continental shelf around Orkney and Shetland. *Journal of Geology* **6**(2), 279-292.

Flinn, D., May, F., Roberts, J. F. & Treagus, J. E. 1972. A revision of the stratigraphic succession of the East Mainland of Shetland. *Scottish Journal of Geology* **8**(4), 335-343.

Flinn, D. 1977. Transcurrent faults and associated cataclasis in Shetland. *Journal of the Geological Society* **133**, 231-248.

Flinn, D. 1985. The Caledonides of Shetland. In: *The Caledonide Orogen - Scandinavia and Related Areas* (edited by Gee, D. G. & Sturt, B. A.). John Wiley &Sons Ltd, 1159-1171.

Flinn, D. 1988. The Moine rocks of Shetland. In: *Later Proterozoic stratigraphy of the northern Atlantic regions* (edited by Winchester, J. A.). Chapman & Hall.

Flinn, D., Miller, J. A. & Roddom, D. 1991. The age of the Norwick hornblendic schists of the Unst and Fetlar and the obduction of the Shetland ophiolite. *Scottish Journal of Geology* **27**(1), 11-19.

Flinn, D. 1992. The History of the Walls Boundary Fault, Shetland - the Northward Continuation of the Great Glen Fault From Scotland. *Journal of the Geological Society* **149**, 721-726.

Fookes, P. G. & Denness, B. 1969. Observational studies on fissure patterns in Cretaceous sediments of south-east England. *Geotechnique* **19**(4), 453-477.

Fossen, H. 1989. Indication of transpressional tectonics in the Gullfaks oil-field, northern North Sea. *Marine and Petroleum Geology* **6**(1), 22-30.

Gabrielsen, R. H. & Ramberg, I. B. 1979. Fracture patterns in Norway from Landsat imagery: results and potential use. In: *Proceedings of the Norwegian Sea Symposium*, Trømso, Norway.

Gabrielsen, R. H., Aarland, R. K. & Alsaker, E. 1998. Identification and spatial distribution of fractures in porous, siliciclastic sediments. In: *Structural geology in reservoir characterization* (edited by Coward, M. P., Daltaban, T. S. & Johnson, H.). *Special publications* **127**. Geological society, London, 49-64.

Gabrielsen, R. H., Odinsen, T. & Grunnaleite, I. 1999. Structuring of the Northern Viking Graben and the Møre Basin; the influence of basement structural grain, and the particular role of the Møre-Trøndelag Fault Complex. *Marine and Petroleum Geology* **16**(5), 443-465.

Gauthier, B. D. M. & Lake, S. D. 1993. Probabilistic Modeling of Faults Below the Limit of Seismic Resolution in Pelican Field, North Sea, Offshore United Kingdom. *AAPG Bulletin* **77**(5), 761-777.

Gee, D. G., Guezou, J. C., Roberts, D. & Wolff, F. C. 1985. The central-southern part of the Scandinavian Caledonides. In: *The caledonide orogen - scandinavia and related areas* (edited by Gee, D. G. & Sturt, B. A.). J. Wiley & Sons Ltd.

Gervais, F., Gentier, S. & Chiles, J. P. 1995. Geostatistical analysis and hierarchical modeling of a fracture network in a stratified rock mass. In: *Fractured and jointed rock masses* (edited by Myer, L. R., Cook, N. G. W., Goodman, R. E. & Tsang, C.). Balkema, Rotterdam.

Ghosh, A. & Daemen, J. J. K. 1993. Fractal characteristics of rock discontinuities. *Engineering geology* **34**, 1-9.

Gillespie, P. A., Howard, C. B., Walsh, J. J. & Watterson, J. 1993. Measurement and characterisation of spatial distributions of fractures. *Tectonophysics* **226**, 113-141.

Gillespie, P. A., Johnston, J. D., Loriga, M. A., McCaffrey, K. J. W., Walsh, J. J. & Watterson, J. 1999. Influence of layering on vein systematics in line samples. In: *Fractures, fluid flow and mineralization* (edited by McCaffrey, K. J. W., Lonergan, L. & Wilkinson, J. J.). *Special publications* **155**. Geological society, London, 35-56.

Gillespie, P. A., Walsh, J. J., Watterson, J., Bonson, C. G. & Manzocchi, T. 2001. Scaling relationships of joint and vein arrays from the Burren, Co. Clare, Ireland. *Journal of structural geology* **23**, 183-201.

Gilotti, J. A. & Hull, J. M. 1993. Kinematic stratification in the hinterland of the central Scandinavian Caledonides. *Journal of structural geology* **15**, 629-646.

Goldstein, A. & Marshak, S. 1988. Analysis of fracture array geometry. In: *Basic methods of structural geology* (edited by Marshak, S. & Mitra, G.). Prentice-Hall, 249-264.

Grønlie, A. & Torsvik, T. H. 1989. On the Origin and Age of Hydrothermal Thorium-Enriched Carbonate Veins and Breccias in the Møre-Trøndelag Fault Zone, Central Norway. *Norsk Geologisk Tidsskrift* **69**(1), 1-19.

Grønlie, A. & Roberts, D. 1989. Resurgent Strike-Slip Duplex Development Along the Hitra-Snasa and Verran Faults, Møre-Trøndelag Fault Zone, Central Norway. *Journal of Structural Geology* **11**(3), 295-305.

Grønlie, A., Nilsen, B. & Roberts, D. 1991. Brittle deformation history of fault rocks on the Fosen Peninsula, Trondelag, Central Norway. *NGU Bulletin* **421**, 39-57.

Grønlie, A., Naeser, C. W., Naeser, N. D., Mitchell, J. G., Sturt, B. A. & Ineson, P. R. 1994. Fission-Track and K-Ar Dating of Tectonic Activity in a Transect Across the Møre-Trøndelag Fault Zone, Central Norway. *Norsk Geologisk Tidsskrift* **74**(1), 24-34.

Gross, M. R., Fischer, M. P., Engelder, T. & Greenfield, R. J. 1995. Factors controlling joint spacing in interbedded sedimentary rocks: integrating numerical models with field observations from the Monterey Formation, USA. In: *Fractography: fracture topography as a tool in fracture mechanics and stress analysis* (edited by Ameen, M. S.). *Special publications* **92**. Geological society, London, 215-233.

Gudmundsson, A., Berg, S. S., Lyslo, K. B. & Skurtveit, E. 2001. Fracture networks and fluid transport in active fault zones. *Journal of structural geology* **23**, 343-353.

Hancock, P. L. 1985. Brittle Microtectonics - Principles and Practice. *Journal of Structural Geology* **7**(3-4), 437-457.

Harris, A. L. & Johnson, M. R. W. 1991. Moine. In: *Geology of Scotland* (edited by Craig, G. Y.). Geological Society, London.

Harris, A. L., Haselock, P. J., Kennedy, M. J. & Mendum, J. R. 1994. The Dalradian supergroup in scotland, Shetland and Ireland. In: *A revised correlation of precambrian rocks in the British Isles* (edited by Gibbons, W. & Harris, A. L.). Geological society.

Hastings, H. M. & Sugihara, G. 1993. *Fractals: a user's guide for the natural sciences.* Oxford University Press.

Hatton, C. G., Main, I. G. & Meredith, P. G. 1994. Non-universal scaling of fracture length and opening displacement. *Nature* **367**, 160-162.

Hays, W. L. & Winkler, R. L. 1971. *Statistics: probability, inference and decision.* Holt, Rinehart & Winston, New York.

Heffer, K. J. & Bevan, T. G. 1990. Scaling relationships in natural fractures - data, theory and applications. *Society of Petroleum Engineers* **20981**, 1-12.

Hesthammer, J., Johansen, T. E. S. & Watts, L. M. 2000. Spatial relationships within fault damage zones in sandstone. *marine and petroleum geology* **17**, 873-893.

Holdsworth, R. E., Strachan, R. A. & Harris, A. L. 1994. Precambrian rocks in northern scotland east of the Moine Thrust: the Moine supergroup. In: *A revised correlation of precambrian rocks in the british isles* (edited by Gibbons, W. & Harris, A. L.). Geological society.

Holdsworth, R. E., Butler, C. A. & Roberts, A. M. 1997. The recognition of reactivation during continental deformation. *Journal of the Geological Society* **154**, 73-78.

Holdsworth, R. E., Stewart, M., Imber, J. & Strachan, R. A. 2001. The structure and rheological evolution of reactivated continental fault zones: a review and case study. In: *Continental Reactivation and Reworking* (edited by Miller, J. A., Holdsorth, R. E., Buick, I. S. & Hand, M.). *Special Publication* **184**. Geological Society, London, 115-137.

Hudson, J. A. & Priest, S. D. 1979. Discontinuities and rock mass geometry. *International Journal of Rock Mechanics and Mining Sciences* **16**, 339-362.

Hudson, J. A. & Priest, S. D. 1983. Discontinuity Frequency in Rock Masses. *International Journal of Rock Mechanics and Mining Sciences* **20**(2), 73-89.

Imber, J., Holdsworth, R. E., Butler, C. A. & Lloyd, G. E. 1997. Fault-zone weakening processes along the reactivated Outer Hebrides Fault Zone, Scotland. *Journal of the Geological Society* **154**, 105-109.

Imber, J., Holdsworth, R. E., Butler, C. A. & Strachan, R. A. 2001. A reappraisal of the Sibson-Scholz fault zone model: The nature of the frictional to viscous ("brittle-ductile") transition along a long-lived, crustal-scale fault, Outer Hebrides, Scotland. *Tectonics* **20**(5), 601-624.

Jackson, P. 1994. Fracture populations in the Curraghinalt gold mine, Co. Tyrone: effects of depth and lithology. In: *Fault populations*, (TSG conference proceedings) 127-129.

Ji, S. & Saruwatari, K. 1998. A revised model for the relationship between joint spacing and layer thickness. *Journal of structural geology* **20**(11), 1495-1508.

Johnson, M. R. W. 1991. Dalradian. In: *Geology of Scotland* (edited by Craig, G. Y.). Geological Society, London.

Johnson, H., Richards, P. C., Long, D. & Graham, C. C. 1993. *The geology of the northern north sea.* BGS, London.

Kanji, G. K. 1993. *100 statistical tests.* Sage, London.
Kelly, P. G., Sanderson, D. J. & Peacock, D. C. P. 1998. Linkage and evolution of conjugate strike-slip fault zones in limestones of Somerset and Northumbria. *Journal of structural geology* **20**(11), 1477-1493.

Kimbell, G. S., Chadwick, R. A., Holliday, D. W. & Werngren, O. C. 1989. The structure and evolution of the Northumberland Trough from new seismic reflection data and its bearing on modes of continental extension. *Journal of the Geological Society* **146**, 775-787.

Knipe, R. J. 1989. Deformation mechanisms - recognition from natural tectonites. *Journal of Structural Geology* **11**, 127-146.

Knipe, R. J., Jones, G. & Fisher, Q. J. 1998. Fauting, fault sealing and fluid flow in hydrocarbon reservoirs: an introduction. In: *Faulting, fault sealing and fluid flow in hydrocarbon reservoirs* (edited by Jones, G., Fisher, Q. J. & Knipe, R. J.). *Special publications* **147**. Geological society, London, vii-xxi.

Knott, S. D., Beach, A., Brockbank, P. J., Lawson Brown, J., McCallum, J. & Welbon, A. 1994. Spatial and mechanical controls on fault populations. In: *Fault populations*, (TSG conference proceedings) 61-63.

Knott, S. D., Beach, A., Brockbank, P. J., Lawson Brown, J., McCallum, J. E. & Welbon, A. I. 1996. Spatial and mechanical controls on normal fault populations. *Journal of structural geology* **18**(2/3), 359-372.

Korvin, G. 1992. *Fractal models in the earth sciences.* Elsevier Science, Amsterdam, London.

Kruhl, J. H. 1994. Fractals and dynamic systems in geoscience. Springer-Verlag, Berlin, New York.

Kulatilake, P. H. S. W. & Wu, T. H. 1984. Estimation of mean trace length of discontinuities. *Rock mechanics and rock engineering* **17**, 215-232.

La Pointe, P. R. 1988. A Method to Characterize Fracture Density and Connectivity through fractal geometry. *International Journal of Rock Mechanics and Mining Sciences* **25**(6), 421-429.

Landes, K. K., Amoruso, J. J., Charlesworth, L. J., Heany, F. & Lesperance, P. J. 1960. Petroleum resources in basement rocks. *AAPG Bulletin* **44**(10), 1682-1691.

Laslett, G. M. 1982. Censoring and edge effects in areal and line transect sampling of rock joint traces. *Mathematical geology* **14**(2), 125-140.

Line, C. E. R., Snyder, D. B. & Hobbs, R. W. 1997. The sampling of fault populations in dolerite sills of Central Sweden and implications for resolution of seismic data. *Journal of structural geology* **19**(5), 687-701.

Long, J. C. S. & Witherspoon, P. A. 1985. The relationship of the degree of interconnection to permeability in fracture networks. *Journal of geophysical research* **90**(B4), 3087-3098.

Long, J. C. S. & Billaux, D. M. 1987. From Field Data to Fracture Network Modeling: an Example Incorporating Spatial Structure. *Water Resources Research* **23**(7), 1201-1216.

Mabee, S. B. & Hardcastle, K. C. 1997. Analyzing outcrop-scale fracture features to supplement investigations of bedrock aquifers. *Hydrogeology Journal* **5**(4), 21-36.

Main, I. G., Leonard, T., Papasouliotis, O., Hatton, C. G. & Meredith, P. G. 1999. One slope or two? detecting statistically significant breaks of slope in geophysical data, with application to fracture scaling relationships. *Geophysical research letters* **26**(18), 2801-2804.

Main, I., Mair, K., Kwon, O., Elphick, S. & Ngwenya, B. 2001. Experimental constraints on the mechanical and hydraulic properties of deformation bands in porous sandstones: a review. In: *The nature and tectonic significance of fault zone weakening.* (edited by Holdsworth, R. E., Strachan, R. A., Magloughlin, J. F. & Knipe, R. J.). *Special Publications* **186**. Geological Society, London, 195-211.

Malthe-Sorenssen, A., Walmann, T., Jamtveit, B., Feder, J. & Jossang, T. 1998. Modeling and characterization of fracture patterns in the Vatnajokull glacier. *Geology* **26**(10), 931-934.

Maltman, A. 1994. On the term "soft-sediment deformation". *Journal of Structural Geology* **6**(5), 589-592.

Mandelbrot, B. B. 1967. How long is the coast of Britain? Statistical self-similarity and fractional dimension. *Science* **156**, 636-639.

Mandelbrot, B. B. 1977. *Fractals, form, chance and dimension.* W. H. Freeman, San Francisco.

Mandelbrot, B. B. 1982. *The fractal geometry of nature.* W. H. Freeman, San Francisco.

Manzocchi, T., Ringrose, P. S. & Underhill, J. R. 1998. Flow through fault systems in high-porosity sandstones. In: *Structural geology in reservoir characterization* (edited by Coward, M. P., Daltaban, T. S. & Johnson, H.). *special publications* **127**. Geological society, London, 65-82.

Marrett, R. & Allmendinger, R. W. 1991. Estimates of strain due to brittle faulting: sampling of fault populations. *Journal of structural geology* **13**(6), 735-738.

Marrett, R. 1994. Some sampling effects and artifacts of fault population analysis. In: *Fault populations*, (TSG conference proceedings) 11-13.

Marrett, R. 1996. Aggregate properties of fracture populations. *Journal of structural geology* **18**(2/3), 169-178.

Mathab, A., Xu, S. & Grasso, P. 1995. Use of alternative distributions for characterizing joint extent and spacing. In: *Fractured and jointed rock masses* (edited by Myer, L. R., Cook, N. G. W., Goodman, R. E. & Tsang, C.). Balkema, Rotterdam.

Mauldon, M., Dunne, W. M. & Rohrbaugh, M. B. 2001. Circular scanlines and circular windows: new tools for characterising the geometry of fracture traces. *Journal of Structural Geology* **23**, 247-258.

McAllister, E. 1994. Investigation of fault populations within and between slow spreading ridges. In: *Fault populations*, (TSG conference proceedings) 14-16.

McBride, J. H. 1994. Structure of a continental strike-slip fault from deep seismic reflection: Walls Boundary fault, northern British Caledonides. *Journal of Geophysical Research* **99**(B12), 23985-24005.

McCaffrey, K. J. W., Johnston, J. D. & Loriga, M. A. 1994. Variation of fractal dimension in vein systems. In: *Fault populations*, (TSG conference proceedings) 103-105.

McCaffrey, K. J. W. & Johnston, J. D. 1996. Fractal analysis of a mineralised vein deposit: Curraghinalt gold deposit, County Tyrone. *Mineralium Deposita* **31**(1-2), 52-58.

McCaffrey, K. J. W., Beacom, L., Holdsworth, R. E. & Sleight, J. M. 2001. Characterisation of fracture systems in onshore analogues of crystalline reservoirs. In: *Hydrocarbons in crystalline rocks*, (Geol. Soc. conference proceedings) London.

McCaffrey, K. J. W., Sleight, J. M., Pugliese, S. & Holdsworth, R. E. in prep. Fractures in crystalline rocks: Insights from spatial attribute data. In: *Characterisation of fractured basement reservoirs* (edited by Petford, N., McCaffrey, K. J. W. & Murray, T.). *Special publications*. Geological Society, London.

McGeary. 1989. Reflection seismic evidence for a Moho offset beneath the Walls Boundary strike-slip fault. *Journal of the Geological Society* **146**, 261-269.

McGrath, A. G. & Davidson, I. 1995. Damage zone geometry around fault tips. *Journal of structural geology* **17**(7), 1011-1024.

Means, W. D. 1987. A newly recognised type of slickenside striation. *Journal of structural geology* **9**(5/6), 585-590.

Miller, R. & Kahn, J. S. 1962 *Statistical analysis in the geological sciences* Wiley, New York

Miller, J. C. & Miller, J. N. 1989. *Statistics for analytical chemistry*. E. Horwood, New York.

Moller, C. 1988. Geology and metamorphic evolution of the Roan area, Vestranden, Western Gneiss region, central Norwegian Caledonides. *Norges geologiske undersokelse Bulletin* **413**, 1-31.

Mykura, W. 1976. *British Regional Geology - Orkney and Shetland.* BGS, Edinburgh.

Mykura, W. & Phemister, J. 1976. *The Geology of Western Shetland.* BGS, Edinburgh.

Mykura, W. 1991. Old Red Sandstone. In: *Geology of Scotland* (edited by Craig, G. Y.). Geological Society, London.
Narr, W. & Lerche, I. 1984. A method for estimating subsurface fracture density in core. *AAPG Bulletin* **68**(5), 637-648.

Narr, W. & Suppe, J. 1991. Joint spacing in sedimentary rocks. *Journal of structural geology* **13**(9), 1037-1048.

Narr, W. 1991. Fracture density in the deep subsurface: techniques with application to Point Arguello oil field. *AAPG Bulletin* **75**(8), 1300-1323.

Narr, W. 1996. Estimating average fracture spacing in subsurface rock. *AAPG Bulletin* **90**(10), 1565-1586.

Needham, T., Yielding, G., Fox, R. 1996. Fault population description and prediction using examples from the offshore U.K. *Journal of structural geology* **18**(2/3), 155-167.

Needham, D. T., Yielding, G. & Freeman, B. 1996. Analysis of fault geometry and displacement patterns. In: *Modern developments in structural interpretation, validation and modeling* (edited by Buchanan, P. G. & Nieuwland, D. A.). *special publications* **99**. Geological society, London, 189-199.

Nelson, R. A. 1979. Natural fracture systems: description and classification. *AAPG Bulletin* **63**(12), 2214-2232.

Nelson, R. A. 1982. An approach to evaluating fractured reservoirs. *Journal of Petroleum Technology* **34**(9), 2167-2170.

Nelson, R. A. 1985. *Geologic analysis of naturally fractured reservoirs.* Gulf Publishing Company, Houston

Nelson, R. A. 1987. Fractured reservoirs: turning knowledge into practice. *Journal of Petroleum technology* **39**, 407-414.

Neuzil, C. & Tracy, J. 1981 Flow through fractures. *Water resources research* **17**(1),191-199

Nicol, A., Walsh, J. J., Watterson, J. & Gillespie, P. 1996. Fault size distributions - Are they really power-law? *Journal of Structural Geology* **18**(2-3), 191-197.

Norton, M. G., McClay, K. R. & Way, N. A. 1987. Tectonic evolution of Devonian basins in northern Scotland and southern Norway. *Norsk Geologisk Tidsskrift* **67**, 323-338.

O'Leary, D.W., Friedman, J. D. & Pohn, H. 1976. Lineament, linear, lineation;some proposed new standards for old terms.*Geological Society of America Bulletin* **87**(10), 1463-1469

Odling, N. 1995. The development of network properties in natural fracture patterns: An example from the Devonian sandstones of western Norway. In: *Fractured and jointed rock masses* (edited by Myer, L. R., Cook, N. G. W., Goodman, R. E. & Tsang, C.). Balkema, Rotterdam.

Odling, N. E. 1997. Scaling and connectivity of joint systems in sandstones from western Norway. *Journal of Structural Geology* **19**(10), 1257-1271.

Odling, N. E. & Roden, J. E. 1997. Contaminant transport in fractures rocks with significant matrix permeability, using natural fracture geometries. *Journal of contaminant hydrology* **27**, 263-283.

Odling, N. E., Gillespie, P., Bourgine, B., Castaing, C., Chiles, J. P., Christensen, N. P., Fillion, E., Genter, A., Olsen, C., Thrane, L., Trice, R., Aarseth, E., Walsh, J. J. & Watterson, J. 1999. Variations in fracture system geometry and their implications for fluid flow in fractured hydrocarbon reservoirs. *Petroleum Geoscience* **5**(4), 373-384.

Park, R. G. 1997. *Foundations of structural geology.* Chapman & Hall, London.

Pascal, C., Angelier, J., Cacas, M. C. & Hancock, P. 1997. Distribution of joints: probabilistic modeling and case study near Cardiff (Wales. U.K.). *Journal of structural geology* **19**(10), 1273-1284.

Passchier, C. W. & Trouw, R. A. J. 1996. *Micotectonics.* Springer-Verlag, Berlin.

Peacock, D. C. P. & Sanderson, D. J. 1992. Effects of Layering and Anisotropy On Fault Geometry. *Journal of the Geological Society* **149**, 793-802.

Peacock, D. C. P. 1996. Field examples of variations in fault patterns at different scales. *Terra Nova* **8**, 361-371.

Pickering, G., Bull, J. M. & Sanderson, D. J. 1995. Sampling Power-Law Distributions. *Tectonophysics* **248**(1-2), 1-20.

Pickering, G., Peacock, D. C. P., Sanderson, D. J. & Bull, J. M. 1997. Modeling tip zones to predict the throw and length characteristics of faults. *AAPG Bulletin* **81**(1), 82-99.

Pollard, D. D. & Aydin, A. 1988. Progress in Understanding Jointing Over the Past Century. *Geological Society of America Bulletin* **100**(8), 1181-1204.

Poulimenos, G. 2000. Scaling properties of normal fault populations in the western Corinth Graben, Greece: implications for fault growth in large strain settings. *Journal of structural geology* **22**, 307-322.

Price, N. J. & Cosgrove, J. W. 1991. *Analysis of geological structures.* Cambridge University Press.

Priest, S. D. & Hudson, J. A. 1976. Discontinuity spacings in rock. *International Journal of*

Roddom, D. S., Miller, J. A. & Flinn, D. 1989. Permo-carboniferous mylonite formation in the Walls Boundary Fault system, Shetland. *Proceedings of the Yorkshire Geological Society* **47**(4), 339-343.

Rogers, D. A., Marshall, J. E. A. & Astin, T. R. 1989. Devonian and Later Movements On the Great Glen Fault System, Scotland. *Journal of the Geological Society* **146**, 369-372.

Rogers, J. D. 1994. Scaling relationships of lineament populations from Landsat imagery, South West England. In: *Fault populations*, (TSG conference proceedings) 82-84.

Rouleau, A. & Gale, J. E. 1985. Statistical Characterization of the Fracture System in the Stripa granite, Sweden. *International Journal of Rock Mechanics and Mining Sciences* **22**(6), 353-367.

Ruf, J. C., Rust, K. A. & Engelder, T. 1998. Investigating the effect of mechanical discontinuities on joint spacing. *Tectonophysics* **295**(1-2), 245-257.

Rutter, E. H., Holdsworth, R. E. & Knipe, R. J. 2001. The nature and tectonic significance of fault-zone weakening: an introduction. In: *The Nature and tectonic significance of fault zone weakening* (edited by Holdsworth, R. E., Strachan, R. A., Magloughlin, J. F. & Knipe, R. J.). *Special publications* **186**. Geological Society, London, 1-11.

Schultz, R. A. & Fori, A. N. 1996. Fault-length statistics and implications of graben sets at Candor Mensa, Mars. *Journal of structural geology* **18**(2/3), 373-383.

Schultz, R. A. 2000. Growth of geologic fractures into large-strain populations: review of nomenclature, subcritical crack growth, and some implications for rock engineering. *International Journal of Rock Mechanics and Mining Sciences* **37**, 403-411.

Schulz, S. E. & Evans, J. P. 2000. Mesoscopic structure of the Punchbowl fault, Southern California and the geologic and geophysical structure of active strike-slip faults. *Journal of structural geology* **22**, 913-930.

Segall, P. & Pollard, D. D. 1983. Joint formation in granitic rock of the Sierra Nevada. *Geological Society of America Bulletin* **94**, 563-575.

Sen, Z. & Kazi, A. 1984. Discontinuity Spacing and RQD Estimates From Finite Length Scanlines. *International Journal of Rock Mechanics and Mining Sciences* **21**(4), 203-212.

Seranné, M. 1992. Devonian extensional tectonics versus Carboniferous inversion in the northern Orcadian basin. *Journal of the Geological Society* **149**, 27-37.

Seranné, M. 1992. Late Paleozoic kinematics of the Møre-Trøndelag Fault Zone and adjacent areas, Central Norway. *Norsk Geologisk Tidsskrift* **72**(2), 141-158.

Sibson, R. H. 1977. Fault rocks and fault mechanisms. *Journal of the Geological Society* **133**, 191-213.

Simpson, C. & Schmid, S. M. 1983. An evaluation of criteria to deduce the sense of movement in deformed rocks. *Geological Society of America Bulletin* **94**, 1281-1288.

Skamvetsaki, A. 1994. Spatial characterisation of fault zones in Yellow Permian Sandstones, Northumberland, NE England. In: *Fault populations*, 85-86.

Smith, L. & Schwartz, F. W. 1984. An analysis of the influence of fracture geometry on mass transport in fractured media. *Water resources research* **20**(9), 1241-1252.

Smith, P. M. 1995. Geological setting of mineralization along the Verran Fault Zone, central Norway. Unpublished PhD thesis, Imperial College of Science, Technology and Medicine.

Sornette, A., Davy, P. & Sornette, D. 1990. Growth of fractal fault patterns. *Physical review letters* **65**(18), 2266-2269.

Stauffer, D. & Aharony, A. 1994. *Introduction to percolation theory*. Taylor & Francis, London.

Stearns, D. W. & Friedman, M. 1972. Reservoirs in fractured rock. In: *Stratigraphic oil and gas fields; Classification, Exploration Methods, and Case Histories* **16**. AAPG memoir, Tusla, Oklahoma, 82-106.

Stewart, M., Strachan, R. A. & Holdsworth, R. E. 1999. Structure and early kinematic history of the Great Glen Fault Zone, Scotland. *Tectonics* **18**(2), 326-342.

Stewart, M., Holdsworth, R. E. & Strachan, R. A. 2000. Deformation processes and weakening mechanisms within the frictional-viscous transition zone of major crustal-scale faults: Insights from the Great Glen Fault Zone, Scotland. *Journal of Structural Geology* **22**, 543-560.

Surlyk, F. 1990. Timing, style and sedimentary evolution of late Palaeozoic-Mesozoic extensional basins of East Greenland. In: *Proceedings of Tectonic events responsible for Britain's oil and gas reserves* (edited by Hardman, R. F. P. & Brooks, J.). *Special Publications* **55**. Geological Society, London, 107-125.

Swan, A. R. H. & Sandilands, M. 1995. *Introduction to geological data analysis*. Blackwell Science Ltd.

Tchalenko. 1970. Similarities between different shear zones of different magnitudes. *Geological Society of America Bulletin* **81**, 1625-1640.

Torsvik, T. H., Sturt, B. A., Ramsay, D. A., Grønlie, A., Roberts, D., Smethurst, M., Atakan, K., Boe, R. & Walderhaug, H. J. 1989. Palaeomagnetic constraints on the early history of the Møre-Trøndelag Fault Zone, Central Norway. In: *Palaeomagnetic Rotations and Continental Deformation* (edited by Kissel, K. & Laj, C.). Kluwer Academic Publishers, 431-457.

Turcotte, D. L. 1992. Fractals, Chaos, Self-Organized Criticality and Tectonics. *Terra Nova* **4**(1), 4-12.

Twiss, R. J. & Moores, E. M. 1992. *Structural geology.* W. H. Freeman, New York.

Uemura, T. & Mizutani, S. 1984. Geological structures. John Wiley & Sons Ltd, Chichester.

Vignes-Adler, M., Le Page, A. & Alder, P. M. 1991. Fractal Analysis of Fracturing in two African Regions, From satellite imagery to ground scale. *Tectonophysics* **196**(1-2), 69-86.
Wallis, P. F. & King, M. S. 1980. Discontinuity spacings in a crystalline rock. *International Journal of Rock Mechanics and Mining Sciences* **17**, 63-66.

Walsh, J. J. & Watterson, J. 1987. Displacement Efficiency of Faults and Fractures - Discussion. *Journal of Structural Geology* **9**(8), 1051-1052.

Walsh, J. J. & Watterson, J. 1989. Displacement gradients on fault surfaces. *Journal of structural geology* **11**(3), 307-316.

Walsh, J. J., Watterson, J. & Yielding, G. 1991. Determination of Fault Populations Below the Limit of Seismic resolution for reservoir models. *AAPG Bulletin* **75**(3), 688-689.

Walsh, J. J. & Watterson, J. 1993. Fractal Analysis of Fracture Patterns Using the Standard Box-counting technique: valid and invalid methodologies. *Journal of Structural Geology* **15**(12), 1509-1512.

Walsh, J. J., Watterson, J. & Yielding, G. 1994. Determination and interpretation of fault size populations: procedures and problems. In: *North Sea Oil and Gas reservoirs* **3**. Kluwer Academic Publishers, 141-155.

Walsh, J. J., Childs, C., Meyer, V., Manzocchi, T., Imber, J., Nicol, A., Tuckwell, G., Bailey, W. A., Bonson, C. G., Watterson, J., Nell, P. A. & Strand, J. 2001. Geometric controls on the evolution of normal fault systems. In: *The nature and tectonic significance of fault zone weakening* (edited by Holdsworth, R. E., Strachan, R. A., Magloughlin, J. F. & Knipe, R. J.). *Special publications* **186**. Geological Society, London, 157-170.

Wantanabe, K. & Takahashi, H. 1995. Fractal geometry characterisation of geothermal reservoir fracture networks. *Journal of geophysical research* **100**(B1), 521-528.

Watterson, J., Walsh, J. J., Gillespie, P. A. & Easton, S. 1996. Scaling systematics of fault sizes on a large-scale range fault map. *Journal of structural geology* **18**(2/3), 199-214.

Watts, L. M. 2001. The Walls Boundary Fault Zone and the Møre Trøndelag Fault Complex: a case study of reactivated fault zones. Unpublished PhD thesis, University of Durham.

White, S. H., Burrows, S. E., Carreras, N. D., Shaw, N. D. & Humphreys, F. J. 1980. On mylonites in ductile shear zones. *Journal of Structural Geology* **2**(1/2), 175-187.

Woodcock, N. H. & Naylor, M. A. 1983. Randomness testing in three-dimensional orientation data. *Journal of Structural Geology* **5**(5), 539-548.

Wu, H. & Pollard, D. D. 1992. Modeling a Fracture Set in a Layered Brittle Material. *Engineering Fracture Mechanics* **42**(6), 1011-1017.

Yielding, G., Needham, T. & Jones, H. 1996. Sampling populations using sub-surface data: a review. *Journal of structural geology* **19**(2/3), 135-146.

Younes, A. I., Engelder, T. & Bosworth, W. 1998. Fracture distribution in faulted basement blocks: Gulf of Suez, Egypt. In: *Structural geology in reservoir characterization* (edited by Coward, M. P., Daltaban, T. S. & Johnson, H.). *Special publications* **127**. Geological Society, London, 167-190.

Zhang, X. & Sanderson, D. J. 1996. Numerical modeling of the effects of fault slip on fluid flow around extensional faults. *Journal of structural geology* **18**(1), 109-119.

Zhang, X. & Sanderson, D. J. 1998. Numerical study of critical behavior of deformation and permeability of fractured rock masses. *Marine and Petroleum Geology* **15**(6), 535-548.

Zhang, L. & Einstein, H. H. 2000. Estimating the intensity of rock discontinuities. *International Journal of Rock Mechanics and Mining Sciences* **37**, 819-837.

Ziegler, P. A. 1981. Evolution of sedimentary basins in North-West Europe. In: *Petroleum geology of the continental shelf of north-west europe* (edited by Illing, L. V. & Hobson, G. D.).

Ziegler, P. A. 1985. Late Caledonian framework of western and central Europe. In: *The Caledonide Orogen-Scandinavian and Related Areas* (edited by Gee, D. G. & Sturt, B. A.). John Wiley & Sons.